UNIVERSITY OF CALIFORNIA, SAN DIEGO

New Approaches for the Chemical and Physical Characterization of Aerosols Using a Single Particle Mass Spectrometry Based Technique

A dissertation submitted in partial satisfaction of the requirements for the degree

Doctor of Philosophy

in

Chemistry

by

Matthew Todd Spencer

Committee in charge:

Professor Kimberly A. Prather, chair
Professor Andrew C. Kummel
Professor Emmanuel A. Theodorakis
Professor Mark H. Thiemens
Professor Ray F. Weiss

2007

This dissertation of Matthew Todd Spencer is approved and acceptable in quality and form for publication on microfilm:

_____

_____

_____

_____

_____

Chair

University of California, San Diego

2007

Dedicated to mediocre high school students around the world

After one look at this planet any visitor from outer space would say 'I want to see the manager.'

William S. Burroughs

Table of Contents

Signature Page iii

Dedication iv

Epigraph v

Table of contents vi

List of figures xi

List of tables xv

Acknowledgements xvi

Vita, publications, and fields of study xxi

Abstract xxiii

1 Introduction 1

1.1 Aerosols 1

1.2 ATOFMS background 4

1.2.1 A brief history of ATOFMS 4

1.2.2 The ATOFMS instrument 5

1.2.3 ATOFMS aerosol inlet 8

1.2.4 ATOFMS aerosol velocity and size measurement region 10

1.2.5 Laser desorption/ionization time-of-flight mass spectrometry 12

1.3 Scope of this thesis 12

1.4 References 16

2 Comparison of Oil and Fuel Particle Chemical Signatures with Particle Emissions from Heavy and Light Duty Vehicles 21
2.1 Synopsis 21
2.2 Introduction 22
2.3 Methods 24
2.3.1 Single particle analysis: ATOFMS 24
2.3.2 Fuel and oil particle generation 24
2.3.3 LDV and HDDV sampling 25
2.3.4 ATOFMS data analysis 27
2.4 Results and discussion 27
2.4.1 New and used oil samples 28
2.4.2 Diesel fuel samples 33
2.4.3 Unleaded fuel samples 33
2.4.4 Comparison with PM emissions 38
2.5 Conclusions 42
2.6 Acknowledgements 43
2.7 References 44
3 Using ATOFMS to Determine OC/EC Mass Fractions in Particles 50
3.1 Synopsis 50
3.2 Introduction 51
3.3 Experimental 54
3.3.1 Particle generation 54
3.3.2 Data analysis 57

3.3.3 Ambient data collection 57
3.4 Results and discussion 58
3.4.1 Uncoated and OC coated electrical mobility size distributions 58
3.4.2 Calculation of EC and OC mass 63
3.4.3 Determining OC and EC mass fractions from mass spectral ion intensities 69
3.5 Conclusions 79
3.6 Acknowledgements 81
3.7 References 82
4 Simultaneous Measurement of the Effective Density and Chemical Composition of Ambient Aerosol Particles 88
4.1 Synopsis 88
4.2 Introduction 89
4.3 Methods 91
4.3.1 DOS and NaCl particle methods 91
4.3.2 Differential mobility analyzer 91
4.3.3 Ultrafine aerosol time-of-flight mass spectrometry 93
4.3.4 Particle chemical classification 93
4.3.5 Ambient measurements 94
4.4 Results and discussion 95
4.4.1 Theory 95
4.4.2 Laboratory validation experiments 96

4.4.3 Ambient particle chemical composition 106
4.4.4 Effective density measurements 111
4.5 Acknowledgements 125
4.6 References 126
5 Size-resolved Chemical Composition of Aerosol Particles During a Monsoonal Transition Period over the Indian Ocean 131
5.1 Synopsis 131
5.2 Introduction 132
5.3 Experimental 135
5.3.1 Location 135
5.3.2 Aerosol characterization instrumentation 135
5.3.3 Data analysis 137
5.4 Results and discussion 138
5.4.1 Chemical composition 141
5.4.2 Temporal trends 147
5.5 Conclusion 160
5.6 Acknowledgements 161
5.7 References 163
6 Gold Nanoparticles as a Matrix for Visible Wavelength Single Particle Matrix-Assisted Laser Desorption/Ionization Mass Spectrometry of Small Molecules 168
6.1 Synopsis 168
6.2 Introduction 169

6.3 Experimental Section 173
6.3.1 Sample preparation 173
6.3.2 Single particle MALDI mass spectrometer 174
6.3.3 Data analysis 176
6.4 Results and discussion 177
6.4.1 Properties of sample particles 177
6.4.2 Aerosol particle mass spectra 177
6.4.3 Effect of GNP size 181
6.4.4 Effect of LDI laser wavelength and power 183
6.4.5 Analysis of sugars 187
6.4.6 VIS-MALDI using other metal particle matrices 190
6.5 Conclusion 192
6.6 Acknowledgements 193
6.7 References 194
7 Conclusion and Future Directions 198
7.1 Conclusion 198
7.2 Future directions 202
7.3 Final thought 205

List of Figures

Figure 1.1 Schematic of the original ATOFMS 6

Figure 1.2 Schematic of the transportable ATOFMS 7

Figure 1.3 Plot of the aerodynamic diameter versus particle velocity 11

Figure 2.1 Oil and fuel experimental setup 26

Figure 2.2 Positive and negative ion AM for chemical classes detected in new and used oil samples 29

Figure 2.3 Positive and negative ion AM for PAH-containing particle class detected exclusively in diesel fuel 34

Figure 2.4 Positive and negative ion AM for five particle types unique to unleaded fuel 36

Figure 2.5 Positive and negative ion AM for the OC-Na-Sulfate-Phosphate particle class detected in both diesel and unleaded fuel samples 37

Figure 2.6 Histogram showing the percent contribution of each particle class to each oil and fuel sample analyzed 39

Figure 2.7 Comparison of the AM from used oil with the AM from LDV and HDV mass spectra 40

Figure 3.1 General measurement set-up 56

Figure 3.2 Scanning mobility particle size distributions 60

Figure 3.3 SMPS scan of uncoated pure spark discharge soot 61

Figure 3.4 Spark discharge soot effective densities calculated from DMA and UF-ATOFMS data plotted versus particle mobility equivalent diameter 68

Figure 3.5 Average area matrix for uncoated spark discharge soot particles and fuel coated spark discharge soot particles 71
Figure 3.6 Calculated fraction of OC contained in each particle is plotted versus the OC/EC ratio from specific ion signals 74
Figure 3.7 The OC/EC ratio is plotted versus vacuum aerodynamic size for particles analyzed at three ambient locations 75
Figure 3.8 Ambient particle measurements taken during SOAR field campaign in Riverside, California 77
Figure 4.1 Vacuum aerodynamic size distribution of 300 nm electrical mobility size selected DOS particles 97
Figure 4.2 Measured vacuum aerodynamic diameter for DOS particles plotted versus the predicted vacuum aerodynamic diameter 99
Figure 4.3 Vacuum aerodynamic size distribution of 300 nm electrical mobility size selected NaCl particles 102
Figure 4.4 Positive and negative ion area matrix for chemical classes detected in Riverside, CA 110
Figure 4.5 Vacuum aerodynamic size distribution of 250 nm electrical mobility size selected ambient particles from Riverside, California 113
Figure 4.6 Pie charts for the particle chemical classes observed in two different vacuum aerodynamic modes during ambient sampling in Riverside, California 115
Figure 4.7 Effective density plotted versus electrical mobility diameter 117

Figure 4.8 Atmospheric water content is plotted versus the average effective density 119
Figure 4.9 The average effective density of particles sampled during SOAR on different days is plotted versus the ambient relative humidity 120
Figure 4.10 Vacuum aerodynamic size distribution of 450 nm electrical mobility size selected ambient particles from Riverside, California 123
Figure 5.1 Comparison of the number of particles hit using ATOFMS and the number of particles per cubic centimeter measured using an APS 139
Figure 5.2 Area matrices for the top eight particle classes 143
Figure 5.3 HYSPLIT back trajectories for six time periods during the APMEX campaign 148
Figure 5.4 The unscaled fraction of different supermicron particle chemical classes 149
Figure 5.5 The fraction of submicron particle chemical classes 152
Figure 5.6 Scaled size distributions for the top seven chemical classes 154
Figure 5.7 Temporal profile for the scaled particle number concentrations 155
Figure 5.8 Correlation between K-biomass and EC-sulfate particles measured during APMEX 160
Figure 6.1 Diagram of the method for generating aerosol particles containing metal nanoparticles 175
Figure 6.2 Positive average mass spectrum is shown for aerosol particles containing gold nanoparticles and the small peptide WGG 179

Figure 6.3 Average mass spectra from aerosol particles that contained different size gold nanoparticles 182
Figure 6.4 The percentage of particles that were hit is plotted versus the LDI wavelength 184
Figure 6.5 Peak area is plotted versus laser power for different desorption/ionization wavelengths 186
Figure 6.6 Stacked plots of the average mass spectrum generated from particles ionized at λ = 440, 500 and 540 nm 188
Figure 6.7 Average mass spectrum from aerosol particles containing a 5 nm gold nanoparticle matrix and D-ribose or L-arabinose 189
Figure 6.8 Average mass spectrum from aerosol particles containing 14 nm silver nanoparticles and the peptide WGG 191

List of Tables

Table 3.1 Average aerodynamic equivalent diameter for each mobility equivalent diameter selected for each experiment 64

Table 3.2 Calculated particle mass and OC mass from assumed material density 67

Table 3.3 Calculated particle mass and OC mass from effective density 70

Table 4.1 Measured values for DOS effective density at different electrical mobility diameters 100

Table 4.2 Measured values for NaCl effective density, shape factor, and particle density at different electrical mobility diameters 104

Table 6.1 Physical characteristics of the aerosol particles that contained 5 nm gold nanoparticles and the WGG peptide 178

Acknowledgements

It is astonishing how many people are willing to give their time and effort to help get your experiments to work, your numbers to crunch, your graphs to plot and your words to flow. Whole chapters could easily be written about the positive influence that numerous people have had on my life leading to this moment.

First and foremost I would like to thank Kim Prather for giving me the opportunity to learn from her and the rest of the Prather group. Kim has given me freedom and trust beyond what I could ask for. She helped teach me how to present, write, and think like a scientist. Kim has really helped open my eyes more to the big picture of both science and life; to keep in mind the larger repercussions of your work, your word and your actions. I know that I can always count on Kim for sound advice as I move on to new endeavors. Kim is more than just an advisor though she is also a friend.

Kim has also managed to associate herself with a fantastic group of people whom I had the great fortune of working with; Joe Meyer, Dr. Hiroshi Furutani, Dr. Yongxuan Su, Dr. Ryan Wenzel, Dr. Keith Coffee, Dr. Sergio Guazzotti, Dr. David Sodeman, Michelle Sipin, Steve Toner, John Holecek, Ryan Moffet, Laura Shields, Xueying "Sharon" Qin, Ryan Sullivan, Kerri Denkenberger, Andy Ault, Meagan Moore, Dr. Ying Wang, Lindsay Hatch, Dr. Thomas Rebotier, Rene Sanchez and Jessie Charrier. Everyone in the group helped me numerous times and in numerous ways throughout the last 5 years and I could not possibly discuss all of them specifically. However, a few group members I worked and interacted with closely and they should be acknowledged directly.

First is Dr. Ryan Wenzel. Ryan was an invaluable resource for learning about everything we do in the Prather lab during my first year. He was always willing to help, sometimes for hours, and he really taught me a lot. Ryan has one of the best attitudes about life and a great sense of humor.

Two post docs, Dr. Hiroshi Furutani and Dr. Yongxuan Su have helped me so much over the last five years. The amount of technical/scientific knowledge they hold and their willingness to share this wisdom with me (sometimes when I asked for it, sometimes when I did not) cannot be praised enough. Their kindness and friendship over the years has made graduate school an even more rewarding experience.

There are not too many people that I would enjoy being stuck on an island with, but John Holecek is one of those. John and I were sent to a remote island in the North Indian Ocean for over a month. John was a great person to be teamed up with. He is one of the most adventurous people I have worked with and it was a pleasure snorkeling, scuba diving, surfing, poking at scorpions, and running in the pouring rain with him…after all our work was done of course. I am grateful that I had the opportunity to work and learn from him.

Other scientists outside our group that I have been fortunate to work with and have helped me in various ways include: Professor V. Ramanathan, Dr. Craig Corrigan, Dr. Greg Roberts, Dr. Muvva Ramana, Professor Jose Jimenez, Professor Jamie Schauer, Dr. Dave Snyder, Professor Phil Hopke, Prasanna Venkatachari, Professor Paul Ziemann, Professor Gunter Oberdorster, Professor Allen Goldstein, Professor Judy Kim, Dr. Steven Oldenburg, and Dr. Thomas Darlington.

I would also like to thank my doctoral committee Professor Andy Kummel, Professor Mark Thiemens, Professor Emmanuel Theodorakis and Professor Ray Weiss for their role in helping me obtain this degree.

My family has also had an integral part in my success in graduate school. My parents Joe Spencer and Carole Weckbaugh gave me so much freedom to explore and ask questions as a kid it is no wonder I am a scientist. Furthermore, they never gave up helping me get back on track even though at a couple points I was clearly off. The problem solving, communication, creative thinking and logical reasoning skills they taught me are the foundation that everything else has been built on. I guess I should admit it, even my older sister Lori Alexander taught me a thing or two growing up which has helped me along the way.

My friend Paul Mueller had an enormous influence on my becoming a scientist. Throughout our adventures Paul always challenged me to take math and science. I don't owe my interest in chemistry to a great high school chemistry teacher, (I did not take high school chemistry…or physics or calculus for that matter) I owe my interest in chemistry to Paul.

Graduate school is a life changing journey even for people that are not graduate students, such as my wife. Andrea left her job and moved to San Diego to marry and be with me while I finished school. She has given me a huge amount of love, support, flexibility and great advice which has helped make my graduate school tenure the success it has been. All the dinners she brought to the lab so that I could work well into the night will not be forgotten. She is the perfect person to have by my side.

Chapter 2 has been published in full and is reprinted here with permission from Elsevier. Spencer, M.T., L.G. Shields, D.A. Sodeman, S.M. Toner, and K.A. Prather, Comparison of oil and fuel particle chemical signatures with particle emissions from heavy and light duty vehicles, Atmospheric Environment, 40 (27), 5224-5235, 2006.

Chapter 3 has been published in full and is reprinted here with permission from Taylor & Francis. Spencer, M.T., and K.A. Prather, Using ATOFMS to determine OC/EC mass fractions in particles, Aerosol Science & Technology, 40 (8), 585-594, 2006.

Chapter 4 has been published in full and is reprinted here with permission from American Chemical Society. Spencer, M.T., L.G. Shields, and K.A. Prather, Simultaneous measurement of the effective density and chemical composition of ambient aerosol particles, Environmental Science & Technology, 41 (4), 1303-1309, 2007b.

Chapter 5 has been submitted in full to Journal of Geophysical Research (Atmospheres) for publication in 2007. Spencer, M. T., J. C. Holecek, C. E. Corrigan, V. Ramanathan, K. A. Prather, Size-resolved chemical composition of individual particles during a monsoonal transition period in the north Indian Ocean, The text is reprinted with permission from American Geophysical Union.

Chapter 6, in full, is in preparation for submission to The Journal of Physical Chemistry-C for publication in 2007. Spencer, M.T., H. Furutani, S. J. Oldenburg, T. Darlington, K. A. Prather, Gold nanoparticles as a matrix for visible wavelength single particle matrix-assisted laser desorption/ionization mass spectrometry of small molecules, The text is reprinted with permission from American Chemical Society.

The work in this dissertation was supported by the California Air Resources Board, Environmental Protection Agency, United Nations Environmental Programme and the National Oceanic & Atmospheric Administration.

Vita

2000	B.S. Chemistry- Colorado State University
2000	B.S. Biochemistry- Colorado State University
2000-2002	Research associate, Dept. of Pharmaceutics, Amgen Inc. Thousand Oaks, California
2003-2004	Teaching assistant, Dept. of Chemistry & Biochemistry, University of California San Diego
2007	Ph.D. in Chemistry, University of California, San Diego
2007-	Senior Scientist, nanoComposix Inc., San Diego, California

Publications

Spencer, M. T.; Furutani, H.; Oldenburg S.; Darlington T.; Prather, K. A. Gold nanoparticles as a matrix for visible wavelength single particle matrix-assisted laser desorption/ionization mass spectrometry of small molecules, *in preparation,* 2007

Spencer, M. T.; Holecek, J. C.; Corrigan, C. E.; Ramanathan, V.; Prather, K. A. Size-resolved chemical composition of individual particles during a monsoonal transition period in the north Indian Ocean. *Journal of Geophysical Research-Atmospheres.* Submitted March 2007

Holecek, J. C.; Spencer, M. T.; Prather, K. A. Single particle analysis of rainwater samples: insoluble particles and direct comparisons with ambient concentrations from the Northeast Pacific and Indian Ocean. *Journal of Geophysical Research-Atmospheres.* Accepted, February 2007

Spencer, M. T.; Shields, L. G.; Prather, K. A. Simultaneous measurement of the effective density and chemical composition of ambient aerosol particles. *Environmental Science and Technology.* 2007, *41*(4) pp 1303 – 1309

Spencer, M. T.; Shields, L. G.; Sodeman, D. A.; Toner, S. M.; Prather, K. A. Comparison of oil and fuel particle chemical signatures with particle emissions from heavy and light duty vehicles. *Atmospheric Environment.* 2006, *40*, 5224-5235.

Spencer, M. T.; Prather, K. A. Using ATOFMS to determine OC/EC mass fractions in particles. *Aerosol Science and Technology,* 2006, *40*, 585-594.

Su, Y. X.; Sipin, M. F.; Spencer, M. T.; Qin, X. Y.; Moffet, R. C.; Shields, L. G.; Prather, K. A.; Venkatachari, P.; Jeong, C. H.; Kim, E.; Hopke, P. K.; Gelein, R. M.; Utell, M. J.; Oberdorster, G.; Berntsen, J.; Devlin, R. B.; Chen, L. C. Real-time characterization of the composition of individual particles emitted from ultrafine particle concentrators. *Aerosol Science and Technology,* 2006, *40*, 437-455.

Fields of Study

Major Field: Chemistry

Studies in Mass Spectrometry:
Professor Kimberly A. Prather

Studies in Atmospheric Chemistry:
Professor Kimberly A. Prather

ABSTRACT OF THE DISSERTATION

New Approaches for the Chemical and Physical Characterization of Aerosols Using a Single Particle Mass Spectrometry Based Technique

by

Matthew Todd Spencer

Doctor of Philosophy in Chemistry

University of California, San Diego, 2007

Professor Kimberly A. Prather, Chair

Aerosols affect the lives of people every day. They can decrease visibility, alter cloud formation and cloud lifetimes, change the energy balance of the earth and are implicated in causing numerous health problems. Measuring the physical and chemical properties of aerosols is essential to understand and mitigate any negative impacts that aerosols might have on climate and human health. Aerosol time-of-flight mass spectrometry (ATOFMS) is a technique that measures the size and chemical composition of individual particles in real time. The goal of this dissertation is to develop new and useful approaches for measuring the physical and/or chemical properties of particles using ATOFMS. This has been accomplished using laboratory experiments, ambient field measurements and sometimes comparisons between them.

A comparison of mass spectra generated from petrochemical particles was made to light duty vehicle (LDV) and heavy duty diesel vehicle (HDDV) particle mass spectra. This comparison has given us new insight into how to differentiate between particles from these two sources.

A method for coating elemental carbon (EC) particles with organic carbon (OC) was used to generate a calibration curve for quantifying the fraction of organic carbon and elemental carbon on particles using ATOFMS. This work demonstrates that it is possible to obtain quantitative chemical information with regards to EC and OC using ATOFMS.

The relationship between electrical mobility diameter and aerodynamic diameter is used to develop a tandem differential mobility analyzer-ATOFMS technique to measure the effective density, size and chemical composition of particles. The method is applied in the field and gives new insight into the physical/chemical properties of particles.

The size resolved chemical composition of aerosols was measured in the Indian Ocean during the monsoonal transition period. This field work shows that a significant fraction of aerosol transported from India was from biomass burning and appeared to be internally mixed with sulfate which suggests it was cloud processed during transport.

Lastly, noble metal nanoparticles are explored as potential matrices for visible wavelength single particle matrix assisted laser desorption/ionization mass spectrometry (VIS-MALDI). This work demonstrates that noble metal nanoparticle matrices can be used for VIS-MALDI analysis.

1 Introduction

1.1 Background

Aerosol particles are a ubiquitous component of the troposphere. They are directly emitted as primary particles or formed in the air through secondary processes from both natural and anthropogenic (man made) sources. Natural sources include the ocean (sea salt particles), wind blown dust (mineral particles), wildfires (biomass burning particles) and volcanoes (ash particles). The majority of anthropogenic particles are emitted from combustion related sources (e.g. industrial processes, vehicle emissions and biomass burning). These diverse sources can lead to chemical and physical (i.e. size and shape) differences between individual particles. The chemical/physical properties of aerosol particles dictate how they interact with various physical media; light, water, surrounding gases (air) and organisms. An understanding of how aerosols interact with these different media is necessary to determine their impact on human health and climate.

From a health perspective it has been shown that increased mass loadings of aerosols below 2.5 μm are correlated with an increase in mortality [*Dockery et al.*, 1993]. However, linking the chemical and physical properties of particles to their toxicological properties has been difficult. This is due in part to a lack of knowing the broad range of chemical compositions, morphologies and how these properties change as particles age [*Donaldson et al.*, 1998; *Gilmour et al.*, 1996; *Oberdorster et al.*, 1995].

From a climate perspective, although the impact of greenhouse gases is becoming relatively well understood, the impact of particles is poorly characterized [IPCC, 2007].

Particles can impact the climate system directly through absorbing or scattering solar/terrestrial radiation thus changing the amount of sunlight (energy) that is normally absorbed or reflected by the earth which changes the earth's energy balance. Aerosols can also change the earths energy balance indirectly by acting as cloud condensation nuclei which can alter cloud reflectivity and cloud life times [*Haywood and Boucher*, 2000]. In general aerosols are thought to have a net cooling effect on the earth meaning that they are reflecting more light back out to space versus absorbing the incoming light [*IPCC*, 2007]. It has been postulated that the effect of global warming from the large increase in greenhouse gases is possibly being masked or offset by a cooling effect from the concomitant increase in anthropogenic aerosols [Charlson et al., 1992; Penner et al., 1994], however the magnitude of the aerosol climate impact has a large degree of uncertainty [Chen and Penner, 2005; IPCC, 2007; Knutti et al., 2002; Lohmann and Feichter, 2005; Morgan et al., 2006; Ramanathan et al., 2005].

The lack of information on ambient particle chemical composition and mixing state leads to a large fraction of this uncertainty [*Chandra et al.*, 2004; *IPCC*, 2007; *Jacobson*, 2001; *Lohmann and Feichter*, 2005; *Myhre et al.*, 2004; *Schwartz*, 2004]. The chemistry and morphology of the individual particle dictates its ability to scatter or absorb solar radiation, the ability to act as a cloud condensation nucleus, and its lifetime in the atmosphere [*Finlayson-Pitts and Pitts*, 2000; *Seinfeld and Pandis*, 1998]. Measuring the chemistry and mixing state is further complicated because these are not static properties but rather evolve over time through aging and over space through transport [*Formenti et al.*, 2003; *Whiteaker and Prather*, 2003; *Wurzler et al.*, 2000]. However a detailed understanding of the sources, chemical composition, chemical

transformations, morphology, lifetimes and transportability of aerosols is necessary to mitigate their impact on climate and health.

The impact of anthropogenic air pollution is of increasing concern given that the growing world economy is leading to a drastic escalation in global energy consumption. The majority of this energy comes from the combustion of hydrocarbons in coal fired power plants, petroleum distillates in automobiles and biomass materials in stoves [*Agency*, 2004; *Kupiainen and Klimont*, 2007]. These combustion processes emit carbonaceous and inorganic particles directly into the atmosphere [*Bond et al.*, 2004; *IPCC*, 2007]. Unburned organic vapors from these sources can also add to the particle burden through secondary organic processing [*Odum et al.*, 1997]. In general, many of the carbonaceous and inorganic particles contain light absorbing materials and thus could have a net warming potential on the earth [*Schauer*, 2003; *Schnaiter et al.*, 2003]. However, as mentioned previously, this potential is difficult to estimate because the mixing state and chemical transformations are not easy to measure. The need to abate any possible effects of increasing aerosol pollution on climate and human health drives the development of improved instrumentation and sampling protocols that can measure particle mixing state and chemical transformations. Improvements such as more detailed chemical information with higher time resolution, along with the capability to make measurements from the ground, sea and air are needed to continue to provide new insights into the climate and health impacts of aerosols.

Aerosol time-of-flight mass spectrometry (ATOFMS) is a technique for measuring the size and chemical composition of individual particles in real time [*Gard et al.*, 1997; *Prather et al.*, 1994]. The ability of ATOFMS to measure these properties

gives us the capacity to use it as a tool to answer questions that are necessary to understand the impact of aerosols on climate and health. The majority of work presented in this thesis uses a new combination of methods for generating aerosols or size selecting aerosols prior to analysis using ATOFMS with the goal of helping to fill the current void in the scientific community's understanding of the atmospheric chemistry of aerosol particles.

1.2 ATOFMS background

1.2.1 A brief history of ATOFMS

The aerosol time-of-flight mass spectrometer (ATOFMS) was developed in the early 1990's for measuring the size and chemical composition of individual aerosol particles (Figure 1.1) [*Prather et al.*, 1994]. The main driver for the development of the ATOFMS was a large void in the scientific community's understanding of the chemistry, lifetime, sources, transport, climate impact and health effects of naturally occurring and anthropogenic aerosol particles. Although the original lab based ATOFMS has helped shed some light on these topics such as some of the first compositionally resolved size distributions [*Noble and Prather*, 1996], its immobility made it fairly limited for ambient aerosol sampling. Thus, a transportable version was needed to measure aerosols under the wide variety of ambient conditions that exist in different regions of the world. By the mid 1990's a field deployable (transportable) version of the ATOFMS was created in collaboration with TSI Inc. (Figure 1.2a) [*Gard et al.*, 1997]. Since 1996, the transportable ATOFMS has been used in close to 30 ambient aerosol field campaigns in 5 different countries spanning 12 time zones by the Prather research group. These

campaigns have shed new light on our understanding of the composition, morphology, chemical transformation, and transport of particles on a regional and global scale [*Sullivan and Prather*, 2005]. Beyond ambient aerosol measurements, the ATOFMS has also been used for the analysis of particles generated from sea water, petrochemicals (oil and fuel), pulmonary inhalers and on-line MALDI analysis of small molecules. TSI Inc. has also commercialized and marketed the ATOFMS and sold numerous instruments to other research groups throughout the world. Overall, there have been close to 70 peer reviewed journal articles pertaining to research using an ATOFMS. The ATOFMS has become a well regarded technique within the atmospheric and mass spectrometry communities for the measurement and characterization of single aerosol particles. The Prather research group continues to improve upon the original idea and 2007 will see the first aircraft measurements using the new aircraft (A)-ATOFMS [*Holecek et al.*, 2007a].

1.2.2 The ATOFMS instrument

It should be noted that there is a significant difference between a conventional matrix assisted laser desorption/ionization mass spectrometer (MALDI-MS) and the aerosol time-of-flight mass spectrometer (ATOFMS) used for research throughout this thesis. ATOFMS measures the aerodynamic size and a mass spectrum for individual aerosol particles. In a conventional MALDI-MS, samples are deposited on a metal plate that is placed in the mass spectrometer; a laser then desorbs and ionizes a fraction of the sample from this metal target. Using an ATOFMS, sample aerosol particles are analyzed on-line: desorbed and ionized "individually" as they enter the source region of the mass spectrometer. The ATOFMS consists of three main regions connected in series; aerosol

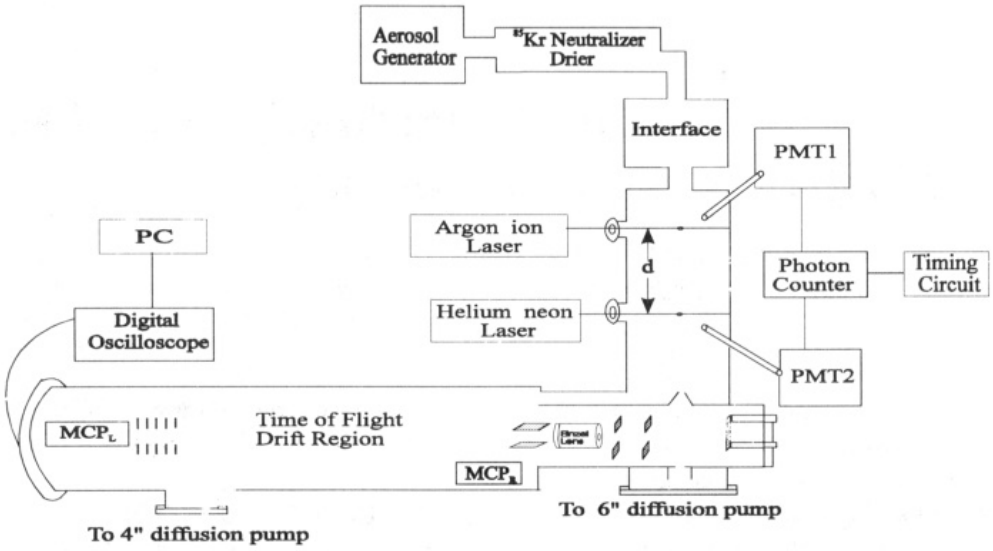

Figure 1.1 Schematic of the original ATOFMS. (Figure 1.1 Reprinted with permission from Prather K. A., Nordmeyer T., Salt K. Real-time characterization of individual aerosol particles using time-of-flight mass spectrometry, *Analytical Chemistry*, *66* (9), 1403-1407, Copyright 1994 American Chemical Society.)

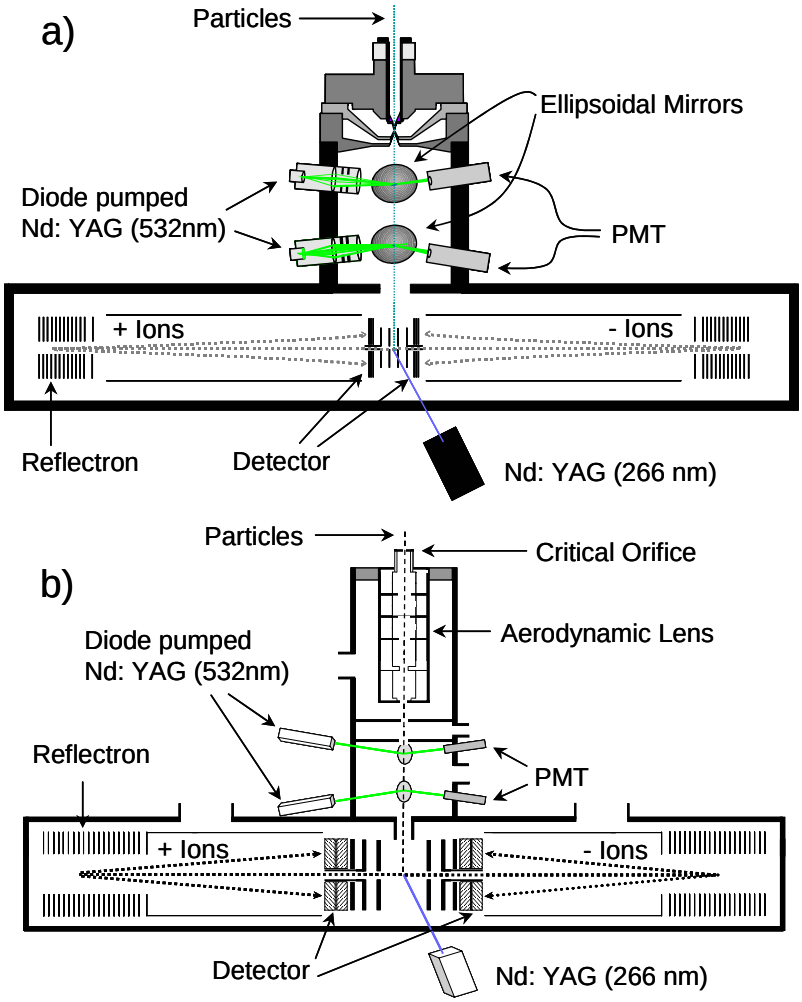

Figure 1.2 Schematic of the transportable ATOFMS with the nozzle inlet a) and aerodynamic lens inlet b). (Figure 1.2a Reprinted with permission from Gard, E., J.E. Mayer, B.D. Morrical, T. Dienes, D.P. Fergenson, and K.A. Prather, Real-time analysis of individual atmospheric aerosol particles: Design and performance of a portable ATOFMS, *Analytical Chemistry*, *69* (20), 4083-4091, Copyright 1997 American Chemical Society. Figure 1.2b Reprinted with permission from Su, Y.X., M.F. Sipin, H. Furutani, and K.A. Prather, Development and characterization of an aerosol time-of-flight mass spectrometer with increased detection efficiency, *Analytical Chemistry*, *76* (3), 712-719. Copyright 2004 American Chemical Society)

inlet, aerosol velocity/size measurement, and the laser desorption/ionization mass spectrometer. [*Gard et al.*, 1997; *Prather et al.*, 1994; *Su et al.*, 2004].

1.2.3 ATOFMS aerosol inlet

Currently two different aerosol inlets are used for introducing aerosol particles into the ATOFMS—a converging nozzle and an aerodynamic lens (Figure 1.2a-b). Chapters in this thesis rely on measurements that were made using both types of aerosol inlets. Experiments in Chapters 2 and 5 were taken using the converging nozzle configuration while the experiments discussed in Chapters 3, 4 and 6 used the aerodynamic lens; therefore each type of inlet is discussed briefly.

The converging nozzle inlet introduces particles into the mass spectrometer through a small capillary. At the exit of the nozzle there is a series of differentially pumped regions separated by gas skimmers [*Prather et al.*, 1994]. As aerosol exits the converging nozzle into the first vacuum region (~ 2 Torr) the aerosol gases undergo a supersonic expansion which causes the particles to accelerate to a terminal velocity dictated by its aerodynamic size (d_a). The aerosol particles pass through the two skimmers where most of the gas is pumped away. The particles then enter the light scattering region. The converging nozzle inlet is useful for particle sizes between 300-3000 nm in diameter. Particles below 300 nm behave more like the aerosol gases and as the aerosol gas expands at the exit of the nozzle these particles diverge with the gas and are pumped away. To measure particles in the 100-1000 nm size range a different inlet design, the aerodynamic lens, can be used.

The aerodynamic lens has been described in detail elsewhere [*Liu et al.*, 1995; *Su et al.*, 2004]. The aerosol enters the aerodynamic lens through a critical orifice (diameter

~ 100 μm). As the aerosol passes through the lens, it experiences a series of expansions and contractions (orifices). These expansions and contractions collimate the particles into a focused beam along the central axis of the lens, which transmits them much more efficiently into the ATOFMS. Thus, smaller size particles can be measured as compared to the nozzle inlet. The aerosol exits the lens into a vacuum (10^{-1} Torr) and the aerosol particles are accelerated to terminal velocity based on their vacuum aerodynamic size (d_{va}). The aerosol passes through 2 skimmers where the associated aerosol gases are pumped away before entering a light scattering region.

It should be noted that there is a difference in the flow regime that particles experience between the nozzle and aerodynamic lens; the nozzle operates in the continuum regime while the aerodynamic lens operates in the free molecular regime. The aerodynamic diameter that is measured by an ATOFMS is based on the following equation:

$$d_a = d_{ve}\sqrt{\frac{1}{\chi}\frac{\rho_p}{\rho_o}\frac{C_c(d_{ve})}{C_c(d_a)}} \qquad \text{Equation 1.1}$$

where d_{ve} is the volume equivalent diameter of a particle, χ is the particle shape factor, ρ_p is the particle density, ρ_o is the standard density (1.0 g·cm^{-3}) and C_c is the Cunningham slip correction factor evaluated at either the volume equivalent or aerodynamic diameters. Both the shape factor (χ) and the Cunningham slip correction factor (C_c) are functions that depend on flow regime and therefore d_a can take on different values depending on which flow regime d_a has been measured [*DeCarlo et al.*, 2004]. This distinction becomes important when comparing the aerodynamic diameter to the diameter measured using other techniques. Chapter 3 and Chapter 4 use a relationship between the

aerodynamic diameter of particles measured in the free molecular regime (termed the vacuum aerodynamic diameter) and measurements of the electrical mobility diameter (d_m), as measured by a differential mobility analyzer (DMA).

1.2.4 ATOFMS aerosol velocity and size measurement region

After passing through the skimmers the particles enter the light scattering region where they pass through two vertically separated (6 cm) continuous wave (CW) Nd:YAG lasers operated at 532 nm. As a particle passes through the first laser it scatters light which is collected by a PMT; this signal starts a timer. The particle then passes through the second CW laser and the scattered light signal stops the timer. The time it takes the particle to transverse both CW lasers is used to calculate the particle velocity. By using a set of standard polystyrene latex spheres that span the range of sizes the ATOFMS can detect, an equation that relates particle velocity to particle aerodynamic diameter can be determined. Thus particle diameter can be calculated. Figure 1.3 shows a typical aerodynamic diameter versus particle velocity calibration curve, and gives a power function that relates the two.

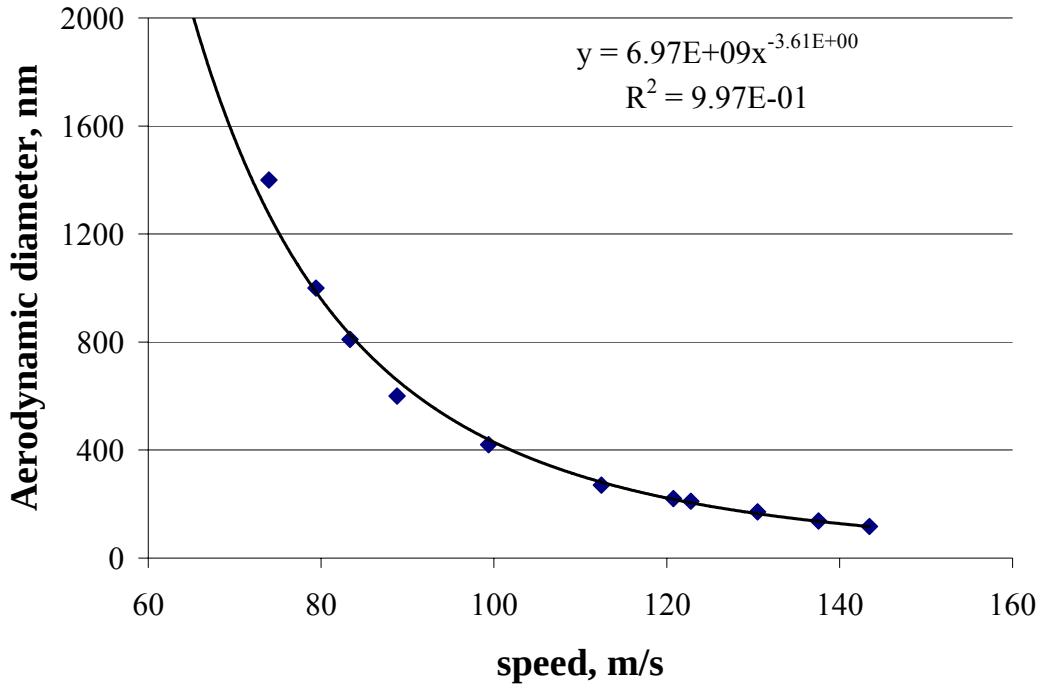

Figure 1.3 Plot of the aerodynamic diameter versus the particle velocity measured using an ATOFMS with an aerodynamic lens inlet.

1.2.5 Laser desorption/ionization time-of-flight mass spectrometry

The particle velocity measured in the light scattering region is used to fire a third Q-switched frequency quadrupled Nd:YAG laser (output λ = 266 nm) that desorbs and ionizes the particle at the precise time it enter the ion source region of the mass spectrometer. The desorption/ionization laser power for each analyzed particle can also be saved.

Time-of-flight mass spectrometry (TOFMS) has been reviewed extensively and numerous books have been published on the topic, therefore a detailed explanation of the TOF mass analyzer is not given here [*Cotter*, 1992; *Cotter*, 1997; *Grotemeyer and Editor*, 2001]. All the experimental results used in this thesis were obtained using the transportable version of the ATOFMS which has a dual polarity reflectron time-of-flight mass spectrometer (see Figure 1.2a-b).

1.3 Scope of this thesis

To better understand particle lifetimes, transport and chemical transformation, the ability to identify and track particles emitted from a specific source is essential. Accomplishing this objective requires knowledge of the chemical signatures from individual sources. Furthermore, because particles chemically evolve over time, the source signature can change or become masked [*Gard et al.*, 1998, Whiteaker, 2002 #26; *Spencer et al.*, 2007]. Therefore an understanding of the chemical composition of the freshly emitted source particles is necessary before any reasonable attempt can be made to track and understand particle transformations. Chapter 2 of this thesis compares the chemical signatures of laboratory generated particles of new and used oil and fuel with the particles emitted from both light duty vehicles (LDV) burning unleaded fuel and

heavy duty diesel trucks (HDD). This work gives us a better understanding of what components (oil or fuel) contribute to the particle emissions from LDV and HDD vehicles and sheds new light on vehicular source apportionment.

Although ATOFMS can provide qualitative information about the chemical composition of aerosol particles, our ability to quantify individual species has been limited [*Bhave et al.*, 2002; *Fergenson et al.*, 2001; *Gross et al.*, 2000; *Qin et al.*, 2006]. This has been attributed to differences in the laser pulse energies encountered by each particle as it is desorbed and ionized in the source region and also particle matrix effects [*Wenzel and Prather*, 2004]. Obtaining quantitative chemical information on a single particle level is critical for obtaining a detailed understanding of the chemical transformations that occur as particles age. Elemental carbon (EC) and organic carbon (OC) are two compound classes commonly found in anthropogenic particles. Measuring EC and OC in particles is necessary to understand how these particle types are processed in the atmosphere. Chapter 3 describes a laboratory technique for generating elemental EC particles, coating them with OC, and then relating the amount of EC and OC on a particle to the mass spectrum marker ions associated with these compounds. The technique uses a DMA to select EC particles of a specific monodisperse size prior to OC coating and ATOFMS analysis (tandem DMA-ATOFMS). This represents a significant step in the direction of obtaining quantitative chemical information using single particle mass spectrometry and should help pave the way for obtaining quantitative chemical information with regards to these species during ambient field measurements.

The work presented in Chapter 3 led to the realization that we could use a portion of the experimental setup described there (tandem DMA-ATOFMS) to measure the

effective density of particles in addition to their size and chemical composition. The effective density is a function of both the material density and particle shape/morphology (see Chapter 4 for a detailed explanation of effective density or [*DeCarlo et al.*, 2004]). The physical morphology and material density generally varies among the different particle sources; chemical transformations also cause changes in these physical properties [*Molina et al.*, 2004; *Pankow*, 1994]. Chapter 4 presents results regarding the development of this technique through laboratory-based testing followed by its application to ambient aerosols, yielding the effective density, size, and chemical composition of individual particles.

Certain regions of the world, such as the Republic of Maldives, have unique meteorological conditions that are ideal for measuring the effects of transported air pollution on climate. The Maldives is a country made up of small islands located roughly 600 miles south of India in the north Indian Ocean. During the wet monsoon the dominant air flow in the region is from the Indian Ocean to the Asian and Indian subcontinent [*Kripalani and Kumar*, 2004; *Ramana and Ramanathan*, 2006]. This puts the Maldives under relatively clean marine air conditions during the wet monsoon. During the dry monsoon the dominant air flow shifts to a southerly direction and air pollution from the Asian and Indian subcontinent is transported to the Maldives and over the Indian Ocean. In 2004 the Asian Brown Cloud Post Monsoonal Experiment (APMEX) took place in the Maldives during the transition period between the wet and dry monsoon (October-November). As part of this field campaign an ATOFMS was deployed to the region to characterize particles during the monsoonal transition period. Chapter 5 discusses the dominant aerosol types, sources and possible atmospheric

processing that occurred as particles were transported from India and Asia over the Indian Ocean. The implications of these measurements to regional aerosol climate models are also discussed.

Beyond atmospheric chemistry, the ATOFMS has also been shown to be a useful technique for the measurement of sea water, rain water, biowarfare agents and biomedical pulmonary inhaler particle chemical compositions [*Fergenson et al.*, 2004; *Holecek et al.*, 2007b; *Noble and Prather*, 1998; *Wenzel*, 2004]. Chapter 6 adds to this list of supplementary applications and describes the development of a new analytical method for the analysis of small molecules using a modified version of the ATOFMS and a gold nanoparticle matrix. Traditional MALDI techniques are generally not used for the analysis of small molecules due to the interference of the fragmented matrix ions in the low mass region ($m/z < 300$). The new MALDI technique discussed in Chapter 6 uses gold nanoparticles as a matrix. A unique characteristic of noble metal nanoparticles is they exhibit a surface plasmon resonance which gives them an appreciable amount of absorption in the visible wavelength region. We take advantage of the gold nanoparticle plasmon absorption in the visible wavelength range to expand the wavelength options for LDI, which is traditionally performed using ultra violet light and an organic acid matrix. The gold nanoparticles are shown to be a useful matrix for small molecule analysis due to the relatively small number of gold fragment ions.

1.4 References

Agency, I.E., Key world energy statistics, edited by International-Enery-Agency, pp. 1-82, 2004.

Bhave, P.V., J.O. Allen, B.D. Morrical, D.P. Fergenson, G.R. Cass, and K.A. Prather, A field-based approach for determining ATOFMS instrument sensitivities to ammonium and nitrate, *Environ. Sci. Technol.*, *36* (22), 4868-4879, 2002.

Bond, T.C., D.G. Streets, K.F. Yarber, S.M. Nelson, J.H. Woo, and Z. Klimont, A technology-based global inventory of black and organic carbon emissions from combustion, *J. Geophys. Res.*, *109* (D14), 2004.

Chandra, S., S.K. Satheesh, and J. Srinivasan, Can the state of mixing of black carbon aerosols explain the mystery of 'excess' atmospheric absorption?, *Geophys. Res. Lett.*, *31* (19), 2004.

Charlson, R.J., S.E. Schwartz, J.M. Hales, R.D. Cess, J.A. Coakley, J.E. Hansen, and D.J. Hofmann, Climate forcing by anthropogenic aerosols, *Science*, *255* (5043), 423-430, 1992.

Chen, Y., and J.E. Penner, Uncertainty analysis for estimates of the first indirect aerosol effect, *Atmos. Chem. Phys.*, *5*, 2935-2948, 2005.

Cotter, R.J., Time-of-flight mass-spectrometry for the structural-analysis of biological molecules, *Anal. Chem.*, *64* (21), A1027-A1039, 1992.

Cotter, R.J., *Time-of-flight mass spectrometry: Instrumentation and applications in biological research*, 326 pp. pp., 1997.

DeCarlo, P., J.G. Slowik, D.R. Worsnop, P. Davidovits, and J.L. Jimenez, Particle morphology and density characterization by combined mobility and aerodynamic diameter measurements. Part 1: Theory, *submitted to Aerosol Sci. Technol.*, 2004.

Dockery, D.W., C.A. Pope, X.P. Xu, J.D. Spengler, J.H. Ware, M.E. Fay, B.G. Ferris, and F.E. Speizer, An association between air-pollution and mortality in 6 United-States cities, *N. Engl. J. Med.*, *329* (24), 1753-1759, 1993.

Donaldson, K., X.Y. Li, and W. MacNee, Ultrafine (nanometer) particle mediated lung injury, *J. Aerosol Sci.*, *29* (5-6), 553-560, 1998.

Fergenson, D.P., M.E. Pitesky, H.J. Tobias, P.T. Steele, G.A. Czerwieniec, S.C. Russell, C.B. Lebrilla, J.M. Horn, K.R. Coffee, A. Srivastava, S.P. Pillai, M.T.P. Shih, H.L. Hall, A.J. Ramponi, J.T. Chang, R.G. Langlois, P.L. Estacio, R.T. Hadley,

M. Frank, and E.E. Gard, Reagentless detection and classification of individual bioaerosol particles in seconds, *Anal. Chem.*, *76* (2), 373-378, 2004.

Fergenson, D.P., X.-H. Song, Z. Ramadan, J.O. Allen, L.S. Hughes, G.R. Cass, P.K. Hopke, and K.A. Prather, Quantification of ATOFMS data by multivariate methods, *Anal. Chem.*, *73* (15), 3535-3541, 2001.

Finlayson-Pitts, B.J., and J.N. Pitts, *Chemistry of the upper and lower atmosphere: Theory, experiments, and applications*, Academic Press, San Diego, 2000.

Formenti, P., W. Elbert, W. Maenhaut, J. Haywood, S. Osborne, and M.O. Andreae, Inorganic and carbonaceous aerosols during the southern African regional science initiative (safari 2000) experiment: Chemical characteristics, physical properties, and emission data for smoke from African biomass burning, *J. Geophys. Res.*, *108* (D13), 2003.

Gard, E., J.E. Mayer, B.D. Morrical, T. Dienes, D.P. Fergenson, and K.A. Prather, Real-time analysis of individual atmospheric aerosol particles: Design and performance of a portable ATOFMS, *Anal. Chem.*, *69* (20), 4083-4091, 1997.

Gard, E.E., M.J. Kleeman, D.S. Gross, L.S. Hughes, J.O. Allen, B.D. Morrical, D.P. Fergenson, T. Dienes, M.E. Galli, R.J. Johnson, G.R. Cass, and K.A. Prather, Direct observation of heterogeneous chemistry in the atmosphere, *Science (Washington, D. C.)*, *279* (5354), 1184-1187, 1998.

Gilmour, P.S., D.M. Brown, T.G. Lindsay, P.H. Beswick, W. MacNee, and K. Donaldson, Adverse health effects of pm(10) particles: Involvement of iron in generation of hydroxyl radical, *Occupational and Environmental Medicine*, *53* (12), 817-822, 1996.

Gross, D.S., M.E. Gaelli, P.J. Silva, and K.A. Prather, Relative sensitivity factors for alkali metal and ammonium cations in single-particle aerosol time-of-flight mass spectra, *Anal. Chem.*, *72* (2), 416-422, 2000.

Grotemeyer, J., and Editor, *Special issue: Time-of-flight mass spectrometry. [in: Int. J. Mass spectrom., 2001; 206(3)]*, 113 pp. pp., 2001.

Haywood, J., and O. Boucher, Estimates of the direct and indirect radiative forcing due to tropospheric aerosols: A review, *Reviews Of Geophysics*, *38* (4), 513-543, 2000.

Holecek, J.C., K.A. Denkenberger, J.E. Mayer, R.C. Moffet, G. Poon, R.O. Sanchez, T. Rebotier, H. Furutani, Y. Su, S. Guazzotti, and K.A. Prather, Development of an aircraft aerosol time-of-flight mass spectrometer, *Anal. Chem.*, *manuscript In preparation*, 2007a.

Holecek, J.C., M.T. Spencer, and K.A. Prather, Analysis of rainwater samples: Comparison of single particle residues with ambient particle chemistry from the northeast Pacific and Indian Oceans, *J. Geophys. Res.*, *Accepted*, 2007b.

IPCC, *Climate change 2007 : The scientific basis : Contribution of working group i to the fourth assessment report of the intergovernmental panel on climate change*, Cambridge University Press, Cambridge ; New York :, 2007.

Jacobson, M.Z., Strong radiative heating due to the mixing state of black carbon in atmospheric aerosols, *Nature*, *409* (6821), 695-7, 2001.

Knutti, R., T.F. Stocker, F. Joos, and G.K. Plattner, Constraints on radiative forcing and future climate change from observations and climate model ensembles, *Nature*, *416* (6882), 719-723, 2002.

Kripalani, R.H., and P. Kumar, Northeast monsoon rainfall variability over south peninsular India vis-a-vis the Indian ocean dipole mode, *International Journal of Climatology*, *24* (10), 1267-1282, 2004.

Kupiainen, K., and Z. Klimont, Primary emissions of fine carbonaceous particles in Europe, *Atmos. Environ.*, *41* (10), 2156-2170, 2007.

Liu, P., P.J. Ziemann, D.B. Kittelson, and P.H. McMurry, Generating particle beams of controlled dimensions and divergence 2: Experimental evaluation of particle motion in aerodynamic lenses and nozzle expansions, *Aerosol Science & Technology*, *22* (3), 314-324, 1995.

Lohmann, U., and J. Feichter, Global indirect aerosol effects: A review, *Atmos. Chem. Phys.*, *5*, 715-737, 2005.

Molina, M.J., A.V. Ivanov, S. Trakhtenberg, and L.T. Molina, Atmospheric evolution of organic aerosol, *Geophys. Res. Lett.*, *31* (22), 2004.

Morgan, M.G., P.J. Adams, and D.W. Keith, Elicitation of expert judgments of aerosol forcing, *Climatic Change*, *75* (1-2), 195-214, 2006.

Myhre, G., F. Stordal, T.F. Berglen, J.K. Sundet, and I.S.A. Isaksen, Uncertainties in the radiative forcing due to sulfate aerosols, *Journal of the Atmospheric Sciences*, *61* (5), 485-498, 2004.

Noble, C.A., and K.A. Prather, Real-time measurement of correlated size and composition profiles of individual atmospheric aerosol particles, *Environmental Science & Technology*, *30* (9), 2667-2680, 1996.

Noble, C.A., and K.A. Prather, Single particle characterization of albuterol metered dose inhaler aerosol in near real-time, *Aerosol Sci. Technol.*, *29* (4), 294-306, 1998.

Oberdorster, G., R.M. Gelein, J. Ferin, and B. Weiss, Association of particulate air-pollution and acute mortality - involvement of ultrafine particles, *Inhalation Toxicol.*, *7* (1), 111-124, 1995.

Odum, J.R., T.P.W. Jungkamp, R.J. Griffin, R.C. Flagan, and J.H. Seinfeld, The atmospheric aerosol-forming potential of whole gasoline vapor, *Science*, *276* (5309), 96-99, 1997.

Pankow, J.F., An absorption-model of the gas aerosol partitioning involved in the formation of secondary organic aerosol, *Atmos. Environ.*, *28* (2), 189-193, 1994.

Penner, J.E., R.J. Charlson, J.M. Hales, N.S. Laulainen, R. Leifer, T. Novakov, J. Ogren, L.F. Radke, S.E. Schwartz, and L. Travis, Quantifying and minimizing uncertainty of climate forcing by anthropogenic aerosols, *Bulletin of the American Meteorological Society*, *75* (3), 375-400, 1994.

Prather, K.A., T. Nordmeyer, and K. Salt, Real-time characterization of individual aerosol particles using time-of-flight mass spectrometry, *Anal. Chem.*, *66* (9), 1403-7, 1994.

Qin, X.Y., P.V. Bhave, and K.A. Prather, Comparison of two methods for obtaining quantitative mass concentrations from aerosol time-of-flight mass spectrometry measurements, *Anal. Chem.*, *78* (17), 6169-6178, 2006.

Ramana, M.V., and V. Ramanathan, Abrupt transition from natural to anthropogenic aerosol radiative forcing: Observations at the ABC-Maldives climate observatory, *J. Geophys. Res.*, *111* (D20), 2006.

Ramanathan, V., C. Chung, D. Kim, T. Bettge, L. Buja, J.T. Kiehl, W.M. Washington, Q. Fu, D.R. Sikka, and M. Wild, Atmospheric brown clouds: Impacts on south Asian climate and hydrological cycle, *Proc. Natl. Acad. Sci. U. S. A.*, *102* (15), 5326-5333, 2005.

Schauer, J.J., Evaluation of elemental carbon as a marker for diesel particulate matter, *Journal of Exposure Analysis and Environmental Epidemiology*, *13* (6), 443-453, 2003.

Schnaiter, M., H. Horvath, O. Mohler, K.H. Naumann, H. Saathoff, and O.W. Schock, UV-VIS-NIR spectral optical properties of soot and soot-containing aerosols, *J. Aerosol Sci.*, *34* (10), 1421-1444, 2003.

Schwartz, S.E., Uncertainty requirements in radiative forcing of climate change, *J. Air Waste Manage. Assoc.*, *54* (11), 1351-1359, 2004.

Seinfeld, J.H., and S.N. Pandis, *Atmospheric chemistry and physics: From air pollution to climate change*, John Wiley & Sons, 1998.

Spencer, M.T., L.G. Shields, and K.A. Prather, Simultaneous measurement of the effective density and chemical composition of ambient aerosol particles, *Environ. Sci. Technol.*, *Web Release Date: 17-Jan-2007*, 2007.

Su, Y., M.F. Sipin, H. Furutani, and K.A. Prather, Development and characterization of an aerosol time-of-flight mass spectrometer with increased detection efficiency, *Anal. Chem.*, *76* (3), 712-719, 2004.

Sullivan, R.C., and K.A. Prather, Recent advances in our understanding of atmospheric chemistry and climate made possible by on-line aerosol analysis instrumentation, *Anal. Chem.*, *77* (12), 3861-3885, 2005.

Wenzel, R.J., Further development and application of laser desorption ionization (LDI) using aerosol time-of-flight mass spectrometry (ATOFMS), University of California, Riverside, Riverside, 2004.

Wenzel, R.J., and K.A. Prather, Improvements in ion signal reproducibility obtained using a homogeneous laser beam for on-line laser desorption/ionization of single particles, *Rapid Commun. Mass Spectrom.*, *18* (13), 1525-1533, 2004.

Whiteaker, J.R., and K.A. Prather, Hydroxymethanesulfonate as a tracer for fog processing of individual aerosol particles, *Atmos. Environ.*, *37* (8), 1033-1043, 2003.

Wurzler, S., T.G. Reisin, and Z. Levin, Modification of mineral dust particles by cloud processing and subsequent effects on drop size distributions, *J. Geophys. Res.*, *105* (D4), 4501-4512, 2000.

2 Comparison of Oil and Fuel Particle Chemical Signatures with Particle Emissions from Heavy and Light Duty Vehicles

2.1 Synopsis

In order to establish effective vehicle emission control strategies, efforts are underway to perform studies which provide insight into the origin of the source of vehicle particle emissions. In this study, the mass spectral signatures of individual particles produced from atomized auto and diesel oil and fuel samples were obtained using aerosol time-of-flight mass spectrometry (ATOFMS). The major particle types produced by these samples show distinct chemistry, falling into several major categories for each sample. Lubricating oils contain calcium and phosphate based additives and although the additives are present in low abundance (~1-2% by mass), calcium and phosphate ions dominate the mass spectra for all new and used oil samples. Mass spectra from used oil contain more elemental carbon (EC) and organic carbon (OC) marker ions when compared to new oils and exhibit a very high degree of similarity to heavy duty diesel vehicle (HDDV) exhaust particles sampled by an ATOFMS. Fewer similarities exist between the used oil particles and light duty vehicle (LDV) emissions. Diesel and unleaded fuel mass spectra contain polycyclic aromatic hydrocarbon (PAH) molecular ions, as well as intense PAH fragment ions $^{25}(C_2H)^-$, $^{49}(C_4H)^-$, and inorganic ions $^{23}Na^+$,

$^{39}K^+$, $^{95}(PO_4)^-$. Unleaded fuel produced spectra which contained Na^+ and K^+; likewise, LDV particle emission spectra also contained Na^+ and K^+. Comparing oil and fuel particle signatures with HDDV and LDV emissions enhances our ability to differentiate between these sources and understand the origin of specific marker ions from these major ambient particle sources.

2.2 Introduction

Atmospheric particles are chemically diverse, ranging from inorganic dust and soil to biological, organic, soot, and sea salt particles. Sources of the different particles in the atmosphere include wind blown dust, vegetative pollen release, fuel combustion, secondary organic aerosol formation, and oceanic bubble bursting [*Fitzgerald*, 1991; *Graham et al.*, 2003; *Pandis et al.*, 1992; *Pinker et al.*, 2001]. To understand the impact of particles on the environment, the ability to differentiate between particles from different sources and determine their ambient contributions is important. Fossil fuel combustion significantly contributes to the particle burden in urban areas [*Hamilton and Mansfield*, 1991; *Schauer and Cass*, 2000] and these particles can be transported to non-urban areas as well [*Hughes et al.*, 2000]. Toxicologically, understanding the chemical composition of combustion particles is important because they have been linked to an increase in morbidity and adverse health effects[*Dockery et al.*, 1993; *Harrison and Yin*, 2000; *Schwartz and Dockery*, 1992]. Combustion particles have also been shown to affect climate by absorbing solar radiation and changing cloud properties [*Ackerman et al.*, 2000; *Andreae et al.*, 2004; *Chung and Seinfeld*, 2005; *Krishnan and Ramanathan*, 2002]. Furthermore, atmospheric oxidation of unburned gasoline vapor has been shown

to contribute to the formation of secondary organic aerosol (SOA) [*Lee et al.*, 2004; *Odum et al.*, 1997].

Light duty vehicles (LDV) and heavy duty diesel vehicles (HDDV) produce a significant number of particles composed of elemental carbon (EC), organic carbon (OC), trace metals, and salts [*Burtscher et al.*, 1998; *Kittelson*, 1998; *Kleeman et al.*, 2000; *Lowenthal et al.*, 1994; *Schauer et al.*, 1999; *Schauer et al.*, 2002; *Silva and Prather*, 1997; *Suess*, 2002]. Oil and fuel formulations can influence the amount of the different species emitted from vehicles [*Alander et al.*, 2004; *Isotalo et al.*, 2002; *Wang et al.*, 2000b], and these formulations vary by brand and type [*Marr et al.*, 1999]. Therefore, identical vehicles using fuel and oil produced by different vendors could potentially emit chemically distinct particles. Determining whether the majority of particulate matter produced by LDV and HDDV results from incomplete fuel combustion, unburned oil, or engine block elements will be useful for evaluating LDV and HDDV particulate emission control strategies, potentially leading to better fuel or oil formulations and/or engine design.

Aerosol time-of-flight mass spectrometry (ATOFMS) was used to analyze 16 different aerosolized fluids: new lubricating oil (10W-30), new lubricating oil (15W-40), used lubricating oil (10W-30), three used (15W-40) lubricating oils, four different 87 octane unleaded fuels, four different diesel fuels, and three diesel fuels taken from the fuel tank of different diesel trucks. The aim of this work is to study the variability of the mass spectral signatures from oil and fuel particles and compare them with LDV and HDDV emission particles. For LDV and HDDV sources, an understanding of the origin

of certain unique ions commonly observed in the single particle spectra will help unravel the differences observed for these two chemically similar ambient particle sources.

2.3 Methods

2.3.1 Single particle analysis: ATOFMS

Single particle size (between 0.2 and 3.0 μm) and chemical analysis was performed using a transportable dual ion ATOFMS instrument with a converging nozzle inlet. A detailed instrumental description has been published [*Gard et al.*, 1997] and is also given in Chapter 1. The Q-switched desorption/ ionization laser was operated at 266 nm and ~ 1.0 mJ/pulse.

2.3.2 Fuel and oil particle generation.

Unleaded and diesel fuel samples (numbered 1-4) were purchased from public gas stations in San Diego, California. New LDV and new HDDV oils were 10W-30 and 15W-40 blends, respectively. Unleaded (87 octane "regular") auto fuel and diesel fuel samples (1-4) were stored in separate plastic petroleum storage containers for one week prior to experiment. Throughout this paper, the 87 octane auto fuel is referred to as "unleaded" and diesel fuel as "diesel". HDDV fuel and HDDV used oil (numbered 1-3) were obtained from three separate diesel trucks (i.e. fuel tank or oil pan) that were used during an ATOFMS dynamometer study [*Shields et al.*, 2006]. Used LDV oil (10W-30) was obtained from a light duty pickup truck. All used oil samples had a dark black visual appearance and were stored in glass containers. The number of operating hours on the engines for each used oil sample is unknown.

Figure 2.1 shows a diagram of the particle generation setup. Particles from the fuels and oils were generated using a Collison nebulizer [*May,* 1973], followed by two Pyrex dilution chambers. Dry laboratory generated, charcoal, Purafil, and HEPA filtered air was used for aerosol production and subsequent dilution. A 2 L dilution chamber was utilized first, followed by a 1 L chamber. The dilution chambers each yielded about a 10-fold dilution for an overall dilution of the initial particle stream of 100-fold. Particle size distributions were measured using the ATOFMS instrument, an Aerodynamic Particle Sizer (APS, TSI Inc. model 3321), and a Scanning Mobility Particle Sizer (SMPS, TSI Inc. model 3936L10).

2.3.3 LDV and HDDV sampling

Methods for sampling LDV and HDDV emissions used for comparison in this study have been reported previously [*Shields et al.,* 2006; *Sodeman et al.,* 2005]. Briefly, particle emissions from 7 different HDDV were sampled on a HDDV transportable dynamometer [*Bata et al.*, 1991]. Twenty eight LDVs were run on a permanent dynamometer at the California Air Resources Board (CARB) vehicle testing facility in El Monte, CA. Vehicles were from various production years and had a wide variety of exhaust and emission control technologies. Each vehicle was operated using a variety of standard testing cycles.

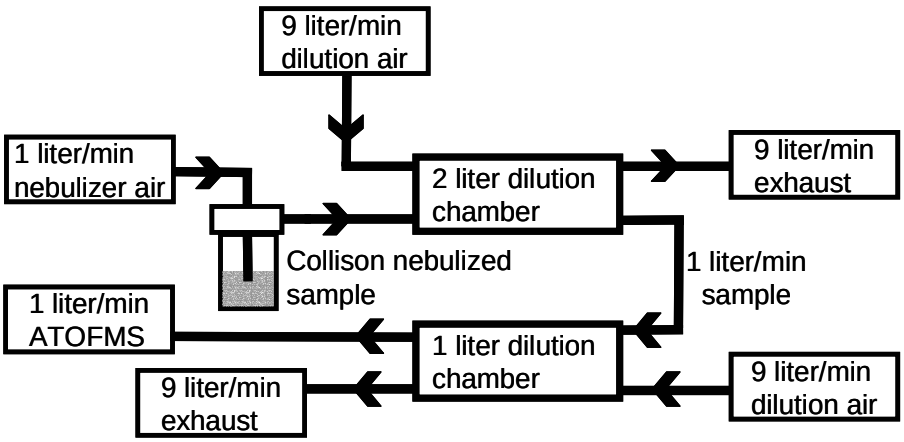

Figure 2.1 Experimental setup. Oil and fuel particles are generated using a Collison nebulizer and diluted with dry, particle free air using a two stage dilution system prior to analysis with ATOFMS.

2.3.4 ATOFMS data analysis

Data were imported into Matlab Version 6.1.0.450 release 12.1 (The Math Works, Inc.) and analyzed using YAADA version 1.2 [http://www.yaada.org]. Mathematical comparisons between the major LDV, HDDV and oil/fuel sample particle types were made using components of the YAADA toolkit.

Particle types were grouped using an Adaptive Resonance Theory neural network, ART-2a [*Hopke and Song*, 1997; *Song et al.*, 2001; *Song et al.*, 1999]. ART-2a groups particles together based on similarities between ion peak intensities in each individual particle mass spectrum. The parameters used for ART-2a in this experiment were: learning rate = 0.05, vigilance factor = 0.85, and iterations = 20. A particle cluster resulting from ART-2a can be used to generate a weight matrix (WM). The WM represents a weighted average of a group of similar mass spectra determined using ART-2a. The WM of different particle types can then be analyzed manually and further refined into distinct chemical classes. From this grouping of similar particles, an area matrix (AM) can then be generated. This AM represents the average intensity for each m/z for all particles within a group. In general, the AM strongly resembles the individual mass spectra of each particle within a group.

2.4 Results and discussion

For the following discussion, the presence and relative intensities of certain ion peaks are used to differentiate EC and OC [*Spencer and Prather*, 2006]. EC is characterized by distinct carbon cluster ion peaks in the positive and negative mass spectra (12, 24, 36…C_n) that are typically higher in intensity than OC peaks occurring in

the same spectra. OC peaks, such as *m/z* (15^+, 27^+, 29^+, 37^+, 43^+, 25^-, and 26^-), can be assigned to a number of different organic fragments [*McLafferty and Tureécek*, 1993]. Some of these include, $^{15}(CH_3)^+$, $^{27}(C_2H_3)^+$, $^{27}(CNH)^+$, $^{29}(C_2H_5)^+$, $^{29}(COH)^+$, $^{43}(CHNO)^+$, $^{43}(C_2H_3O)^+$, $^{43}(C_3H_7)^+$, $^{91}(C_7H_7)^+$, $^{25}(C_2H)^-$, and $^{26}(CN)^-$. Organic compounds can also produce ions at m/z 12, 24, 36, etc. [*Silva and Prather*, 2000], however, these are significantly lower in intensity than other OC markers at *m/z* 15^+, 27^+, 29^+, 43^+, 25^-, and 26^-.

Lab generated oil and diesel fuel particles ranged in size from 500 – 5000 nm (aerodynamic diameter). Oil particles from all samples produced a mode centered at roughly 2300 nm and the diesel fuel particle mode was centered at 1000 nm as measured by an APS. Very few oil and diesel fuel particles were generated within the size range between 10-250 nm. Unleaded fuel particle sizes ranged from 20-250 nm and 500-1500 nm, as measured with an SMPS and APS, respectively. Unleaded fuel particles showed a mode at 100 nm on the SMPS and 670 nm on the APS. These size distributions are directly related to the method used to generate the particles, and a different formation method would produce different size distributions.

2.4.1 New and used oil samples

Figure 2.2 (a-d) contains the area matrices (AM) for the different particle classes detected in the new and used oil samples. Particle classes are labeled by order of ion intensity in the mass spectra. Figure 2.2a shows the AM of a particle type containing Ca, phosphate, and OC that was observed exclusively in the new oils. Positive ion mass spectra of particles in this cluster are dominated by an intense $^{40}Ca^+$ peak as well as peaks

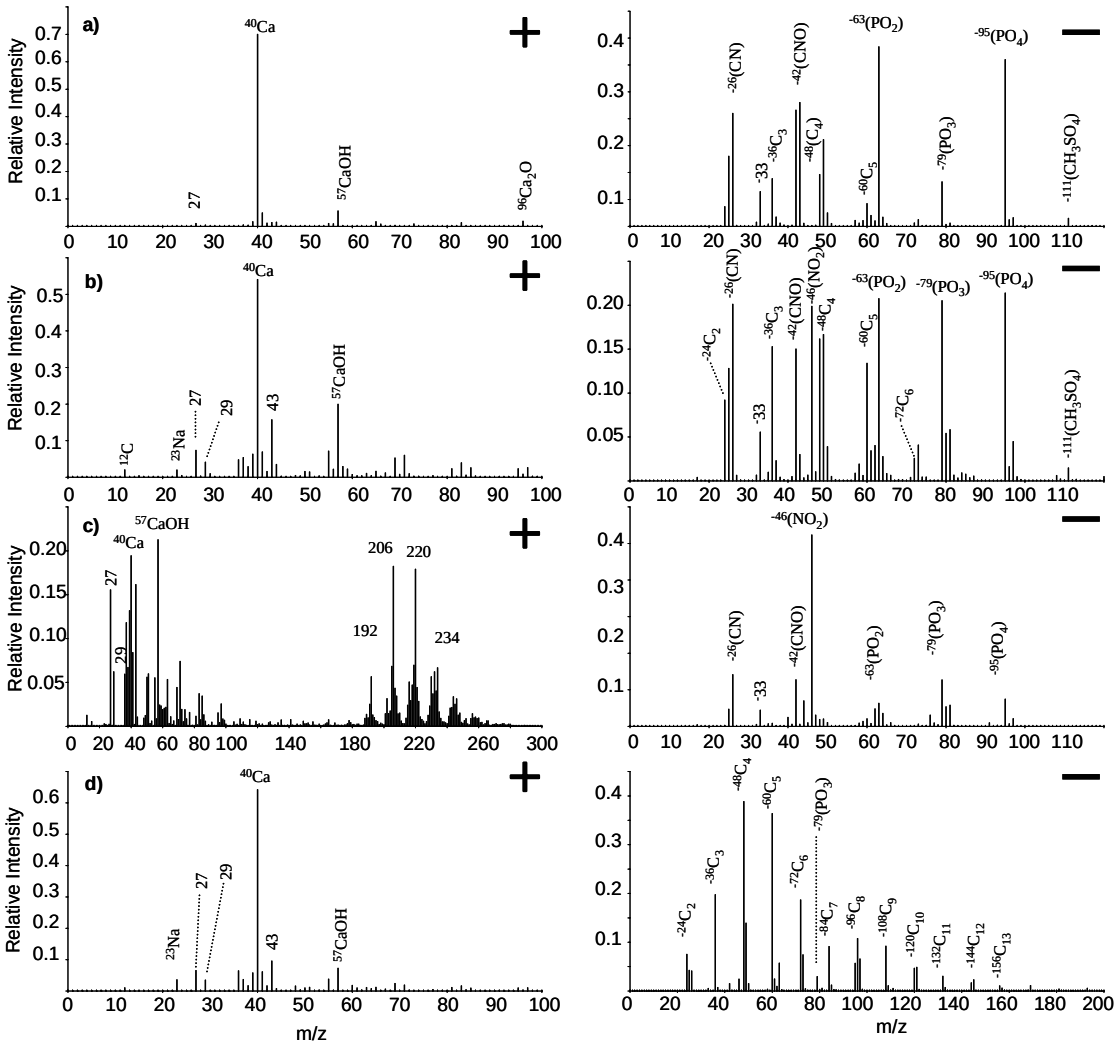

Figure 2.2 Positive (left side) and negative (right side) ion AM for chemical classes detected in new and used oil samples. The five different major classes shown are: a) Ca-Phosphate-OC, b) Ca-EC-OC-Phosphate-NO_2-Na, c) Ca-PAH-OC-Phosphate, and d) Ca-EC-OC-Phosphate. Mass-to-charge values and chemical assignment for some ions are given above the peak.

at $^{57}(CaOH)^+$, $^{96}(Ca_2O)^+$, and *m/z* 27^+. The peak at 27^+ is most likely $^{27}HCN^+$, based on the simultaneous presence of an intense $^{26}(CN)^-$ in the negative ion spectra of the same particle, and attributed to the presence of nitrogen-containing organics [*Silva and Prather*, 2000]. The corresponding negative ion spectrum in Figure 2.2a shows the presence of phosphate $^{63}(PO_2)^-$, $^{79}(PO_3)^-$, and $^{95}(PO_4)^-$, carbon clusters out to $^{60}C_5^-$, $^{26}(CN)^-$, $^{42}(CNO)^-$, and $^{111}(CH_3SO_4)^-$. Calcium is added to engine lubricants as part of a detergent complex as well as to serve as a base to neutralize acids and stabilize highly polar compounds that are formed in the engine during combustion [*Lyyranen et al.*, 1999; *Rudnick*, 2003]. Zinc dialkyldithiophosphate (ZDDP) is also added to commercial lubricants and serves as an anti-wear and extreme-pressure agent [*Gautam et al.*, 1999]. ZDDP and the thermo-oxidative breakdown products orthophosphate and pyrophosphate have been measured in lubricant films, and therefore the presence of phosphates is expected [*Canning et al.*, 1999; *Willermet*, 1998]. The presence of zinc is also expected, however due to a relatively low sensitivity of the ATOFMS instrument to organometallic zinc, no zinc ions were detected during this study. It is important to note that calcium makes up 1-2% of the oil mass, however the calcium ion peak at *m/z* 40^+ dominates the spectrum, demonstrating how Ca^+ can suppress the organic and trace metal ion intensities in this matrix. Furthermore, desorption and ionization of base mineral oil which did not contain the additive package (i.e. no calcium and phosphate) at the same wavelength (266 nm laser) and power (1.5 mJ) produced only a few particle spectra containing low intensity ions, indicating weak absorption. This is not surprising given the composition of mineral oil is dominated by long chain hydrocarbons which do not absorb 266 nm

radiation. However, the oil samples in these experiments which did include additive packages strongly absorbed the 266 nm radiation.

Figures 2.2b-2.2d show the AM for particles detected in used LDV and HDDV oil samples. Figure 2.2b shows the particle type (*Ca-EC-OC-Phosphate-NO_2-Na*) that is readily distinguished from the new oil shown in Figure 2.2a by the increased intensities of the EC ion peaks ($^{36}C_3^-$, $^{48}C_4^-$, $^{60}C_5^-$, $^{72}C_7^-$), OC ion markers (i.e. 27^+, 29^+, 43^+, 55^+, 69^+, 71^+, 81^+, 83^+, 85^+, 93^+, 95^+), the presence of $^{23}Na^+$, and an intense peak at $^{46}(NO_2)^-$. Normal and branched alkanes typically fragment to ions at m/z 29^+, 43^+, 57^+, and 71^+, while alkenes and cycloalkanes will yield ions at m/z 27^+, 41^+, 55^+, 69^+ and 83^+ [*McLafferty and Tureécek,* 1993]. These fragment ions are observed for used oil and HDDV exhaust particles by the ATOFMS instrument, as well as in previous studies with a thermal desorption particle beam mass spectrometer and an Aerodyne aerosol mass spectrometer (AMS) [*Alfarra et al.*, 2004; *Canagaratna et al.*, 2004; *Tobias et al.*, 2001]. These are most likely the non-absorbing aliphatic hydrocarbons in the base oil described above. Apparently, the additional EC in these particles acts as a strongly absorbing matrix, enhancing the signals from these non-absorbing aliphatic species in direct analogy to matrix assisted laser desorption ionization [*Karas and Kruger,* 2003]. The presence of a strong peak at m/z 46^- can be explained by several factors. NO_x formation occurs during the combustion process from reactions between oxygen and nitrogen in the fuel-air mixture [*Heywood,* 1988]. It can react to form nitrogen-containing species that can then be absorbed into the oil and stabilized as inorganic salts [*Rudnick,* 2003]. It has also been shown that nitro-PAH's commonly fragment into CN^- and NO_2^- when ionized using a 266 nm laser which was used in these experiments [*Bezabeh et al.*, 1997]. Peaks

at $^{26}(CN)^-$ and $^{46}(NO_2)^-$ could therefore derive from nitro-PAH's which have been measured in both used oil and diesel exhaust particles [*Bezabeh et al.*, 1997; *Zielinska et al.*, 2004].

Used LDV oil particles are distinguished from HDDV oil particles by the unique particle class (*Ca-PAH-OC-Phosphate*) shown in Figure 2.2c. This particle type is characterized by a $^{40}Ca^+$ peak, OC peaks at 27^+, 29^+, and intense ion signals at 192^+, 206^+, 220^+ and 234^+. Each of these ions are separated by a mass difference of 14, which suggests they could be phenanthrene, anthracene, or possibly heteroatom PAH's with increasing numbers of methyl or ethyl substituents. Previous work has shown that over one hundred different PAH species accumulate in LDV oil over prolonged vehicle operation [*Wang et al.*, 2000a]. Zielinska (2004) and Wong (2001) observed similar PAH species in oil, fuel, and HDDV and LDV tailpipe emissions. Zielinska (2004) also shows that lubricating oil in gasoline engines contains a larger amount of PAH's compared to diesel oil.

All three used HDDV oils contained a significant amount of the *Ca-EC-OC-Phosphate* particle type. In Figure 2.2d, the positive ion AM for this particle class shows dominant peaks for $^{40}Ca^+$, $^{57}(CaOH)^+$, $^{96}(Ca_2O)^+$, and OC peaks 27^+, 29^+ and 43^+. The negative ion AM shows a carbon envelope extending out to $^{156}C_{13}^-$ and the presence of $^{63}(PO_2)^-$, $^{79}(PO_3)^-$, and $^{95}(PO_4)^-$/$^{95}(CH_3SO_3)^-$. It has been well documented that diesel powered engines generate more EC than spark ignition engines [*Burtscher et al.*, 1998; *Zielinska et al.*, 2004]. One function of lubricating oil is to help disperse agglomerated EC particles in the oil. Because diesel engines generate more EC, more EC agglomerates are observed in the used HDDV oil than the used LDV oil.

2.4.2 Diesel fuel samples

Diesel fuel and regular unleaded fuel particles are readily distinguished from each other based on the presence of unique PAH ions. Figure 2.3 shows the AM that makes up between 40-80% of the mass spectra for the different diesel fuel samples. This class is labeled *PAH-containing* and is comprised of any clusters containing intense ion signals at *m/z* 181^{+},195^{+}, 206^{+}, 220^{+}, 234^{+} and *m/z* 193^{-}, 207^{-},208^{-}, 222^{-}, and 236^{-}. Two series of PAH are observed, one at m/z 181^{+} and 195^{+} (separated by 14 amu) and the other series at m/z 206^{+}, 220^{+}, 234^{+} (also separated by 14 amu). PAH compounds have been shown to comprise a large fraction of diesel fuel [*Rhead and Hardy*, 2003]. The formation of negative ion PAH species is a unique feature of the diesel fuel. One possible explanation for the negative ion PAHs is they contain electronegative functionalities such as oxy-PAHs which have been measured in diesel fuel [*Zielinska et al.*, 2004]. For example, anthraquinone, has a molecular weight (MW) of 208, and methyl-anthraquinone has a MW of 222. However, assignment of these negative ions to oxy-PAHs is speculative until further analysis is performed on these samples. Peaks for OC are also observed at *m/z*, 27^{+}, 29^{+}, 43^{+}, $^{26}(CN)^{-}$, 25^{-}, and 49^{-}. Ions at 25^{-}, 49^{-}, and 73^{-} have been shown to come from PAH fragmentation [*Silva and Prather*, 2000].

2.4.3 Unleaded fuel samples

Figure 2.4 (a-e) shows the AM for the five different particle classes that are unique to the unleaded fuel samples. Each of the particle classes shown in Figure 2.4 contain PAH fragment ions at 25^{-}, 49^{-}, 73^{-} and sulfate peaks at $^{97}(HSO_4)^{-}$. Organic carbon fragment peaks at *m/z* $^{15}CH_3^{+}$, 27^{+}, 29^{+}, 43^{+}, sulfur-containing ions at $^{80}(SO_3)^{-}$ and

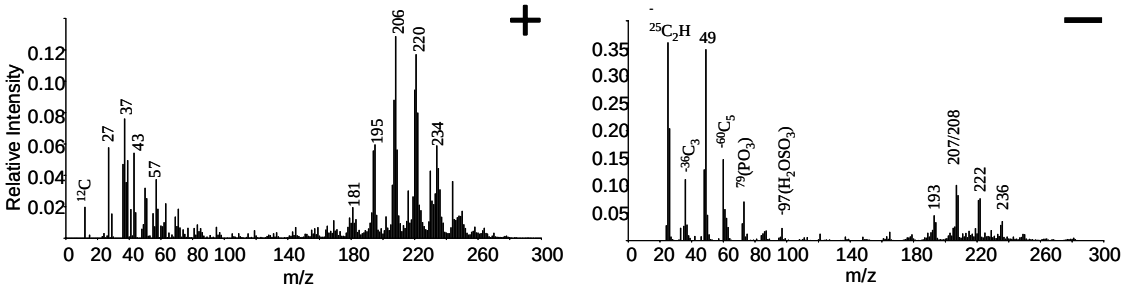

Figure 2.3 Positive and negative ion AM for PAH-containing particle class detected exclusively in diesel fuel.

$^{81}(HSO_3)^-$ and peaks at *m/z* 109^-, 123^-, and 137^- are also observed in many of the AM shown in Figure 2.4. Shown in Figure 2.4a is the AM of particles observed for all of the unleaded fuel samples (*PAH-Sulfate-NO_2-Cl*). The AM of this particle type is characterized by intense peaks attributed to PAH ions at *m/z*, 192^+, 206^+, 218^+, 230^+, and 242^+, as well as peaks due to $^{35}Cl^-$ and $^{46}(NO_2)^-$. The largest fraction of particles in the unleaded fuel samples were an *OC-K-Na-Sulfate-Phosphate* type, shown in Figure 2.4b. The presence of potassium in this unleaded fuel class distinguishes it from diesel fuel. Potassium is not generally used as a fuel additive; however it is clearly present in all of the unleaded fuel samples. ATOFMS has a high sensitivity to potassium so even though it is present in low concentrations in fuel, it produces a large ion peak in the ATOFMS spectra [*Gross et al.*, 2000]. Phosphate $^{79}(PO_3)^-$ and carbon cluster peaks extending out to *m/z* 72^- also are detected in Figure 2.4b negative ion AM. Unleaded fuel samples #1 and #3 contain an *OC-Sulfate-Phosphate* particle class which is unique to these samples (Figure 2.4c). This AM contains unique peaks at 130^+, 162^+, and 214^+, that other fuel types did not contain. Figures 2.4d and 2.4e show the AMs for OC particle classes almost exclusive to unleaded fuel samples #2 and #4, respectively. The major difference between Figures 2.4d and 2.4e is an ion at *m/z* 57^+ (Figure 2.4d), instead of 58^+ (Figure 2.4e)

Both unleaded and diesel fuel produced an *OC-Na-Sulfate-Phosphate* particle class. Figure 2.5 shows the AM for this class characterized by the presence of OC at 27^+, 29^+, 43^+, 91^+, PAH fragment ions at 25^-, 49^-, 73^-, sulfate at $^{97}(HSO_4)^-$, and phosphate at $^{79}(PO_3)^-$. Higher molecular weight ions at 165^+, 179^+, and 193^+ are present as well. These ions could be attributed to nitrogen-containing aromatics with alkyl substitutions

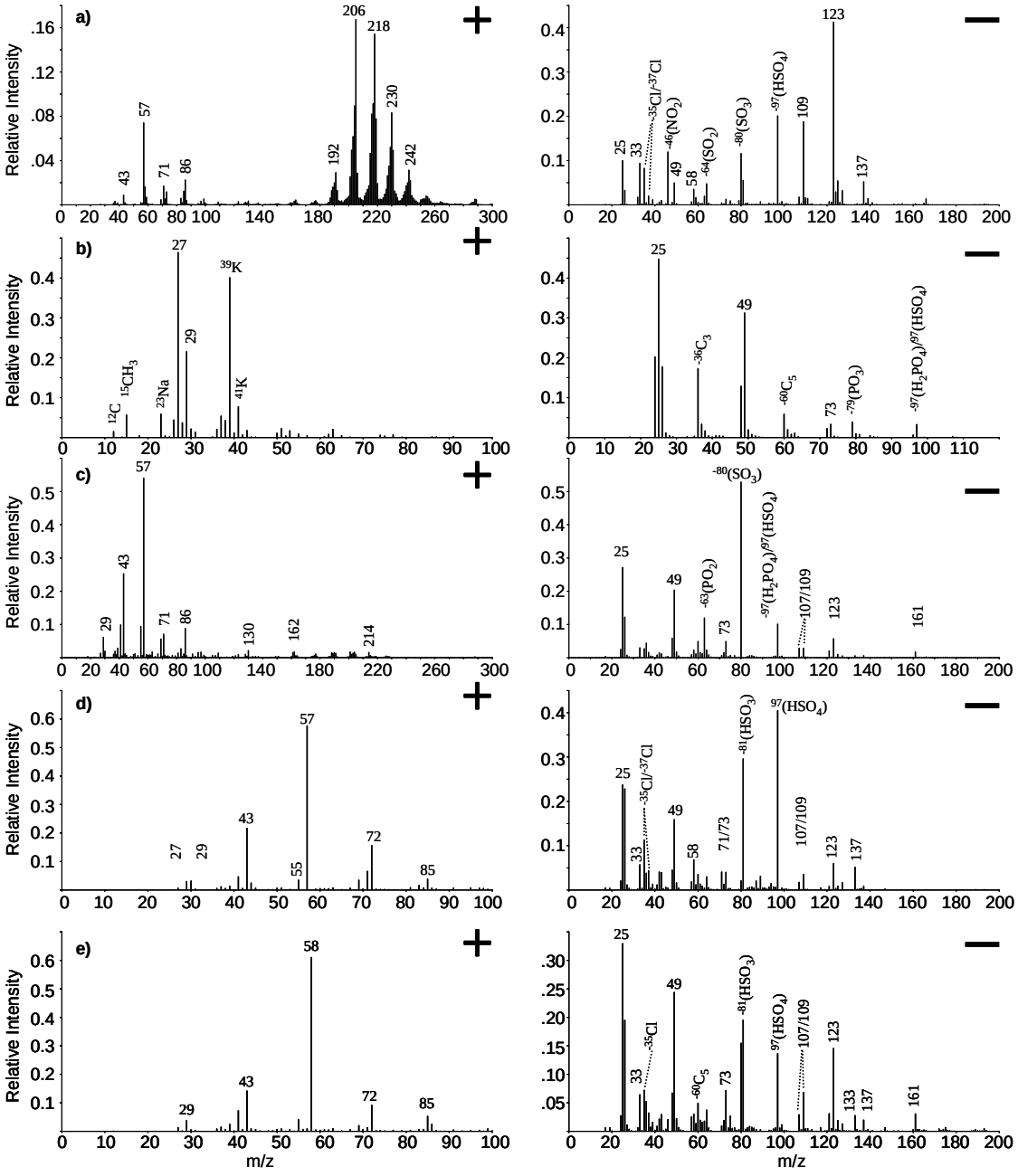

Figure 2.4 Positive and negative ion AM for five particle types unique to unleaded fuel. The five different types shown are: a) PAH-Sulfate-NO_2-Cl, b) OC-K-Na-Sulfate-Phosphate, c) OC-Sulfate-Phosphate, d) OC-Sulfur containing and e) OC-Sulfate-Other.

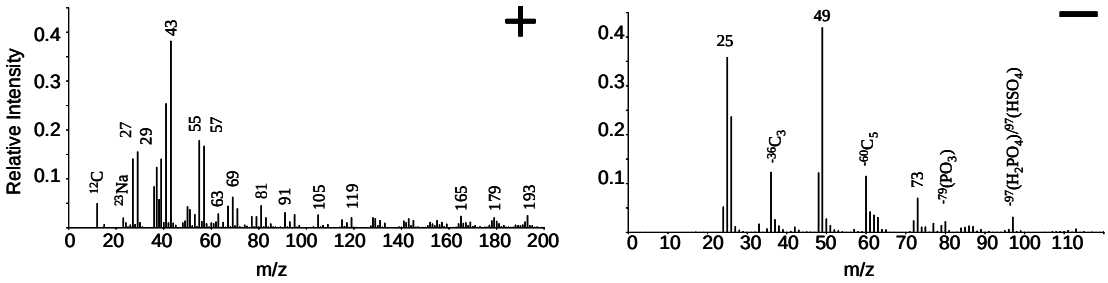

Figure 2.5 Positive and negative ion AM for the OC-Na-Sulfate-Phosphate particle class detected in both diesel and unleaded fuel samples.

based on the presence of odd masses [*McLafferty and Tureécek*, 1993]. Further, ions at *m/z* 119^+, 105^+, 91^+ are attributed to fragmentation of phenylalkyl (substituted mono-aromatic) type compounds [*McLafferty and Tureécek*, 1993]. However, given the enormous number of organic species present in gasoline and diesel fuels, these assignments are speculative without further analysis.

Figure 2.6 shows the fractional contributions of the different particles types for each oil and fuel sample determined using ART-2a analysis. Figure 2.6 clearly shows that new oil, used oil, diesel fuel, and unleaded fuel can be distinguished from each other at the single particle level. New oil samples are dominated by calcium, phosphate, and OC signatures (*Ca-Phosphate-OC* chemical class). Used HDDV oil samples show additional marker ions from NO_2^- and Na^+ (*Ca-EC-OC-Phosphate-NO_2-Na*), as well as elemental carbon (EC) (*Ca-EC-OC-Phosphate*). Used LDV oil differs from used HDDV oil by the presence of PAH-containing particles (*Ca-PAH-OC-Phosphate* type). Diesel fuel particle mass spectra are dominated by PAH's (40-80% of particles contain PAH's), OC, Na, sulfates, and phosphates. The majority (50%) of unleaded fuel particles contained K^+, which differentiates it from diesel fuel. Furthermore, a fraction (10-20%) of unleaded fuel particles contained PAH, NO_2, and Cl ions, another distinguishing feature.

2.4.4 **Comparison with PM emissions**

When comparing particle types observed in fuel and oil samples with HDDV exhaust particles between 500-2500 nm, the calcium and phosphate dominated types (*Ca-OC-Phosphate-NO_2-Na* and *Ca-ECOC-Phosphate)* detected in the used HDDV oil samples

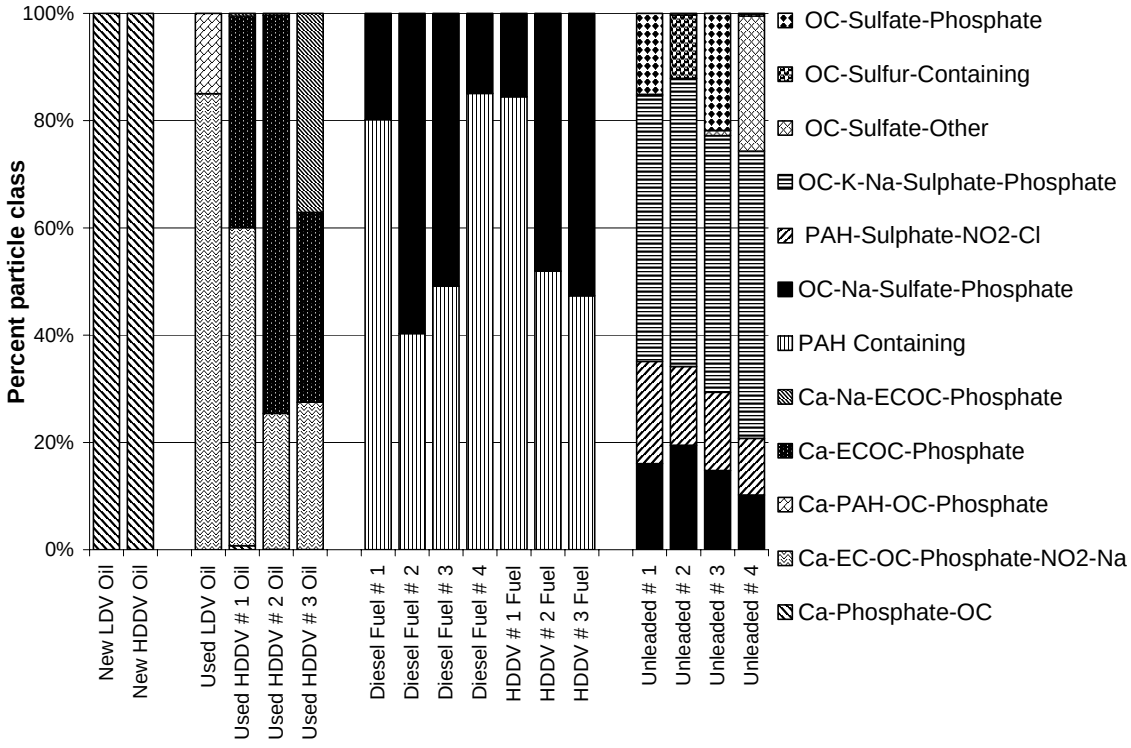

Figure 2.6 Histogram showing the percent contribution of each particle class to each oil and fuel sample analyzed. Oil or fuel type is listed across the x-axis, and the percent (normalized) of each particle class observed within a sample is given on the y-axis. Colors corresponding to different particle classes are listed in the legend.

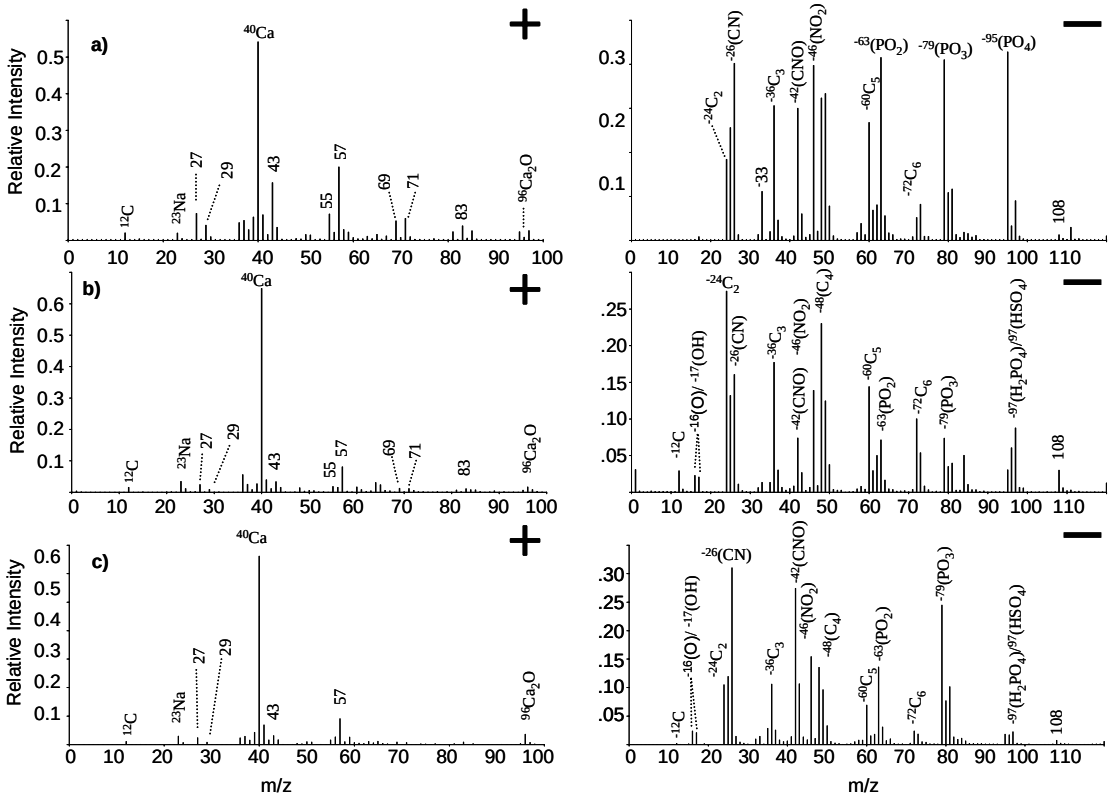

Figure 2.7 Comparison of a) the *Ca-ECOC-Phosphate* AM from used oil, b) the AM of the largest particle class from the exhaust of heavy duty diesel trucks, and c) the AM of a class of particles that made up ~2% of "smoker" LDV mass spectra.

show a strong degree of similarity to the most dominant particle type detected in HDDV exhaust. The dot products of the weight matrices for the used oil particle types (*Ca-EC-OC-Phosphate-NO_2-Na* and *Ca-ECOC-Phosphate* particle class) with the corresponding HDDV exhaust particle types were 0.87 and 0.85, respectively. A significant fraction (~60%) of freshly emitted HDDV particles in the 500-2500 nm size range showed the same mass spectral fingerprint as used HDDV oil [*Shields et al.,* 2006]. Figures 2.7a and 2.7b show the dual ion AM for the *Ca-ECOC-Phosphate* mass spectral class from used oil and the AM for the most abundant particle class from a HDDV dynamometer study using ATOFMS [*Shields et al.*, 2006]. By visual inspection, one can see the two area matrices are strikingly similar. Shields (2006) and Toner (2006) show that a dominant particle class from diesel trucks from 50-500 nm is an *EC-Ca* particle type which differs from the *Ca-ECOC-Phosphate* type discussed above in the relative intensity of the Ca^+ ion peak to the carbon ion clusters in the positive ion mass spectra. This would suggest that EC particles in this smaller size range from diesel trucks are a mixture of freshly generated EC with a small fraction of unburned oil. These findings are consistent with a previous report that states up to 95% of the volatile component of nanoparticles and accumulation-mode particles emitted from diesel trucks are from unburned oil [*Sakurai et al.,* 2003]. Other research has shown a significant fraction of Ca coming from fuel [*Sharma et al.,* 2005; *Wang et al.,* 2003]. Data here would suggest that unburned oil might also be a significant source of Ca in diesel particle emissions.

Recent results from a study by Shields (2006) show that the particle emissions can reflect the oil signatures from HDDV trucks. Specifically, a particle type from used oil showed increased amounts of Na (HDDV #3 oil); correspondingly, the emissions from

the HDDV from which this sample was taken produced exhaust particle spectra with higher amounts of Na^+. This finding provides further evidence that HDDV exhaust particles contain a significant fraction of unburned oil and that the chemical composition of the oil is reflected in the chemistry of the HDDV particle emissions.

Comparison of the dominant particle class detected in used LDV oil with LDV exhaust particle classes yielded few similarities, suggesting that LDV emissions are not normally composed of a large fraction of unburned oil. However, one LDV that emitted heavy amounts of smoke from its tailpipe (i.e. "smoker") did contain a small fraction (~2%) of the LDV oil particle class (*Ca-OC-Phosphate-NO_2-Na*). The area matrix for the comparable particle class from the LDV smoker is shown in Figure 2.7c for comparison with the HDDV oil type [*Sodeman et al.*, 2005].

Unleaded fuel and diesel fuel particles do not resemble LDV and HDDV exhaust particles, suggesting vehicle emissions do not contain a large fraction of unburned fuel particles. However unburned fuel vapor could condense on other particle cores; these vapor coated particles may not be comparable to pure fuel particles. Potassium and sodium were observed in the fuel samples and LDV emissions also show peaks due to K^+ and Na^+ [*Shields et al.*, 2006; *Sodeman et al.*, 2005; *Toner et al.*, 2006], suggesting that these elements could be coming from the fuel.

2.5 Conclusions

To differentiate between fresh particle emissions from HDDV and LDV (with the exception of "smoker" LDV) using ATOFMS, the used HDDV oil particle mass spectra provide good indicators for HDDV exhaust particles. Using ATOFMS, lubricating oil is

characterized by a very intense Ca^+ peak accompanied by less intense organic fragment ions. Ambient particles sampled using ATOFMS containing a combination of intense Ca^+, $CaOH^+$, and EC/OC marker ions are likely to be fresh diesel combustion particles composed of a significant amount of unburned lubricating oil. Comparing oil and fuel particle signatures with particle characterization studies of HDDV and LDV emissions enhances our ability to differentiate between HDDV and LDV sources and understand the origin of specific marker ions from these major ambient particle sources.

2.6 Acknowledgements

This study was supported by the California Air Resources Board (CARB 00-331).

Chapter 2 reproduced with permission from Spencer, M.T., L.G. Shields, D.A. Sodeman, S.M. Toner, and K.A. Prather, Comparison of oil and fuel particle chemical signatures with particle emissions from heavy and light duty vehicles, *Atmospheric Environment, 40* (27), 5224-5235, 2006.

2.7 References

Ackerman, A.S., O.B. Toon, D.E. Stevens, A.J. Heymsfield, V. Ramanathan, and E.J. Welton, Reduction of tropical cloudiness by soot, *Science, 288* (5468), 1042-1047, 2000.

Alander, T.J.A., A.P. Leskinen, T.M. Raunemaa, and L. Rantanen, Characterization of diesel particles: Effects of fuel reformulation, exhaust after-treatment, and engine operation on particle carbon composition and volatility, *Environmental Science & Technology, 38* (9), 2707-2714, 2004.

Alfarra, M.R., H. Coe, J.D. Allan, K.N. Bower, H. Boudries, M.R. Canagaratna, J.L. Jimenez, J.T. Jayne, A.A. Garforth, S.M. Li, and D.R. Worsnop, Characterization of urban and rural organic particulate in the lower Fraser valley using two aerodyne aerosol mass spectrometers, *Atmos. Environ., 38* (34), 5745-5758, 2004.

Andreae, M.O., D. Rosenfeld, P. Artaxo, A.A. Costa, G.P. Frank, K.M. Longo, and M.A.F. Silva-Dias, Smoking rain clouds over the Amazon, *Science, 303* (5662), 1337-1342, 2004.

Bata, R., N. Clark, M. Gautam, A. Howell, T. Long, J. Loth, D. Lyons, G. Palmer, J. Smith, and W. Wang, A transportable heavy duty engine testing laboratory, *SAE Trans., 100*, 433-440, 1991.

Bezabeh, D.Z., T.M. Allen, E.M. McCauley, P.B. Kelly, and A.D. Jones, Negative ion laser desorption ionization time-of-flight mass spectrometry of nitrated polycyclic aromatic hydrocarbons, *J. Am. Soc. Mass Spectrom., 8* (6), 630-636, 1997.

Burtscher, H., S. Kunzel, and C. Huglin, Characterization of particles in combustion engine exhaust, *J. Aerosol Sci., 29* (4), 389-396, 1998.

Canagaratna, M.R., J.T. Jayne, D.A. Ghertner, S. Herndon, Q. Shi, J.L. Jimenez, P.J. Silva, P. Williams, T. Lanni, F. Drewnick, K.L. Demerjian, C.E. Kolb, and D.R. Worsnop, Chase studies of particulate emissions from in-use New York city vehicles, *Aerosol Science & Technology, 38* (6), 555-573, 2004.

Canning, G.W., M.L.S. Fuller, G.M. Bancroft, M. Kasrai, J.N. Cutler, G. De Stasio, and B. Gilbert, Spectromicroscopy of tribological films from engine oil additives. Part I. Films from zddp's, *Tribology Letters, 6* (3-4), 159-169, 1999.

Chung, S.H., and J.H. Seinfeld, Climate response of direct radiative forcing of anthropogenic black carbon, *J. Geophys. Res., 110* (D11), 2005.

Dockery, D.W., C.A. Pope, X.P. Xu, J.D. Spengler, J.H. Ware, M.E. Fay, B.G. Ferris, and F.E. Speizer, An association between air-pollution and mortality in 6 United-States cities, *N. Engl. J. Med., 329* (24), 1753-1759, 1993.

Fitzgerald, J.W., Marine aerosols: A review, *Atmospheric Environment Part a-General Topics, 25* (3-4), 533-545, 1991.

Gard, E., J.E. Mayer, B.D. Morrical, T. Dienes, D.P. Fergenson, and K.A. Prather, Real-time analysis of individual atmospheric aerosol particles: Design and performance of a portable ATOFMS, *Anal. Chem., 69* (20), 4083-4091, 1997.

Gautam, M., K. Chitoor, M. Durbha, and J.C. Summers, Effect of diesel soot contaminated oil on engine wear - investigation of novel oil formulations, *Tribology International, 32* (12), 687-699, 1999.

Graham, B., P. Guyon, P.E. Taylor, P. Artaxo, W. Maenhaut, M.M. Glovsky, R.C. Flagan, and M.O. Andreae, Organic compounds present in the natural Amazonian aerosol: Characterization by gas chromatography-mass spectrometry, *J. Geophys. Res., 108* (D24), 2003.

Gross, D.S., M.E. Gaelli, P.J. Silva, and K.A. Prather, Relative sensitivity factors for alkali metal and ammonium cations in single-particle aerosol time-of-flight mass spectra, *Anal. Chem., 72* (2), 416-422, 2000.

Hamilton, R.S., and T.A. Mansfield, Airborne particulate elemental carbon - its sources, transport and contribution to dark smoke and soiling, *Atmospheric Environment Part a-General Topics, 25* (3-4), 715-723, 1991.

Harrison, R.M., and J.X. Yin, Particulate matter in the atmosphere: Which particle properties are important for its effects on health?, *Sci. Total Environ., 249* (1-3), 85-101, 2000.

Heywood, J.B., *Internal combustion engine fundamentals*, xxix, 930 p., McGraw-Hill, New York, 1988.

Hopke, P.K., and X.H. Song, Classification of single particles by neural networks based on the computer-controlled scanning electron microscopy data, *Anal. Chim. Acta, 348* (1-3), 375-388, 1997.

Hughes, L.S., J.O. Allen, P. Bhave, M.J. Kleeman, G.R. Cass, D.Y. Liu, D.P. Fergenson, B.D. Morrical, and K.A. Prather, Evolution of atmospheric particles along trajectories crossing the Los Angeles basin, *Environ. Sci. Technol., 34* (15), 3058-3068, 2000.

Isotalo, S., T. Kuljukka-Rabb, L. Rantanen, S. Mikkonen, and K. Savela, The effect of diesel fuel reformulation on the exhaust measured by ames mutagenicity and DNA adducts, *Int. J. Environ. Anal. Chem.*, *82* (2), 87-95, 2002.

Karas, M., and R. Kruger, Ion formation in MALDI: The cluster ionization mechanism, *Chemical Reviews*, *103* (2), 427-439, 2003.

Kittelson, D.B., Engines and nanoparticles - a review, *J. Aerosol Sci.*, *29* (5-6), 575-588, 1998.

Kleeman, M.J., J.J. Schauer, and G.R. Cass, Size and composition distribution of fine particulate matter emitted from motor vehicles, *Environ. Sci. Technol.*, *34* (7), 1132-1142, 2000.

Krishnan, R., and V. Ramanathan, Evidence of surface cooling from absorbing aerosols, *Geophys. Res. Lett.*, *29* (9), 2002.

Lee, S.D., M.S. Jang, and R.M. Kamens, SOA formation from the photooxidation of alpha-pinene in the presence of freshly emitted diesel soot exhaust, *Atmos. Environ.*, *38* (16), 2597-2605, 2004.

Lowenthal, D.H., B. Zielinska, J.C. Chow, J.G. Watson, M. Gautam, D.H. Ferguson, G.R. Neuroth, and K.D. Stevens, Characterization of heavy-duty diesel vehicle emissions, *Atmos. Environ.*, *28* (4), 731-43, 1994.

Lyyranen, J., J. Jokiniemi, E.I. Kauppinen, and J. Joutsensaari, Aerosol characterization in medium-speed diesel engines operating with heavy fuel oils, *J. Aerosol Sci.*, *30* (6), 771-784, 1999.

Marr, L.C., T.W. Kirchstetter, R.A. Harley, A.H. Miguel, S.V. Hering, and S.K. Hammond, Characterization of polycyclic aromatic hydrocarbons in motor vehicle fuels and exhaust emissions, *Environmental Science & Technology*, *33* (18), 3091-3099, 1999.

May, K.R., Collision nebulizer. Description, performance, and application, *J. Aerosol Sci.*, *4* (3), 235-43, 1973.

McLafferty, F.W., and F. Tureécek, *Interpretation of mass spectra*, 371 pp., University Science Books, Mill Valley, Calif., 1993.

Odum, J.R., T.P.W. Jungkamp, R.J. Griffin, R.C. Flagan, and J.H. Seinfeld, The atmospheric aerosol-forming potential of whole gasoline vapor, *Science*, *276* (5309), 96-99, 1997.

Pandis, S.N., R.A. Harley, G.R. Cass, and J.H. Seinfeld, Secondary organic aerosol formation and transport, *Atmospheric Environment Part a-General Topics*, *26* (13), 2269-2282, 1992.

Pinker, R.T., G. Pandithurai, B.N. Holben, O. Dubovik, and T.O. Aro, A dust outbreak episode in sub-Sahel west Africa, *J. Geophys. Res.*, *106* (D19), 22923-22930, 2001.

Rhead, M.M., and S.A. Hardy, The sources of polycyclic aromatic compounds in diesel engine emissions, *Fuel*, *82* (4), 385-393, 2003.

Rudnick, L.R., *Lubricant additives : Chemistry and applications*, xiii, 735 pp., Marcel Dekker, New York, 2003.

Sakurai, H., K. Park, P.H. McMurry, D.D. Zarling, D.B. Kittelson, and P.J. Ziemann, Size-dependent mixing characteristics of volatile and nonvolatile components in diesel exhaust aerosols, *Environ. Sci. Technol.*, *37* (24), 5487-5495, 2003.

Schauer, J.J., and G.R. Cass, Source apportionment of wintertime gas-phase and particle-phase air pollutants using organic compounds as tracers, *Environmental Science & Technology*, *34* (9), 1821-1832, 2000.

Schauer, J.J., M.J. Kleeman, G.R. Cass, and B.R.T. Simoneit, Measurement of emissions from air pollution sources. 2. C-1 through c-30 organic compounds from medium duty diesel trucks, *Environmental Science & Technology*, *33* (10), 1578-1587, 1999.

Schauer, J.J., M.J. Kleeman, G.R. Cass, and B.R.T. Simoneit, Measurement of emissions from air pollution sources 5: C-1-c-32 organic compounds from gasoline-powered motor vehicles, *Environmental Science & Technology*, *36* (6), 1169-1180, 2002.

Schwartz, J., and D.W. Dockery, Increased mortality in Philadelphia associated with daily air-pollution concentrations, *Am. Rev. Respir. Dis.*, *145* (3), 600-604, 1992.

Sharma, M., A.K. Agarwal, and K.V.L. Bharathi, Characterization of exhaust particulates from diesel engine, *Atmos. Environ.*, *39* (17), 3023-3028, 2005.

Shields, L.G., D.T. Suess, S.A. Guazzotti, and K.A. Prather, Determination of single particle mass spectral signatures from heavy duty vehicle emissions, *Atmos. Environ., accepted*, 2006.

Silva, P.J., and K.A. Prather, Online characterization of individual particles from automobile emissions, *Environ. Sci. Technol.*, *31* (11), 3074-3080, 1997.

Silva, P.J., and K.A. Prather, Interpretation of mass spectra from organic compounds in aerosol time-of-flight mass spectrometry, *Anal. Chem., 72* (15), 3553-3562, 2000.

Sodeman, D.A., S.M. Toner, and K.A. Prather, Determination of single particle mass spectral signatures from light duty vehicle emissions, *Environmental Science & Technology, 39* (12), 4569-4580, 2005.

Song, X.-H., N.M. Faber, P.K. Hopke, D.T. Suess, K.A. Prather, J.J. Schauer, and G.R. Cass, Source apportionment of gasoline and diesel by multivariate calibration based on single particle mass spectral data, *Anal. Chim. Acta, 446* (1-2), 329-343, 2001.

Song, X.-H., P.K. Hopke, D.P. Fergenson, and K.A. Prather, Classification of single particles analyzed by ATOFMS using an artificial neural network, ART-2a, *Anal. Chem., 71* (4), 860-865, 1999.

Spencer, M.T., and K.A. Prather, Using ATOFMS to determine OC/EC mass fractions in particles, *Aerosol Sci. Technol., 40* (8), 585-594, 2006.

Suess, D.T., Single particle mass spectrometry combustion source characterization and atmospheric apportionment of vehicular, coal, and biofuel exhaust emissions, Ph.D.Thesis, University of California Riverside, 2002.

Tobias, H.J., D.E. Beving, P.J. Ziemann, H. Sakurai, M. Zuk, P.H. McMurry, D. Zarling, R. Waytulonis, and D.B. Kittelson, Chemical analysis of diesel engine nanoparticles using a nano-DMA/thermal desorption particle beam mass spectrometer, *Environ. Sci. Technol., 35* (11), 2233-2243, 2001.

Toner, S.M., D.A. Sodeman, and K.A. Prather, Single particle characterization of ultrafine and accumulation mode particles from heavy duty diesel vehicles using aerosol time-of-flight mass spectrometry, *Environmental Science & Technology, 40* (12), 3912-3921, 2006.

Wang, J., C.R. Jia, C.K. Wong, and P.K. Wong, Characterization of polycyclic aromatic hydrocarbons created in lubricating oils, *Water, Air, & Soil Pollution, 120* (3-4), 381-396, 2000a.

Wang, W.G., D.W. Lyons, N.N. Clark, M. Gautam, and P.M. Norton, Emissions from nine heavy trucks fueled by diesel and biodiesel blend without engine modification, *Environmental Science & Technology, 34* (6), 933-939, 2000b.

Wang, Y.F., K.L. Huang, C.T. Li, H.H. Mi, J.H. Luo, and P.J. Tsai, Emissions of fuel metals content from a diesel vehicle engine, *Atmos. Environ., 37* (33), 4637-4643, 2003.

Willermet, P.A., Some engine oil additives and their effects on antiwear film formation, *Tribology Letters*, *5* (1), 41-47, 1998.

Zielinska, B., J. Sagebiel, W.P. Arnott, C.F. Rogers, K.E. Kelly, D.A. Wagner, J.S. Lighty, A.F. Sarofim, and G. Palmer, Phase and size distribution of polycyclic aromatic hydrocarbons in diesel and gasoline vehicle emissions, *Environ. Sci. Technol.*, *38* (9), 2557-2567, 2004.

3 Using ATOFMS to Determine OC/EC Mass Fractions in Particles

3.1 Synopsis

Historically, obtaining quantitative chemical information using laser desorption ionization mass spectrometry for analyzing individual aerosol particles has been quite challenging. This is due in large part to fluctuations in the absolute ion signals resulting from inhomogeneities in the laser beam profile, as well as chemical matrix effects. Progress has been made in quantifying atomic species using high laser powers, but very few studies have been performed quantifying molecular species. In this study, promising results are obtained using a new approach to measure the fraction of organic carbon (OC) associated with elemental carbon (EC) in aerosol particles using single particle laser desorption ionization. A tandem differential mobility analyzer (TDMA) is used to generate OC/EC particles by size selecting EC particles of a given mobility diameter and then coating them with known thicknesses of OC measured using a second DMA. The mass spectra of the OC/EC particles exiting the second DMA are measured using an ultrafine aerosol time-of-flight mass spectrometer (UF-ATOFMS). A calibration curve is produced with a linear correlation (R^2 = 0.98) over the range of OC/EC ion intensity ratios observed in source and ambient studies. Importantly, the OC/EC values measured in ambient field tests with the UF-ATOFMS show a linear correlation (R^2 = 0.69) with

OC/EC mass ratios obtained using semi-continuous filter based thermo-optical measurements. The calibration procedure established herein represents a significant step toward quantification of OC and EC in sub-micron ambient particles using laser desorption ionization mass spectrometry.

3.2 Introduction

Carbonaceous species contribute up to as much as 90% of the total $PM_{2.5}$ particulate mass [*Herner et al.*, 2005; *Lim and Turpin*, 2002; *Zheng et al.*, 2002]. Carbonaceous aerosols are traditionally sub-divided into two major fractions: elemental carbon (EC) and organic carbon (OC). Ambient carbonaceous aerosols range from pure OC and EC to a mixture of the two [*Burtscher et al.*, 1998; *Katrinak et al.*, 1992; *Kwon et al.*, 2003; *Mader et al.*, 2002]. EC is formed from the incomplete combustion of organic species and originates from sources such as vehicle emissions, industrial emissions, and biomass burning. The EC fraction is often referred to as soot or black carbon due to the absorbing properties in the atmosphere [*Horvath*, 1993]. OC is also released from vehicles, biomass burning, as well as biogenic sources. OC can be directly emitted into the atmosphere in the particle (primary organic aerosol) or the gas phase. OC species in the gas phase often undergo oxidation reactions that lead to the formation of secondary organic aerosol (SOA) [*Odum et al.*, 1997]. SOA will form by homogeneous or heterogeneous nucleation on preexisting seed aerosols. Homogeneous nucleation is less common in urban environments due to the presence of significant numbers of “seed” aerosols. The relative fraction of EC and OC in particles vary as a function of the particle source [*Kleeman et al.*, 2000] and change as particles age [*Liousse et al.*, 1995].

EC particles absorb incoming solar radiation leading to an increase in radiative forcing (direct effect) [*Penner et al.*, 1998]. The mixing state of EC strongly influences the overall absorbing properties of EC particles [*Jacobson*, 2001]. The addition of an organic coating to an EC core has been shown to increase the absorption coefficient of the aerosol by up to 35% [*Schnaiter et al.*, 2003]. Furthermore, EC, which is normally considered a hydrophobic aerosol species, often undergoes aging processes that result in increased hydrophilic properties via direct oxidation or coating with polar organic species [*Zuberi et al.*, 2005]. This change in the surface properties of EC particles increases their ability to act as cloud condensation nuclei (CCN), enhancing their indirect effect on climate [*Novakov and Penner*, 1993; *Saxena et al.*, 1995; *Weingartner et al.*, 1997]. A better understanding of the level of mixing between EC and OC in ambient particles is needed to quantitatively assess the overall impact carbonaceous aerosols have on climate change.

Single particle mass spectrometry is a tool that can be used to directly probe the particle mixing state of laboratory generated soot particles and ambient particles [*Guazzotti et al.*, 2001a; *Kirchner et al.*, 2003; *Whiteaker*, 2002]. The ATOFMS measures the aerodynamic diameter of individual particles and then uses laser ablation/ ionization coupled with a dual polarity time-of-flight mass spectrometer to obtain positive and negative ion information on individual particles [*Gard et al.*, 1997; *Prather et al.*, 1994]. ATOFMS has been used in a number of atmospheric measurement campaigns and provides complementary information on aerosol chemistry and particle variability in the environment [*Guazzotti et al.*, 2001b; *Qin et al.*, 2006]. Single particle

mass spectrometers such as ATOFMS provide information on the number concentrations of chemically distinct particle types, showing how these concentrations change over time [*Liu et al.*, 2003; *Pastor et al.*, 2003].

It has been questioned as to whether laser desorption ionization (LDI) analysis of aerosols can be used to quantitatively assess the amounts of specific chemical species such as OC and EC in ambient particles. Achieving quantitative chemical information on aerosols using ion intensities produced by LDI has had limited success to date [*Bhave et al.*, 2002; *Fergenson et al.*, 2001; *Gross et al.*, 2000; *Lee et al.*, 2005; *Smith et al.*, 2002; *Woods et al.*, 2001]. The most promising quantitative results have been for LDI processes producing atomic ions [*Lee et al.*, 2005; *Reents and Ge*, 2000]. However, more detailed information on the organic species or the source producing the species contained within a particle is lost when the particle is ablated and ionized to the atomic level. Indeed, determining the relative fractions of chemical species within a single particle is quite challenging due to differences in the laser pulse energy encountered by each particle during the ionization process. Absolute ion area has been shown to fluctuate by as much as 59% from monodisperse aerosol particles with the same composition [*Gross et al.*, 2000]. These differences in ionization between chemically similar particles have been attributed to an inhomogeneous laser beam profile [*Wenzel and Prather*, 2004]. Furthermore, matrix effects between dissimilar particles can also produce differences in the ion abundances. However, as shown herein, averaging the mass spectra of an ensemble of particles of the same size with similar chemical composition reduces the effects of the shot-to-shot single particle ion signal fluctuations.

This paper describes an initial effort to use the ratios of mass spectral ion signal intensities to establish OC/EC mass fractions in ambient carbonaceous aerosols using an ultrafine aerosol time-of-flight mass spectrometer (UF-ATOFMS). A key component of this study involves creating and characterizing the ion response to laboratory generated OC/EC particles using a tandem differential mobility analyzer (TDMA) [*Rader and McMurry*, 1986] coupled with an ATOFMS. The resulting OC/EC values measured with an ATOFMS are compared to those obtained with a standard OC/EC thermo-optical method for carbonaceous particles sampled during vehicle source tests. Establishing correlations between ion signals and OC/EC mass fractions in particles represents a significant step in our ability to quantitatively assess the different chemical components in ambient aerosols using single particle mass spectrometry.

3.3 Experimental

A description of the ATOFMS is given in Chapter 1 and published in detail elsewhere [*Su et al.*, 2004]. The UF-ATOFMS in this work has an aerodynamic lens inlet and measures the vacuum aerodynamic equivalent diameter (d_{ae}) of particles between 50-1000 nm and a dual polarity mass spectrum for each individual particle.

3.3.1 Particle generation

A schematic of the experimental set-up used for these experiments is shown in Figure 3.1. Elemental carbon (EC) particles were generated using a spark discharge across graphite rods with a commercially available instrument (GfG 1000, Palas generator) [*Helsper et al.*, 1993; *Roth et al.*, 2004]. A spark frequency of 200 Hz was

used. Argon was used as a purge gas at a flow rate of 5.0 L min^{-1}. EC particles were further diluted downstream in a 1 L dilution chamber with approximately 25 L min^{-1} of dry, purified (using activated carbon and Purafil adsorbents), and HEPA-filtered air. One L min^{-1} of the diluted EC particle stream was pulled through a differential mobility analyzer (DMA-1) (TSI 3080), to select particles with a desired electrical mobility equivalent diameter (d_{me}). The sheath flow for DMA-1 was set at 10 L min^{-1}. These size selected particles then passed through a 1.5 L cylindrical flask containing ~ 200 mL 85-octane (regular) unleaded fuel at the bottom. Aerosols entered this flask approximately 3 inches above the liquid (within the headspace). The temperature of unleaded fuel was regulated using a heated water bath. Fresh unleaded fuel was used for each temperature run. Each experiment lasted approximately 15 minutes and no changes in the particle mass spectra occurred from beginning to end of any experiment. For analysis of EC particles with no organic coating, the particles passed through the same flask containing no unleaded fuel. Depending on the experiment, OC coated or uncoated EC particles were pulled through a second DMA (DMA-2), with a condensation particle counter attached to it. DMA-2 coupled to a CPC was used to obtain the electrical mobility size distribution of uncoated and coated EC particles. Sample flow through DMA-2 was 1 L min^{-1} and the sheath flow was set at 10 L min^{-1}. Uncoated monodisperse EC particles could also be sent directly to the UF-ATOFMS for aerodynamic sizing and chemical analysis, bypassing DMA-2. DMA-2 was also used to size select EC particles coated with organic material at size of 100, 150, and 250 nm.

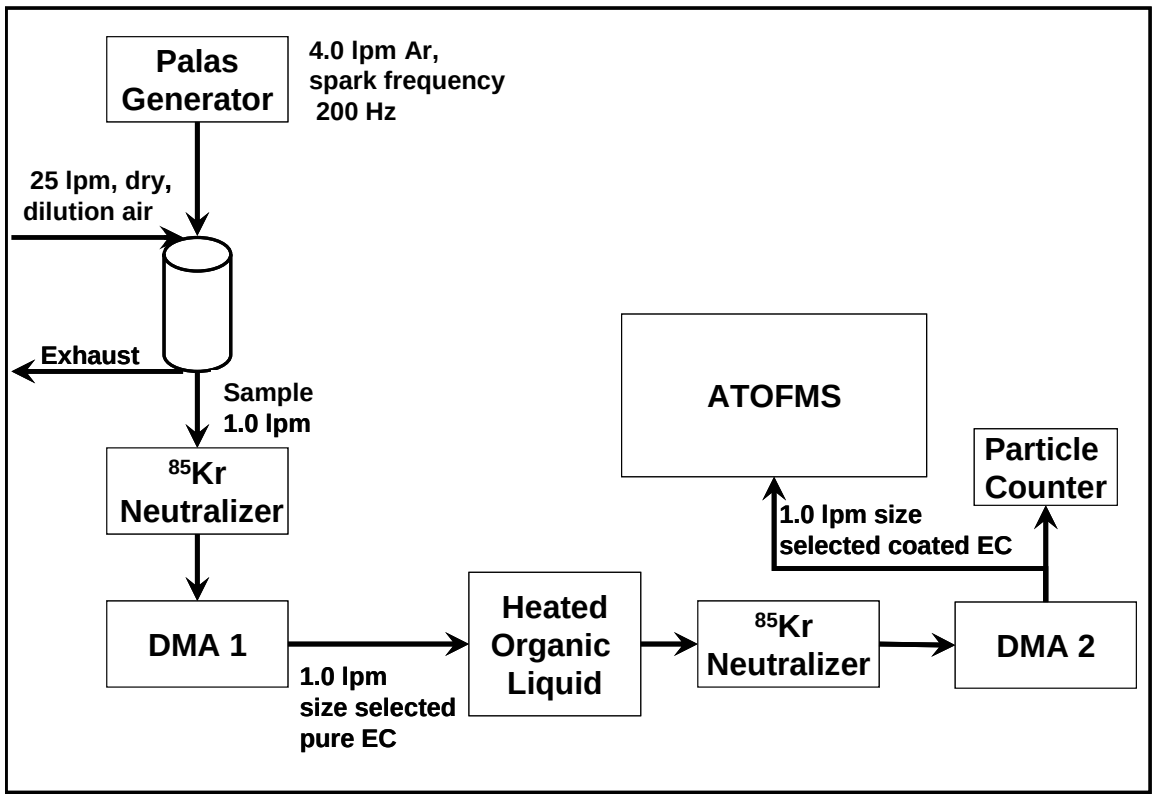

Figure 3.1 General measurement set-up. Pure EC aerosol flows from the Palas generator to a dilution chamber, a charge neutralizer, and then DMA-1 where they are size selected. Aerosols can be measured with UF-ATOFMS as pure EC or OC coating EC in a temperature regulated flask containing gasoline. Uncoated and coated aerosol size distributions are measured with DMA-2 and a condensation particle counter. For coated aerosols, DMA-2 size selects coated aerosols, which are sent to the UF-ATOFMS for size (vacuum aerodynamic diameter) and composition analysis.

These size selected OC coated aerosols were then sampled by the UF-ATOFMS for aerodynamic size and chemical analysis.

3.3.2 Data analysis

Approximately 500 dual ion mass spectra were obtained for each experiment. UF-ATOFMS data were imported into Matlab Version 6.1.0.450 Release 12.1 (The MathWorks, Inc.) and analyzed using YAADA version 1.2 [http://www.yaada.org]. For each experiment, the set of mass spectra were converted into a relative area matrix. The relative area matrix represents the average of all mass spectra generated for each experiment. To create a relative area matrix, all ion peaks in each individual mass spectrum are first normalized to the most intense peak within the spectrum and then all of the normalized individual mass spectra are averaged.

3.3.3 Ambient data collection

UF-ATOFMS ambient field data were collected during field studies conducted at three locations: the I-5 Freeway [*Toner et al.*, 2007] in San Diego in 2004, as well as the cities of Boston in 2003, and Atlanta in 2002. Three vehicle source characterization data sets are also used in this study: diesel powered truck data [*Shields et al.*, 2006] acquired in 2001, gasoline powered vehicle particle data [*Sodeman et al.*, 2005] acquired in 2002, and diesel powered truck particle data [*Toner et al.*, 2006] acquired in 2003.

Ambient field measurements were made during the Secondary Organic Aerosols in Riverside (SOAR) field campaign in Riverside California during July and August of 2005. A Sunset Labs OC EC monitor, which uses the National Institute for

Occupational Safety and Health (NIOSH) method, was used for thermal-optical OC and EC mass analysis. The Sunset Labs instrument was operated to give one hour time resolution. The UF-ATOFMS was operated down stream of a multiple orifice uniform deposit impactor (MOUDI) which removed over 50% of particles greater then 450 nm (aerodynamic diameter). For UF-ATOFMS data analysis we only analyzed particles between 50-400 nm.

3.4 Results and discussion

3.4.1 Uncoated and OC coated electrical mobility size distributions

To explore the feasibility of using EC and OC ion markers from an UF-ATOFMS to quantify the relative OC/EC mass fraction in particles, we begin by discussing the electrical mobility size distributions of uncoated EC and OC coated EC particles. This provides information on particle size and shape that is needed for accurate determination of particle mass as described below. A TDMA arrangement coupled with a flow tube where an organic liquid (gasoline) could be heated to different temperatures was used to add OC coatings to EC cores.

Figure 3.2 shows three different scans taken with a scanning mobility particle sizer (SMPS) for OC coated and uncoated EC particles. Each size distribution in Figure 3.2 has been normalized to the size bin with the largest number of particle counts to show how the relative size distribution of each curve changes during the coating process. Figure 3.2 shows the electrical mobility size distribution of 100 nm EC particles size selected from DMA-1 without an OC coating. The total particle concentration for uncoated EC particles was 80,000 particles/cm^3. Uncoated EC particles showed a major

peak at 106 nm. Other peaks at 71 nm and 57 nm are attributed to doubly and triply charged 106 nm EC particles respectively. A small peak at 157 nm is also observed. This peak at 157 nm is due to particles that were emitted from the first DMA at a mobility diameter of 100 nm that contained two charges (larger particles, with two charges), and became singly charged in the second neutralizer. A slight positive deviation in the expected SMPS size distribution was also observed for 110 nm polystyrene latex spheres which showed a major peak at 113 nm. The peak at 106 nm in Figure 3.2 occurs at 106 nm instead of 100 nm most likely due to miscalibration of the DMA. Figure 3.2 shows the distribution of 100 nm size selected EC particles sent through a flask containing unleaded fuel heated to 75^{o} C. The total particle concentration for EC particles coated with fuel vapor at 75 ^{o}C was 11,000 particles/cm^{3}. Note that the major peak observed for the uncoated particles at 106 nm is shifted down to 76 nm upon coating, suggesting the 100 nm EC particles have collapsed. Using Scanning Electron Microscopy (SEM) and SMPS, spark discharge EC and diesel generated EC has been observed to collapse (rearrange) into a more spherical particle when coated with OC [*Saathoff et al.*, 2003; *Schnaiter et al.*, 2003; *Weingartner et al.*, 1997]. Because these particles went through an aerosol neutralizer prior to the SMPS, the peak observed at 76 nm is mostly singly charged [*Wiedensohler*, 1988]. The plots show a broad distribution of particle sizes. This wide distribution corresponds to EC particles coated with varying amounts of OC, as well as EC particles with a distribution of shapes. It should be noted that particles were not observed during blank (no EC particles) runs with fuel heated to 75 ^{o}C.

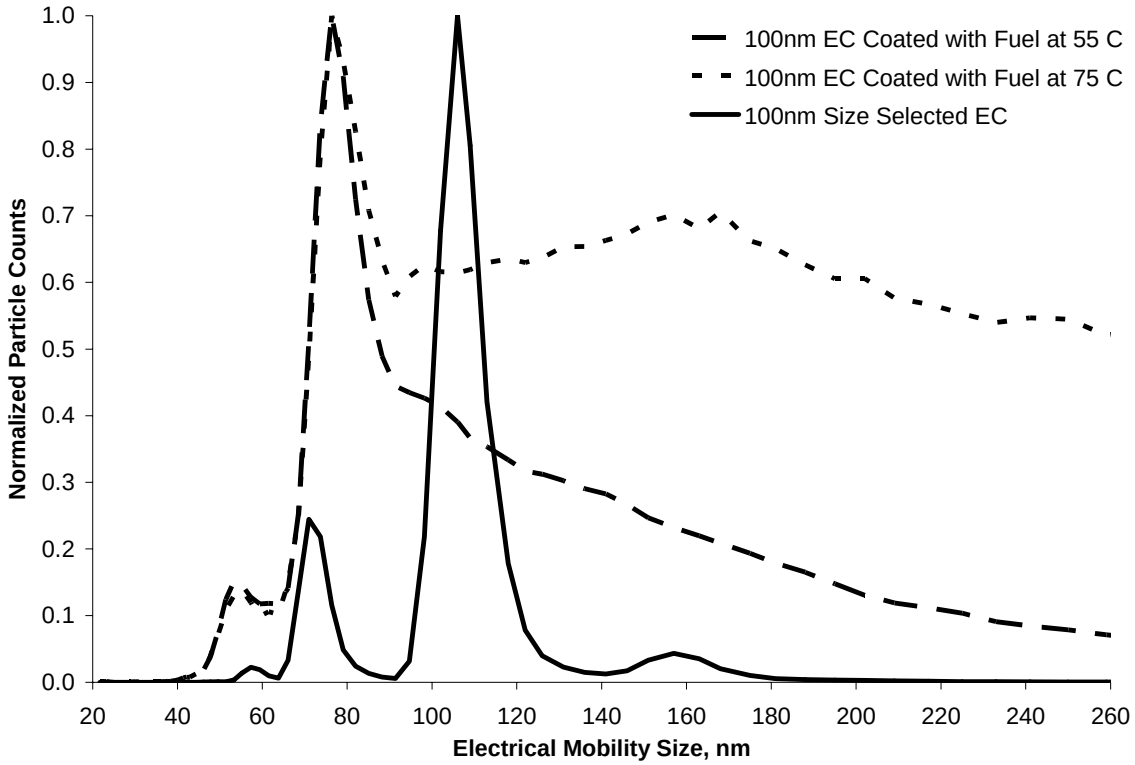

Figure 3.2 Scanning mobility particle size distributions for 100 nm size selected uncoated EC (solid curve), 100 nm size selected EC coated with OC from a 75° C unleaded fuel sample (dotted curve), and 100 nm size selected EC coated with OC using a 55° C unleaded fuel sample (dashed curve). Each curve has been normalized to the size bin with the greatest number of particles to allow a better visual comparison of the size distribution profile between each curve.

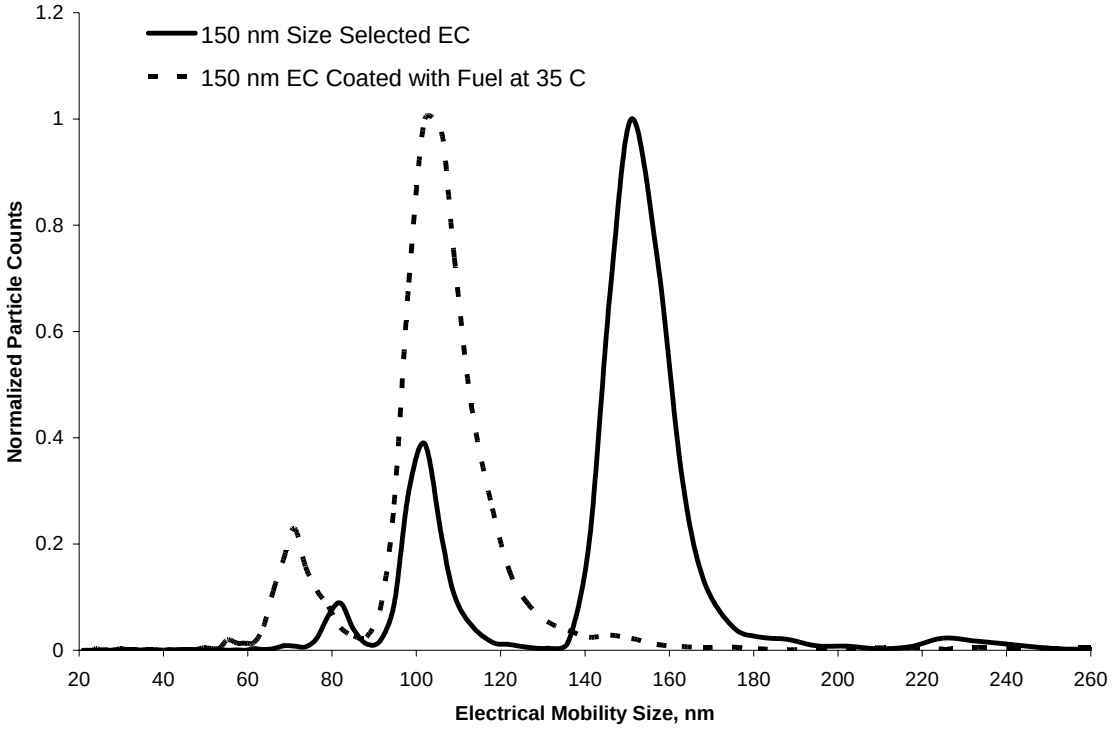

Figure 3.3 SMPS scan of uncoated pure spark discharge soot, size selected at 150nm (solid curve), and 150nm EC passed through a cylinder of fuel at 35 C (dotted curve). Each curve has been normalized to the size bin with the largest number of particles to allow a better visual comparison of the size distribution profile between each curve.

This indicates that self-nucleation of the fuel vapor is not occurring and there is no outside contamination from other particles. Finally, the size distribution of particles coated with unleaded fuel heated to 55^{o} C is shown. The total particle concentration for EC particles coated with fuel vapor at 55 ^{o}C was 55,000 particles/cm^{3}. At 55 ^{o}C, the relative concentration of coated particles (electrical mobility diameter larger then 76 nm) was lower than at 75^{o} C because less organic vapor is available to condense on the EC particles. To explore EC particle collapse further, a coating experiment was performed to lightly coat 150 nm EC particles with fuel vapor at 35^{o} C. Figure 3.3 shows the SMPS scan of uncoated 150 nm size selected spark discharge EC particles and 150 nm size selected spark discharge EC particles sent through unleaded fuel vapor (at 35^{o} C). Figure 3.3 shows that 150 nm EC particles collapsed to an electrical mobility diameter of 100 nm and very few particles grew to larger sizes. OC coated EC particles in Figure 3.3 maintained a very monodisperse size profile after collapse. Again, because an aerosol neutralizer was used, the major peak should not be from doubly charged particles [*Wiedensohler*, 1988]. It should be noted that the fuel coated particles in Figure 3.3 entered a flow tube downstream of the flask containing the unleaded fuel and were diluted 5-fold with nitrogen. The lack of heavily coated particles for the 35^{o} C experiment is attributed to dilution of the coated particles with nitrogen and a lower amount of OC vapor due to a lower (35^{o} C) bath temperature. Diluting the particle stream after coating shifts the OC gas-particle equilibrium, producing more OC in the gas phase.

3.4.2 Calculation of EC and OC mass

Using the UF-ATOFMS, the average vacuum aerodynamic equivalent diameter (d_{ae}) was determined for each experiment by averaging all diameters for a given experiment together. A 95% confidence interval was used to obtain high and low values for the average aerodynamic size. Using a 5 % range in the electrical mobility size and the 95% confidence interval range of aerodynamic size, the mass of EC and OC on uncoated and coated particles are calculated two different ways as described below.

Because pure spark discharge EC particles have very irregular shapes, using d_{me} or d_{ae} as the true physical diameter for uncoated EC is not entirely accurate. However, the volume equivalent diameter (d_{ve}), which is the volume of a sphere that has the same volume as the irregular shaped particle, can be calculated using the equation for the electrical mobility, Z, of irregularly shaped particles [*Kasper*, 1982]. This is given as

$$Z = \frac{neC_{me}}{3\pi\mu d_{me}} = \frac{neC_{ve}}{3\pi\mu d_{ve}\chi} \qquad \text{Equation 3.1}$$

where n is the number of elementary charges on each particle, e is the charge of an electron, C_{me} and C_{ve} are the Cunningham slip correction factors for d_{me} and $d_{ve,}$ respectively, μ is the absolute viscosity of air and χ is the dynamic shape factor. Non-spherical particles will have an electrical mobility that is related to a volume equivalent particle diameter through the dynamic shape factor, χ. Dynamic shape factors have been calculated for EC particles [*Park et al.*, 2003; *Park et al.*, 2004; *Slowik et al.*, 2004]. Shape factors for 150 nm (d_{me}) propane generated EC particles from Slowik et al. ranged between 1.5 and 2.4. Park et al. found shape factors vary between 1.1 and 2.1 for diesel

Table 3.1 Average aerodynamic equivalent diameter for each mobility equivalent diameter selected for each experiment.

Experiment Type	**SMPS mobility diameter, d_{me}**	**Mean ATOFMS aerodynamic diameter, (95 % CI)**	**Volume equivalent diameter range, d_{ve}[c]**
Uncoated	95-105	90 (85-96)	68-75[a]
Uncoated	114-126	94 (91-97)	81-89[a]
Uncoated	142-158	109 (106-112)	100-110[a]
OC Coated 75C	95-105	169 (164-174)	95-105[b]
OC Coated 75C	114-126	256 (250-263)	142-158[b]
OC Coated 75C	232-268	310 (304-315)	238-262[b]

a) Calculated based on an assumed shape factor of 1.8
b) OC coated EC particles are assumed to be spherical, so shape factor = 1 and $d_{ve} = d_{me}$
c) Volume equivalent diameter was calculated based on a 5% range in the given mobility diameter

EC as a function of electrical mobility size between 50 and 200 nm, respectively. To calculate d_{ve} here, we assume a dynamic shape factor of 1.8, which is a reasonable assumption based upon published values for EC agglomerates. Table 3.1 gives the experiment type, electrical mobility diameter before entering the UF-ATOFMS, the average aerodynamic diameter for each experiment and a calculated range of volume equivalent diameters. The range of estimated volume equivalent diameters shown in Table 3.1 is based on using a 5 % error in the DMA resolution. Table 3.1 shows pure spark discharge EC particles with electrical mobility diameters between 95-105, 114-126, and 142-158 nm have volume equivalent diameters between 68-75, 81-89, and 100-110 nm, respectively. It should be noted the estimated volume equivalent diameters are similar to the collapsed particle diameter observed in Figures 3.2 and 3.3. As discussed by DeCarlo, 2004, particles in a compact aggregate state, such as OC coated EC, have more spherical morphologies and shape factors closer to 1. Therefore we assume a shape factor for collapsed OC coated EC particles of 1.0. When one assumes a shape factor of 1, then mobility diameter will be equal to the volume equivalent diameter. The values for d_{ve} are therefore reported as d_{me} (+/-5%) in Table 1 for coated particles.

An OC coated EC particle can be thought of as a collapsed EC sphere surrounded by an OC shell. Using d_{ve}, the volume of both the pure EC core and the total particle volume for a coated particle can be calculated. Subtracting the EC core volume from the total coated particle volume leaves the volume of the shell, which is attributed to OC. By assuming bulk material densities for EC and OC, the masses of the EC core and the OC shell can be determined. Values for the total particle mass, OC mass, and OC mass fraction for each of the experiments are given in Table 3.2. Column 1 lists the

experiment name and the electrical mobility diameter before entering the ATOFMS. Column 2 gives the range of particle masses calculated using a range of possible material densities and a 5 % range in the electrical mobility diameter for each experiment. The EC mass given in Table 3.2 was calculated using a density range for EC between 1.6-2.0 g/cm^3, which encompasses the material density range reported for flame generated soot [*Choi et al.*, 1995]. We assume the material density of spark discharge EC is within the range for flame soot. OC mass given in Table 3.2 was obtained using values of 0.65-0.85 g/cm^3 for the density of gasoline based on the density for gasoline provided by the National Institute of Standards and Technology (NIST) (0.7-0.8 g/cm^3). Column 3 and Column 4 show the calculated ranges for the mass of OC and mass fraction of OC, respectively.

A second method for estimating the mass of the different uncoated and coated particles involves determining the effective density using the vacuum aerodynamic diameter and electrical mobility diameter. By multiplying the effective density and the volume (volume based on mobility diameter) one obtains particle mass. Using d_{me} and d_{ae} the effective density for the particles can be calculated using the equation

$$\frac{d_{ae}}{d_{me}}\rho_o = \rho_{eff} \qquad \text{Equation 3.2}$$

where d_{ae} it the vacuum aerodynamic diameter, d_{me} is the electrical mobility diameter, ρ_{eff} is the effective density, and ρ_o is the unit density (1.0 g/cm^3) [*DeCarlo et al.*, 2004; *Jimenez et al.*, 2003]. Figure 3.4 shows a plot of the calculated effective densities for uncoated EC particles versus d_{me} compared with values reported by Park et al. 2003 for diesel soot particles of the same electrical mobility size. The vertical error bars in Figure

Table 3.2 Calculated particle mass and OC mass from assumed material density.

Experiment / Final d_{me}	**Range of particle mass, fg**	**OC mass range, fg**	**Average % OC mass fraction +/- STDV**
Uncoated /100 nm EC [a]	0.3 - 0.4	0	0
Uncoated /120 nm EC [a]	0.5 - 0.7		
Uncoated /150 nm EC [a]	0.8 - 1.4	0	0
OC 75^{o} C /100 nm [b]	0.5 - 0.8	0.2 - 0.3	42.2 +/- 4.1
OC 75^{o} C /150 nm [b]	1.1 -2.0	0.9 -1.6	77.4 +/- 3.0
OC 75^{o} C / 250 nm [b]	4.7 – 8.3	4.5 - 7.8	94.6 +/- 0.9

a) Assumed a density of 1.6- 2.0 g/cm^3, and a shape factor of 1.8
b) Assumed a density for OC of 0.65-0.85 g/cm^3, and a shape factor of 1.0

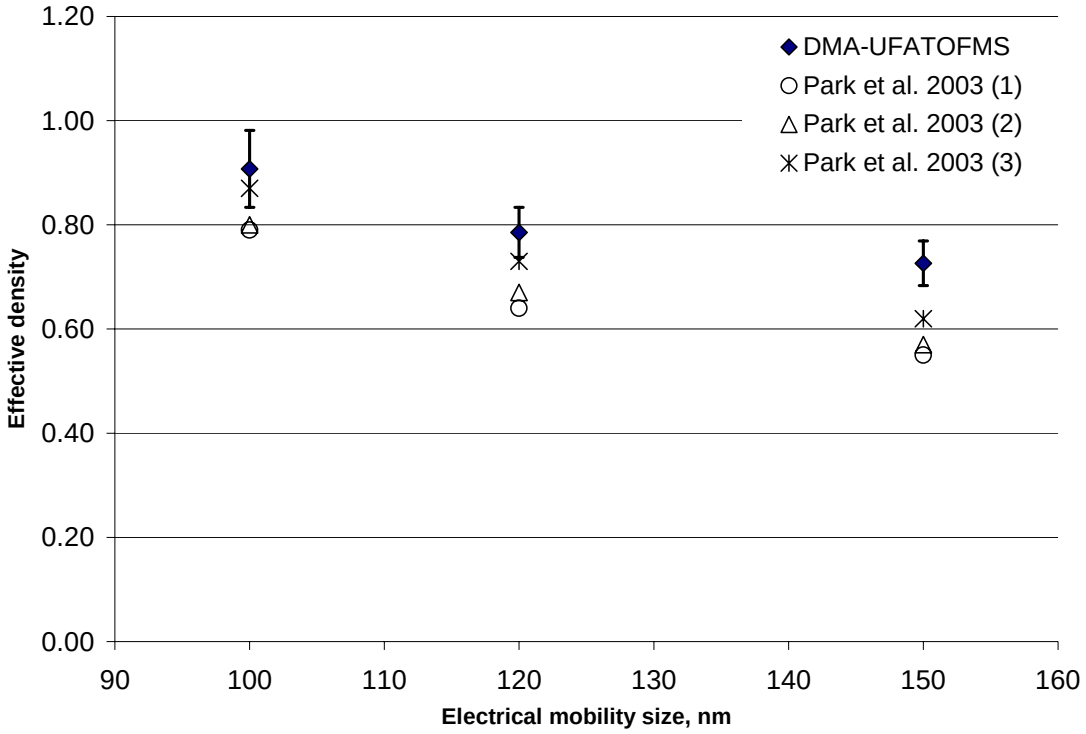

Figure 3.4 Spark discharge soot effective densities calculated from DMA and UF-ATOFMS data plotted versus particle mobility equivalent diameter. Vertical error bars represent the standard deviation in the effective density generated from using aerodynamic diameters within a 95% confidence interval and a 5 % range in the chosen mobility diameter. For comparison, values reported for diesel soot by Park et al. 2003 are also shown.

3.4 were generated from effective densities calculated using a 5% range in the electrical mobility diameter and a 95 % confidence interval of the mean aerodynamic diameter. It is clear from Figure 3.4 that the effective densities calculated here are systematically higher but in good agreement with those reported by Park et al. This density difference likely reflects the difference in soot structure that has been observed for spark discharge and diesel engine EC[*Kirchner et al.*, 2003; *Saathoff et al.*, 2003; *Schnaiter et al.*, 2003].

Using the effective density and the electrical mobility diameter, the OC/EC mass fractions for the particles were determined. Table 3.3 shows the total mass per particle, the mass of OC associated with coated particles, and the OC mass fraction. Column 1 lists the experiment name and the electrical mobility diameter measured before entering the ATOFMS. Column 2 gives the total particle mass for each experiment. The mass of OC given in Column 3 was calculated by subtracting the mass of the EC core from the total particle mass. A comparison of the results presented in Tables 3.2 and 3.3 shows the mass fractions of OC calculated using the two different approaches agree to within 10%.

3.4.3 Determining OC and EC mass fractions from mass spectral ion intensities

As stated earlier, the major goal of this work is to establish a correlation between the intensities of EC and OC ions in single particle mass spectra with the actual OC/EC mass fractions for a collection of carbonaceous particles. This correlation results in a calibration curve that will allow one to quantitatively relate ion intensities in source and ambient studies with OC/EC mass fractions. Figure 3.5 shows an average, positive ion relative area matrix for 140 uncoated spark discharge EC particles and 98 OC coated

Table 3.3 Calculated particle mass and OC mass from effective density.

Experiment / Final d_{me}	**Total particle mass range, fg**	**OC mass range, fg**	**Average % OC mass fraction +/- STDV**
Uncoated /100 nm EC	0.4 -0.6	0	0
Uncoated /120 nm EC	0.6 -0.8	0	0
Uncoated /150 nm EC	1.1 -1.5	0	0
OC 75^{o} C /100 nm	0.8 -1.0	0.2 - 0.6	45.9 +/- 8.8
OC 75^{o} C /150 nm	2.7 – 3.4	2.1 – 3.0	84.5 +/- 2.5
OC 75^{o} C / 250 nm	9.0 -11.3	8.5 -10.9	95.3 +/ 0.7

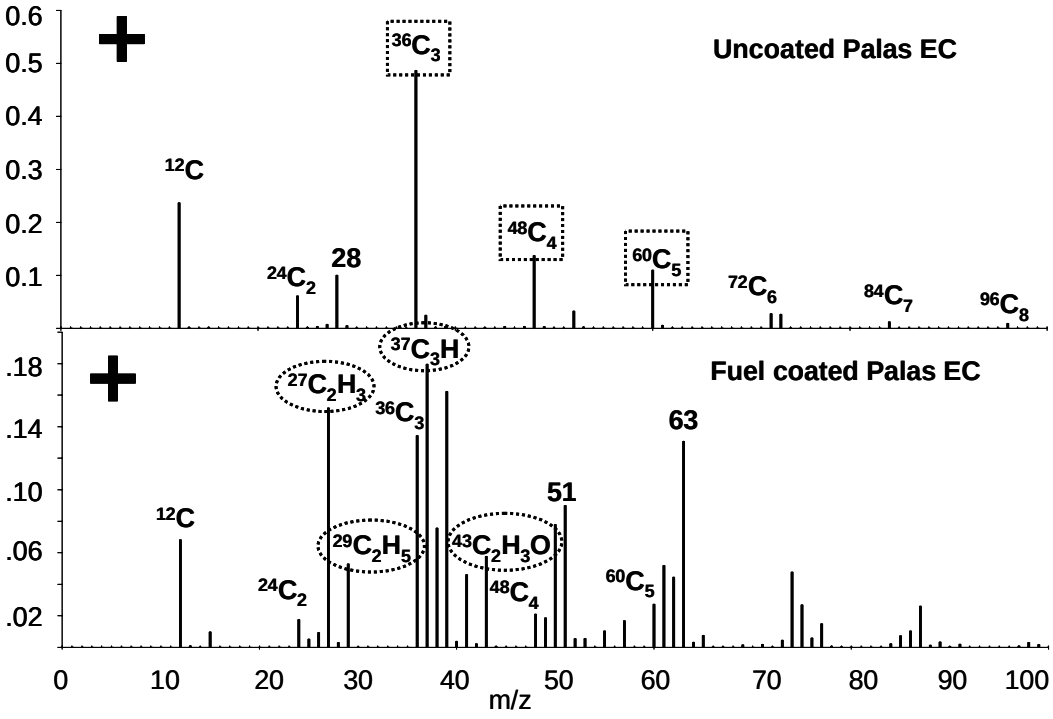

Figure 3.5 Average area matrix from approximately 140 uncoated spark discharge soot particles and 98 fuel coated spark discharge soot particles. Squares indicate ion markers used for EC, and ovals for OC.

spark discharge EC particles. A description of how an area matrix is created is given in the Methods section. The two particle types shown in Figure 3.5 are readily distinguishable. The uncoated EC area matrix is dominated by positive ion carbon cluster peaks $^{12}C_1$ to $^{96}C_8$ attributed to EC. A peak at m/z +28 is also observed which is attributed to silicon [*Wentzel et al.*, 2003]. The OC coated spark discharge EC in Figure 3.5 shows many peaks attributed to EC, however, it also contains OC peaks at m/z 27 (CNH^+, $C_2H_3^+$), 29 ($C_2H_5^+$), 37 (C_3H^+), 39 ($C_3H_3^+$), 43 ($C_3H_7^+$, $C_2H_3O^+$), 51 ($C_4H_3^+$) and 63 ($C_5H_3^+$). The ions listed in parentheses are possible ion peak assignments based on previous lab studies by our group and electron impact spectra of organic compounds compiled by others [*McLafferty and Tureécek*, 1993]. In general, as a particle grows in size, the OC peak intensities increase while the EC peaks are reduced in intensity, suggesting the addition of OC to EC changes the matrix and the overall response of the instrument to EC ion signals. The ATOFMS shows a higher sensitivity to fresh EC particles with higher absolute signal intensities measured for fresh uncoated EC particles. To establish a correlation between OC/EC intensity ratios and the mass of OC and EC in particles, the ion markers shown in Figure 3.5 attributed to OC (*m/z* 27+, 29+, 37+, 43+) and EC (*m/z* 36+, 48+, 60+) are used as they are commonly observed in ambient particles. Other ions for OC such as *m/z* 39+, 41+ and 51+ were not chosen because ions from potassium and vanadium are also observed at these *m/z* in ambient particles. More then one ion was chosen because individual ion areas fluctuate much more than the sum of multiple ions. As mentioned, large shot-to-shot ion intensity variations are observed in most single particle mass spectrometers. However, the signals tend to increase and decrease in the same proportion [*Gross et al.*, 2000], and thus by using the *ratio* of OC to

EC ion intensities to calculate the OC/EC mass fractions, the effect of the ion signal fluctuations on quantification are minimized.

Figure 3.6 shows a graph of the mass percentage of OC using material densities (open circles) as well as those obtained from a calculation of effective density (asterisks) versus the OC/EC mass spectral ion intensity ratios. The OC mass percentages and error bar values correspond to data from the last column of Tables 3.2 and 3.3. A linear correlation exists between the OC/EC ion ratio and mass percentage of OC calculated from assumed material densities with an R^2 value of 0.98. Figure 3.6 shows a point for an uncoated 100 nm (d_{me}) spark discharge generated EC particle, which falls almost at zero (OC/EC ratio) as expected. A linear correlation with an R^2 value of 0.99 is shown in Figure 3.6 for the percent of OC mass calculated from effective densities and the OC/EC ratios. It should be noted these linear correlations do not imply the response of the UF-ATOFMS is linear with respect to OC and EC concentration; we are plotting a ratio versus a percentage which would diverge if there was a linear instrument response. These correlations show it is possible to calibrate the ATOFMS using ion intensity ratios and obtain quantitative chemical information for particles with similar chemical matrices. It is important to note that a break at 1 μm separates particles composed of predominately organic versus inorganic matrices [*Noble and Prather*, 1996; *Pastor et al.*, 2003]. Thus this calibration curve will most likely be most effective for sub-μm particles since these will have similar carbonaceous matrices and thus similar ion signal responses.

To determine whether laboratory generated OC-EC particles produce OC/EC ion intensity ratios that fall in the range of those measured for ambient particles in the same size range, the OC/EC ion intensity ratios for a number of source and ambient study

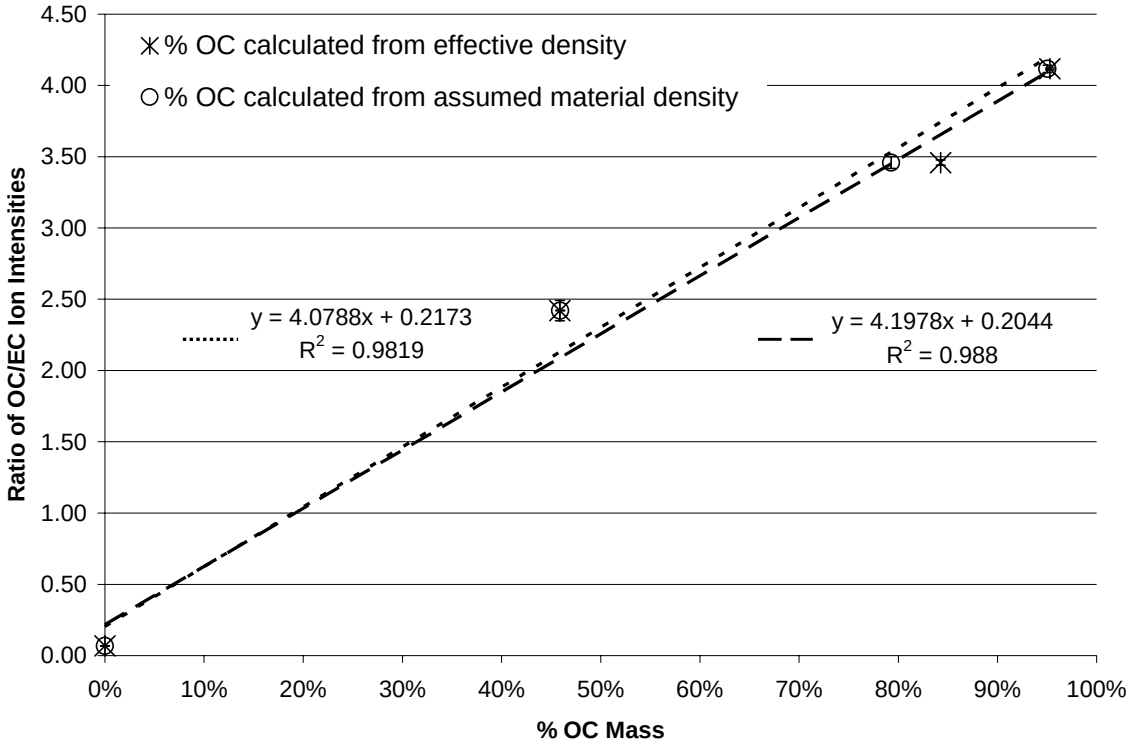

Figure 3.6 Calculated fraction of OC contained in each particle is plotted versus the OC/EC ratio from specific ion signals. Open circles represent OC mass calculated from an estimation of material densities. Error bars for the open circles were generated using a range of assumed material densities and a 5% range in the electrical mobility diameter. Asterisks represent OC mass calculated from the measurement of effective density. Vertical error bars for the asterisks indicate the standard deviation in the %OC mass generated from using the mean aerodynamic diameters within a 95% confidence interval and a 5% range in the mobility diameter. The points at 0 % OC mass represent uncoated pure EC.

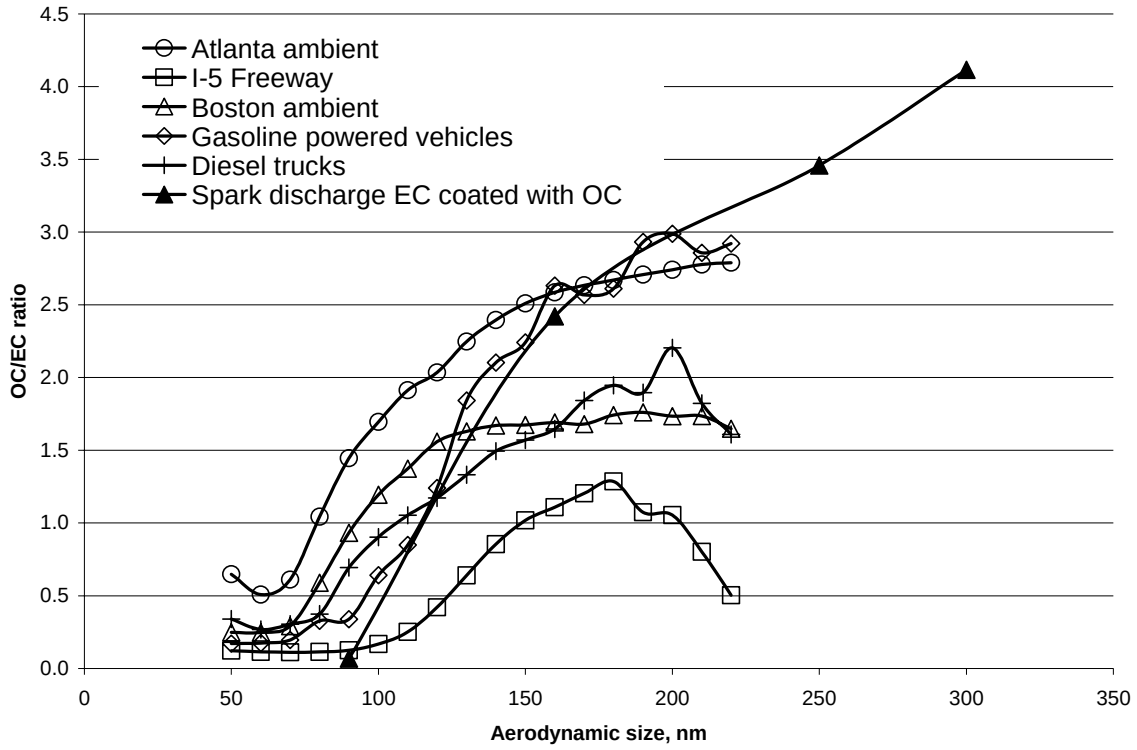

Figure 3.7 The OC/EC ratio is plotted versus vacuum aerodynamic size for particles analyzed at three ambient locations (I-5 Freeway, Boston, Atlanta) and two vehicle dynamometer studies (gasoline powered vehicles, diesel powered trucks). For comparison, the OC/EC ratio for spark discharge EC coated with different amounts of OC is also plotted versus its average aerodynamic size.

particles were calculated. Figure 3.7 shows a plot of the OC/EC ion intensity ratioversus the vacuum aerodynamic size for the laboratory generated OC-EC particles, three ambient locations (San Diego-Freeway, Boston, Atlanta) and two vehicle dynamometer studies (gasoline powered vehicles, diesel powered trucks). As shown, the OC/EC ratios for the ambient and vehicle data sets lie within the range of OC/EC ion intensity ratios observed for the laboratory generated OC-EC particles presented here. This suggests the OC/EC ratios calculated using laboratory generated OC-EC particle standards indeed have atmospheric relevance and can be used to estimate the fractions of OC and EC in ambient particles with similar chemical composition and size.

To further explore the significance of using OC/EC ion intensity ratios to estimate the OC/EC mass fraction in particles, a comparison of the UF-ATOFMS OC/EC ion intensity ratios was made to the OC/EC mass ratios measured with a Sunset Lab semi-continuous thermal/optical method. Figure 3.8 exhibits eight days of ambient data taken from July 30-August 7, 2005 in Riverside, California. The UF-ATOFMS data contains all particles analyzed between 50-400 nm and the thermal-optical data is for all particles < 2.5 μm. In Figure 3.8a, the left y-axis is UF-ATOFMS OC/EC ion ratio and the right y-axis thermal-optical OC/EC mass ratio with date given along the x-axis. Both the UF-ATOFMS and thermal-optical instrument show daily fluctuations in their respective OC/EC ratio with very comparable relative intensity between each method. The correlation between the UF-ATOFMS and thermal-optical data in Figure 3.8a yields an $R^2 = 0.69$. This shows that a change in the UF-ATOFMS OC/EC ion ratio for ambient particles reflects changes in the OC/EC mass ratio measured with the thermal-optical method. Figure 3.8b shows UF-ATOFMS ambient data from Riverside calibrated using

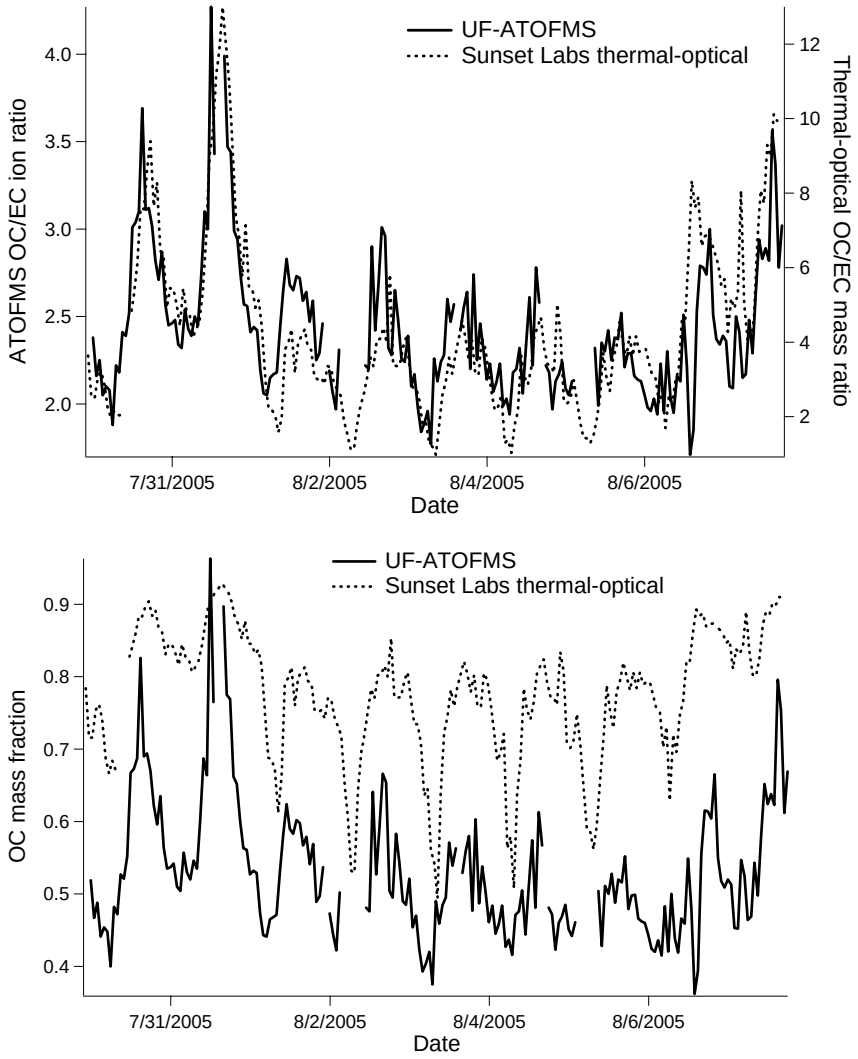

Figure 3.8 Ambient particle measurements taken during SOAR field campaign in Riverside California, July-August of 2005. a) The UF-ATOFMS OC/EC ion intensity ratio is plotted on the left y-axis and semi-continuous thermal optical OC/EC mass ratio on the right y-axis, with date given along the x-axis. b) The OC mass fraction estimated using UF-ATOFMS (using calibration curve given in Figure 3.6) and OC mass fraction measured using thermal optical OC EC instrument is given on the y-axis with date given along x-axis.

the curve from Figure 3.6 to estimate the OC mass fraction. Also shown in Figure 3.8b is the thermal-optical OC mass fraction. Overall, Figure 3.8b shows daily fluctuations in the OC mass fraction are captured by both techniques and there is approximately a 20% difference between them. It should be pointed out that comparisons between similar thermal-optical techniques differing in temperature protocol or optical correction technique (thermal optical reflectance (TOR) versus thermal optical transmission (TOT)) have shown errors for estimating amount of EC or OC of more then 40%[*Arhami et al.*, 2006; *Chow et al.*, 2004; *Chow et al.*, 2005a; *Chow et al.*, 2001; *Chow et al.*, 2005b; *Schauer et al.*, 2003]. The NIOSH thermal-optical TOT protocol used here has been shown to measure half the amount of EC as measured using the IMPROVE method [*Chow et al.*, 2001]. Therefore, this comparison of the ATOFMS data with thermal-optical data, two techniques which rely on very different operating principles, is quite good. One other reason the ATOFMS underestimates the amount of OC relative to EC could be the UF-ATOFMS used for this study only sampled particles up to 400 nm, whereas the thermal-optical instrument measured particles up to 2.5 μm. Particles in Riverside grow in size throughout the day from condensation of semi-volatile organics; therefore the larger size particles sampled by the thermal-optical method likely have a larger OC mass fraction. It is important to remember here that the thermal-optical method produces operationally defined values of EC and OC, whereas the ATOFMS is based on actual structural differences of EC and OC leading to different ion patterns in the mass spectra. In future studies, examining periods where the ATOFMS agrees or disagrees with the EC/OC mass concentration values may yield insight into the most

appropriate operating conditions and protocols to be used by these thermal-optical instruments.

3.5 Conclusions

In these experiments, EC particles of known size were coated with OC species from unleaded fuel vapor to create standard particles with different OC/EC mass fractions. The OC/EC mass fractions were determined using two separate approaches; first, assumptions were made about the shape and density of the particles based on literature values, and second, by calculating the effective densities of particles using the measured vacuum aerodynamic (UF-ATOFMS) and electrical mobility diameters (SMPS). Effective densities of pure spark discharge EC determined in these experiments are within 20 % of values reported for diesel EC with the same mobility diameters. Using the two estimation methods for EC and OC mass, the OC/EC mass fraction as a function of particle size was determined. A calibration curve was created by plotting OC/EC ion intensity ratios against the calculated mass fractions of OC estimated from the two different methods. Strong linear correlations exist between the OC/EC ion ratio and the mass percentage of OC, estimated from assumed material densities (R^2 = 0.98) and the measured effective density (R^2 =0.99). Both OC/EC mass correlations are within the range of uncertainties of each other.

The OC/EC ion intensity ratios derived from laboratory generated OC-EC standard particles compared well with particles in the same size range measured in multiple ambient and source data sets. Furthermore, the OC/EC values measured with the UF-ATOFMS showed a strong correlation with OC/EC values simultaneously

measured for ambient data using traditional thermal-optical methods. Ambient OC mass fractions measured here were within ~20% of that measured using a traditional thermal-optical technique and showed similar daily fluctuations. Using UF-ATOFMS, obtaining quantitative information regarding the OC/EC mass fractions in ambient particles with similar size and chemical composition appears to be quite feasible for carbonaceous particles.

With the recent interest in moving beyond mass measurements of atmospheric aerosols, there is a major need for methods which can be used to generate particles that can be used for instrument calibration. The method used herein to generate OC/EC particles could be used for characterizing other instruments besides ATOFMS. For example, laboratory studies could be performed using these particles with known OC and EC mass concentrations to better understand observed differences in responses between similar methodologies such as the IMPROVE or NIOSH thermo-optical methods[*Schauer et al.*, 2003]. This study shows it is possible to generate particles with similar composition to ambient particles that can be used to perform laboratory calibrations. A calibration curve can be used to relate the measured relative ion intensities in the mass spectra of unknown ambient particles to the relative amounts of specific species in/on ambient particles. The next step will be to perform further lab studies comparing calibration curves generated with EC coated with different classes of organic species. The response of such calibration curves to different organic material will yield information on the uncertainties of this approach. Furthermore, ATOFMS data will be compared with traditional thermal-optical methods, as well as other methods for measuring EC and OC, in future ambient field and source studies to further test the

robustness of this procedure. Information regarding the relative amount of OC on EC particles will be critical to assessing the roles of these species in climate change and human health.

3.6 Acknowledgements

We would like to thank Professor Günter Oberdörster from University of Rochester for allowing us to use his EC spark discharge generator. James Schauer and Dave Snyder from University of Wisconsin-Madison generously collected, processed and made available the SOAR thermal-optical OC EC data. Ambient and vehicle emissions ATOFMS data was collected and made available from the generosity of the following people: Steve Toner, David Sodeman, Laura Shields, Yongxuan Su, Michelle Sipin, and Xueying Qin. This work was carried out with the support of the Environmental Protection Agency PM center under grant # R827354.

3.7 References

Arhami, M., T. Kuhn, P.M. Fine, R.J. Delfino, and C. Sioutas, Effects of sampling artifacts and operating parameters on the performance of a semicontinuous particulate elemental carbon/organic carbon monitor, *Environmental Science & Technology*, *40* (3), 945-954, 2006.

Bhave, P.V., J.O. Allen, B.D. Morrical, D.P. Fergenson, G.R. Cass, and K.A. Prather, A field-based approach for determining ATOFMS instrument sensitivities to ammonium and nitrate, *Environ. Sci. Technol.*, *36* (22), 4868-4879, 2002.

Burtscher, H., S. Kunzel, and C. Huglin, Characterization of particles in combustion engine exhaust, *J. Aerosol Sci.*, *29* (4), 389-396, 1998.

Choi, M.Y., G.W. Mulholland, A. Hamins, and T. Kashiwagi, Comparisons of the soot volume fraction using gravimetric and light extinction techniques, *Combust. Flame*, *102* (1-2), 161-169, 1995.

Chow, J.C., J.G. Watson, L.W.A. Chen, W.P. Arnott, and H. Moosmuller, Equivalence of elemental carbon by thermal/optical reflectance and transmittance with different temperature protocols, *Environmental Science & Technology*, *38* (16), 4414-4422, 2004.

Chow, J.C., J.G. Watson, L.W.A. Chen, G. Paredes-Miranda, M.C.O. Chang, D. Trimble, K.K. Fung, H. Zhang, and J.Z. Yu, Refining temperature measures in thermal/optical carbon analysis, *Atmos. Chem. Phys.*, *5*, 2961-2972, 2005a.

Chow, J.C., J.G. Watson, D. Crow, D.H. Lowenthal, and T. Merrifield, Comparison of IMPROVE and NIOSH carbon measurements, *Aerosol Science & Technology*, *34* (1), 23-34, 2001.

Chow, J.C., J.G. Watson, P.K.K. Louie, L.W.A. Chen, and D. Sin, Comparison of PM2.5 carbon measurement methods in Hong Kong, China, *Environ. Pollut.*, *137* (2), 334-344, 2005b.

DeCarlo, P.F., J.G. Slowik, D.R. Worsnop, P. Davidovits, and J.L. Jimenez, Particle morphology and density characterization by combined mobility and aerodynamic diameter measurements. Part 1: Theory, *Aerosol Sci. Technol.*, *38* (12), 1185-1205, 2004.

Fergenson, D.P., X.-H. Song, Z. Ramadan, J.O. Allen, L.S. Hughes, G.R. Cass, P.K. Hopke, and K.A. Prather, Quantification of ATOFMS data by multivariate methods, *Anal. Chem.*, *73* (15), 3535-3541, 2001.

Gard, E., J.E. Mayer, B.D. Morrical, T. Dienes, D.P. Fergenson, and K.A. Prather, Real-time analysis of individual atmospheric aerosol particles: Design and performance of a portable ATOFMS, *Anal. Chem.*, *69* (20), 4083-4091, 1997.

Gross, D.S., M.E. Gaelli, P.J. Silva, and K.A. Prather, Relative sensitivity factors for alkali metal and ammonium cations in single-particle aerosol time-of-flight mass spectra, *Anal. Chem.*, *72* (2), 416-422, 2000.

Guazzotti, S.A., K.R. Coffee, and K.A. Prather, Continuous measurements of size-resolved particle chemistry during INDOEX-intensive field phase 99, *Journal of Geophysical Research, [Atmospheres]*, *106* (D22), 28607-28627, 2001a.

Guazzotti, S.A., J.R. Whiteaker, D. Suess, K.R. Coffee, and K.A. Prather, Real-time measurements of the chemical composition of size-resolved particles during a Santa Ana wind episode, California USA, *Atmos. Environ.*, *35* (19), 3229-3240, 2001b.

Helsper, C., W. Molter, F. Loffler, C. Wadenpohl, S. Kaufmann, and G. Wenninger, Investigations of a new aerosol generator for the production of carbon aggregate particles, *Atmospheric Environment Part a-General Topics*, *27* (8), 1271-1275, 1993.

Herner, J.D., J. Aw, O. Gao, D.P. Chang, and M.J. Kleeman, Size and composition distribution of airborne particulate matter in northern California: I-particulate mass, carbon, and water-soluble ions, *J. Air Waste Manage. Assoc.*, *55* (1), 30-51, 2005.

Horvath, H., Atmospheric light-absorption - a review, *Atmospheric Environment Part a-General Topics*, *27* (3), 293-317, 1993.

Jacobson, M.Z., Strong radiative heating due to the mixing state of black carbon in atmospheric aerosols, *Nature*, *409* (6821), 695-7, 2001.

Jimenez, J.L., R. Bahreini, D.R. Cocker, H. Zhuang, V. Varutbangkul, R.C. Flagan, J.H. Seinfeld, C.D. O'Dowd, and T. Hoffmann, New particle formation from photooxidation of diiodomethane (CH2I2), *J. Geophys. Res.*, *108* (D10), 2003.

Kasper, G., Dynamics and measurement of smokes .1. Size characterization of non-spherical particles, *Aerosol Sci. Technol.*, *1* (2), 187-199, 1982.

Katrinak, K.A., P. Rez, and P.R. Buseck, Structural variations in individual carbonaceous particles from an urban aerosol, *Environmental Science & Technology*, *26* (10), 1967-1976, 1992.

Kirchner, U., R. Vogt, C. Natzeck, and J. Goschnick, Single particle MS, SNMS, SIMS, XPS, and FTIR spectroscopic analysis of soot particles during the AIDA campaign, *J. Aerosol Sci.*, *34* (10), 1323-1346, 2003.

Kleeman, M.J., J.J. Schauer, and G.R. Cass, Size and composition distribution of fine particulate matter emitted from motor vehicles, *Environ. Sci. Technol.*, *34* (7), 1132-1142, 2000.

Kwon, S.-B., K.W. Lee, K. Saito, O. Shinozaki, and T. Seto, Size-dependent volatility of diesel nanoparticles: Chassis dynamometer experiments, *Environ. Sci. Technol.*, *37* (9), 1794-1802, 2003.

Lee, D., K. Park, and M.R. Zachariah, Determination of the size distribution of polydisperse nanoparticles with single-particle mass spectrometry: The role of ion kinetic energy, *Aerosol Sci. Technol.*, *39* (2), 162-169, 2005.

Lim, H.J., and B.J. Turpin, Origins of primary and secondary organic aerosol in Atlanta: Results of time-resolved measurements during the Atlanta supersite experiment, *Environmental Science & Technology*, *36* (21), 4489-4496, 2002.

Liousse, C., C. Devaux, F. Dulac, and H. Cachier, Aging of savanna biomass burning aerosols - consequences on their optical-properties, *J. Atmos. Chem.*, *22* (1-2), 1-17, 1995.

Liu, D.Y., R.J. Wenzel, and K.A. Prather, Aerosol time-of-flight mass spectrometry during the Atlanta supersite experiment: 1. Measurements, *J. Geophys. Res.*, *108* (D7), 8426, 2003.

Mader, B.T., R.C. Flagan, and J.H. Seinfeld, Airborne measurements of atmospheric carbonaceous aerosols during ACE-Asia, *J. Geophys. Res.*, *107* (D23), 2002.

McLafferty, F.W., and F. Tureécek, *Interpretation of mass spectra*, 371 pp., University Science Books, Mill Valley, Calif., 1993.

Noble, C.A., and K.A. Prather, Real-time measurement of correlated size and composition profiles of individual atmospheric aerosol particles, *Environ. Sci. Technol.*, *30* (9), 2667-2680, 1996.

Novakov, T., and J.E. Penner, Large contribution of organic aerosols to cloud-condensation-nuclei concentrations, *Nature*, *365* (6449), 823-826, 1993.

Odum, J.R., T.P.W. Jungkamp, R.J. Griffin, R.C. Flagan, and J.H. Seinfeld, The atmospheric aerosol-forming potential of whole gasoline vapor, *Science*, *276* (5309), 96-99, 1997.

Park, K., F. Cao, D.B. Kittelson, and P.H. McMurry, Relationship between particle mass and mobility for diesel exhaust particles, *Environmental Science & Technology*, *37* (3), 577-583, 2003.

Park, K., D.B. Kittelson, and P.H. McMurry, Structural properties of diesel exhaust particles measured by transmission electron microscopy (TEM): Relationships to particle mass and mobility, *Aerosol Science & Technology*, *38* (9), 881-889, 2004.

Pastor, S.H., J.O. Allen, L.S. Hughes, P. Bhave, G.R. Cass, and K.A. Prather, Ambient single particle analysis in Riverside, California by aerosol time-of-flight mass spectrometry during the SCOS97-NARSTO, *Atmos. Environ.*, *37* (Suppl. 2), 239-258, 2003.

Penner, J.E., C.C. Chuang, and K. Grant, Climate forcing by carbonaceous and sulfate aerosols, *Climate Dynamics*, *14* (12), 839-851, 1998.

Prather, K.A., T. Nordmeyer, and K. Salt, Real-time characterization of individual aerosol particles using time-of-flight mass spectrometry, *Anal. Chem.*, *66* (9), 1403-7, 1994.

Qin, X.Y., P.V. Bhave, and K.A. Prather, Comparison of two methods for obtaining quantitative mass concentrations from aerosol time-of-flight mass spectrometry measurements, *Anal. Chem.*, *78* (17), 6169-6178, 2006.

Rader, D.J., and P.H. McMurry, Application of the tandem differential mobility analyzer to studies of droplet growth or evaporation, *J. Aerosol Sci.*, *17* (5), 771-787, 1986.

Reents, W.D., and Z.Z. Ge, Simultaneous elemental composition and size distributions of submicron particles in real time using laser atomization/ionization mass spectrometry, *Aerosol Sci. Technol.*, *33* (1-2), 122-134, 2000.

Roth, C., G.A. Ferron, E. Karg, B. Lentner, G. Schumann, S. Takenaka, and J. Heyder, Generation of ultrafine particles by spark discharging, *Aerosol Sci. Technol.*, *38* (3), 228-235, 2004.

Saathoff, H., K.H. Naumann, M. Schnaiter, W. Schock, O. Mohler, U. Schurath, E. Weingartner, M. Gysel, and U. Baltensperger, Coating of soot and (NH4)(2)SO4 particles by ozonolysis products of alpha-pinene, *J. Aerosol Sci.*, *34* (10), 1297-1321, 2003.

Saxena, P., L.M. Hildemann, P.H. McMurry, and J.H. Seinfeld, Organics alter hygroscopic behavior of atmospheric particles, *J. Geophys. Res.*, *100* (D9), 18755-18770, 1995.

Schauer, J.J., B.T. Mader, J.T. Deminter, G. Heidemann, M.S. Bae, J.H. Seinfeld, R.C. Flagan, R.A. Cary, D. Smith, B.J. Huebert, T. Bertram, S. Howell, J.T. Kline, P. Quinn, T. Bates, B. Turpin, H.J. Lim, J.Z. Yu, H. Yang, and M.D. Keywood, ACE-Asia intercomparison of a thermal-optical method for the determination of particle-phase organic and elemental carbon, *Environmental Science & Technology*, *37*, 993-1001, 2003.

Schnaiter, M., H. Horvath, O. Mohler, K.H. Naumann, H. Saathoff, and O.W. Schock, UV-Vis-nIR spectral optical properties of soot and soot-containing aerosols, *J. Aerosol Sci.*, *34* (10), 1421-1444, 2003.

Shields, L.G., D.T. Suess, S.A. Guazzotti, and K.A. Prather, Determination of single particle mass spectral signatures from heavy duty vehicle emissions, *Atmos. Environ.*, *accepted*, 2006.

Slowik, J.G., K. Stainken, P. Davidovits, L.R. Williams, J.T. Jayne, C.E. Kolb, D.R. Worsnop, Y. Rudich, P.F. DeCarlo, and J.L. Jimenez, Particle morphology and density characterization by combined mobility and aerodynamic diameter measurements. Part 2: Application to combustion-generated soot aerosols as a function of fuel equivalence ratio, *Aerosol Sci. Technol.*, *38* (12), 1206-1222, 2004.

Smith, G.D., E. Woods, III, C.L. DeForest, T. Baer, and R.E. Miller, Reactive uptake of ozone by oleic acid aerosol particles: Application of single-particle mass spectrometry to heterogeneous reaction kinetics, *J. Phys. Chem. A*, *106* (35), 8085-8095, 2002.

Sodeman, D.A., S.M. Toner, and K.A. Prather, Determination of single particle mass spectral signatures from light duty vehicle emissions, *Environmental Science & Technology*, *39* (12), 4569-4580, 2005.

Su, Y., M.F. Sipin, H. Furutani, and K.A. Prather, Development and characterization of an aerosol time-of-flight mass spectrometer with increased detection efficiency, *Anal. Chem.*, *76* (3), 712-719, 2004.

Toner, S.M., L.G. Shields, D.A. Sodeman, and K.A. Prather, Source apportionment of freeway-side ambient aerosols using ATOFMS, *manuscript in preparation*, 2007.

Toner, S.M., D.A. Sodeman, and K.A. Prather, Single particle characterization of ultrafine and accumulation mode particles from heavy duty diesel vehicles using aerosol time-of-flight mass spectrometry, *Environmental Science & Technology*, *40* (12), 3912-3921, 2006.

Weingartner, E., H. Burtscher, and U. Baltensperger, Hygroscopic properties of carbon and diesel soot particles, *Atmos. Environ.*, *31* (15), 2311-2327, 1997.

Wentzel, M., H. Gorzawski, K.H. Naumann, H. Saathoff, and S. Weinbruch, Transmission electron microscopical and aerosol dynamical characterization of soot aerosols, *J. Aerosol Sci.*, *34* (10), 1347-1370, 2003.

Wenzel, R.J., and K.A. Prather, Improvements in ion signal reproducibility obtained using a homogeneous laser beam for on-line laser desorption/ionization of single particles, *Rapid Commun. Mass Spectrom.*, *18* (13), 1525-1533, 2004.

Whiteaker, J.R., Analysis of atmospheric aerosol processes using single particle mass spectrometry, 2002.

Wiedensohler, A., An approximation of the bipolar charge-distribution for particles in the sub-micron size range, *J. Aerosol Sci.*, *19* (3), 387-389, 1988.

Woods, E., III, G.D. Smith, Y. Dessiaterik, T. Baer, and R.E. Miller, Quantitative detection of aromatic compounds in single aerosol particle mass spectrometry, *Anal. Chem.*, *73* (10), 2317-2322, 2001.

Zheng, M., G.R. Cass, J.J. Schauer, and E.S. Edgerton, Source apportionment of PM2.5 in the southeastern united states using solvent-extractable organic compounds as tracers, *Environmental Science & Technology*, *36* (11), 2361-2371, 2002.

Zuberi, B., K.S. Johnson, G.K. Aleks, L.T. Molina, and A. Laskin, Hydrophilic properties of aged soot, *Geophys. Res. Lett.*, *32* (1), 2005.

4 Simultaneous measurement of the effective density and chemical composition of ambient aerosol particles

4.1 Synopsis

Simultaneous measurements of the effective density and chemical composition of individual ambient particles were made in Riverside, California by coupling a differential mobility analyzer (DMA) with an ultrafine aerosol time-of-flight mass spectrometer (UF-ATOFMS). In the summer, chemically diverse particle types (i.e. aged-OC, vanadium-OC-sulfate-nitrate, biomass) all had similar effective densities when measured during the same time period. This result suggests that during the summer study, the majority of particle mass for the different particle types was dominated by secondary species (OC, sulfates, nitrates) of the same density, while only a small fraction of the total particle mass is accounted for by the primary particle cores. Also shown herein, the effective density is a dynamic characteristic of the Riverside, CA ambient aerosol, changing by as much as 40% within 16 hours. During the summer measurement period, changes in the ambient atmospheric water content correlated with changes in the measured effective densities which ranged from ~1.0-1.5 g cm^{-3}. This correlation is potentially due to evaporation of water from particles in the aerodynamic lens. In contrast, in the fall during a Santa Ana meteorological event, ambient particles with a mobility diameter of 450 nm showed three distinct effective densities, each related to a chemically unique

particle class. Particles with effective densities of ~ 0.27 g cm^{-3}, 0.87 g cm^{-3}, and 0.93 g cm^{-3} were composed mostly of elemental carbon, lubricating oil, and aged organic carbon, respectively. It is interesting to contrast the seasonal differences where in the summer, particle density and mass were determined by high amounts of secondary species, whereas in the fall, relatively clean and dry Santa Ana conditions resulted in freshly emitted particles which retained their distinct source chemistries and densities.

4.2 Introduction

Particles emitted directly or formed through secondary processes in the atmosphere are continually evolving, both chemically and physically. Condensation, evaporation, oxidation, and changes in pH can alter the amount and type of chemical species present in the particle phase [*Molina et al.*, 2004; *Pankow*, 1994]. Coagulation, crystallization, dissolution, condensation and oxidation can change the size and shape of atmospheric particles [*Colberg et al.*, 2004; *Jacobson*, 2002; *Katrib et al.*, 2005; *Molina et al.*, 2004; *Schlenker and Martin*, 2005; *Weingartner et al.*, 1997]. Their environmental and health effects are largely determined by their chemical and physical properties. Environmentally, the chemical and physical properties influence particle optical properties and their ability to act as cloud condensation nuclei (CCN); the optical properties and CCN ability dictate the magnitude of the direct and indirect effects of particles on climate respectively [*Cruz and Pandis*, 1997; *Liao and Seinfeld*, 2005; *Novakov and Corrigan*, 1996; *Ramana et al.*, 2004; *Saxena et al.*, 1995]. Health impacts are influenced by the chemical toxicity of the particle and the ability of particles to penetrate deep into the lung [*Hesterberg et al.*, 1998; *Oberdorster et al.*, 1994; *Pauluhn*,

2004]. Furthermore, environmental and health effects are exacerbated by increased particle concentrations [*Dockery and Pope*, 1994; *Ramanathan et al.*, 2005]. Therefore, an understanding of individual particle chemical and physical characteristics is needed to estimate how particles impact climate and health.

Techniques such as a DMA-electrical low pressure impactor and a DMA-aerosol particle mass analyzer have been reported in the literature for calculating particle effective density and shape factor [*McMurry et al.*, 2002; *Park et al.*, 2003; *Van Gulijk et al.*, 2004]. However, these methods do not directly provide information on the chemical composition of particles. Mass spectrometry techniques are being used more and more to quantify the physical characteristics of particles, such as shape factor and density while simultaneously measuring chemical information. Combined measurements of particle size, density, and chemical information on individual particles have been published [*Cai et al.*, 2006; *Jimenez et al.*, 2003; *Katrib et al.*, 2005; *Moffet and Prather*, 2005; *Murphy et al.*, 2004; *Slowik et al.*, 2004; *Spencer and Prather*, 2006; *Zelenyuk et al.*, 2005; *Zelenyuk et al.*, 2006a; *Zelenyuk et al.*, 2006b; *Zhang et al.*, 2005]. The majority of published work focuses on laboratory generated aerosols and not ambient particles [*Jimenez et al.*, 2003; *Katrib et al.*, 2005; *Slowik et al.*, 2004; *Spencer and Prather*, 2006; *Zelenyuk et al.*, 2005; *Zelenyuk et al.*, 2006a; *Zelenyuk et al.*, 2006b].

In this study, ambient particles are measured using a differential mobility analyzer (DMA) / UF-ATOFMS technique. Mobility size selected particles are transported into a UF-ATOFMS, where the vacuum aerodynamic diameter and chemical composition are measured. Using this DMA/UF-ATOFMS technique, the information that is normally obtained by UF-ATOFMS (vacuum aerodynamic size and chemical composition) is

expanded to include particle effective density. This combined approach offers the ability to separate particles based on differences in density and/or shape prior to chemical analysis. Particle density measurements are essential for determining mass distributions using number concentrations measured with a scanning mobility particle sizer (SMPS) and aerosol particle sizer (APS). Furthermore, these measurements are important for establishing the accuracy of using SMPS data for scaling aerodynamic diameter number concentrations [*Lake et al.*, 2003; *Sodeman et al.*, 2005].

4.3 Methods

4.3.1 DOS and NaCl particle methods

Dioctyl sebacate (DOS) used in these experiments was technical grade (> 90 % pure) purchased from Sigma-Aldrich. DOS particles were generated using DOS "neat" in a Collison type nebulizer using a flow of 1.0 $L \cdot min^{-1}$ nitrogen. The DOS particle stream was then diluted in a 1.5 liter Pyrex flow tube using 5.0 $L \cdot min^{-1}$ of dry nitrogen.

A 0.1 M NaCl solution was made using 99.99% pure solid sodium chloride (Aldrich) mixed with milli-Q water. Particles of NaCl were generated using a Collison nebulizer with 1.0 $L \cdot min^{-1}$ of dry nitrogen and the 0.1 M salt solution. Particles exiting the nebulizer were first passed through a silica gel dryer with a volume of approximately 1.5 liter. After passing through a silica gel drier, the NaCl particle stream was diluted with 4.0 $L \cdot min^{-1}$ dry nitrogen. The relative humidity of the NaCl particle stream was less then 3% at the exit of the flow tube as measured by an in line RH meter (Vaisala HMP230) with Pt 100 sensor. Particles then entered a DMA where they were electrical mobility size selected (150-350 nm). Particles that enter the DMA are mixed with a sheath flow of

particle free air. After mixing with the sheath air, the particle stream exiting the DMA was at 55% RH and was directed to the UF-ATOFMS.

4.3.2 Differential mobility analyzer

A TSI model 3080 electrostatic classifier (DMA) was used to size select particles of a specific electrical mobility diameter during each experiment. Specific dimensions of the DMA used here are: DMA rod length (L = 43.6 cm), inner radius of the DMA annular space (r_1 = 0.937 cm), outer radius of the DMA annular space (r_2 = 1.961 cm). For ambient particle measurements during July and August in Riverside, CA the sample flow was held at 1.0 L min^{-1} and a sheath flow of 10.0 L min^{-1} was used. Ambient measurements made in November in Riverside used a sample flow of 0.5 L min^{-1} and sheath flow of 5.0 L min^{-1}. The lower flow rates in November were chosen so larger mobility size particles could be selected with the DMA. A scanning mobility particle sizer was used at the end of the secondary organic aerosols in Riverside (SOAR) field campaigns to confirm the sizes of the mobility diameters being emitted from the size selecting DMA; the mobility diameters measured with the SMPS were consistent with the selected mobility diameters from the DMA. The viscosity of air (μ = 0.0001865 poise) was used in all DMA calculations [*Lide*, 2002].

A DMA sample flow of 0.4 L·min^{-1} and a sheath flow of 4.0 L·min^{-1} were used during experiments with DOS particles. A DMA sample flow of 0.5 L·min^{-1} and a sheath flow of 5.0 L·min^{-1} were used during experiments with NaCl particles. DMA sheath and sample flows were calibrated prior to experimental measurements using a bubble flow meter (Gilibrator).

4.3.3 Ultrafine aerosol time-of-flight mass spectrometry

An ultrafine aerosol time-of-flight mass spectrometer was used to measure the vacuum aerodynamic diameter and dual polarity mass spectra of individual particles from 50-1000 nm. A detailed description of UF-ATOFMS is given by Su et al (2004) [*Su et al.*, 2004] and also Chapter 1. To determine particle sizes, an eleven point particle size calibration was made using polystyrene latex spheres of known physical diameter ranging from 117-1400 nm. During experiments, particles were desorbed and ionized using 266 nm radiation from a Q-switched Nd:YAG laser operating at ~ 1.4 mJ.

4.3.4 Particle chemical classification

Ambient particle data were imported into Matlab (The MathWorks, Inc.) and analyzed using YAADA version 1.2 [http://www.yaada.org]. Particle types were clustered using an Adaptive Resonance Theory neural network (ART-2a) [*Hopke and Song*, 1997; *Song et al.*, 1999]. ART-2a clusters chemically similar particles together based on the ion peak intensity pattern in each mass spectrum. Parameters for ART-2a used in this experiment were: learning rate = 0.05, vigilance factor = 0.85, and iterations = 20. Particle clusters resulting from ART-2a were further refined by combining chemically similar clusters into distinct chemical classes. For example, multiple elemental carbon-sulfate-nitrate (EC-SN) containing clusters showing minor differences in their mass spectral ion intensity patterns were grouped together and labeled collectively as “EC-SN”. The given chemical class names do not necessarily reflect all the species present within a class; instead, the names reflect most of the dominant

chemical species and/or the possible source in an attempt to keep the naming scheme simplified.

4.3.5 Ambient measurements

Ambient measurements were made as part of the SOAR field campaign [*Jimenez*, Accessed 2006]. The location for this field campaign was the University of California at Riverside campus. Ambient measurements were made during the summer (July-August, 2005) and fall (November, 2005). Ambient sampling occurred on 8 non-consecutive days in July-August (various times) and 5 consecutive days in November during two different time periods (7-9 am and 4-6 pm). Each sampling period was limited to 2hr. in duration. An aerosol sampling line extended roughly six meters above ground. To try and prevent condensation or evaporation during the measurement, the indoor portion of the sampling lines were insulated. It should be noted that the aerosol was not dried prior to sampling.

Relative humidity was measured by the Allen Goldstein research group from University of California at Berkeley.

4.4 Results and discussion

4.4.1 Theory

A detailed theoretical treatment of the relationships between particle aerodynamic diameter, electrical mobility diameter, effective density and particle shape is given by DeCarlo et al.[*DeCarlo et al.*, 2004]. Briefly, measuring the electrical mobility diameter (d_m) and vacuum aerodynamic diameter (d_{va}) of a particle allows the effective density (ρ_{eff}) to be measured using the equation

$$\rho_{eff} = \frac{d_{va}}{d_m}\rho_o \qquad [1]$$

where ρ_o is the standard density (1.0 g cm^{-3}). If the particle is spherical, the ρ_{eff} is equal to the particle density (ρ_p). If the particle is spherical and contains no internal voids, the particle density will be equal to the material density (ρ_m). For non-spherical particles, the effective density is less than the particle/material density. Equation 1 and the relationship between effective/particle/material densities will be used throughout the following discussion.

The majority of size selected particles exiting the DMA contain an electrostatic charge of +1. However, there is a small fraction of particles that contain charges of +2, +3…etc. These multiply charged particles have the same electrical mobility diameter but different vacuum aerodynamic diameters. Therefore, particles with a different number of charges can be distinguished based on their different vacuum aerodynamic diameters. To determine if different aerodynamic diameters are indeed particles with different number of charges, the equation

$$\frac{d_p}{C} = \frac{2neVL}{3\mu q_{sh}\ln(\frac{r_2}{r_1})} \qquad [2]$$

is used to calculate the particle diameter (d_p) for particles with different number of charges (n) at a set DMA voltage (V), DMA rod length (L), gas viscosity (μ), sheath flow (q_{sh}), inner radius of the DMA annular space (r_1), outer radius of the DMA annular space (r_2), and where C is the Cunningham slip factor evaluated at d_p [*Knutson and*

Whitby, 1976]. The values of L, μ , $r_{1,}$ $r_{2,}$ and q_{sh} are given in the methods section. If the number of charges on a particle equals one, then d_p will be equal to d_m. For charges greater than one, d_p will be larger than d_m. Substituting d_p (from Equation 2) into Equation 1 and using the material density, a calculation of the theoretical vacuum aerodynamic diameter for particles with the same mobility diameter and density but different physical diameter due to different charge states can be made. The particles are assumed to be spherical for this calculation.

4.4.2 Laboratory validation experiments

An important part of the presented work was to validate this method using standard Dioctyl sebacate (DOS) and NaCl particles. Figure 4.1 shows the vacuum aerodynamic size distribution of 300 nm mobility size-selected DOS particles measured using UF-ATOFMS. A distinct feature that can be seen from this figure is the presence of three well separated vacuum aerodynamic modes centered at 276, 497 and 680 nm (d_{va}). These three modes represent three different charge states for particles with the same electrical mobility diameter. It should be noted that the relative heights of the modes in Figure 4.1 do not represent the distribution of particles with a particular charge emitted from the DMA. Particles of larger sizes are counted more efficiently within the light scattering region of the UF-ATOFMS.

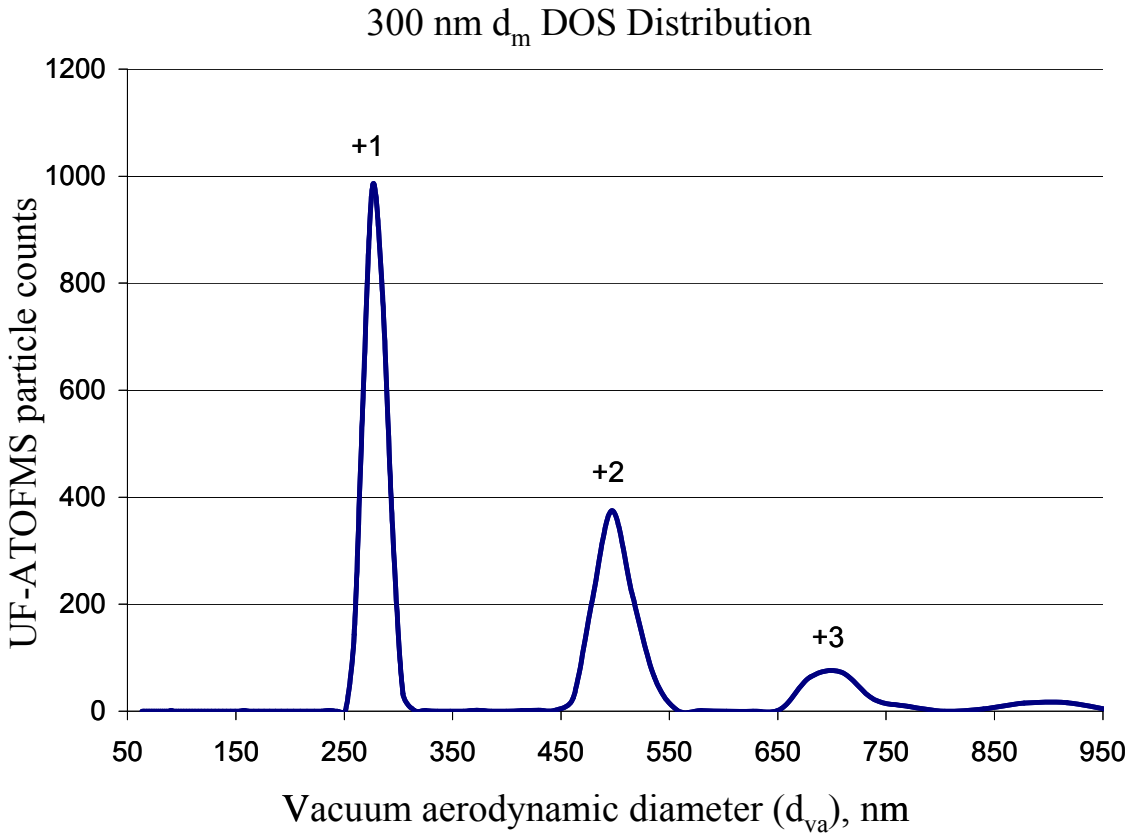

Figure 4.1 Vacuum aerodynamic size distribution of 300 nm electrical mobility size selected DOS particles.

Figure 4.2 shows a graph of the measured vacuum aerodynamic diameter versus the predicted vacuum aerodynamic diameter for particles with electrical mobility diameters of 500, 400, 350, 300, 250, 200, 150 and 120 nm. This plot includes the vacuum aerodynamic diameter for particles with multiple charges. There is a linear correlation of 0.995 between the measured and predicted diameter values for DOS particles. Furthermore, 23 out of the 25 points shown in Figure 4.2 are within 6% of the predicted value. This finding reveals that multiply charged particles emitted from the DMA are observed using UF-ATOFMS as well separated peaks.

Using Equation 1, the effective densities of DOS particles were calculated for different mobility diameters. These values are given in Table 4.1. Because DOS particles are likely spherical with no void spaces, one would expect the effective density to equal the material density of DOS (0.911 $g \cdot cm^{-3}$). Indeed, Table 4.1 shows the average calculated density for DOS particles is 0.90 $g \cdot cm^{-3}$, which is within 1.2% of the material density. Table 4.1 also shows there is a systematic pattern of increasing densities for increasing mobility diameters. This pattern has also been observed by Zelenyuk et al. and attributed to a small systematic difference in the calibration between the DMA and vacuum aerodynamic sizing [*Zelenyuk et al.*, 2005]; this pattern is present after calibration of each instrument. It should be noted that even with this small systematic difference the largest error in the measured density is ~5.6%. For DOS particles, and likely other spherical particles, the DMA/UF-ATOFMS technique is quite accurate at measuring the material density.

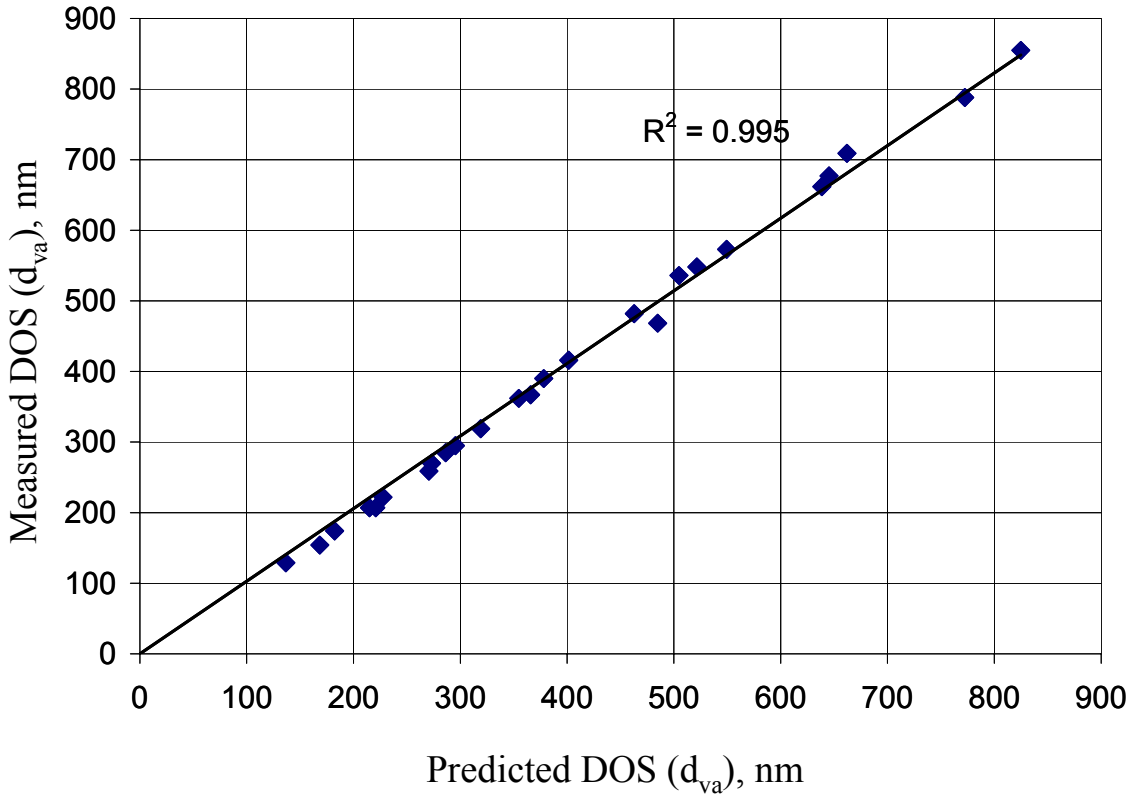

Figure 4.2 Measured vacuum aerodynamic diameter for DOS particles, mobility selected between 120-500 nm d_m, is plotted versus the predicted vacuum aerodynamic diameter. Equation 1 was used to calculate the physical diameter for multiply charged DOS particles. The physical diameter and the density of DOS were used to calculate the "predicted" vacuum aerodynamic diameter of the particle.

Table 4.1 Measured values for DOS effective density at different electrical mobility diameters.

Electrical mobility diameter (d_m)	**DOS density, g/cm3**
150	0.86
200	0.87
250	0.89
300	0.90
350	0.91
400	0.91
500	0.94
Average density / Std Dev	0.90 +/- 0.03
Error vs material density, %	1.2

To examine the effect of particle shape on measurements of particle density, dry NaCl particles were examined. Figure 4.3 illustrates the vacuum aerodynamic size distribution for 300 nm (d_m) NaCl particles. Two peaks are observed, representing particles with +1 and +2 charges. Notice the +1 peak has an aerodynamic size of ~540 nm indicating that these particles have an effective density of 1.8 g·cm^{-3}, which differs from the density of NaCl (2.17 g·cm^{-3}) by about 16%. This difference is caused by the non-spherical structure of dry NaCl particles. The effective density measured here is in agreement with the measured effective density for dry 300nm NaCl cubes by Zelenyuk et al (~1.8 g·cm^{-3}) [*Zelenyuk et al.*, 2006a].

To estimate the NaCl shape factor, the following equations stemming from the definitions of mobility diameter (Equation 3) and vacuum aerodynamic diameter (Equation 4) are used

$$\frac{d_m}{C_c(d_m)} = \frac{d_{ve}\chi_t}{C_c(d_{ve})} \qquad [3]$$

$$d_{va} = \frac{\rho_p d_{ve}}{\rho_o \chi_v} \qquad [4]$$

where d_m is the electrical mobility diameter, d_{ve} is the volume equivalent diameter, d_{va} is the vacuum aerodynamic diameter, C_c is the Cunningham slip factor evaluated at a given diameter, ρ_p is the particle density, ρ_o is the standard density (1.0 g·cm^{-3}) and χ_t and χ_v are shape factors in the transition and free molecular regime respectively.

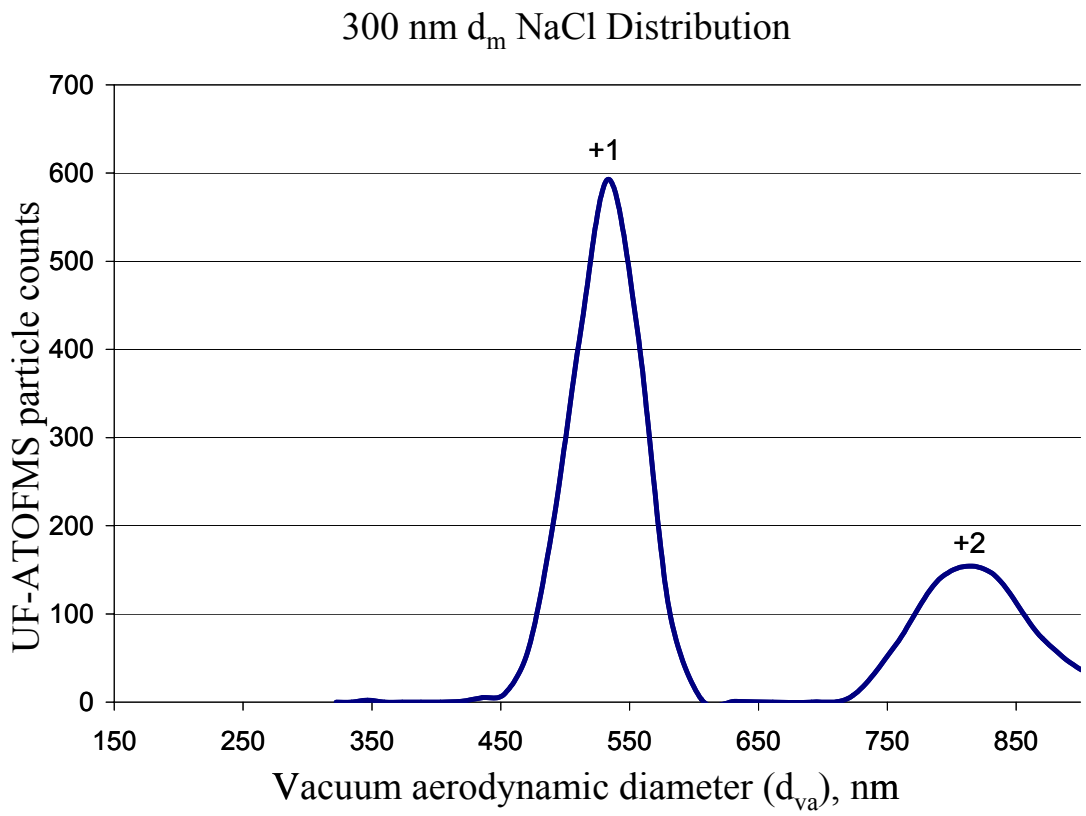

Figure 4.3 Vacuum aerodynamic size distribution of 300 nm electrical mobility size selected NaCl particles

.

Equations 3 and 4 are combined to yield an equation that relates the effective density to particle density and particle shape factor:

$$\frac{d_{va}}{d_m} = \frac{\rho_p C_c(d_{ve})}{\rho_o \chi_v \chi_t C_c(d_m)} \qquad [5]$$

Using the slip correction factor in the free molecular regime (Equation 6)

$$C_c(d) \approx \frac{2\lambda}{d}(\alpha + \beta) \qquad [6]$$

and Equation 3, the ratio $C_c(d_{ve})/C_c(d_m)$ is simplified to $\sim \chi_t^{1/2}$. The variables α, β and λ in Equation 6 are empirical constants which have been determined for solid and liquid particles [*Allen and Raabe*, 1985]. Substitution of $\chi_t^{1/2}$ into Equation 5 with the assumption $\chi_t \sim \chi_v$ yields

$$\chi = \left(\frac{d_m \rho_p}{d_{va}} \right)^{2/3} \qquad [7]$$

It should be noted, the assumption $\chi_t \sim \chi_v$ is likely a good approximation for mildly non-spherical particles ($\chi < 2$), but is questionable for highly irregular particles [*DeCarlo et al.*, 2004]. Equation 7 can be used to make an estimate of the shape factor for particles when one has a good idea of the particle density and measurement of mobility and vacuum aerodynamic diameters. Assuming there are no void spaces, the particle density for NaCl is equal to the material density. Table 4.2 shows the calculated effective density, shape factor, and particle density ($\rho_p = \chi\ \rho_{eff}$) for NaCl particles of different mobility diameters. On average the effective density is within 16% of the material density. Shape factors for NaCl particles ranged between 1.11 and 1.14, which are close to that of a cube (1.08) and in close agreement with values measured by Zelenyuk et al

Table 4.2 Measured values for NaCl effective density, shape factor, and particle density at different electrical mobility diameters.

Electrical mobility diameter (d_m)	**NaCl effective density, g/cm3**	**Shape factor (χ) (free molecular regime)**	**Particle density (using shape factor)**
150	1.86	1.11	2.06
200	1.82	1.12	2.05
250	1.80	1.13	2.04
300	1.79	1.14	2.04
350	1.79	1.14	2.03
Average density	1.81	-	2.04
Error vs material density, %	16.50	-	5.8

(1.06-1.17) [*Zelenyuk et al.*, 2006a]. Using the shape factor and effective density yields an average NaCl particle density of 2.04, which is within 6% of the material density. This measurement of NaCl shape factor represents a best case scenario, because we know the material density of NaCl which allows us to calculate the shape factor. For non-spherical ambient particles, calculating the shape factor without prior knowledge of the material density could yield larger errors. Some of this error could be minimized using the coupled chemical information to make estimates of the particle density based on materials with similar composition.

In general, these validation experiments show that the method is accurate at measuring the density for DOS to within ~2%; however there is a small systematic bias in the density measurement with increasing d_m giving errors up to ~6% at larger mobility sizes. Similar validation experiments have also been published by Zelenyuk et al [*Zelenyuk et al.*, 2005; *Zelenyuk et al.*, 2006a; *Zelenyuk and Imre*, 2005].

A recent paper by Zelenyuk et al. shows evaporation of water occurs from different types of salt particles sampled through an aerodynamic lens [*Zelenyuk et al.*, 2006b]. Because the ambient aerosol sampled in this study was not dried, the potential exists for evaporation of water from particles prior to measuring d_{va}. This evaporation would lead to an error in the measured effective density. As will be shown and discussed, ambient relative humidity appears to influence the effective densities measured in this work. Regardless of the potential for evaporation, useful physical and chemical information is still obtained from these measurements. In future studies using the aerodynamic lens, it would be the author's recommendation to follow the advice of Zelenyuk et al. and dry ambient particles prior to making effective density measurements.

4.4.3 Ambient particle chemical composition

DMA/UF-ATOFMS measurements of ambient particles were made in Riverside, California during July-August and November. During the summer time period, ambient particle concentrations were high enough (PM 2.5 ~ 40 μg m^{-3}) [*California-Air-Resource-Board*, Accessed 2006] to measure five different mobility sizes (d_m-150, 175, 200, 250 and 300 nm) with the UF-ATOFMS within 2hr., obtaining ~2000 mass spectra for each size. During the November measurement period, particle concentrations were low (PM 2.5 ~ 2 μg m^{-3}) and only one or two mobility sizes (d_m-175 and 450 nm) could be selected to obtain 1000-2000 mass spectra per size in 2 hr.

Figure 4.4 shows the area matrix for each chemical class that is used throughout the discussion. An area matrix resembles an individual particle mass spectrum for particles within a cluster. The particle chemical classes are: aged organic carbon-sulfate-nitrate (Aged-OC-SN), amine-sulfate-nitrate (amine), elemental carbon-sulfate-nitrate (EC-SN), EC with sulfate type 2 (EC-2), organic carbon type 2 (OC-2), vanadium-OC-sulfate-nitrate (Vanadium-SN), calcium-elemental carbon-sulfate (Ca-EC-sulfate), potassium-biomass (K-Biomass).

Aged-OC-SN mass spectra are characterized by OC fragment ions including *m/z* $^{15}(CH_3)^+$, $^{27}(C_2H_3)^+$, $^{27}(CNH)^+$, $^{29}(C_2H_5)^+$, $^{29}(COH)^+$, $^{43}(CHNO)^+$, $^{43}(C_2H_3O)^+$, sulfate $^{97}(HSO_4)^-$ and nitrate $^{62}(NO_3)^-$. The amine particle mass spectrum is characterized by intense ions at *m/z* $^{58}C_2H_5NHCH_2^+$, $^{86}(C_2H_5)_2NHCH_2^+$ and $^{118}(C_2H_5)_3NOH^+$, sulfate $^{97}(HSO_4)^-$ and nitrate $^{62}(NO_3)^-$. EC-SN is characterized by carbon cluster ions at *m/z* 12, 24, 36, 48, 60, sulfate $^{97}(HSO_4)^-$ and nitrate $^{62}(NO_3)^-$. EC-2 is characterized by intense long chain carbon cluster ions in the mass spectrum that extend out to C_{15} in both

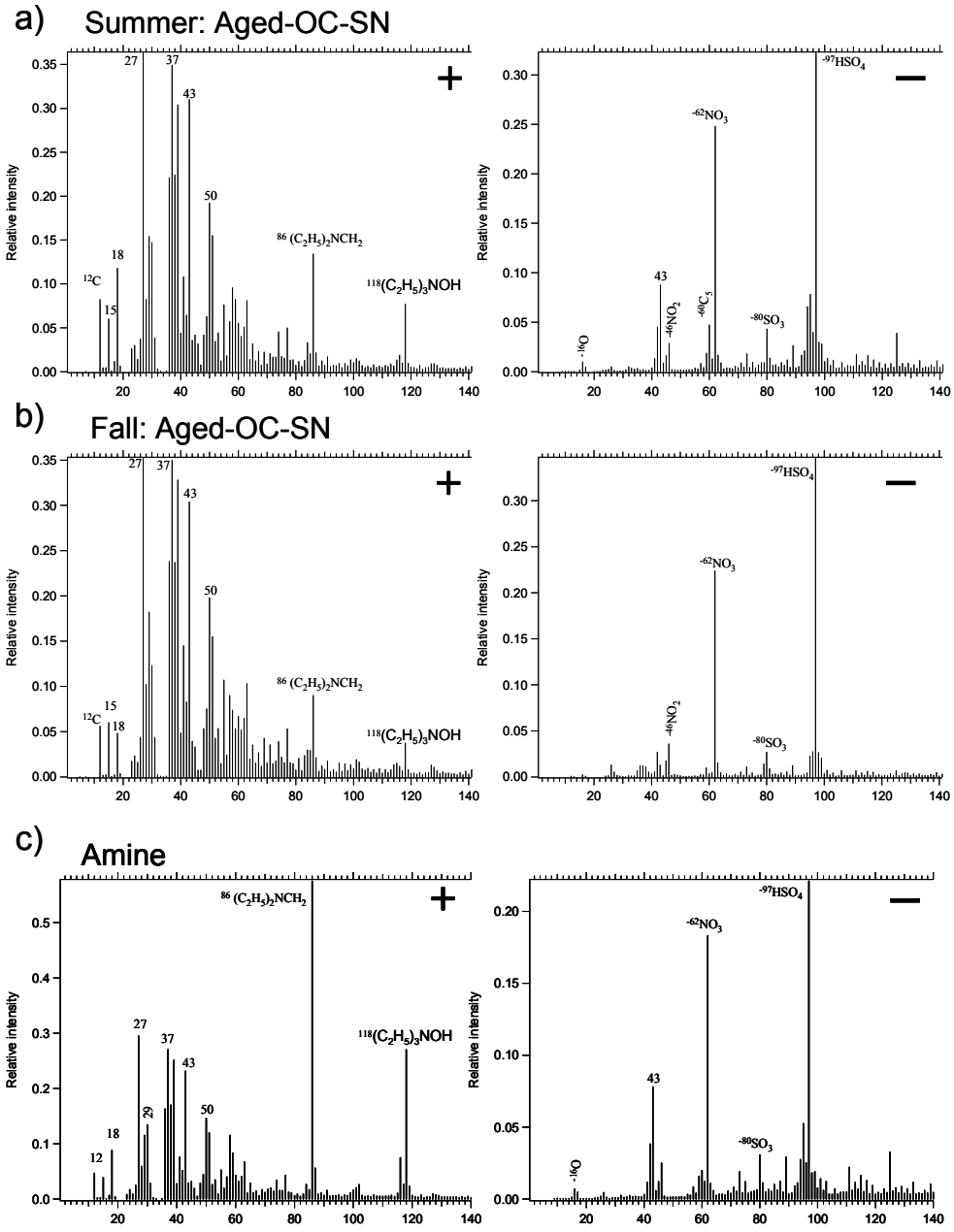

Figure 4.4 Positive (left side) and negative (right side) ion area matrix for chemical classes detected in Riverside CA in the summer and fall. An area matrix represents the average intensity of each m/z for all particles within a cluster. In general, the area matrix resembles individual mass spectra of particles within a cluster. The eight major particle classes shown are: a) Summer: Aged-OC-sulfate-nitrate, b) Fall: Aged-OC-sulfate-nitrate, c) amine-sulfate-nitrate, d) Summer: EC-sulfate-nitrate, e) Fall: EC-sulfate-nitrate, f) EC-2, g) OC-2, h) Vanadium-OC-sulfate, i) Ca-EC-sulfate, j) Summer: K-biomass, k) Fall: K-biomass. Mass-to-charge values and chemical assignment for some ions are given above the peak.

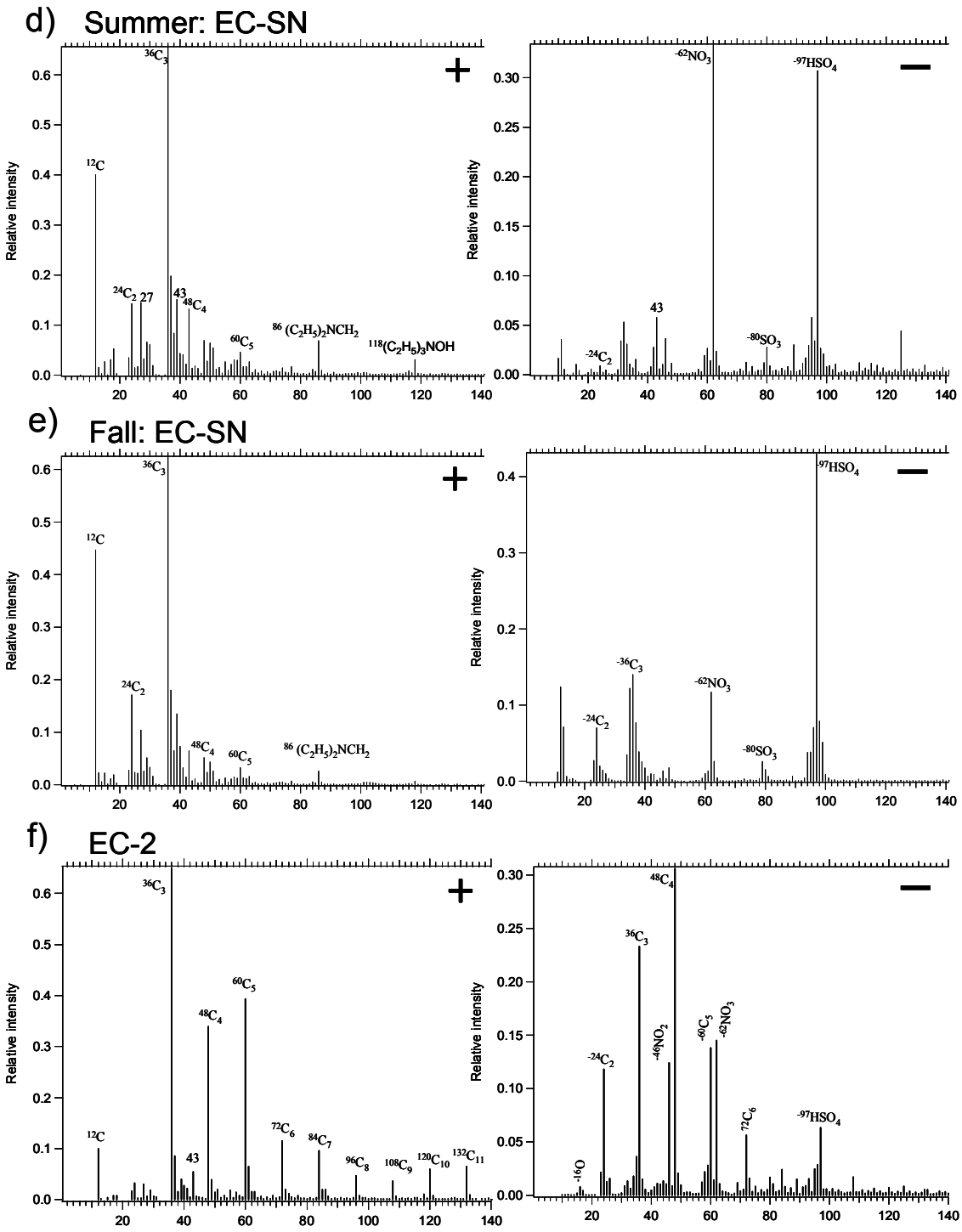

Figure 4.4 continued

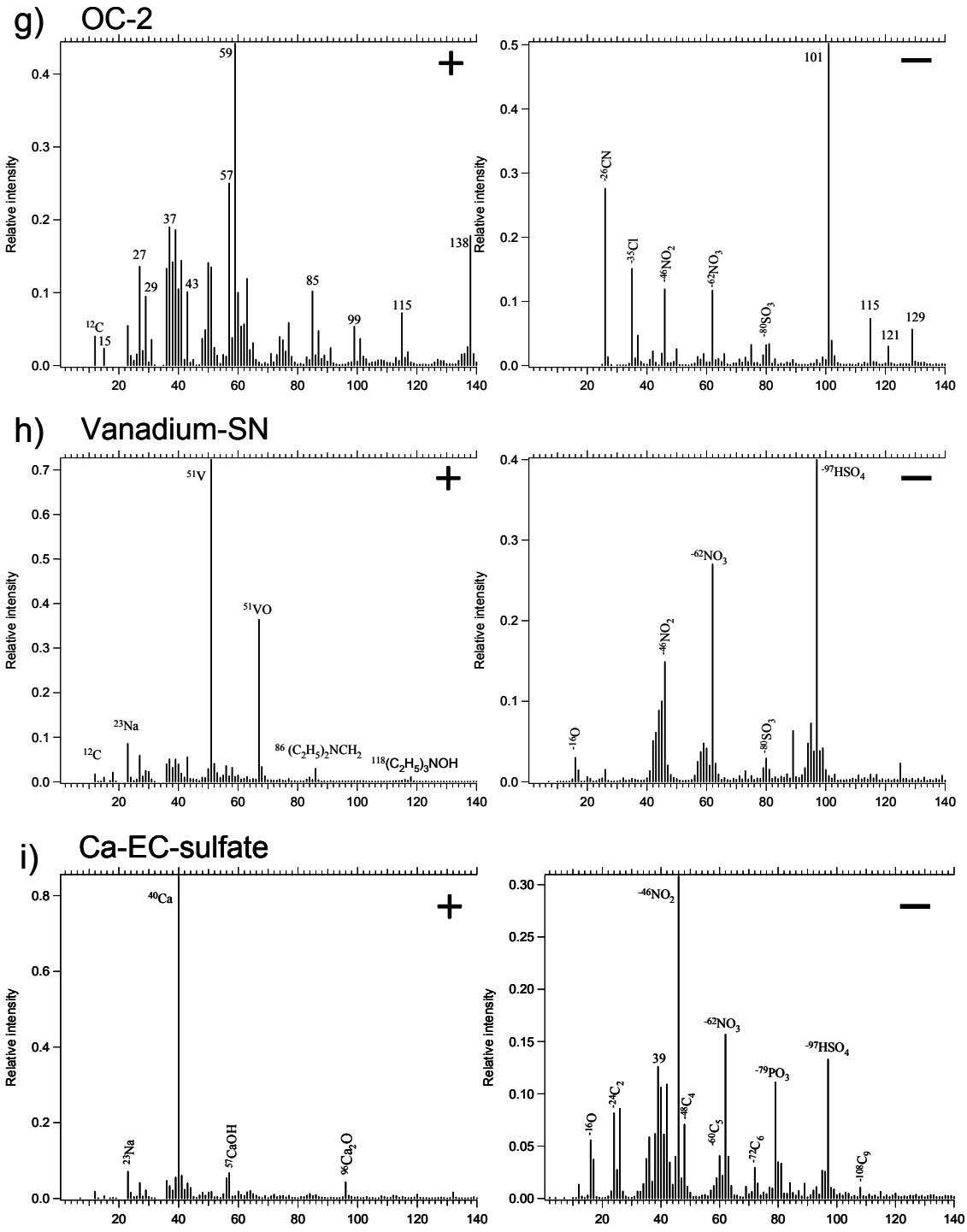

Figure 4.4 continued

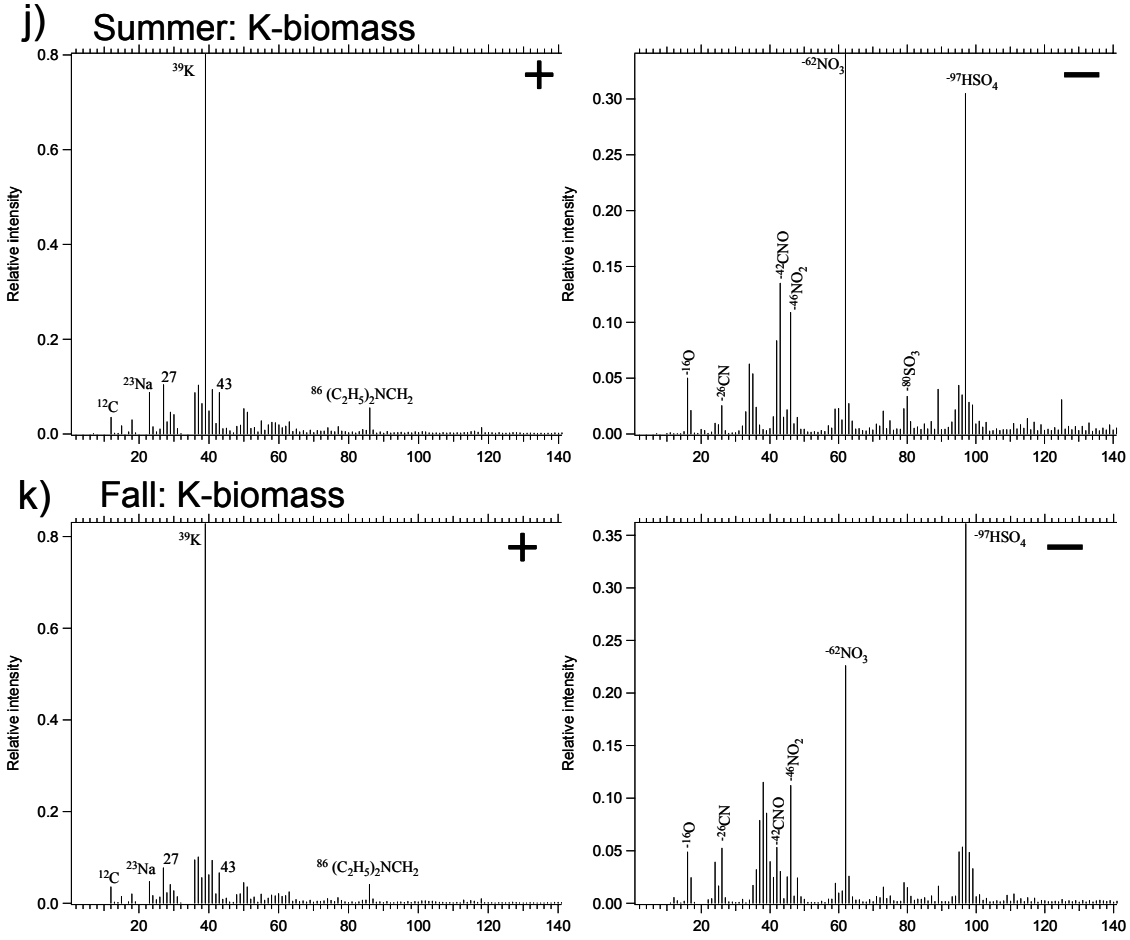

Figure 4.4 Continued

positive and negative polarities. Vanadium-SN is characterized by vanadium and vanadium oxide ions at m/z 51^+ and 67^+, sulfate $^{97}(HSO_4)^-$ and nitrate $^{62}(NO_3)^-$. The Ca-EC-sulfate mass spectrum is characterized by an intense $^{40}Ca^+$ ion and intense sulfate ion ($^{97}HSO_4^-$), with less intense positive and negative EC cluster ions (12, 24, 36…C_n). K-biomass generally has an intense potassium ion at *m/z* 39^+, a less intense sodium ion at *m/z* 23^+, and various low intensity OC and EC fragment ions. The chemical assignments of the ions discussed above are based on previous lab studies of organic standards and provided as the most likely assignments; other possible chemical assignments can and do exist.

Significant numbers of three classes (Aged-OC-SN, EC-SN, K-biomass) were observed during both the summer and fall Santa Ana period. The area matrices for these three classes have been further separated into summer and fall in Figure 4.4 to show the variations in these types during the different time periods. In general during the summer, more intense ion peaks were present from organic fragment ions (m/z 43 in particular), nitrates and amines.

4.4.4 Effective density measurements

Figure 4.5a shows the vacuum aerodynamic size distribution of 250 nm electrical mobility selected ambient particles from Riverside, CA during 4 days of the summer sampling period. The dominant size modes observed on July 27th (275 nm) and July 28th (370 nm) in Figure 4.5a differ by ~95 nm, which represents an effective density range of 1.09-1.49 $g \cdot cm^{-3}$. The dominant modes on August 4th (365 nm) and August 14th (315 nm) correspond to particles with effective densities of 1.46 and 1.26 $g \cdot cm^{-3}$, respectively.

The effective densities given above deviate by less then 8 %, based on the variability calculated at the full width at half the maximum height of the aerodynamic mode. Other less intense modes in the size distributions are also observed (Figure 4.5a). Data on July 27th show a second mode at ~ 370 nm, July 28th and August 4th a second mode at ~550 nm, and August 14th a second mode at ~480 nm. Other mobility diameters showed similar results. Assuming these are spherical particles which contain no voids, the aerodynamic size of a doubly charged particle can be calculated using Equations 1 and 2, which are discussed above in the theory section. For example, a doubly charged spherical particle exiting the DMA with a mobility diameter of 250 nm should have a physical diameter of ~ 415 nm. Using the effective densities given above, the less intense modes on July 28th, August 4th, and August 14th are observed within 10% of the predicted d_{va} which is reasonable given the complex nature of ambient particles. However, the observed peak at 370 nm on July 27th is 82 nm smaller than predicted or about 20% different then the predicted d_{va}. This significant difference suggests this second mode is not due to doubly charged particles, rather singly charged particles with an effective density of ~1.48 g cm^{-3}. Further evidence for this is shown in Figure 4.5b. Figure 4.5b shows the aerodynamic size distribution of 150 nm electrical mobility selected particles on July 27. At 150 nm d_m there are 4 vacuum aerodynamic modes. The two smallest aerodynamic diameter modes labeled 1 and 2 have effective densities of ~1.25 and 1.44 g cm^{-3}, respectively (similar to the two modes at d_m 250 nm). The two modes labeled 3 and 4 are within 5% of where doubly charged particles at the two different densities are estimated to be. One might expect particles with an effective density of 1.48 g cm^{-3} to have a unique chemical

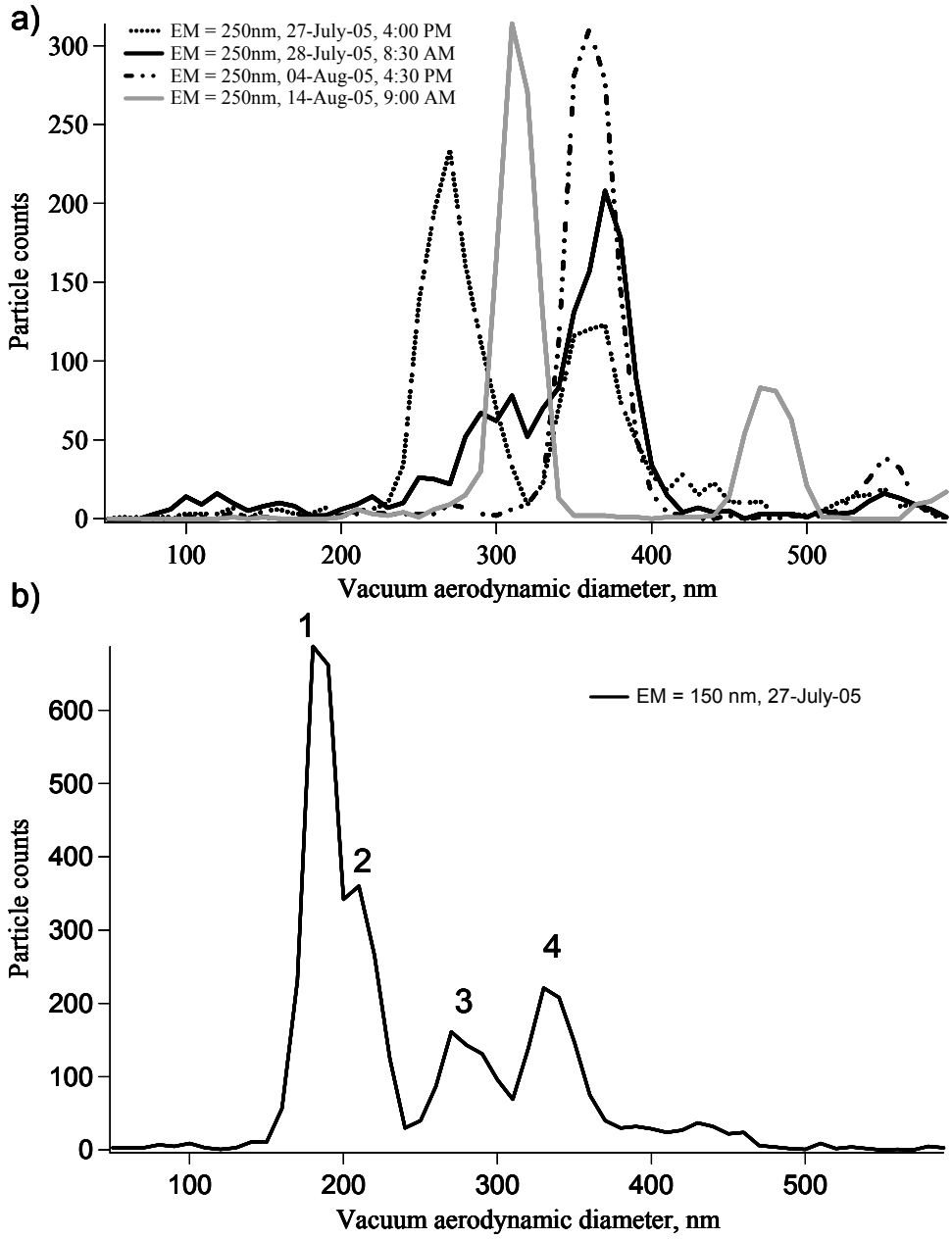

Figure 4.5 Vacuum aerodynamic size distribution of 250 nm electrical mobility size selected ambient particles from Riverside, California in July and August. Date and time for each trace is given in the upper left corner.

composition compared to particles with effective density of 1.09 g cm^{-3}. However, Figure 4.6 shows that this is not the case for these particles.

The percentages of the different particle chemical classes observed for the two vacuum aerodynamic modes on July 27th are shown in Figure 4.6. The particle chemical classes are: aged organic carbon-sulfate-nitrate (Aged-OC-SN), vanadium-OC-sulfate-nitrate (Vanadium-SN), elemental carbon-sulfate-nitrate (EC-SN), amine-sulfate-nitrate (amine), potassium-biomass (K-Biomass), and EC with sulfate type 2 (EC-2). As mentioned in the methods section, the chemical class names reflect some of the dominant chemical species or the source in an attempt to keep the names short. The area matrix for each of the particle classes and a detailed description of what distinguishes each class is given above. Some of these particle types have also been discussed and published previously [*Angelino et al.*, 2001; *Liu et al.*, 2000b; *Silva and Prather*, 2000]. Figure 4.6 shows the percentages of the chemical classes within the two aerodynamic modes differ slightly, but there is not a unique particle class that makes up a significant fraction of one aerodynamic mode versus the other. This observation suggests the two aerodynamic modes contain chemically similar particles. As will be discussed later, a plot of effective density versus different mobility diameters for the two modes observed on July-27 suggests the smaller aerodynamic size mode contains more non-spherical particles (smaller effective density), and the larger mode more spherical particles. Whether these two effective density populations existed prior to sampling or were formed by complex transformations of liquid droplets into solids due to evaporation in the aerodynamic lens, as observed by Zelenyuk et al. for NaCl, cannot be determined in this set of experiments [*Zelenyuk et al.*, 2006b].

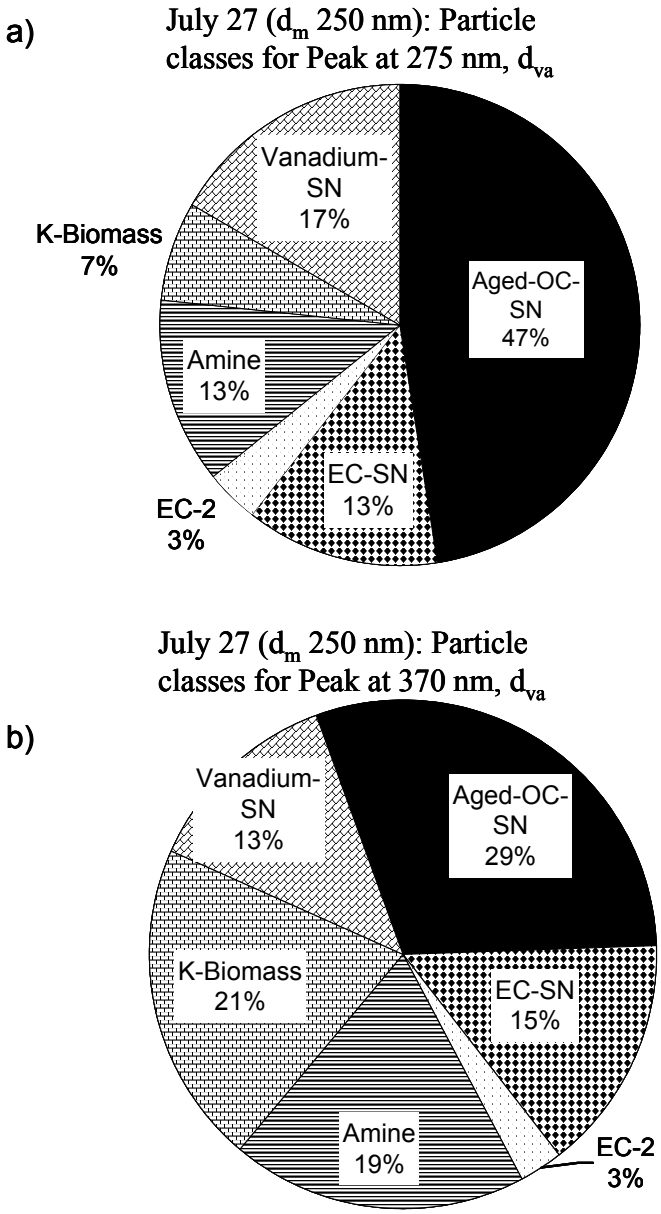

Figure 4.6 Pie charts for the particle chemical classes observed in two different vacuum aerodynamic modes during ambient sampling in Riverside, California on July 27th. Particles have d_m = 250 nm. Top pie chart contains the particle chemical classes observed in the vacuum aerodynamic mode at ~275 nm. The bottom pie chart contains classes for the mode at ~370 nm.

It is interesting to note that all the particles, regardless of their chemistry, appear to have similar effective densities. Similar results (not shown) were observed for different days and for different electrical mobility sizes during the summer time period. Similarities in effective density are likely due to atmospheric processing (aging) of the different particle types. During the summer sampling period, the majority of particles analyzed by ATOFMS contained the same secondary processing markers including amines, nitrate, and sulfate (Qin et al. manuscript in preparation).

As the particles age in Riverside, secondary organic carbon and secondary inorganic species (such as ammonia, nitrate and sulfate) condense on the particles[*Hughes et al.*, 2000; *Liu et al.*, 2000a; *Pastor et al.*, 2003; *Sardar et al.*, 2005]. This condensation occurs to such an extent, that the majority of the particle mass is likely from the secondary species. It is important to note that the ART-2a analysis inherently separates particles into different particle classes based on the different primary cores of these particles which in the case of highly aged aerosols represent only a small fraction of the mass. This highlights the potential of this technique for classifying particles based on their primary particle core and monitoring the addition of condensed secondary species over time. In essence, this approach would provide a two dimensional classification scheme.

A comparison of the effective densities for the different electrical mobility sizes on different days during the July-August sampling period is shown in Figure 4.7. The vertical error bars in Figure 4.7 were calculated using the full width at half the maximum of the aerodynamic mode. During most sampling intervals, the effective density remained fairly constant (+/- 0.05 g cm^{-3}) across a range of mobility sizes. This pattern suggests

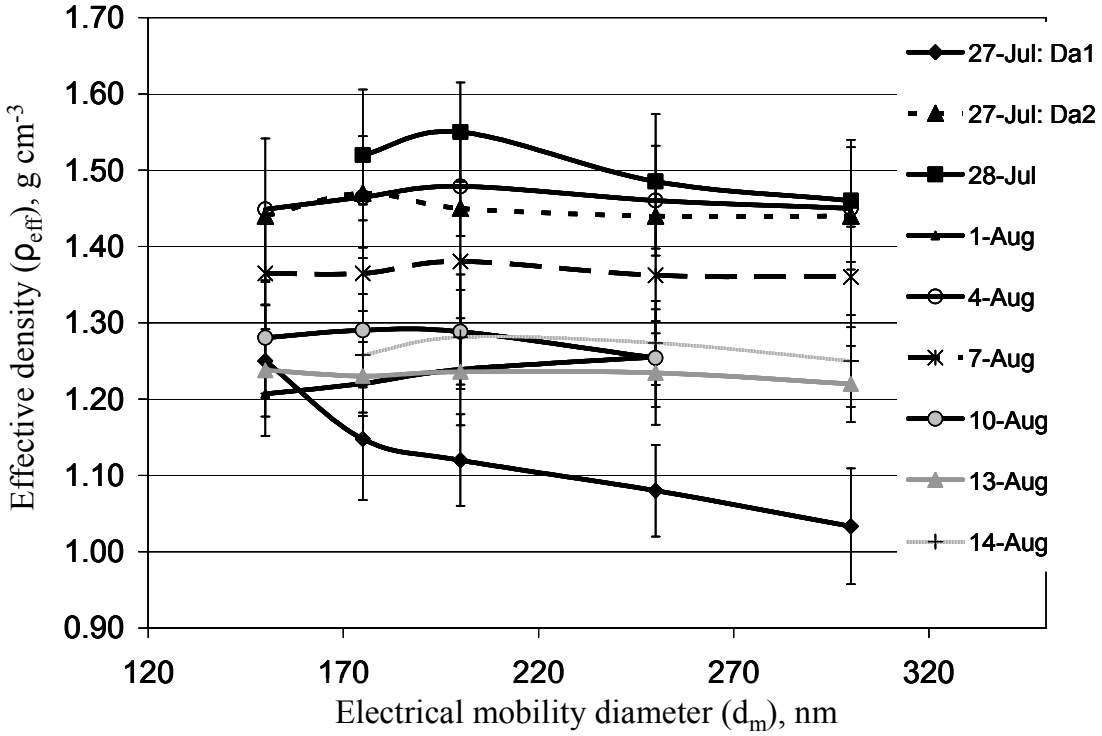

Figure 4.7 Effective density is plotted versus electrical mobility diameter for measurements taken on different days. The vertical error bars in Figure 4.3 were calculated using the full width at half the maximum of the aerodynamic mode.

that during these times the particles had a spherical morphology since the effective density has been shown to decrease as electrical mobility size increases for irregularly shaped particles [*Park et al.*, 2003; *Slowik et al.*, 2004; *Zelenyuk et al.*, 2006a]. Figure 4.7 shows that on July 27th the effective density decreases as mobility size increases for the mode at smaller aerodynamic diameter (labeled as 27-Jul: Da1). This suggests the smaller aerodynamic mode particles are non-spherical. Effective density for the larger aerodynamic diameter mode on July 27th (labeled as 27-Jul: Da2) remains fairly constant, suggesting these particles are spherical. Although it is not possible to derive shape factors without knowledge of particle density, determining if particles are spherical or non-spherical is possible using this technique. For the entire July-August sampling period, the effective density ranged between ~1.0 and 1.5 g cm^{-3}. The largest difference in the effective density occurred between July 27th and July 28th, which demonstrates the effective density can fluctuate by over 40% for the same mobility diameter particles within a 16 hour period. This is a significant change, and highlights a dynamic difference between mobility and vacuum aerodynamic diameter at different times.

Temporal fluctuations in effective density indicate changes in particle shape or density. These changes could be due to new particle types arriving in air masses or particles undergoing physical/chemical processing. To determine if there are chemical/physical changes leading to changes in the effective density over the different sampling periods, ambient ozone concentration, relative humidity, and atmospheric water content were compared to the average effective densities (averaged across different mobility sizes) of ambient particles. Absolute atmospheric water content and relative humidity show a trend. Figure 4.8 shows the atmospheric water content during each

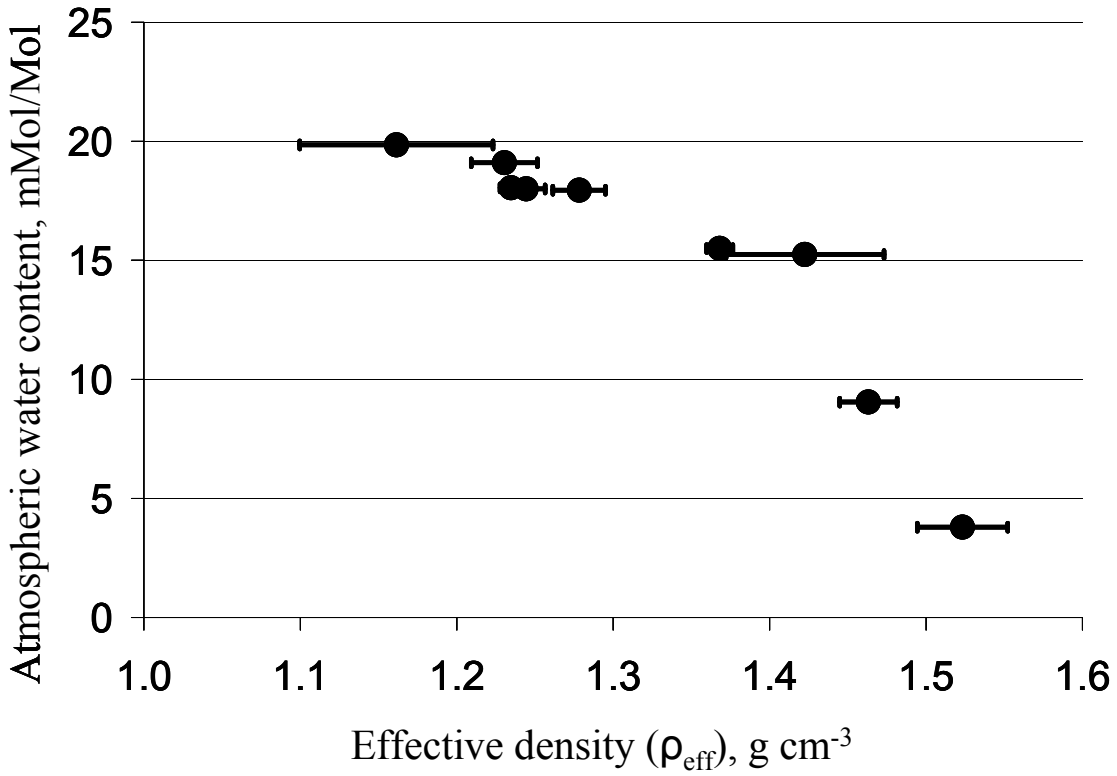

Figure 4.8 Atmospheric water content is plotted versus the average effective density across different mobility sizes. The horizontal bars represent the standard deviation in the average.

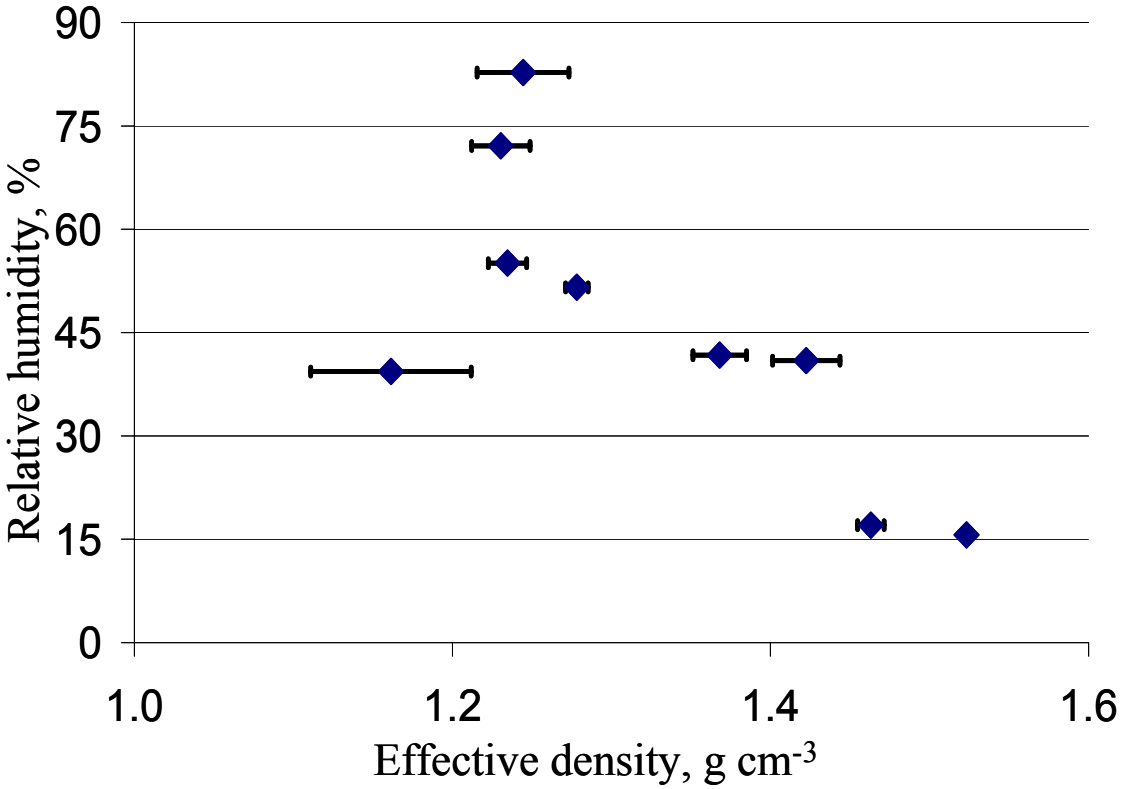

Figure 4.9 The average effective density of particles sampled during SOAR on different days (x-axis) is plotted versus the ambient relative humidity (y-axis). The horizontal error bars represent the standard deviation of the average effective density across different mobility diameters.

sampling period on the y-axis and the average effective density on the x-axis. Figure 4.8 shows that as the atmospheric water content increases the effective density tends to decrease. Figure 4.9 shows the average effective density during each sampling period versus the ambient relative humidity for the summer and fall during SOAR. This represents an average of the effective density measured at different mobility diameters within the 2hr. sampling periods. The horizontal bars represent the standard deviation in this average. In general there appears to be a trend to smaller effective density as relative humidity increases. The point at density ~1.1 $g \cdot cm^{-3}$ and 40% relative humidity is from the smallest aerodynamic diameter mode on July-27. These particles are thought to be non-spherical which might explain the discrepancy in this particular data point. If the second largest aerodynamic mode observed on July 27 is considered singly charged (yielding an effective density of ~1.4) it is in line with the rest of the data. A possible reason the effective density is tracking air water content better then ambient relative humidity is that the particles experienced a relatively constant temperature in the sampling line in the trailer. This new RH would be directly proportional to the atmospheric water content but not necessarily the outdoor relative humidity. This also implies that the insulated sampling line may not have been entirely effective.

There are two possible explanations for the correlations between the effective density with atmospheric water content and RH. First, as water evaporates or condenses on these particles at different relative humidity, it increases or decreases the particle density, respectively. This would suggest that some water is retained on these particles after passing through the aerodynamic lens. Another possibility is water is evaporating from particles in the aerodynamic lens and at high relative humidity there is more water

on the particle that can evaporate, leading to a smaller d_{va} and hence smaller effective density. This second possibility would be in line with the laboratory results of Zelenyuk et al. However, the extent of water evaporation from ambient particles (complex mixtures) cannot be definitively determined. This leaves open the possibility for future experiments to explore evaporation of water from ambient particles in the aerodynamic lens by measuring differences in effective density between ambient and dried-ambient particles. Another logical step, to further understand the effects of water, temperature, and ozone on particle density and morphology, will be to perform laboratory experiments on ambient particles where relative humidity, ozone, and temperature can be controlled in a systematic manner. Also, longer and more continuous ambient sampling may uncover effects on particle density and shape from reactions with gases such as ozone.

During the fall study in November, differences in the densities and/or shapes of the particles were observed. Ambient particles were size selected at 175 nm and 450 nm. Figure 4.10 shows the vacuum aerodynamic size distribution for 450 nm electrical mobility selected particles on November 21st from 8:00 am-10:00 am. These 450 nm electrical mobility selected particles show three distinct vacuum aerodynamic size modes at 120, 390, and 420 nm. Figure 4.10 also shows three pie charts with the percentages of different chemical classes observed within each aerodynamic mode. A representative area matrix (which resembles the mass spectra) and description of each chemical class is given in the Supporting Information section. The aerodynamic size mode at 120 nm in Figure 4.10 contains 73% EC-SN, 14% Ca-EC-sulfate, and 9% EC-2 particles. The particles in the 120 nm d_{va} mode have an effective density of ~ 0.27 g cm^{-3} and represent more than 80% EC type particles. Such a low effective density would be expected for

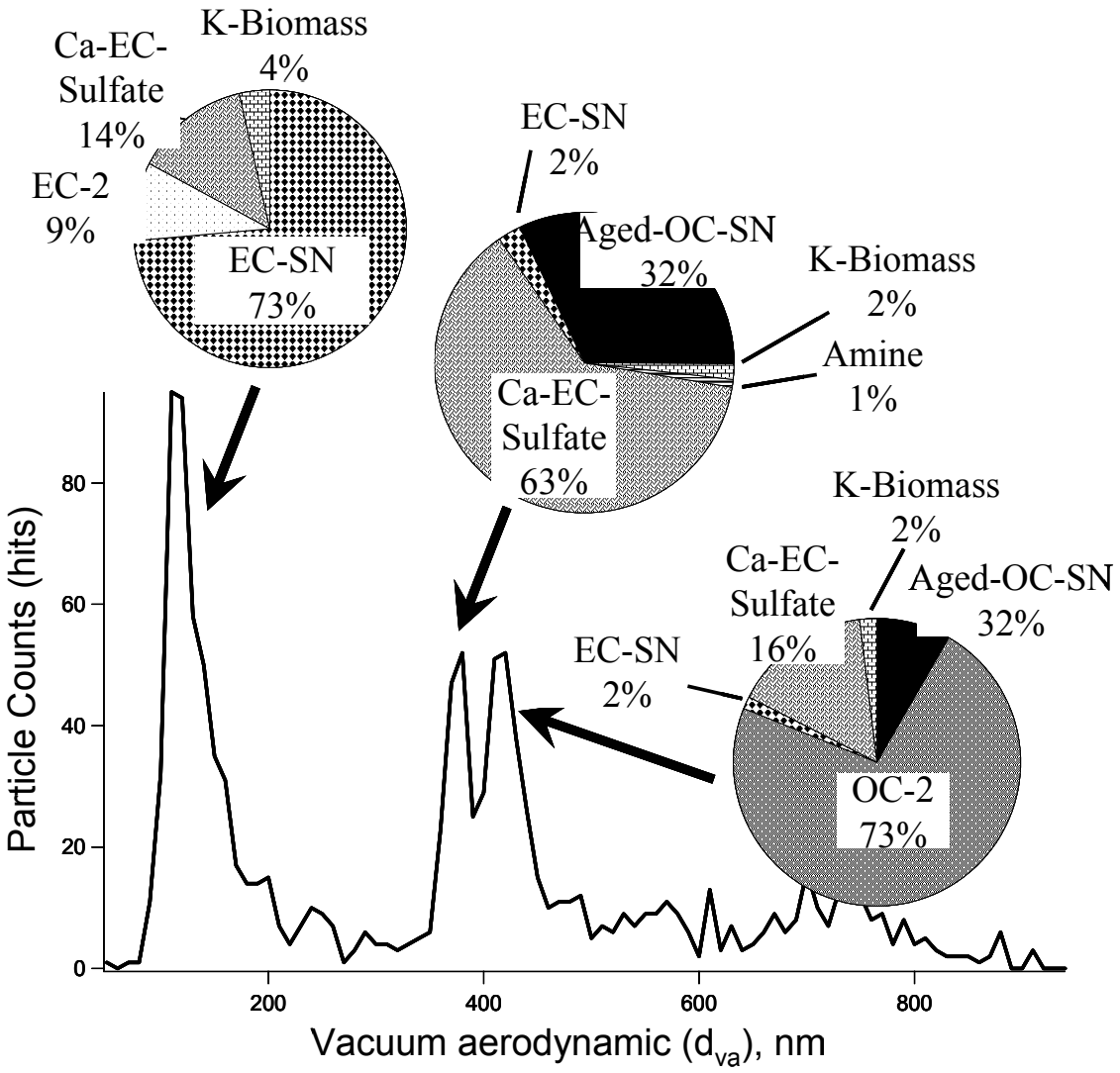

Figure 4.10 Vacuum aerodynamic size distribution of 450 nm electrical mobility size selected ambient particles from Riverside, California on November 21. Inset pie charts show the fraction of different particle chemical classes within each vacuum aerodynamic size mode.

particles with a highly irregular shape. EC particles have been shown to consist of agglomerated primary spherules that yield branched irregularly shaped particles [*Wentzel et al.*, 2003]. The aerodynamic size mode at ~390 nm contains 63% and 32% of the Ca-EC-sulfate and aged-OC particle types respectively. Used automotive oil particles have mass spectral (chemical) signatures very similar to the Ca-EC-sulfate particle type [*Shields et al.*, 2006; *Spencer et al.*, 2006]. Automotive oil particles are likely spherical in shape and thus effective density will equal the material density. The effective density of the particles at 390 nm d_{va} is ~ 0.87 g cm^{-3}, which is similar to the density of automotive oil (0.85-0.95 g cm^{-3}) [*ExxonMobil.com*, Accessed 2005]. Particles in the aerodynamic size mode centered at 450 nm d_{va} have an effective density of 0.93 g cm^{-3} and contain 73%, 16% and 8% of the OC-2, Ca-EC-sulfate and aged-OC particle types respectively. OC-2 is characterized by ions at *m/z* 57^{+} and 59^{+} which are not present in aged-OC particle types. Similar results were observed for the 175 nm size selected particles.

Unlike the 250 nm electrical mobility size selected particles in July-August, the three aerodynamic modes observed for 450 nm electrical mobility selected particles in November each contain a significant fraction of different particle types. This observation suggests the different size modes for the 450 nm electrical mobility selected particles are not from different particle charge states, but rather from chemically distinct particles with different shapes and/or densities. This also highlights the potentially large difference between mobility and aerodynamic diameter: elemental carbon particles with a 400 nm mobility diameter have a 100 nm vacuum aerodynamic diameter. To properly scale the aerodynamic size distribution of an instrument such as the ATOFMS using SMPS

particle number data, this significant size difference for EC particles must be properly taken into account.

There was a Santa Ana wind episode during the November sampling period. These wind episodes are characterized by a shift in wind pattern from onshore to offshore flow; bringing clean air and particles from the desert regions into Riverside, CA. Santa Ana events change the air mass, which leads to the presence of particle types that are not observed the majority of the time [*Guazzotti et al.*, 2001]. Particles in the fall are not as aged as those in the summer due to the less polluted conditions. Thus, the fall particle types retain the distinct densities and shapes of freshly emitted (i.e. non-aged) particles. Therefore, the differences between the July-August and November measurements strongly reflect the effects of seasonal meteorological and air quality differences on the physical and chemical properties of ambient aerosols in Riverside, CA.

4.5 Acknowledgements

The authors thank Xueying Qin for helping set up instrumentation during SOAR. Professor Allen Goldstein and his research group (Megan McKay, Angela Miller and Brent Williams) from University of California at Berkeley for making the relative humidity and atmospheric water content measurements.

4.6 References

Allen, M.D., and O.G. Raabe, Slip correction measurements of spherical solid aerosol-particles in an improved Millikan apparatus, *Aerosol Sci. Technol.*, *4* (3), 269-286, 1985.

Angelino, S., D.T. Suess, and K.A. Prather, Formation of aerosol particles from reactions of secondary and tertiary alkylamines: Characterization by aerosol time-of-flight mass spectrometry, *Environ. Sci. Technol.*, *35* (15), 3130-3138, 2001.

Cai, Y., A. Zelenyuk, and D. Imre, A high resolution study of the effect of morphology on the mass spectra of single PSL particles with Na-containing layers and nodules, *Aerosol Sci. Technol.*, *40* (12), 1111-1122, 2006.

California-Air-Resource-Board, Riverside-rubidoux: Beta attenuation monitor (BAM) PM 2.5, in *www.arb.ca.gov*, edited by A.Q.M.D.A. 061, California Air Resource Board, Accessed 2006.

Colberg, C.A., U.K. Krieger, and T. Peter, Morphological investigations of single levitated H2SO4/NH3/H2O aerosol particles during deliquescence/efflorescence experiments, *J. Phys. Chem. A*, *108* (14), 2700-2709, 2004.

Cruz, C.N., and S.N. Pandis, A study of the ability of pure secondary organic aerosol to act as cloud condensation nuclei, *Atmos. Environ.*, *31* (15), 2205, 1997.

DeCarlo, P.F., J.G. Slowik, D.R. Worsnop, P. Davidovits, and J.L. Jimenez, Particle morphology and density characterization by combined mobility and aerodynamic diameter measurements. Part 1: Theory, *Aerosol Sci. Technol.*, *38* (12), 1185-1205, 2004.

Dockery, D.W., and C.A. Pope, Acute respiratory effects of particulate air pollution, *Annual review of public health*, *15*, 107-32., 1994.

ExxonMobil.com, Material safety data sheet 15w-40, in *http://www.Host1.Exxonmobil.Com/psims/psims.Aspx*, Accessed 2005.

Guazzotti, S.A., J.R. Whiteaker, D. Suess, K.R. Coffee, and K.A. Prather, Real-time measurements of the chemical composition of size-resolved particles during a Santa Ana wind episode, California USA, *Atmos. Environ.*, *35* (19), 3229-3240, 2001.

Hesterberg, T.W., G.A. Hart, J. Chevalier, W.C. Miiller, R.D. Hamilton, J. Bauer, and P. Thevenaz, The importance of fiber biopersistence and lung dose in determining the chronic inhalation effects of x607, rcf1, and chrysotile asbestos in rats, *Toxicol. Appl. Pharmacol.*, *153* (1), 68-82, 1998.

Hopke, P.K., and X.H. Song, Classification of single particles by neural networks based on the computer-controlled scanning electron microscopy data, *Anal. Chim. Acta*, *348* (1-3), 375-388, 1997.

Hughes, L.S., J.O. Allen, P. Bhave, M.J. Kleeman, G.R. Cass, D.Y. Liu, D.P. Fergenson, B.D. Morrical, and K.A. Prather, Evolution of atmospheric particles along trajectories crossing the Los Angeles basin, *Environ. Sci. Technol.*, *34* (15), 3058-3068, 2000.

Jacobson, M.Z., Analysis of aerosol interactions with numerical techniques for solving coagulation, nucleation, condensation, dissolution, and reversible chemistry among multiple size distributions, *J. Geophys. Res.*, *107* (D19), -, 2002.

Jimenez, J.L., Study of organic aerosols in Riverside, *http://cires.colorado.edu/jimenez-group/Field/Riverside05/*, Accessed 2006.

Jimenez, J.L., R. Bahreini, D.R. Cocker, H. Zhuang, V. Varutbangkul, R.C. Flagan, J.H. Seinfeld, C.D. O'Dowd, and T. Hoffmann, New particle formation from photooxidation of diiodomethane (CH2I2), *J. Geophys. Res.*, *108* (D10), 2003.

Katrib, Y., S.T. Martin, Y. Rudich, P. Davidovits, J.T. Jayne, and D.R. Worsnop, Density changes of aerosol particles as a result of chemical reaction, *Atmos. Chem. Phys.*, *5*, 275-291, 2005.

Knutson, E.O., and K.T. Whitby, Aerosol classification by electric mobility: Apparatus, theory, and applications, *J. Aerosol Sci.*, *6*, 443-451, 1976.

Lake, D.A., M.P. Tolocka, M.V. Johnston, and A.S. Wexler, Mass spectrometry of individual particles between 50 and 750 nm in diameter at the Baltimore supersite, *Environ. Sci. Technol.*, *37* (15), 3268-3274, 2003.

Liao, H., and J.H. Seinfeld, Global impacts of gas-phase chemistry-aerosol interactions on direct radiative forcing by anthropogenic aerosols and ozone, *J. Geophys. Res.*, *110* (D18), 2005.

Lide, R.D., *CRC handbook of chemistry and physics*, Florida, 2002.

Liu, D.-Y., K.A. Prather, and S.V. Hering, Variations in the size and chemical composition of nitrate-containing particles in Riverside, CA, *Aerosol Sci. Technol.*, *33* (1-2), 71-86, 2000a.

Liu, D.Y., K.A. Prather, and S.V. Hering, Variations in the size and chemical composition of nitrate-containing particles in Riverside, CA, *Aerosol Sci. Technol.*, *33* (1-2), 71-86, 2000b.

McMurry, P.H., X. Wang, K. Park, and K. Ehara, The relationship between mass and mobility for atmospheric particles: A new technique for measuring particle density, *Aerosol Science & Technology*, *36* (2), 227-238, 2002.

Moffet, R.C., and K.A. Prather, Extending ATOFMS measurements to include refractive index and density, *Anal. Chem.*, *77* (20), 6535-6541, 2005.

Molina, M.J., A.V. Ivanov, S. Trakhtenberg, and L.T. Molina, Atmospheric evolution of organic aerosol, *Geophys. Res. Lett.*, *31* (22), 2004.

Murphy, D.M., D.J. Cziczo, P.K. Hudson, M.E. Schein, and D.S. Thomson, Particle density inferred from simultaneous optical and aerodynamic diameters sorted by composition, *J. Aerosol Sci.*, *35* (1), 135-139, 2004.

Novakov, T., and C.E. Corrigan, Cloud condensation nucleus activity of the organic component of biomass smoke particles, *Geophys. Res. Lett.*, *23* (16), 2141-2144, 1996.

Oberdorster, G., J. Ferin, and B.E. Lehnert, Correlation between particle-size, in-vivo particle persistence, and lung injury, *Environ. Health Perspect.*, *102*, 173-179, 1994.

Pankow, J.F., An absorption-model of the gas aerosol partitioning involved in the formation of secondary organic aerosol, *Atmos. Environ.*, *28* (2), 189-193, 1994.

Park, K., F. Cao, D.B. Kittelson, and P.H. McMurry, Relationship between particle mass and mobility for diesel exhaust particles, *Environmental Science & Technology*, *37* (3), 577-583, 2003.

Pastor, S.H., J.O. Allen, L.S. Hughes, P. Bhave, G.R. Cass, and K.A. Prather, Ambient single particle analysis in Riverside, California by aerosol time-of-flight mass spectrometry during the SCOS97-NARSTO, *Atmos. Environ.*, *37* (Suppl. 2), 239-258, 2003.

Pauluhn, J., Acute inhalation studies with irritant aerosols: Technical issues and relevance for risk characterization, *Arch. Toxicol.*, *78* (5), 243-251, 2004.

Ramana, M.V., V. Ramanathan, I.A. Podgorny, B.B. Pradhan, and B. Shrestha, The direct observations of large aerosol radiative forcing in the Himalayan region, *Geophys. Res. Lett.*, *31* (5), 5111, 2004.

Ramanathan, V., C. Chung, D. Kim, T. Bettge, L. Buja, J.T. Kiehl, W.M. Washington, Q. Fu, D.R. Sikka, and M. Wild, Atmospheric brown clouds: Impacts on south Asian climate and hydrological cycle, *Proc. Natl. Acad. Sci. U. S. A.*, *102* (15), 5326-5333, 2005.

Sardar, S.B., P.M. Fine, P.R. Mayo, and C. Sioutas, Size-fractionated measurements of ambient ultrafine particle chemical composition in Los Angeles using the nanoMOUDI, *39* (4), 932-944, 2005.

Saxena, P., L.M. Hildemann, P.H. McMurry, and J.H. Seinfeld, Organics alter hygroscopic behavior of atmospheric particles, *J. Geophys. Res.*, *100* (D9), 18755-18770, 1995.

Schlenker, J.C., and S.T. Martin, Crystallization pathways of sulfate-nitrate-ammonium aerosol particles, *J. Phys. Chem. A*, *109* (44), 9980-9985, 2005.

Shields, L.G., D.T. Suess, S.A. Guazzotti, and K.A. Prather, Determination of single particle mass spectral signatures from heavy duty vehicle emissions, *Atmos. Environ.*, *accepted*, 2006.

Silva, P.J., and K.A. Prather, Interpretation of mass spectra from organic compounds in aerosol time-of-flight mass spectrometry, *Anal. Chem.*, *72* (15), 3553-3562, 2000.

Slowik, J.G., K. Stainken, P. Davidovits, L.R. Williams, J.T. Jayne, C.E. Kolb, D.R. Worsnop, Y. Rudich, P.F. DeCarlo, and J.L. Jimenez, Particle morphology and density characterization by combined mobility and aerodynamic diameter measurements. Part 2: Application to combustion-generated soot aerosols as a function of fuel equivalence ratio, *Aerosol Sci. Technol.*, *38* (12), 1206-1222, 2004.

Sodeman, D.A., S.M. Toner, and K.A. Prather, Determination of single particle mass spectral signatures from light duty vehicle emissions, *Environmental Science & Technology*, *39* (12), 4569-4580, 2005.

Song, X.-H., P.K. Hopke, D.P. Fergenson, and K.A. Prather, Classification of single particles analyzed by ATOFMS using an artificial neural network, ART-2a, *Anal. Chem.*, *71* (4), 860-865, 1999.

Spencer, M.T., and K.A. Prather, Using ATOFMS to determine OC/EC mass fractions in particles, *Aerosol Sci. Technol.*, *40* (8), 585-594, 2006.

Spencer, M.T., L.G. Shields, D.A. Sodeman, S.M. Toner, and K.A. Prather, Comparison of oil and fuel particle chemical signatures with particle emissions from heavy and light duty vehicles, *Atmos. Environ.*, *40* (27), 5224-5235, 2006.

Su, Y., M.F. Sipin, H. Furutani, and K.A. Prather, Development and characterization of an aerosol time-of-flight mass spectrometer with increased detection efficiency, *Anal. Chem.*, *76* (3), 712-719, 2004.

Van Gulijk, C., J.C.M. Marijnissen, M. Makkee, J.A. Moulijn, and A. Schmidt-Ott, Measuring diesel soot with a scanning mobility particle sizer and an electrical low-pressure impactor: Performance assessment with a model for fractal-like agglomerates, *J. Aerosol Sci.*, *35* (5), 633-655, 2004.

Weingartner, E., H. Burtscher, and U. Baltensperger, Hygroscopic properties of carbon and diesel soot particles, *Atmos. Environ.*, *31* (15), 2311-2327, 1997.

Wentzel, M., H. Gorzawski, K.H. Naumann, H. Saathoff, and S. Weinbruch, Transmission electron microscopical and aerosol dynamical characterization of soot aerosols, *J. Aerosol Sci.*, *34* (10), 1347-1370, 2003.

Zelenyuk, A., Y. Cai, L. Chieffo, and D. Imre, High precision density measurements of single particles: The density of metastable phases, *Aerosol Sci. Technol.*, *39* (10), 972-986, 2005.

Zelenyuk, A., Y. Cai, and D. Imre, From agglomerates of spheres to irregularly shaped particles: Determination of dynamic shape factors from measurements of mobility and vacuum aerodynamic diameters, *Aerosol Sci. Technol.*, *40* (3), 197-217, 2006a.

Zelenyuk, A., and D. Imre, Single particle laser ablation time-of-flight mass spectrometer: An introduction to SPLAT, *Aerosol Sci. Technol.*, *39* (6), 554-568, 2005.

Zelenyuk, A., D. Imre, and L.A. Cuadra-Rodriguez, Evaporation of water from particles in the aerodynamic lens inlet: An experimental study, *Anal. Chem.*, *78* (19), 6942-6947, 2006b.

Zhang, Q., M.R. Alfarra, D.R. Worsnop, J.D. Allan, H. Coe, M.R. Canagaratna, and J.L. Jimenez, Deconvolution and quantification of hydrocarbon-like and oxygenated organic aerosols based on aerosol mass spectrometry, *Environmental Science & Technology*, *39* (13), 4938-4952, 2005.

5 Size-resolved Chemical Composition of Aerosol Particles During a Monsoonal Transition Period over the Indian Ocean

5.1 Synopsis

An aerosol time-of-flight mass spectrometer (ATOFMS) was used to measure the size-resolved mixing state of particles in the North Indian Ocean in October and November 2004. This period was chosen to observe the impact of the monsoonal transition on aerosol size, chemistry, sources, and radiative properties. Overall, elemental carbon with sulfate (EC-sulfate), K-biomass, fresh sea salt (SS), aged sea salt, fly ash, and EC mixed with sea salt were the dominant supermicron particle types, whereas EC-sulfate, K-biomass, and fly ash were the dominant submicron particle types. Interestingly, nominally pure aged organic carbon particles and particles containing nitrate were virtually absent during the campaign. This can be explained by high VOC/NO_x ratio from 2 stroke engines and hence low ozone formation in the region or selective scavenging during transport. Notably, during long range transport periods when an aethalometer measured the highest black carbon concentrations, 77% of the submicron particles and 71% of EC/soot particles contained an intense $^{39}K^+$ ion (a known tracer for biomass/biofuel). These observations suggest when the air mass originates from India,

biofuel combustion can be a significant source of the regional atmospheric brown cloud. The majority (~80%) of EC and K-biomass particles were mixed with significant amounts of sulfate due to extensive secondary processing of these particles during transport. EC mixed with sea salt was also observed suggesting they had undergone cloud processing and become internally mixed during transport. These measurements support the use of an internal mixture of sulfate with EC/soot and biomass in models to accurately calculate radiative forcing by aerosol in this region.

5.2 Introduction

Predicting the effect of air pollution on climate change is critical for hedging increasing world economic growth with environmental impacts from rising global air pollution. Large uncertainties still remain in accurately predicting the effects aerosol particles have on the hydrological cycle, direct and indirect radiative forcing, and overall climate change [*Chen and Penner*, 2005; *IPCC*, 2001; *Knutti et al.*, 2002; *Lohmann and Feichter*, 2005; *Morgan et al.*, 2006; *Ramanathan et al.*, 2005]. A large fraction of this uncertainty stems from limited information on the chemical composition and mixing state of particles in the atmosphere [*Chandra et al.*, 2004; *IPCC*, 2001; *Jacobson*, 2001; *Lohmann and Feichter*, 2005; *Myhre et al.*, 2004; *Schwartz*, 2004]. As an air mass ages, changes in particle chemical composition and mixing state further complicate predicting aerosols' effect on climate. Sulfate can decrease atmospheric absorption by increasing the hydrophilic nature of soot particles, thus increasing their wet removal rate. Many research groups, including most recently Stier et al., have shown that internally mixed elemental carbon-sulfate particles will increase atmospheric absorption by increasing a

particle's absorption efficiency [see *Stier et al.*, 2006 and references therein]. To quantify the direct climate forcing of aerosol particles, it is essential to understand the dynamic nature of particle chemical composition and mixing state.

Project Atmospheric Brown Cloud (ABC) was designed to monitor changes in aerosol chemical composition, optical depth, radiative forcing and cloud properties within the Indo-Asian and Pacific regions (http://www-abc-asia.ucsd.edu). The goals of the ABC project involve using data collected from climate observatories for input into climate models to help increase their predictive power and better understand the environmental impact of rising air pollution on a regional and global scale. Specifically, ABC aims to address the significance of environmental changes due to rising air pollution in the Indo-Asian and Pacific region. Climate observatories are being operated on a long term basis (2004-2008), with intermittent intense aerosol characterization periods at select observatory sites. This paper describes measurements made at the first operational ABC climate observatory, which lies in the Northern Indian Ocean on Hanimaadhoo Island, Republic of Maldives. The Northern Indian Ocean experiences an annual monsoonal transition in the month of October. This transition period is characterized by a shift in regional wind pattern from a southwesterly to a northeasterly flow [*Kripalani and Kumar*, 2004]. During the transition period, the regional air mass fluctuates until the dry monsoon period when there is a dominant northeasterly flow [*Ramana and Ramanathan*, 2006]. This northeasterly flow carries air pollution from Asia over the relatively unpolluted Indian Ocean [*Guazzotti et al.*, 2001; *Guazzotti et al.*, 2003; *Neususs et al.*, 2002; *Quinn et al.*, 2002; *Reiner et al.*, 2001]. Thus, the transition period offers a unique opportunity to monitor and compare aerosol physical/chemical properties,

cloud physical/chemical properties and radiation flux, as air pollution is transported into the unpolluted North Indian Ocean. The ABC Post Monsoonal Experiment (APMEX) was an intensive aerosol characterization experiment that took place during this transition period (October 15-November 5, 2004) at the Republic of Maldives Climate Observatory on Hanimaadhoo Island (MCOH).

During APMEX, an aerosol time-of-flight mass spectrometer (ATOFMS), aethalometer, nephelometer, aerosol particle sizer (APS), scanning mobility particle sizer (SMPS), and a suite of solar radiation instrumentation were operated at MCOH [*Corrigan et al.*, 2006; *Ramana and Ramanathan*, 2006]. This paper focuses on results obtained with ATOFMS during APMEX. A more detailed discussion of other instrumentation operated during the APMEX campaign has been published [*Corrigan et al.*, 2006; *Ramana and Ramanathan*, 2006].

The ATOFMS used in this study measures the aerodynamic size (0.3-2.5 μm) and chemical composition of individual particles in real time. A general discussion of the particle chemical composition and mixing state during the campaign is presented along with a discussion of the air mass back trajectories to identify particle source locations. The trajectories are then correlated with the temporal evolution of the chemically different particle types observed for the duration of the study. In future work, these results can be combined with solar radiation measurements to help advance our understanding of the major sources and processes contributing to the aerosol radiative forcing in this region of the world.

5.3 Experimental

5.3.1 Location

Measurements were made from 15-October-2004 through 05-November-2004 on the island of Hanimaadhoo (6.776°N, 73.183°E), Republic of Maldives. Hanimaadhoo Island is approximately 4 km (north-south) by 1 km (east-west) in size. There are approximately 1200 residents on the island. The MCOH observatory is located at the northern tip of the island where the prevailing winds come from over the ocean. The majority of the island's residents live approximately 2 km south of the observatory; therefore local pollution sources are minimal.

5.3.2 Aerosol characterization instrumentation

Ambient aerosol particles were sampled from a 15 meter high, 20 cm diameter sampling mast with laminar flow. The sampling mast entered a temperature controlled room in the MCOH. This room was kept at ambient temperature to sample particles at ambient relative humidity (RH) and prevent condensation or evaporation during particle measurements. Aerodynamic particle sizer, mobility particle sizer, total particle counter, aethalometer, and nephelometer instruments were located within the ambient temperature room. A more detailed description of the MCOH observatory has been published previously [*Corrigan et al.*, 2006]. The ATOFMS was located in an air conditioned room adjacent to the ambient temperature room. A one meter-long piece of insulated sampling line was used between the ambient temperature sampling mast and the ATOFMS. Particle losses due to gravitational settling during transport from the exit of

the sampling mast to the ATOFMS were estimated to be less than 5 % for 2.5 μm particles with a density of 1.0 $g \cdot cm^{-3}$.

Filter based samples were collected at the top of the 15 meter tower every 24 hours. A detailed discussion of the methods used and overall results for the filter based data is given by Stone et al. [*Stone et al.*, 2007]. The nephelometer data was corrected for truncation errors and other measurement errors using the method outlined in Anderson and Ogren [*Anderson and Ogren*, 1998]. The black carbon and absorption data obtained from the aethalometer were corrected using the approach presented in Arnott et al.[*Arnott et al.*, 2005].

The aerodynamic size and chemical composition of individual particles (0.3-3.0 μm) was measured using a transportable aerosol time-of-flight mass spectrometer (ATOFMS). A detailed description of the ATOFMS has been published previously and is also given in Chapter 1 [*Gard et al.*, 1997; *Prather et al.*, 1994]. Aerosol enters into the vacuum pumped ATOFMS through a converging nozzle inlet at a flow of ~0.96 lpm. Upon entering the ATOFMS, aerosol gasses undergo a supersonic expansion due to a drop in pressure from ~760 to ~3 Torr. This gas expansion accelerates particles to a terminal velocity based on the aerodynamic size of the particle (smaller particles are accelerated to a faster terminal velocity). After this acceleration, particles pass through two skimmers where a large fraction of the associated gasses are pumped away. Particles then pass through two vertically separated (6 cm) continuous wave (CW) lasers. Light scattered by each particle as it passes through the CW lasers is detected with a photomultiplier tube (PMT). The difference in time between the two PMT signals is used to measure the velocity of the particle, and ultimately the aerodynamic size. The

measured particle velocity is then used to calculate the precise time the particle is within the source region of a dual ion time-of-flight mass spectrometer. At the precise time a particle enters the ion source region, a Q-switched YAG laser operated at λ = 266 nm with an 8 ns pulse length and 400 μm spot diameter is fired at the particle. Positive and negative ions formed from laser ablation/ionization of the particle are detected using a dual ion time-of-flight mass spectrometer.

5.3.3 Data analysis

ATOFMS data were imported into Matlab 6.5.1 (The Math Works, Inc.) using YAADA version 1.2 (http://www.yaada.com). Portions of the YAADA toolkit were also used for data analysis. Particle chemical classes were derived by clustering individual particle mass spectra together using an Adaptive Resonance Theory neural network (ART-2a) [*Hopke and Song*, 1997; *Song et al.*, 1999]. Similarities between individual mass spectra (using the presence and intensity of ion peaks) are calculated using ART-2a. Mass spectra that have a similarity above a set threshold (vigilance factor) are clustered together and considered chemically similar. The ART-2a parameters used for chemical classification were: learning rate = 0.05, vigilance factor = 0.85 and iterations = 20. Approximately 380,000 unique particles (mass spectra) were analyzed using ART-2a which yielded ~320 unique clusters. Only the 60 most populated clusters were used in this analysis, however these 60 clusters contain over 92% of all the mass spectra. Although these 60 clusters are unique with regard to each other by ART-2a analysis, many of the clusters exhibit a similar dominant ion pattern when compared to other clusters by visual inspection. For example, it is not uncommon to find numerous clusters

that each consists of mass spectra with dominant elemental carbon ions (^{12}C, $^{24}C_2$…$C_n^{+/-}$) and an intense $^{97}HSO_4$-. Small differences in peak ratios or a miscalibrated peak are a couple reasons why ART-2a (and other clustering algorithms) generates unique but similar looking clusters {Rebotier, 2007 #2172}. Clusters are grouped into the same chemical class when only minor differences in their mass spectral ion intensity patterns are observed by visual inspection. Using this method the top 60 clusters were refined into 8 chemical classes.

Relative area matrices for different particle chemical classes were generated using the most populated cluster within a chemical class. Relative area matrices are created by normalizing each mass spectrum to the most intense ion peak in the spectrum and then averaging together all normalized individual mass spectra within the cluster. In general, the relative area matrix resembles an individual particle mass spectrum within a particle class.

5.4 Results and discussion

Comparing the number of ATOFMS hit particles (< 2.5 μm) versus the particle number concentration measured with an APS (< 2.5 μm) can be used to validate whether particles analyzed using ATOFMS track the majority of ambient particle concentrations between 0.3 and 2.5 μm. Figure 5.1 shows the time series of ATOFMS particle counts (hit particles only) on the left axis and the particle number concentration (particles/cubic centimeter) measured by an APS on the right axis, with one hour time resolution.

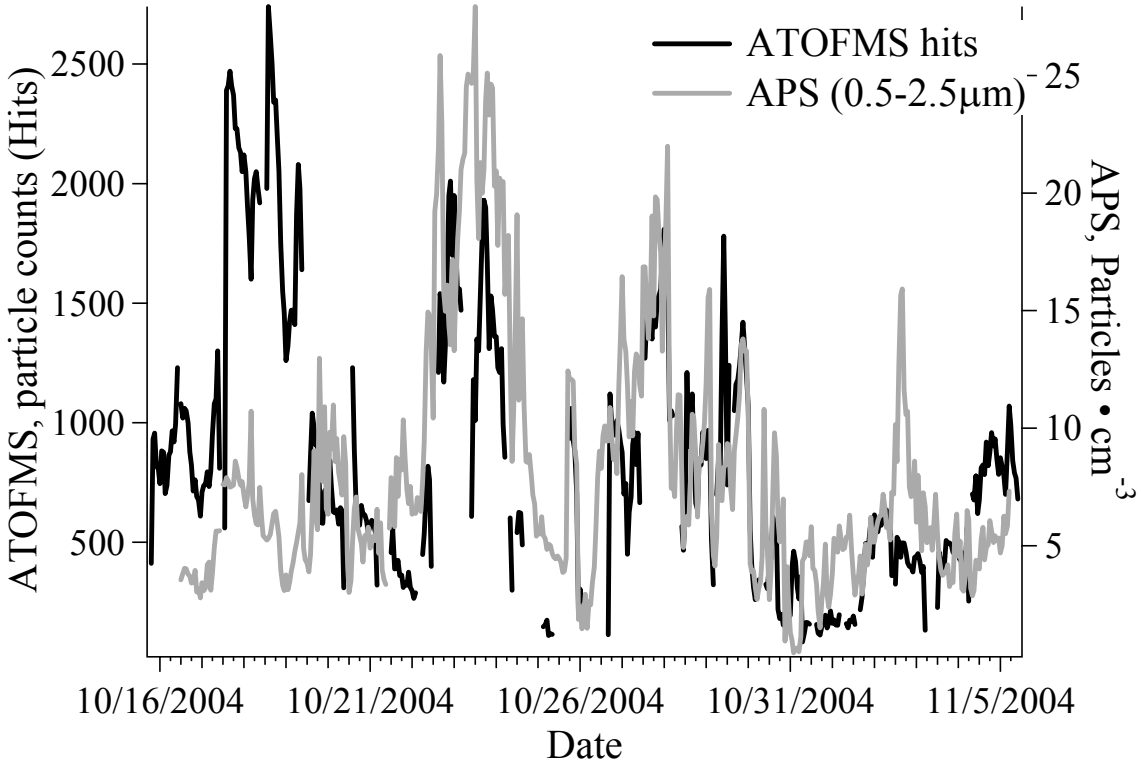

Figure 5.1 Comparison of the number of particles analyzed (hit) using ATOFMS (left y-axis) and the number of particles per cubic centimeter measured using an APS (right y-axis) for the duration of the APMEX field campaign (x-axis).

In general, the ATOFMS particle counts track (with different magnitudes) the APS particle concentration throughout the study; however there are a few exceptions. From October 16-20, the ATOFMS detected a relatively high number of particles, and on October 22, October 27, and November 2-3 the APS shows a sharp spike in particle concentration while the ATOFMS counts actually decrease. Excluding the anomalous periods from October 16-20 and the sharp spike on November 2-3, a correlation between the APS and ATOFMS hit particles gives an $R^2 \sim 0.52$.

As will be discussed later, from October 16-20 there was a large fraction of supermicron fly-ash particles. The ATOFMS is sensitive to fly ash particles because they are easily desorbed/ionized by the ionization laser. From October 16-20 the percentage of all scattered particles that generated a mass spectrum (% hit particles) was ~20%. For comparison, the average percentage of hit particles from October 20-November 1 was ~8%. This suggests the ATOFMS has a chemical bias that enhanced the concentrations of fly ash by about 2.5 times compared to other particle types during this first time period. As discussed later, this bias must be taken into account when scaling the ATOFMS data [*Wenzel et al.*, 2003].

During the other bias periods on October 22, October 27, and November 2-3 the APS shows a spike in particle number concentrations while the ATOFMS shows a decrease in hit particles. The percentage of hit particles decreases by ~50%. As will be shown later, during this period, aethalometer absorption measurements decrease while the scattering coefficient (b_{sp}) increases as measured with a nephelometer. The number of particle scatters measured with the ATOFMS, particles which are sized but do not produce mass spectra, track the nephelometer data (not shown). The coupled increase in

the scattering coefficient and number of ATOFMS scatters, along with a subsequent decrease in the absorptivity of the aerosol and fraction of ATOFMS hit particles is used to indicate the presence of a "missed" particle type. Wenzel et al. observed a missed particle type using ATOFMS in Atlanta Georgia and through comparison with other measurements concluded the particles to be composed of pure ammonium sulfate [*Wenzel et al.*, 2003]. Ammonium sulfate does not absorb laser radiation from the ionization laser (266 nm), thus the ATOFMS is not as sensitive to ammonium sulfate particles and does not detect them as efficiently as other particle types [*Thomson et al.*, 1997]. Wenzel et al. also observed that the missed particles became increasingly abundant in the smallest detectable size range of the ATOFMS used in that study (between 0.3-0.5 μm). The missed particle types observed here are observed across a much broader size range (0.6-2.0 μm), with the lowest hit percentage between ~1.0-1.5 μm. The composition of the missed particles during these time periods is therefore only speculative; however they are non-absorbing and have a broad size distribution into the supermicron range. Due to the larger size of the missed particle type, another possibility is that these could be wet sea salt. If however the missing particle type is ammonium sulfate, this is one of the rare times where nominally pure sulfate particles in these large sizes are observed. The majority of measurements with the ATOFMS for this study show the sulfate mixed with biomass and EC or soot particles.

5.4.1 Chemical composition

Eight major particle types were observed during the APMEX field campaign: fresh sea salt (Fresh-SS), aged sea salt (Aged-SS), elemental carbon with sea salt (EC-SS), elemental carbon with sulfate (EC-sulfate), fly ash, potassium-biomass (K-biomass),

organic carbon (OC), and calcium-dust (Ca-dust). An area matrix for each of these particle types is given in Figure 5.2 and a brief description of each type follows. Fresh-SS is characterized by ion peaks for $^{23}Na^+$, $^{81/83}Na_2Cl^+$, and $^{35/37}Cl^-$. In addition to the major peaks in Fresh-SS, Aged-SS contains intense ions at $^{46}NO_2^-$ and $^{62}NO_3^-$. EC-SS has sea salt marker ions and also carbon cluster ions ^{12}C, $^{24}C_2\ldots C_n^{+/-}$. EC-sulfate contains dual polarity carbon cluster ions (^{12}C, $^{24}C_2\ldots C_n^{+/-}$), a smaller $^{39}K^+$ peak as well as an intense peak for sulfate ($^{97}HSO_4^-$). Fly ash is characterized by ion peaks for $^{39}K^+$ along with $^7Li^+$, $^{23}Na^+$, $^{27}Al^+$, $^{46}NO_2^-$, $^{62}NO_3^-$, and $^{35/37}Cl^-$ [*Suess*, 2002, *Guazzotti et al.*, 2003]. K-biomass particles show intense $^{39}K^+$ and $^{97}HSO_4^-$ ions, as well as less intense OC marker ions such as $^{15}CH_3^+$, $^{27}C_2H_3^+$, $^{29}C_2H_5^+$, $^{43}C_2H_3O^+$, and EC marker ions (^{12}C, $^{24}C_2,\ldots C_n^{+/-}$) [*Silva et al.*, 1999]. The K-biomass particle class is a mixture of EC and OC. The OC particle class is characterized by OC marker ions: $^{15}CH_3^+$, $^{27}C_2H_3^+$, $^{29}C_2H_5^+$, $^{37}C_3H^+$, $^{43}C_2H_3O^+$, and ions at +77, and +91 which are generally attributed to fragment ions from phenyl-alkyl compounds; no negative ions were detected for this OC particle class. Ca-dust is characterized by an intense $^{40}Ca^+$, $^{57}CaOH^+$, $^{97}Ca_2O^+$, $^{17}OH^-$, $^{37}Cl^-$, $^{42}CNO^-$ and $^{46}NO2^-$.

The sulfate ion ($^{97}HSO_4^-$), observed mixed with EC and K-biomass particle types discussed above, was much more intense than has been observed in previous ATOFMS combustion source characterization studies [*Silva et al.*, 1999; *Sodeman et al.*, 2005; *Toner et al.*, 2006]. This intense sulfate ion signal suggests these particles have undergone significant secondary processing.

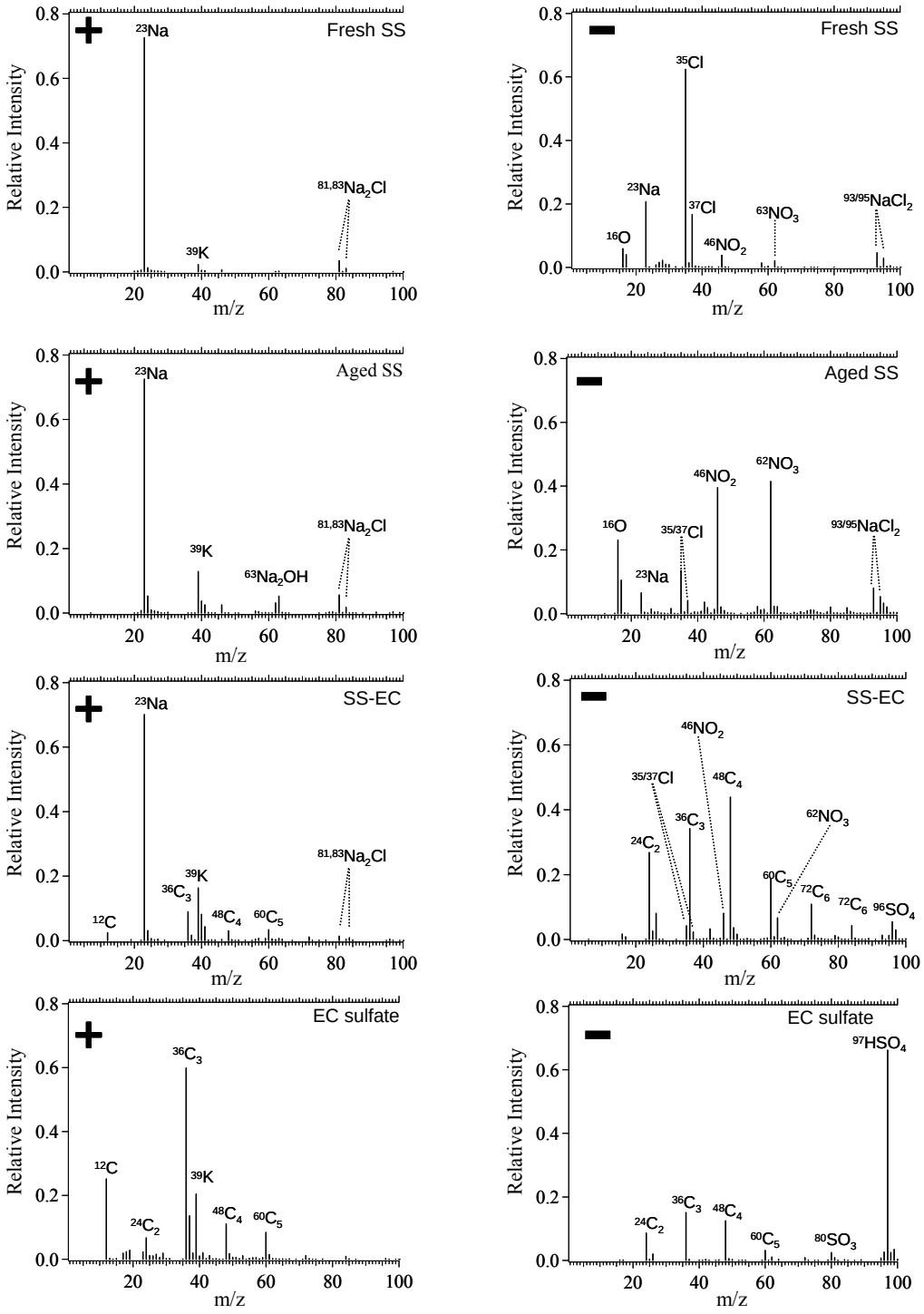

Figure 5.2 Area matrices for the top eight particle classes (Fresh-SS, Aged-SS, EC-SS, EC-sulfate, Fly ash, K-biomass, OC and Ca-dust) observed during APMEX.

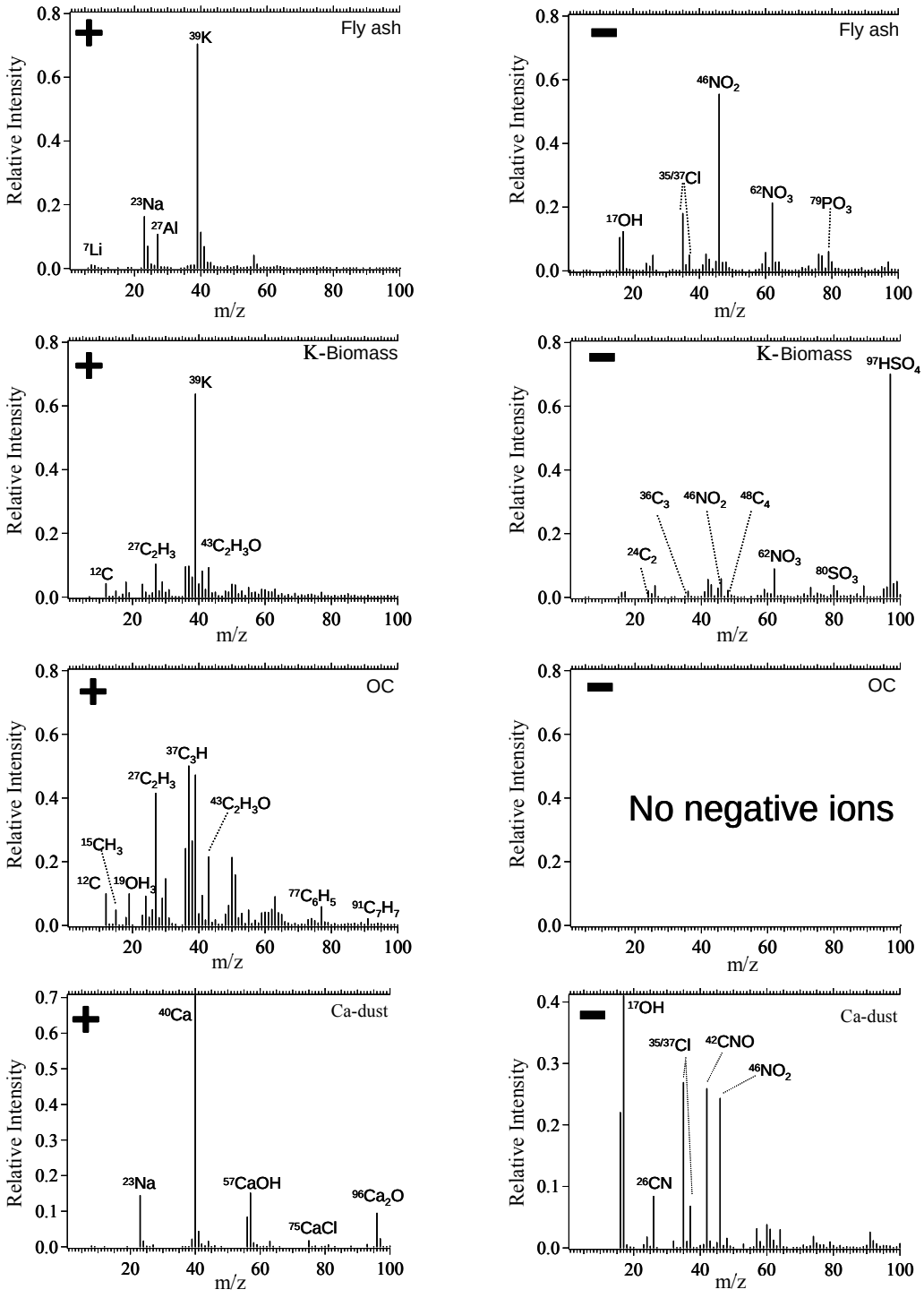

Figure 5.2, Continued.

Previous studies have shown that aerosols become internally mixed as they get further from the source [*Clarke et al.*, 2004]. Our results are consistent with this previous study as we detect EC/K-biomass and sulfate as internal mixtures far from the source. EC mixed with sulfate was also observed during INDOEX and has been observed over the mid latitudes of the North Pacific Ocean [*Alfaro et al.*, 2003; *Kaneyasu and Murayama*, 2000; *Neususs et al.*, 2002]. The presence of EC and sea salt within the same particle (EC-SS) suggests these particles have undergone coagulation most likely during cloud processing to become a mixed particle type. EC mixed with NaCl has been shown to act as a good cloud condensation nuclei (CCN) [*Dusek et al.*, 2006]. Light absorption by sulfate-coated or organic carbon-coated EC particles (EC core surrounded by sulfate or organic shell) has been shown to be 2-4 times higher then uncoated EC [*Bond et al.*, 2006; *Fuller et al.*, 1999; *Jacobson*, 2001; *Schnaiter et al.*, 2005]. Furthermore, during INDOEX, Neususs et al. observed an increase in the absorption effeciency with decreasing EC mass fraction and attributed this to increasing amounts of light scattering material on the EC particles [*Neususs et al.*, 2002]. The EC-sulfate, K-biomass and EC-SS particles described above could have this core-shell structure; however, this cannot be definitively determined with the current dataset. Complementary single particle measurements using techniques such as scanning electron microscopy might be able to help determine the actual physical state of these mixed particles. Simultaneous measurements of particle density and shape would also help unravel the physical state of these particles [*Moffet and Prather*, 2005; *Spencer et al.*, 2007]

Organic carbon and nitrate are two species which are commonly detected with ATOFMS in other regions of the world. Nominally pure OC, OC mixed with EC, and

particles containing significant amounts of nitrate were virtually absent (compared to other ATOFMS field campaigns) during APMEX. Filter based measurements also showed a low abundance of nitrate [*Stone et al.*, 2007]. As will be discussed later, much of the black carbon, sulfate, and K-biomass measured during APMEX originated from India. Dickerson et al. have shown that due to the large number of two stroke engines used in India, there is a large atmospheric VOC/NO_x ratio (220 ppm carbon/ppm NO_x) [*Dickerson et al.*, 2002]. The large amount of VOC and small amount of NO_x emitted from 2 stroke engines leads to NO_x limited ozone formation, and thus there is only modest amounts of ozone formed and lower levels of NO_x compared to concentrations normally encountered in western cities. Ozone concentrations have also been shown to be lower in the month of October in rural southeast India [*Debaje et al.*, 2003], and in general rarely exceed 100 ppb in the north Indian Ocean [*Lal et al.*, 2000; *Stehr et al.*, 2002]. These lower ozone concentrations could lead to less oxidation of VOC's and hence less secondary organic material condensing on primary particles such as EC before they are transported over the Indian Ocean. Furthermore, particles containing organic material and nitrate are possibly scavenged by clouds and rain during transport over the Indian Ocean. It should be noted that filter based methods did measure a significant fraction of PM < 2.5 μm OC (average~0.6 $\mu g \cdot m^{-3}$). It is likely that most of the filter-OC was mixed with biomass particles and marine aerosols. ATOFMS organic carbon ion signals are suppressed by intense inorganic ions such as Na and K generated from sea salt and K-biomass particles during laser ionization and thus organic material in these particle types are masked by the inorganic ions. ATOFMS measurements in a southern India

metropolitan area would be very useful to compare the differences between the primary sources and the chemically transformed particles measured at MCOH.

5.4.2 Temporal trends

Figure 5.3 shows HYSPLIT five day air mass back trajectories (500 and 1000 meters above ground level) representative of six distinct time periods where the particle chemical class fractions changed [*HYSPLIT*]. During these six different time periods, changes in the air mass back trajectories corresponded with changes in the chemical mixing state of the single particles. In Figure 5.3a, the HYSPLIT model shows the air mass coming from the west-northwest (long range transport-Arabian Sea) on October 17, 2004. Figure 5.3b and Figure 5.3d show that on October 22, 2004 and October 27, 2004 the air mass originated from the east-northeast (Southern India/ Sri Lanka). Figure 5.3c shows the air mass was coming from the east-southeast (Indian Ocean/ southern Sri Lanka) on October 25, 2004. Figure 5.3e shows the air mass was coming from the south (Indian Ocean/ Maldives) on October 31, 2004. Figure 5.3f shows the air mass was coming from the west-southwest (Indian Ocean) on November 5, 2004.

Figure 5.4a shows the supermicron (1.0-2.5 μm) time series of the fractions of different particle classes described above. Figure 5.4a represents approximately 90% of the supermicron particles clustered using ART-2a. Note that ~10% of the particles were unclassified (not shown in Figure 5.4a) and are made up of some mis-calibrated particles and small numbers of particles that generated unique looking mass spectra. Figure 5.4a shows the six distinct periods where there were significant changes in the chemistry of the supermicron sized particles; from October 15-20 (Period 1), October 20-24 (Period

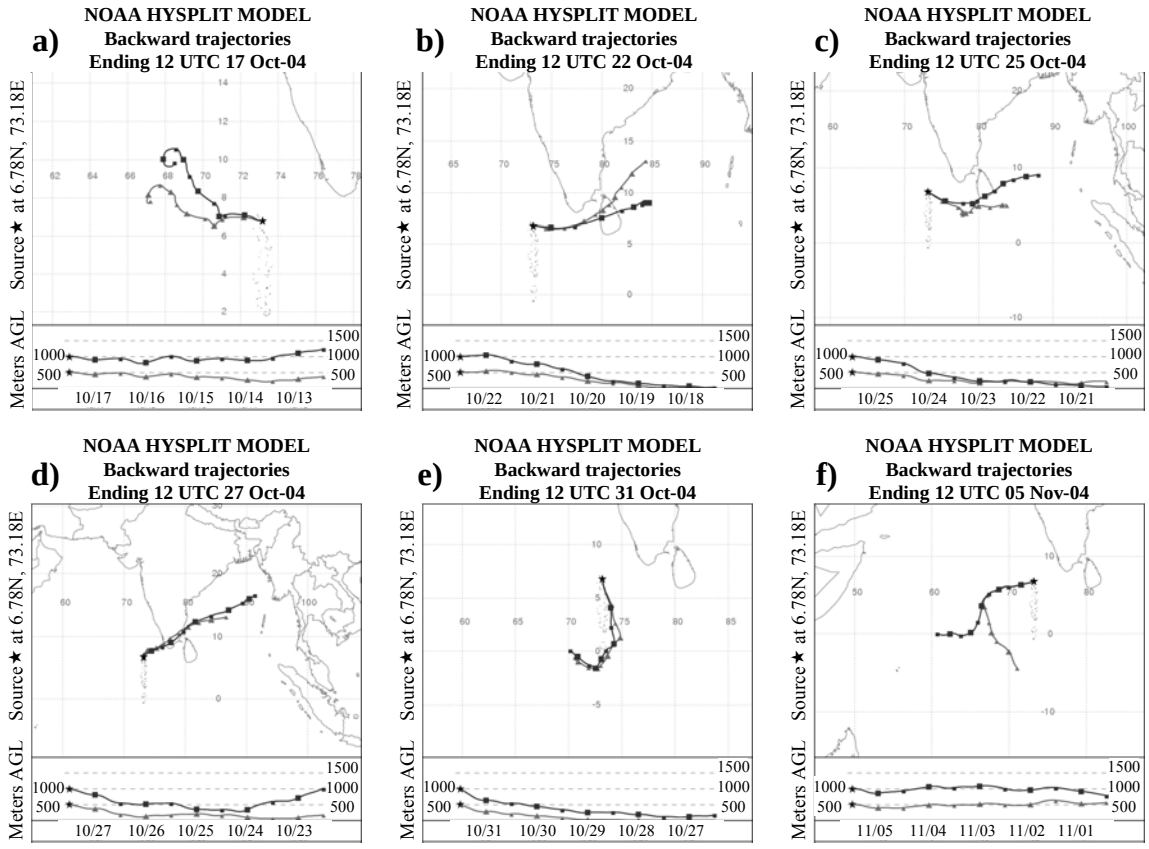

Figure 5.3 HYSPLIT back trajectories for six time periods during the APMEX campaign. a) October 17, 2004, b) October 22, 2004, c) October 25, 2004, d) October 27, 2004, e) October 31, 2004, f) November 05, 2004.

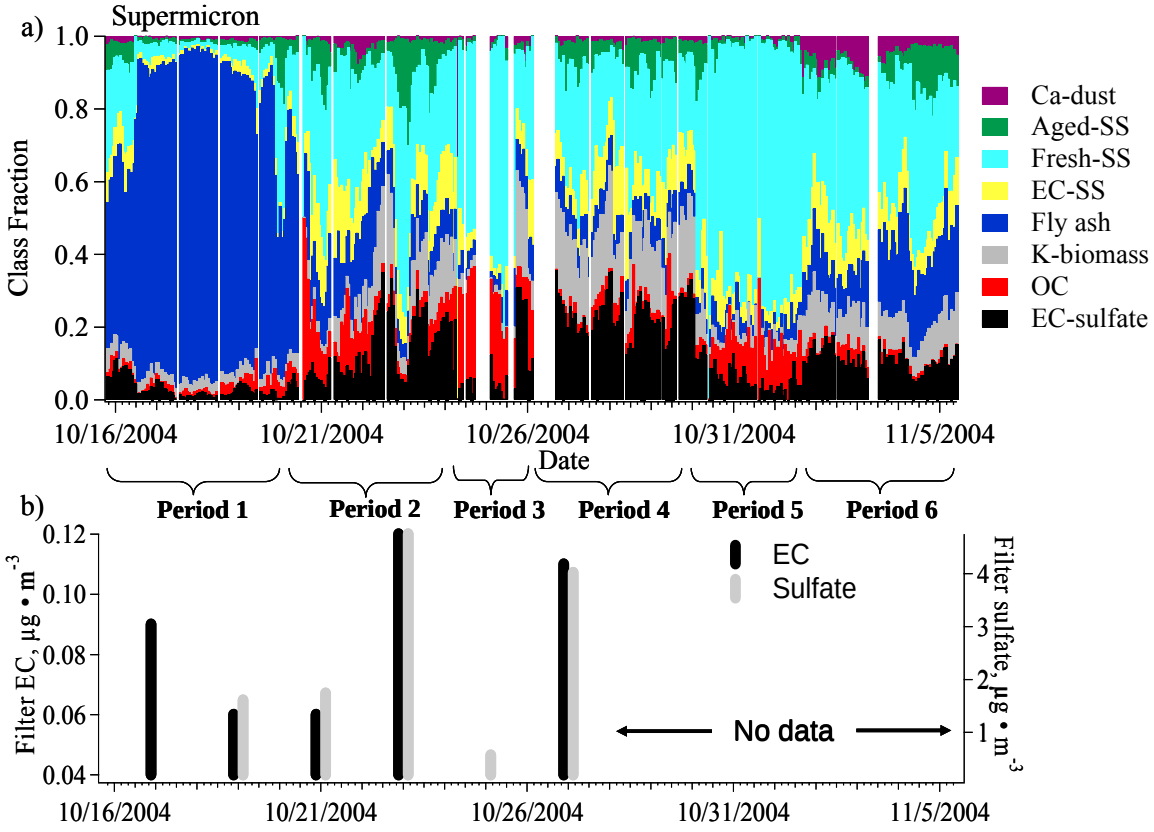

Figure 5.4 a) The unscaled fraction of different supermicron particle chemical classes in one hour time resolution for the duration of the APMEX field campaign. b) Mass of EC and sulfate per cubic meter as determined by 24 hr filter measurements during APMEX.

2), October 24-26 (Period 3), October 26-30 (Period 4), October 30- November 2 (Period 5) and November 2-5 (Period 6). During Period 1, the site was impacted by a dominant fraction of supermicron fly ash particles. The presence of fly ash during this period is supported by an increase in the mass of different metals known to exist in fly ash (Al, Mn, Li, Fe, Ti, V, Cr) [*Vijayan et al.*, 1997; *Zhang et al.*, 2005] measured on filters [*Stone et al.*, 2007]. A possible source for these fly ash particles could be an incinerator or coal combustion. The fly ash does not resemble K-biomass burning or vehicular exhaust particles that have been measured in previous ATOFMS source characterization studies. As discussed in Guazzotti et al, the mass spectral signature resembles fly ash particles formed by coal combustion (*Guazzotti et al.*, 2003; *Suess, 2002*). In particular, the Li^+ ion signal was observed in 55% of the supermicron particle spectra during Period 1. Similar to a previous ATOFMS study conducted by Guazzotti et al. during INDOEX, this signature was mainly detected when there was extensive transport from the Arabian peninsula (*Guazzotti et al.*, 2003).

When the air mass comes from heavily populated areas near India and Sri Lanka to the east-northeast (Periods 2 and 4) the relative contributions of EC-sulfate, OC, K-biomass, Fresh-SS, and EC-SS particle types increases substantially with a significant decrease in Li-containing fly ash particles. During Periods 2 and 4, there is also a corresponding increase in the fraction of sub-micron particles. When the air mass comes from the east or south (Periods 3 and 5) over the ocean, Fresh-SS dominates with a concurrent decrease in K-biomass, EC-sulfate, EC-SS and particle number concentrations. During Period 6, fly ash, Ca-dust, K-biomass, and EC-sulfate particles increased. In both cases when the HYSPLIT model shows the air mass coming from the

west (Figure 5.3a and Figure 5.3f), an increase in the amount of fly ash particle types was detected.

Figure 5.4b shows filter based data (24 hr PM < 2.5 μm) for EC (left y-axis) and sulfate (right y-axis) mass measured during the first half of APMEX. In general, the mass concentrations of EC and sulfate increased during the times when ATOFMS detected increased fractions of EC-sulfate and K-biomass particles (Periods 2 and 4). A corresponding decrease in the mass concentrations of EC and sulfate occurred during times when Fresh-SS dominated the supermicron fraction (Period 3). Increased EC-sulfate and K-biomass fractions observed by ATOFMS correlate with an increase in filter mass for EC and sulfate. During INDOEX similar results were observed, showing the highest levels of pollution originating from India and Southeast Asia and decreased levels from the Arabian Sea and southern Indian Ocean [*Ball et al.*, 2003; *Guazzotti et al.*, 2001; *Guazzotti et al.*, 2003; *Lobert and Harris*, 2002; *Neususs et al.*, 2002; *Quinn et al.*, 2002; *Reiner et al.*, 2001]. Our results show that approximately 80% of EC and 84% of K-biomass particles during APMEX were internally mixed with sulfate which suggests they underwent significant processing during transport to the sampling site.

Figure 5.5 shows the same 6 distinct periods for submicron (0.3-1.0 μm) particles. Similar to the super-micron particles, a period with an increased fraction of submicron fly ash (October 15-20) particles was followed by a period dominated by EC-sulfate and K-biomass-sulfate particles (October 20-24), a period with Fresh-SS (October 24-26), followed by a period with EC-sulfate and K-biomass (October 26-30), another period of Fresh-SS (October 30-November 2), ending with a period of increasing EC-sulfate and K-biomass number concentrations. It is important to note that ATOFMS studies in most

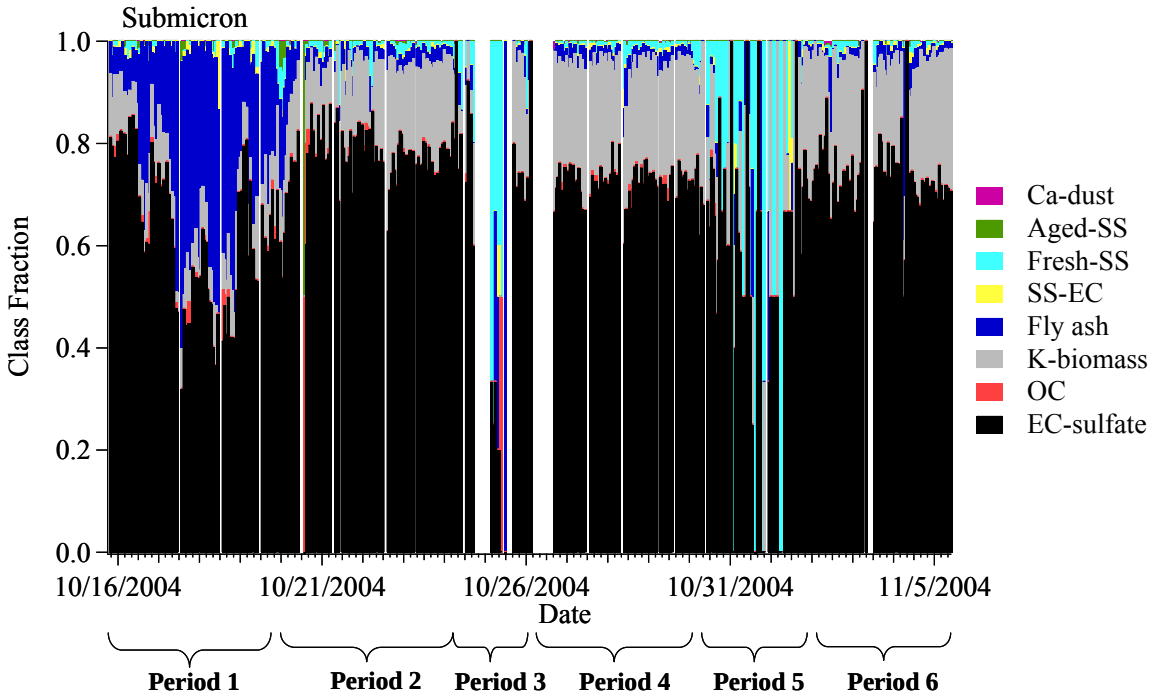

Figure 5.5 The fraction of submicron particle chemical classes in one hour time resolution for the duration of the APMEX field campaign.

urban areas usually detect 5-7 diverse particle types in the sub-micron size range, whereas in this study, just two types, EC-sulfate and K-biomass particles, dominated the sub-micron sizes as shown in Figure 5.5. The chemical homogeneity of the aerosol in this region suggests two possibilities: 1) a single dominating aerosol source in the region, or 2) significant atmospheric processing and/or scavenging occurring during transport which converts the particles into an internally mixed homogeneous composition. Given the measured particles types and what is known about sources from previous studies, the second explanation seems to be the most likely.

An accurate depiction of the size distributions for the different particle chemical classes requires use of a scaling procedure to correct for the detection bias for different particle sizes measured using ATOFMS [*Qin et al.*, 2006; *Wenzel et al.*, 2003]. The particle number concentrations measured with a co-located APS is used to scale the ATOFMS particle counts to obtain a more accurate representation of the chemical class size distributions. A detailed description of this scaling procedure has been reported previously [*Qin et al.*, 2006]. Figure 5.6 shows the scaled particle number concentrations for the 7 major chemical classes observed during APMEX. The particle number concentrations represent an average for the entire field campaign. The size distribution for the Ca particle class is not shown because of the low number concentrations observed during the study. Figure 5.6a shows that the size distributions for K-biomass and EC-sulfate particles has a steep increase in number concentration below 1 μm as would be expected for K-biomass and automobile combustion particles [*Noble and Prather*, 1996]. Figure 5.6b shows that Aged-SS, Fresh-SS, SS-EC, and OC are broadly distributed with a dominant mode at ~1.7 μm. Fly ash has an aerodynamic size mode centered at ~1.1 μm.

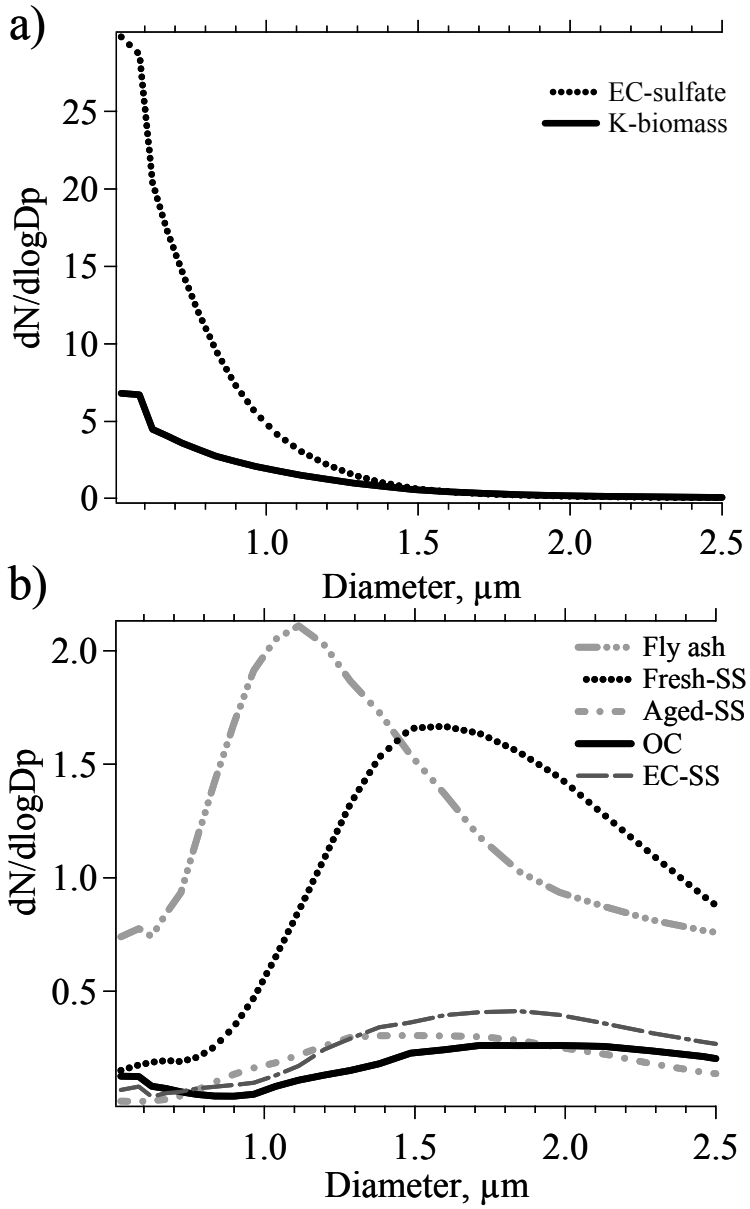

Figure 5.6 Scaled size distributions for the top seven chemical classes measured during APMEX.

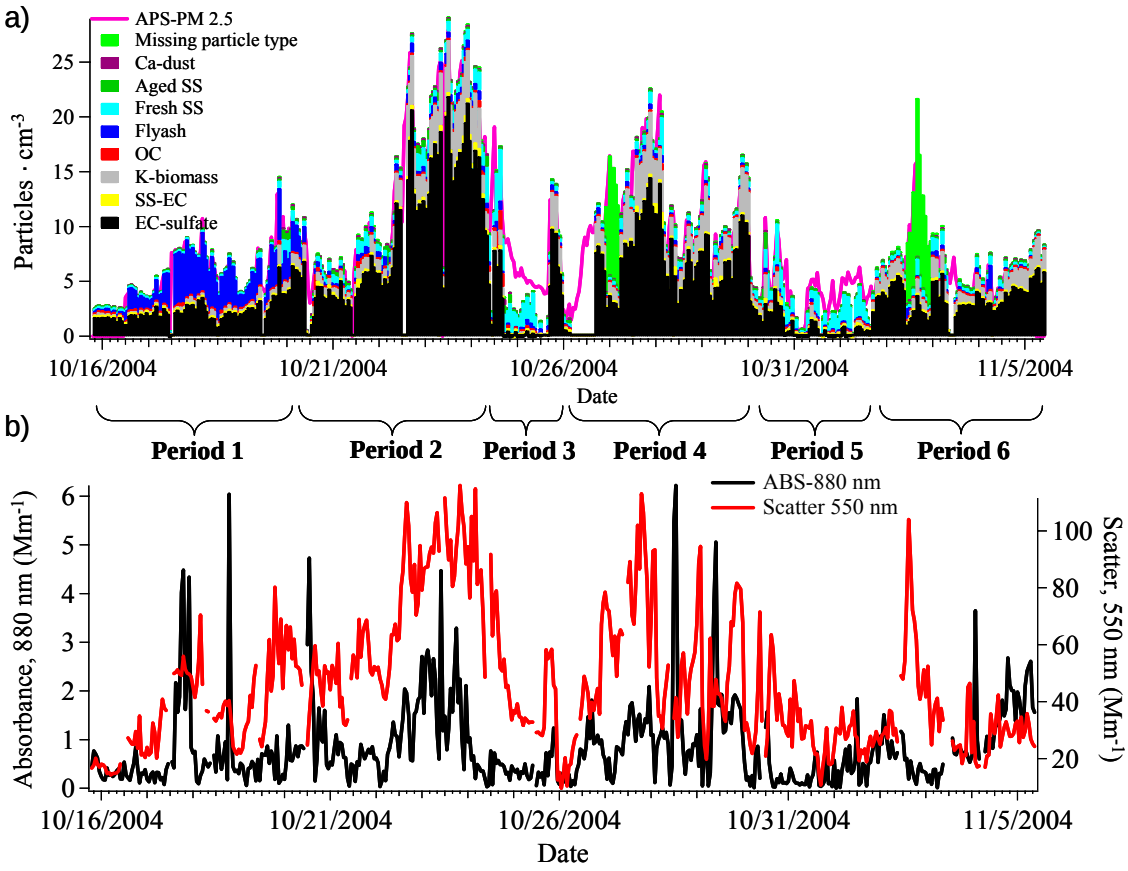

Figure 5.7 a) Temporal profile for the scaled particle number concentrations for the eight chemical classes measured during APMEX. The missing particle type periods are shown in bright green. Each color represents the number of particles for a given particle type. For comparison, the total particle concentration < 2.5 µm as measured by an APS is plotted as the pink line. b) Aethalometer absorption coefficient (black line) is plotted on the left y-axis, and nephelometer scattering coefficient (red line) is plotted on the right y-axis for the duration of APMEX.

Figure 5.7a shows the time series with 1 hour resolution for the particle number concentrations of particles with sizes less than 2.5 μm for the different chemical classes that have been scaled using the APS as described above. For comparison, the APS $PM_{2.5}$ number concentrations are also shown (pink line). The different colors within each hourly bar represent the number of particles for the different particle chemical classes. The six time periods discussed above are readily apparent even after scaling. Period 1 is characterized by the presence of a high abundance of supermicron Li-containing fly ash particles. It should be noted that the number concentration of fly ash particles shown in Figure 5.7a is likely over-estimated (~2x) due to the ATOFMS enhanced sensitivity for fly ash particles as discussed above. In general, during Periods 2 and 4 there is an increase in total particle concentrations, dominated by submicron K-biomass and EC-sulfate particles, and a corresponding decrease in Li-containing particles When particle concentrations were at their lowest (Periods 3 and 5), supermicron sea salt particles dominate.

The episodes with the "missing particle" type (possibly wet sea salt or ammonium sulfate) are shaded in green in Figure 5.7 (Periods 4 and 6). During these time periods, the ATOFMS hit percentage was ~1/2 of the average hit rate during the rest of the field study. It should be noted that during the missing particle time periods, most of the missed particles had sizes above 1 μm diameter, suggesting wet sea salt could have been contributing. Furthermore, the scanning mobility particle sizer (SMPS) data (not shown) do not show an increased number of fine and ultrafine particles during these periods. Out of ~360 hours of sampling, approximately ~24 hours contain significant fractions of the missing particle type. If these were nominally pure sulfate aerosols, they occurred for

less than 10% of the total sampling time. This observation suggests that sulfate aerosols, used in the IPCC report and many climate models, is not an appropriate model aerosol to use in radiative forcing calculations of the Indo-Asian haze. Using a sulfate aerosol type would result in an under-prediction of the aerosol forcing in this region, as internal mixtures of sulfate and EC lead to more warming of the atmosphere. Figure 5.7b shows a temporal plot of the absorbance (b_{ab}) measured with an aethalometer at 880 nm (left y-axis) and the scattering coefficient (b_{sp}) measured with a nephelometer at 550 nm (right y-axis). Both the absorbance and scattering increase during Periods 2 and 4; as discussed, these are long range transport periods from southern India. Figure 5.7b also shows that during the two episodes with the missing particle types, there was a sharp increase in scattering with a corresponding decrease in the absorption of the aerosol. This is completely consistent with the ATOFMS scattering light from of these particles but not absorbing UV light and producing mass spectra.

The missing particle type observations are different than those by Wenzel et al. who observed that the fraction of missed particles increased with decreasing size and attributed them to ammonium sulfate. It is difficult to envision large nominally pure ammonium sulfate particles, without smaller ones also being present. Thus, it is possible the missing particle type observed during this study could be a substance other than ammonium sulfate. Lab studies have shown that the ATOFMS hit rate dramatically decreases when wet versus dry sea salt particles are analyzed. Wet sea salt and ammonium sulfate are the only two particle types the ATOFMS has been shown to miss.

Roden et al. report that biofuel burning from cook stoves (which is common in India) leads to a larger EC fraction than open vegetative burning [*Roden et al.*, 2006].

Notably, during long range transport periods (Periods 2 and 4) when the highest BC concentrations were measured with the aethalometer, 73% of the submicron particles were classified as EC, 77% of the submicron particles contain an intense $^{39}K^{+}$ ion which is a known tracer for biomass and biofuel particles, and 71% of the EC particles also had a large $^{39}K^{+}$ signal associated with them. Similarly, Guazzotti et al. have reported that during INDOEX a significant fraction (75%) of the particles transported from India were from a biomass/biofuel source [*Guazzotti et al.*, 2003]. Figure 5.8 shows the strong correlation observed between the hourly K-biomass and EC-sulfate particle counts (R^2 = 0.92) for the entire study. This is further evidence that biofuel burning makes significant contributions to EC/soot in the region. A similar correlation (R^2 = 0.93) was observed by Stone et al. between mass concentrations of EC and water soluble K-containing particles.

There is an interesting contrast in source contributions when the air masses were coming from the Indian (Periods 2 and 4) versus Arabian (Period 1) regions. A similar observation was made previously by Guazzotti, et al. 2003. All periods show a high fraction of K-containing particles, however, when the air mass comes from India ~75% of EC/soot is combined with K, which is indicative of biofuel signatures. In contrast, when the air mass comes from the Arabian peninsula, a large majority of K-containing particles are combined with Li^{+} and other inorganic metal ions, a source signature for coal combustion or fly ash particles. Single particle mass spectral signatures are a powerful tool to distinguish between different sources with common overlapping marker ions.

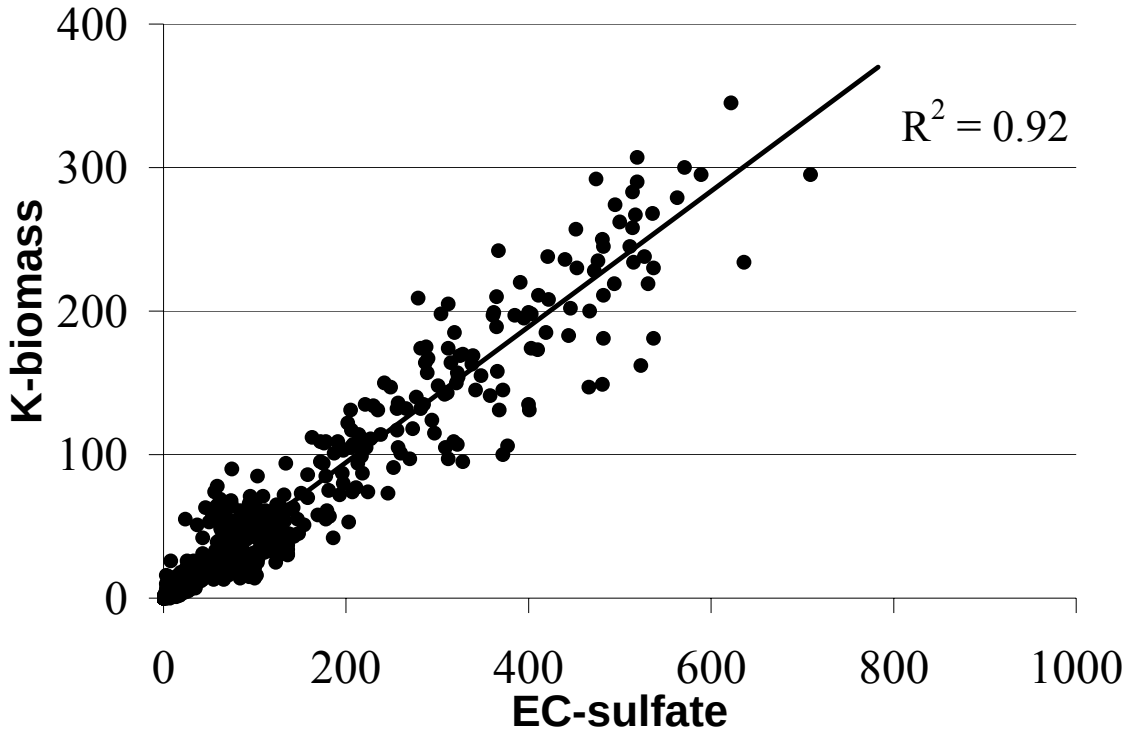

Figure 5.8 Correlation between the number of K-biomass and EC-sulfate particles measured each hour during APMEX.

5.5 Conclusion

During the monsoonal transition period, Hanimaadhoo experienced changes in the relative fraction and total number concentrations for different particle types that can be correlated with the direction of the arriving air masses. When the air mass comes from the north and northeast from India and Sri Lanka, biofuel/biomass particles represent a significant fraction of the supermicron and submicron particles at Hanimaadhoo. When the air mass shifts to an easterly or southerly direction, a significant decrease in total particle concentrations and number of EC-sulfate and K-biomass particles occurs with a corresponding increase in the fraction of Fresh-SS. When the air mass comes from a westerly direction, Hanimaadhoo experiences an influx of supermicron and submicron fly ash type particles, possibly transported from the Arabian or African peninsulas.

In order to develop proper control strategies for the aerosols that have the largest impact on direct forcing, we must better understand the sources and processing of the aerosols in the region of the Atmospheric Brown Cloud. The single particle mixing state of biomass/fuel and elemental carbon particles in this region provides some insight into the major sources. During APMEX, biomass/fuel accounts for ~75% of the EC/soot and overall particle number concentrations when the air mass originated from southern India. In contrast, when the air originated from the Arabian peninsula, a high fraction (55%) of Li-dust or fly ash particles were detected. Similar contrasting source contributions were reported by our group previously during INDOEX in 1999 for this region (*Guazzotti*, et al. 2003). The measured K-biomass and EC particles contained more sulfate than freshly emitted EC (from vehicles) and biomass, showing these particles have undergone extensive secondary processing. Correspondingly, during long range transport from

southern India, a larger fraction of EC mixed with sea salt was observed which also suggests EC has been cloud processed with sea salt. Interestingly, nominally pure organic particles and particles containing significant amounts of nitrate which are normally observed with ATOFMS in urban environments were not observed during the long range transport periods from India. This is possibly due to the high VOC/NO_x emission from the major combustion sources in India (ie. two stroke engines), selective scavenging by clouds or rain during transport, or a lack of photochemistry and ozone in this region. The hygroscopicity of EC particles transported from India and Sri Lanka to Hanimaadhoo is increased due to the fact that it has become internally mixed with secondary sulfate during transport. Furthermore, the light absorption by carbonaceous particles transported over the Indian Ocean from India and Sri Lanka could be significantly enhanced if sulfate and NaCl mixed with EC exists as a shell around an absorbing EC core. The observed single particle mixing of sulfate with biomass and EC/soot particles thus offers an explanation for the large solar heating observed during INDOEX observations [*Ramanathan et al.*, 2001] of atmospheric brown clouds. Biomass and EC particles transported from India and Sri Lanka over the Indian Ocean should be represented as being internally mixed with sulfate in climate models for the region. Future studies will explore the expected forcing of the measured size-resolved single particle mixing state of aerosols in this region.

5.6 Acknowledgements

Filter data was kindly made available by James Schauer and Elizabeth Stone from University of Wisconsin-Madison. Financial support for this research was given by the

Atmospheric Brown Cloud project funded under the United Nations Environmental Programme and the National Oceanic & Atmospheric Administration.

Chapter 5, in full, has been submitted for publication: M. T. Spencer, J. C. Holecek, C. E. Corrigan, V. Ramanathan, K. A. Prather, Size-resolved Chemical Composition of Aerosol Particles During a Monsoonal Transition Period over the Indian Ocean, *Journal of Geophysical Research-Atmospheres*, Unpublished work, Copyright 2007 American Geophysical Union.

5.7 References

Alfaro, S.C., A. Gaudichet, J.L. Rajot, L. Gomes, M. Maille, and H. Cachier, Variability of aerosol size-resolved composition at an Indian coastal site during the Indian Ocean Experiment (INDOEX) intensive field phase, *J. Geophys. Res.*, *108* (D8), 2003.

Anderson, T.L., and J.A. Ogren, Determining aerosol radiative properties using the TSI 3563 integrating nephelometer, *Aerosol Sci. Technol.*, *29* (1), 57-69, 1998.

Arnott, W.P., K. Hamasha, H. Moosmuller, P.J. Sheridan, and J.A. Ogren, Towards aerosol light-absorption measurements with a 7-wavelength aethalometer: Evaluation with a photoacoustic instrument and 3-wavelength nephelometer, *Aerosol Sci. Technol.*, *39* (1), 17-29, 2005.

Ball, W.P., R.R. Dickerson, B.G. Doddridge, J.W. Stehr, T.L. Miller, D.L. Savoie, and T.P. Carsey, Bulk and size-segregated aerosol composition observed during INDOEX 1999: Overview of meteorology and continental impacts, *J. Geophys. Res.*, *108* (D10), 2003.

Bond, T.C., G. Habib, and R.W. Bergstrom, Limitations in the enhancement of visible light absorption due to mixing state, *J. Geophys. Res.*, *111* (D20), 2006.

Chandra, S., S.K. Satheesh, and J. Srinivasan, Can the state of mixing of black carbon aerosols explain the mystery of 'excess' atmospheric absorption?, *Geophys. Res. Lett.*, *31* (19), 2004.

Chen, Y., and J.E. Penner, Uncertainty analysis for estimates of the first indirect aerosol effect, *Atmos. Chem. Phys.*, *5*, 2935-2948, 2005.

Clarke, A.D., Y. Shinozuka, V.N. Kapustin, S. Howell, B. Huebert, S. Doherty, T. Anderson, D. Covert, J. Anderson, X. Hua, K.G. Moore, C. McNaughton, G. Carmichael, and R. Weber, Size distributions and mixtures of dust and black carbon aerosol in Asian outflow: Physiochemistry and optical properties, *J. Geophys. Res.*, *109* (D15), 2004.

Corrigan, C.E., V. Ramanathan, and J.J. Schauer, Impact of monsoon transitions on the physical and optical properties of aerosols, *J. Geophys. Res.*, *111* (D18), 2006.

Debaje, S.B., S.J. Jeyakumar, K. Ganesan, D.B. Jadhav, and P. Seetaramayya, Surface ozone measurements at tropical rural coastal station Tranquebar, India, *Atmos. Environ.*, *37* (35), 4911-4916, 2003.

Dickerson, R.R., M.O. Andreae, T. Campos, O.L. Mayol-Bracero, C. Neususess, and D.G. Streets, Analysis of black carbon and carbon monoxide observed over the Indian

Ocean: Implications for emissions and photochemistry, *J. Geophys. Res.*, *107* (D19), 2002.

Dusek, U., G.P. Reischl, and R. Hitzenberger, CCN activation of pure and coated carbon black particles, *Environmental Science & Technology*, *40* (4), 1223-1230, 2006.

Fuller, K.A., W.C. Malm, and S.M. Kreidenweis, Effects of mixing on extinction by carbonaceous particles, *J. Geophys. Res.*, *104* (D13), 15941-15954, 1999.

Gard, E., J.E. Mayer, B.D. Morrical, T. Dienes, D.P. Fergenson, and K.A. Prather, Real-time analysis of individual atmospheric aerosol particles: Design and performance of a portable ATOFMS, *Anal. Chem.*, *69* (20), 4083-4091, 1997.

Guazzotti, S.A., K.R. Coffee, and K.A. Prather, Continuous measurements of size-resolved particle chemistry during INDOEX-intensive field phase 99, *J. Geophys. Res.*, *106* (D22), 28607-28627, 2001.

Guazzotti, S.A., D.T. Suess, K.R. Coffee, P.K. Quinn, T.S. Bates, A. Wisthaler, A. Hansel, W.P. Ball, R.R. Dickerson, C. Neususs, P.J. Crutzen, and K.A. Prather, Characterization of carbonaceous aerosols outflow from India and Arabia: Biomass/biofuel burning and fossil fuel combustion, *J. Geophys. Res.*, *108* (D15), ACL13/1-ACL13/14, 2003.

Hopke, P.K., and X.H. Song, Classification of single particles by neural networks based on the computer-controlled scanning electron microscopy data, *Anal. Chim. Acta*, *348* (1-3), 375-388, 1997.

HYSPLIT, Hybrid single-particle lagrangian integrated trajectory, *http://www.arl.noaa.gov/ready/hysplit4.html*.

IPCC, *Climate change 2001 : The scientific basis : Contribution of working group I to the third assessment report of the intergovernmental panel on climate change*, Cambridge University Press, Cambridge ; New York :, 2001.

Jacobson, M.Z., Strong radiative heating due to the mixing state of black carbon in atmospheric aerosols, *Nature*, *409* (6821), 695-7, 2001.

Kaneyasu, N., and S. Murayama, High concentrations of black carbon over middle latitudes in the north pacific ocean, *J. Geophys. Res.*, *105* (D15), 19881-19890, 2000.

Knutti, R., T.F. Stocker, F. Joos, and G.K. Plattner, Constraints on radiative forcing and future climate change from observations and climate model ensembles, *Nature*, *416* (6882), 719-723, 2002.

Kripalani, R.H., and P. Kumar, Northeast monsoon rainfall variability over south peninsular India vis-a-vis the Indian Ocean dipole mode, *International Journal of Climatology*, *24* (10), 1267-1282, 2004.

Lal, S., M. Naja, and B.H. Subbaraya, Seasonal variations in surface ozone and its precursors over an urban site in India, *Atmos. Environ.*, *34* (17), 2713-2724, 2000.

Lobert, J., and J.M. Harris, Trace gases and air mass origin at Kaashidhoo, Indian Ocean, *J. Geophys. Res.*, *107* (D19), 2002.

Lohmann, U., and J. Feichter, Global indirect aerosol effects: A review, *Atmos. Chem. Phys.*, *5*, 715-737, 2005.

Moffet, R.C., and K.A. Prather, Extending ATOFMS measurements to include refractive index and density, *Anal. Chem.*, *77* (20), 6535-6541, 2005.

Morgan, M.G., P.J. Adams, and D.W. Keith, Elicitation of expert judgments of aerosol forcing, *Climatic Change*, *75* (1-2), 195-214, 2006.

Myhre, G., F. Stordal, T.F. Berglen, J.K. Sundet, and I.S.A. Isaksen, Uncertainties in the radiative forcing due to sulfate aerosols, *Journal of the Atmospheric Sciences*, *61* (5), 485-498, 2004.

Neususs, C., T. Gnauk, A. Plewka, H. Herrmann, and P.K. Quinn, Carbonaceous aerosol over the Indian Ocean: OC/EC fractions and selected specifications from size-segregated onboard samples, *J. Geophys. Res.*, *107* (D19), 2002.

Noble, C.A., and K.A. Prather, Real-time measurement of correlated size and composition profiles of individual atmospheric aerosol particles, *Environ. Sci. Technol.*, *30* (9), 2667-2680, 1996.

Prather, K.A., T. Nordmeyer, and K. Salt, Real-time characterization of individual aerosol particles using time-of-flight mass spectrometry, *Anal. Chem.*, *66* (9), 1403-7, 1994.

Qin, X.Y., P.V. Bhave, and K.A. Prather, Comparison of two methods for obtaining quantitative mass concentrations from aerosol time-of-flight mass spectrometry measurements, *Anal. Chem.*, *78* (17), 6169-6178, 2006.

Quinn, P.K., D.J. Coffman, T.S. Bates, T.L. Miller, J.E. Johnson, E.J. Welton, C. Neususs, M. Miller, and P.J. Sheridan, Aerosol optical properties during INDOEX 1999: Means, variability, and controlling factors, *J. Geophys. Res.*, *107* (D19), 2002.

Ramana, M.V., and V. Ramanathan, Abrupt transition from natural to anthropogenic aerosol radiative forcing: Observations at the ABC-Maldives climate observatory, *J. Geophys. Res.*, *111* (D20), 2006.

Ramanathan, V., C. Chung, D. Kim, T. Bettge, L. Buja, J.T. Kiehl, W.M. Washington, Q. Fu, D.R. Sikka, and M. Wild, Atmospheric brown clouds: Impacts on south Asian climate and hydrological cycle, *Proc. Natl. Acad. Sci. U. S. A.*, *102* (15), 5326-5333, 2005.

Ramanathan, V., P.J. Crutzen, J. Lelieveld, A.P. Mitra, D. Althausen, J. Anderson, M.O. Andreae, W. Cantrell, G.R. Cass, C.E. Chung, A.D. Clarke, J.A. Coakley, W.D. Collins, W.C. Conant, F. Dulac, J. Heintzenberg, A.J. Heymsfield, B. Holben, S. Howell, J. Hudson, A. Jayaraman, J.T. Kiehl, T.N. Krishnamurti, D. Lubin, G. McFarquhar, T. Novakov, J.A. Ogren, I.A. Podgorny, K. Prather, K. Priestley, J.M. Prospero, P.K. Quinn, K. Rajeev, P. Rasch, S. Rupert, R. Sadourny, S.K. Satheesh, G.E. Shaw, P. Sheridan, and F.P.J. Valero, Indian ocean experiment: An integrated analysis of the climate forcing and effects of the great Indo-Asian haze, *J. Geophys. Res.*, *106* (D22), 28371-28398, 2001.

Reiner, T., D. Sprung, C. Jost, R. Gabriel, O.L. Mayol-Bracero, M.O. Andreae, T.L. Campos, and R.E. Shetter, Chemical characterization of pollution layers over the tropical Indian Ocean: Signatures of emissions from biomass and fossil fuel burning, *J. Geophys. Res.*, *106* (D22), 28497-28510, 2001.

Roden, C.A., T.C. Bond, S. Conway, A. Benjamin, and O. Pinel, Emission factors and real-time optical properties of particles emitted from traditional wood burning cookstoves, *Environ. Sci. Technol.*, *40* (21), 6750-6757, 2006.

Schnaiter, M., C. Linke, O. Mohler, K.H. Naumann, H. Saathoff, R. Wagner, U. Schurath, and B. Wehner, Absorption amplification of black carbon internally mixed with secondary organic aerosol, *J. Geophys. Res.*, *110* (D19), 2005.

Schwartz, S.E., Uncertainty requirements in radiative forcing of climate change, *J. Air Waste Manage. Assoc.*, *54* (11), 1351-1359, 2004.

Silva, P.J., D.-Y. Liu, C.A. Noble, and K.A. Prather, Size and chemical characterization of individual particles resulting from biomass burning of local southern California species, *Environ. Sci. Technol.*, *33* (18), 3068-3076, 1999.

Sodeman, D.A., S.M. Toner, and K.A. Prather, Determination of single particle mass spectral signatures from light duty vehicle emissions, *Environmental Science & Technology*, *39* (12), 4569-4580, 2005.

Song, X.-H., P.K. Hopke, D.P. Fergenson, and K.A. Prather, Classification of single particles analyzed by ATOFMS using an artificial neural network, Art-2a, *Anal. Chem.*, *71* (4), 860-865, 1999.

Spencer, M.T., L.G. Shields, and K.A. Prather, Simultaneous measurement of the effective density and chemical composition of ambient aerosol particles, *Environ. Sci. Technol.*, *Web Release Date: 17-Jan-2007*, 2007.

Stehr, J.W., W.P. Ball, R.R. Dickerson, B.G. Doddridge, C.A. Piety, and J.E. Johnson, Latitudinal gradients in O-3 and CO during INDOEX 1999, *J. Geophys. Res.*, *107* (D19), 2002.

Stier, P., J.H. Seinfeld, S. Kinne, J. Feichter, and O. Boucher, Impact of nonabsorbing anthropogenic aerosols on clear-sky atmospheric absorption, *J. Geophys. Res.*, *111* (D18), 2006.

Stone, E.A., G.C. Lough, J. Schauer, P. Siva, C. Corrigan, and V. Ramanathan, Understanding the origin of black carbon in the atmospheric brown cloud over the Indian Ocean, *J. Geophys. Res.*, *Accepted*, 2007.

Suess, D.T., Single particle mass spectrometry combustion source characterization and atmospheric apportionment of vehicular, coal, and biofuel exhaust emissions, Ph.D. Thesis, University of California Riverside, 2002.

Thomson, D.S., A.M. Middlebrook, and D.M. Murphy, Thresholds for laser-induced ion formation from aerosols in a vacuum using ultraviolet and vacuum-ultraviolet laser wavelengths, *Aerosol Sci. Technol.*, *26* (6), 544-559, 1997.

Toner, S.M., D.A. Sodeman, and K.A. Prather, Single particle characterization of ultrafine and accumulation mode particles from heavy duty diesel vehicles using aerosol time-of-flight mass spectrometry, *Environ. Sci. Technol.*, *40* (12), 3912-3921, 2006.

Vijayan, V., S.N. Behera, V.S. Ramamurthy, S. Puri, J.S. Shahi, and N. Singh, Elemental composition of fly ash from a coal-fired thermal power plant: A study using PIXE and EDXRF, *X-Ray Spectrom.*, *26* (2), 65-68, 1997.

Wenzel, R.J., D.-Y. Liu, E.S. Edgerton, and K.A. Prather, Aerosol time-of-flight mass spectrometry during the Atlanta supersite experiment: 2. Scaling procedures, *Journal of J. Geophys. Res.*, *108* (D7), SOS 15/1-SOS 15/8, 2003.

Zhang, C.F., Y. Qiang, and J.M. Sun, Characteristics of particulate matter from emissions of four typical coal-fired power plants in China, *Fuel Process. Technol.*, *86* (7), 757-768, 2005.

6 Gold Nanoparticles as a Matrix for Visible Wavelength Single Particle Matrix-Assisted Laser Desorption/Ionization Mass Spectrometry of Small Molecules

6.1 Synopsis

Gold nanoparticles (GNPs) are used as a matrix for assisting the visible wavelength laser desorption/ionization (VIS-MALDI) of individual aerosol particles containing about 50 attomole of a small peptide. A dual polarity time-of-flight mass spectrometer was used to obtain both positive and negative ion mass spectra simultaneously from individual particles using a tunable wavelength desorption/ionization laser. The wavelength of the laser was changed from λ = 440 to 680 nm to observe the wavelength dependence of analyte ion formation. Positive sodiated-molecular ions and deprotonated negative molecular ion of a small peptide was only obtainable using 5 nm GNPs as opposed to 19 and 44 nm GNPs. While the mass of gold within the sample particles were similar, surface areas were about ten times more in the 5 nm GNPs, suggesting the total surface area of GNPs within the sample particles is an important factor that affects the formation of molecular ions. At wavelengths near the peak plasmon resonance of the GNPs (λ = 500~540 nm), negative polarity molecular ion

signal from a small peptide was higher compared to desorption/ionization at λ = 440 nm, while increased fragmentation was observed at λ = 440 nm. At wavelengths longer than the peak plasmon absorption the ability to generate a detectable ion signal decreased rapidly, which is consistent with the steep decrease in the absorbance of gold nanoparticles by surface plasmon resonance at these wavelengths. Silver nanoparticles, which also exhibit a surface plasmon resonance, were also tested. Present results show that the noble metal nanoparticle matrices can be used for VIS-MALDI analysis of small molecules such as peptides or sugars.

6.2 Introduction

Since the late 1980's matrix assisted laser desorption ionization mass spectrometry (MALDI-MS) has emerged as a favorable technique for the mass analysis of high molecular weight analytes (proteins and polymers) [*Karas and Hillenkamp*, 1988; *Tanaka et al.*, 1988]. The success of the MALDI-MS technique is based on using a matrix compound that strongly absorbs the pulsed laser radiation causing effective desorption of analyte imbedded in the matrix into the gas phase and facilitates the soft ionization of the analyte [*Dreisewerd*, 2003]. The vast majority of MALDI-MS that is performed today utilizes an ultraviolet (UV) laser such as nitrogen (λ = 337 nm) or frequency-tripled Nd:YAG (λ = 355 nm) to irradiate a sample embedded in a UV absorbing matrix [*Dreisewerd*, 2003]. IR lasers such as CO_2 (λ = 10.6 μm) or Er:YAG (λ = 2.94 μm) with IR absorbing matrices such as glycerol are also used [*Overberg et al.*, 1990; *Overberg et al.*, 1991]. The majority of highly successful matrices are small

organic acids such as 3,5-Dimethoxy-4-hydroxycinnamic acid or 2,5-Dihydroxybenzoic acid. Although these acid matrices do not interfere with the analysis of large polymers or proteins, the extensive fragmentation of the matrix materials can cause considerable interference in the low mass range of the mass spectrum. This has been a major limitation for using conventional MALDI-MS as a tool in small molecule analysis, although given this limitation, the technique is still used in small molecule analysis to some degree [*Cohen and Gusev*, 2002] .

Inorganic nanoparticles/rods/tubes and inorganic surfaces of various compositions have also been pursued as a matrix for MALDI with some success [*Chen et al.*, 2007a; *Chen et al.*, 2007b; *Furutani et al.*, ; *Furutani et al.*, ; *Kinumi et al.*, 2000; *Kirk and Bohn*, 2004; *McLean et al.*, 2005; *Schurenberg et al.*, 1999; *Sunner et al.*, 1995; *Tanaka et al.*, 1988; *Ugarov et al.*, 2004; *Wei et al.*, 1999; *Wen et al.*, 2007]. These matrices circumvent the problem of interference in the low mass range by avoiding the use of an organic matrix and some have been used in small molecule analysis [*Chen et al.*, 2007a; *Furutani et al.*, ; *Furutani et al.*, ; *Kinumi et al.*, 2000; *Wei et al.*, 1999; *Wen et al.*, 2007]. . Of particular interest are matricies comprised of noble metal nanoparticles. A unique characteristic of gold and silver nanoparticles is that they exhibit a surface plasmon resonance (SPR) at visible wavelengths. The SPR is responsible for the deep red color GNPs and the yellow color of silver nanoparticles in solution [*Kreibig and Genzel*, 1985; *Link and El-Sayed*, 2000]. One of the advantages of using noble metal nanoparticles such as GNPs as a matrix is the absence of severe fragmentation of matrix materials [*Furutani et al.*]. It was shown that the reduced fragmentation of the GNP matrix allowed for the effective analysis of small molecules (MW < 600) in UV-MALDI [*Furutani et al.*]. As

suggested by Chen et al. and Furutani et al., the SPR in the visible wavelength region opens the possibility for noble metal nanostructures to be used as matrices for visible wavelength MALDI (VIS-MALDI).

VIS-MALDI may offer advantages over traditional UV-MALDI for the analysis of some organic molecules, such as those have absorption at UV region and are susceptible to fragmentation using UV-MALDI. The majority of small organic molecules do not have an absorbance in the visible wavelength and therefore are less likely to undergo fragmentation by direct absorption of visible wavelength radiation. However, there are relatively few reports on VIS-MALDI mass spectrometry due to the limited number of suitable matrices which absorb visible wavelength light. Organic dyes, graphite surfaces and inorganic nanoparticles/rods are a few matrices that have been employed for VIS-MALDI [*Chen et al.*, 2007a; *Chen et al.*, 2007b; *Cornett et al.*, 1993; *Kim et al.*, 2002; *Schurenberg et al.*, 1999; *Smith et al.*, 1995; *Tang et al.*, 1992]. However, in most cases, there are still limitations of using the matrix for small molecule analysis due to the large number of fragment ions in the low mass region.

Here, GNPs are used as a matrix for single particle VIS-MALDI mass spectrometry. Utilizing a GNP matrix for VIS-MALDI has several benefits. For example the GNP matrix has been shown to produce less fragment ions particularly in the low mass range using UV-MALDI [*Furutani et al.*, ; *Furutani et al.*]. Furthermore, the SPR can be tuned from the visible to near-infrared wavelengths by modifying shape and/or structure of the nanoparticle [*Kamat*, 2002; *Kelly et al.*, 2003; *Oldenburg et al.*, 1998; *Sun and Xia*, 2003]. This tunability is not attainable with ordinary organic matrices because the absorption spectra is intrinsic to the individual matrix molecules. By tuning

the optimal resonance of the GNP matrix to a wavelength that is optimally coupled to a visible wavlength laser, a high performance and cost effective VIS-MALDI methodology can be established. It has also been shown that SPR excitation enhances the local electromagnetic fields by orders of magnitude resulting in ultra-high sensitive optical spectroscopy [*Barnes et al.*, 2003; *Otto et al.*, 1992]. Such enhancement by the SPR may also assist further improvement in the detection of organic molecules via mass spectroscopy.

Here we discuss the analysis of small quantities of organic molecules (~50 attomole) in individual aerosol particles using GNPs as a matrix for VIS-MALDI using a single particle dual polarity time-of-flight mass spectrometer. Gold nanoparticles of different sizes are evaluated to examine the effect of GNP size on analyte signal intensity. The wavelength of the LDI laser is varied from λ = 440-680 nm to understand the effect of SPR on the VIS-MALDI process. A brief discussion of possible applications using the GNP VIS-MALDI technique and the potential for using other noble metal nanoparticles as a VIS-MALDI matrix are also presented.

The single particle mass spectrometer used in this work offers the unique ability of obtaining both positive and negative polarity mass spectra simultaneously which is not possible with conventional MALDI instruments. This gives us the advantage of being able to compare changes in the positive and negative ions generated from every laser shot directly. Furthermore, it should be pointed out that single particle mass spectrometry has the unique capability of rapid on-line analysis.

6.3 Experimental section

6.3.1 Sample preparation

Gold nanoparticles were fabricated by nanoComposix Inc. (San Diego, CA) using a previously established method [*Duff et al.*, 1993]. Silver nanoparticles were also fabricated by nanoComposix Inc. using a base-catalyzed reduction of silver nitrate. Particle sizes were determined using transmission electron microscopy. GNP stock solutions contained 5 ± 2 nm (2.3×10^{15} particles/ml), 19 ± 3 nm (8.3×10^{11} particles/ml), or 44 ± 8 nm (6.28×10^{10} particles/ml) diameter gold nanoparticles. For experiments using silver nanoparticles, 14 ± 7 nm particles were used (~1.1×10^{14} particles/ml).

All reagents were obtained commercially and used without further purification. Stock solutions of NH_2-Tryptophan-Glycine-Glycine-CO_2H (WGG) peptide (~ 3 mg/ml) and the sugars D-ribose and L-arabinose (~2 M) were prepared using milli-Q purified water, stored at 4 ^{o}C and used within 24 hours of preparation. An aliquot of peptide or sugar stock solution was pipetted into ~10 ml of metal nanoparticle solution. 5 nm gold particle solutions were prepared by diluting ~50 µl of gold stock solution into ~10 ml of milli-Q purified water. 19 nm gold particle solutions were prepared by diluting ~1.5 ml of gold stock solution into ~10 ml of milli-Q purified water. 44 nm gold particle solutions were prepared by diluting ~ 2.0 ml of gold stock solution into ~10 ml of milli-Q purified water. Silver nanoparticle solution was prepared by diluting ~500 µl silver stock solution into 10 ml milli-Q purified water.

Figure 6.1 shows a schematic of how particles containing matrix (metal nanoparticles) and analyte were aerosolized and subsequently dried. Particles were

generated by nebulizing the metal nanoparticle solutions using a Collison type nebulizer operated at a flow rate of 1.5-1.7 lpm. The aerosol stream from the nebulizer was passed through a diffusion dryer which consists of a Pyrex flow tube (50 cm length x 6 cm I.D.) with a coaxial stainless steel fine mesh tube (50 cm length x 1 cm I.D.) on the inside. The space between these coaxial tubes was filled with silica gel which dries the aerosols as they flow through the inner mesh tube. After passing through the diffusion drier the aerosol stream was diluted with ~ 1.0 lpm of dry nitrogen as it entered a second flow tube (100 cm length x 5 cm I.D.). The relative humidity at the exit of this flow tube was < 15 %. A 0.08 lpm flow of the dried aerosol was then drawn into the single particle mass spectrometer for VIS-MALDI analysis.

6.3.2 Single particle MALDI mass spectrometer

A detailed description of the ATOFMS has been given in Chapter 1 and published elsewhere, however a few modifications to the usual ATOFMS setup were made for these experiments so a brief description is also given here [*Gard et al.*, 1997; *Holecek et al.*, 2007; *Prather et al.*, 1994; *Su et al.*, 2004]. Particle charges were neutralized before particles entered the ATOFMS using a polonium-210 neutralizer to prevent deflection of charged particles within the electric field of the ion source region. Particles enter the ATOFMS through an aerodynamic lens which collimates the particles into a tightly focused beam [*Liu et al.*, 1995a; *Liu et al.*, 1995b; *Su et al.*, 2004].

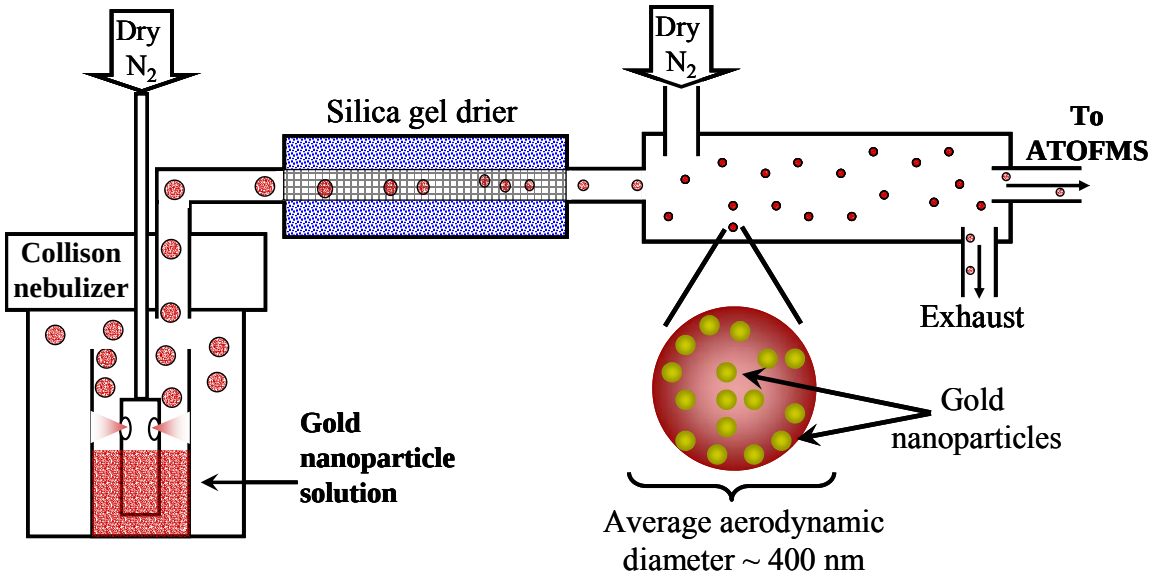

Figure 6.1 Diagram of the method for generating aerosol particles containing metal nanoparticles and analyte prior to VIS-MALDI analysis.

A wavelength tunable laser (λ = 410-680 nm) consisting of a Quantel Brilliant Q-switched Nd:YAG laser operated at 355 nm and OPOTEK Magic Prism optical parametric oscillator (OPO) was used for desorption/ionization of particles. The spot size of the laser in the source region of the mass spectrometer was ~0.8 mm. Changing the wavelength of the laser system caused small changes in the position of the output laser spot. Small movements of the laser spot position in the source region can cause changes in the detected ion intensity and the mass calibration. Therefore significant care was taken to assure that the laser spot position in the source region could be kept constant as the wavelength of the laser was adjusted. This was accomplished by passing the laser through two apertures and projecting the laser spot at the exit of the mass spectrometer on a fixed position. A Continuum Minilite II, Q-switched Nd:YAG laser operated at 532 nm was also used as a desorption/ionization laser in some experiments.

6.3.3 Data analysis

Mass spectra were imported into a database on Matlab (The MathWorks, Inc.) and analyzed using portions of the YAADA toolkit [http://www.yaada.org]. Within Matlab, a group of individual mass spectra can be averaged together creating an average mass spectrum (AM).

6.4 Results and discussion

6.4.1 Properties of sample particles

Table 1 shows measured and calculated physical characteristics of the individual sample particles that contained the WGG peptide and 5 nm GNPs. The average vacuum aerodynamic diameter of sample particles was measured as ~400 nm. Using the concentration of GNPs and WGG peptide in solution a composite density for a dried WGG-GNP sample particle is estimated to be ~1.38 $g \cdot cm^{-3}$ (we assume the density of the WGG peptide is similar to that of other small peptides, ~1.2 $g \cdot cm^{-3}$). The vacuum aerodynamic diameter can be converted to a physical diameter using the composite density and is calculated to be ~290 nm [*DeCarlo et al.*, 2004]. The volume percent of gold and WGG peptide in an individual sample particle is estimated to be ~1.0% and 99.0% respectively. The volume percent of gold and WGG leads to an estimate of approximately 2000 GNPs and 50 attomole of WGG peptide per 290 nm sample particle.

6.4.2 Aerosol particle mass spectra

Figure 6.2a-b shows a positive polarity AM from single sample particles that contained only GNPs (denoted as "pure gold") and an AM from single sample particles that contained GNPs and WGG (gold-WGG); Figure 6.2c-d shows the corresponding negative polarity AM. The data shown in Figure 6.2 was generated using laser desorption/ionization from 540 nm laser radiation. It should be noted that no mass spectra could be generated from pure WGG sample particles (particles containing no GNPs) under the current experimental conditions; that is GNPs were necessary for ion formation.

Table 6.1 Physical characteristics of the aerosol particles that contained 5 nm gold nanoparticles and the WGG peptide.

Property	Value
Average particle aerodynamic diameter	400 nm
Estimate of gold-WGG composite density	1.38 $g \cdot cm^{-3}$
Average physical diameter	290 nm
Volume percent of gold	~1.0%
Volume percent of WGG	~99.0%
Number of 5 nm GNPs per particle	~2000
Moles of WGG per particle	~50 attomole

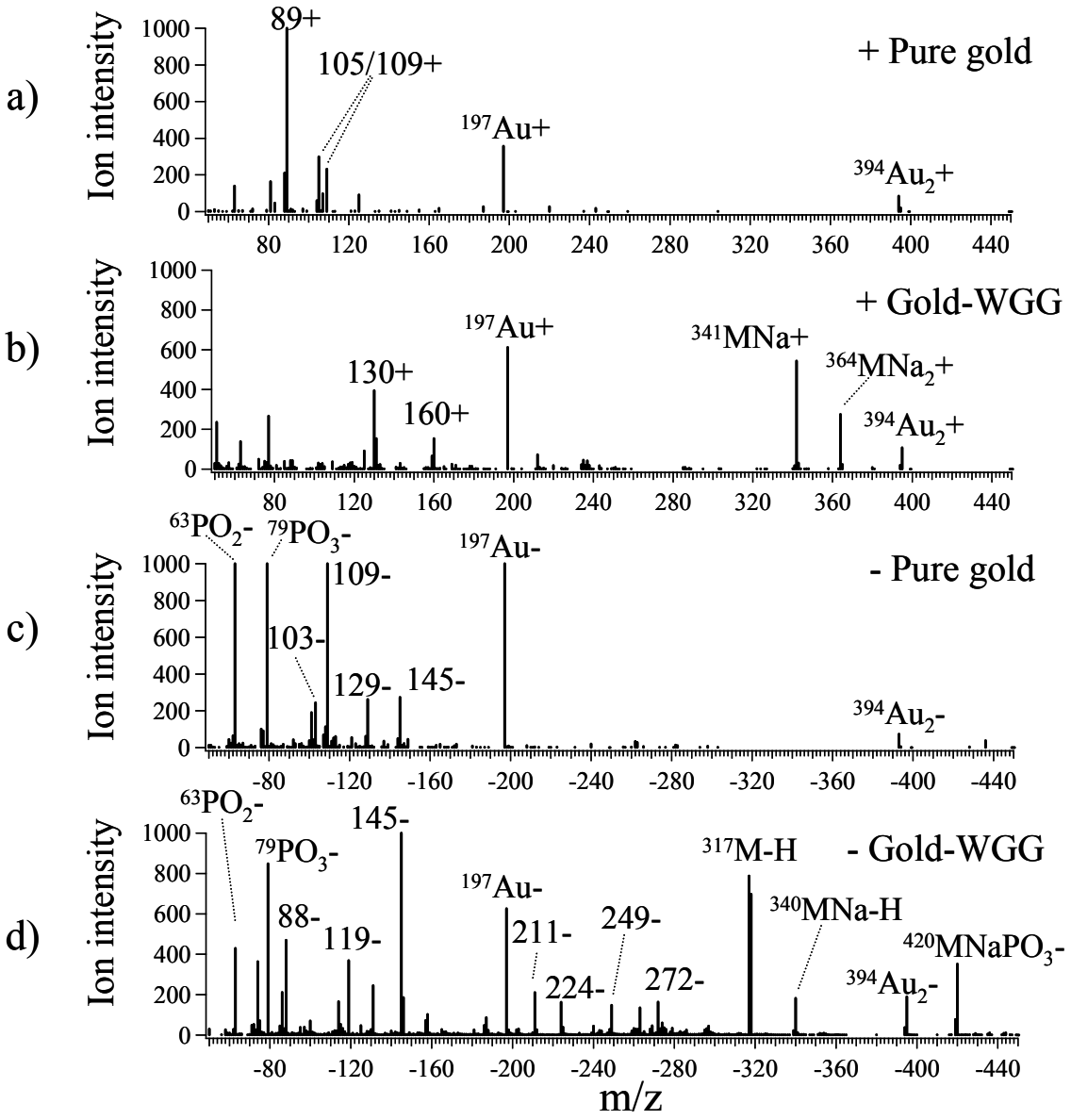

Figure 6.2 Positive average mass spectrum is shown for a) aerosol particles containing only gold nanoparticles (pure gold) and b) aerosol particles containing both gold nanoparticles and the small peptide WGG. Plot c) and d) show the corresponding negative polarity average mass spectrum. The spectra were generated using a 540 nm desorption/ionization laser.

Sample particles containing GNPs without analyte (Figure 6.2a) show positive ion peaks for gold at $^{197}Au+$ and $^{394}Au_2+$ and also peaks at 89+, 105+ and 109+ which could be from tetramethyl-phosphonium chloride (THPC) or other impurities that were not completely removed during the purification of the GNPs. Figure 6.2b shows the positive ion AM for particles containing GNPs and WGG contain peaks for gold ($^{197}Au+$ and $^{394}Au_2+$), sodium adducts of WGG ($^{341}MNa+$ and $^{364}MNa_2+$) and fragments of WGG at 130+ and 160+. Formation of the sodium-adducted molecular ions with GNP matrix using VIS-LDI laser is quite similar to those observed with GNP matrix using UV-MALDI [*Furutani et al.*]. The ions 89+, 105+ and 109+ that appeared in the pure GNPs are not present in the sample containing WGG. We observed that the presence of these ions was dependent on the concentration of analyte. At low analyte concentrations these ions were still present but decreased as analyte concentration is increased. This is possibly caused by the addition of compounds (WGG, Na, etc.) that are more easily ionized then the THPC fragment ions at m/z 89+, 105+ and 109+. The negative ion AM for pure GNPs is shown in Figure 6.2c and contains peaks for gold ($^{197}Au-$ and $^{394}Au_2-$), phosphate ($^{63}PO_2-$ and $^{79}PO_3-$), and other ions at 103-, 109-, 129-, and 145-. Again, the phosphate and "other ions" are likely from residual THPC left over after fabrication and purification of GNPs. Figure 6.2d shows the negative ion AM for GNPs with WGG contain peaks for gold ($^{197}Au-$ and $^{394}Au_2-$), phosphate ($^{63}PO_2-$ and $^{79}PO_3-$), deprotonated WGG ($^{317}M-H-$), deprotonated sodium adduct WGG ($^{340}MNa-H$), sodium phosphate adduct WGG ($^{420}MNaPO_3-$), ions that were present in the gold blank (129- and 145-), and ions presumably from the fragmentation of the WGG peptide at 211-, 224-, 249- and 272-. Figure 6.2 clearly demonstrates that GNPs can act as a VIS-MALDI matrix for the

analysis of small peptides using single particle mass spectrometry and give little interference in the low mass range particularly in $150 < m/z < 400$.

6.4.3 Effect of GNP size

Measurements using different size GNPs were made to determine the effect of the GNPs size on analyte ion signal. Figure 6.3a shows a waterfall plot of the positive ion AM for samples containing similar amounts of the peptide WGG but different size gold nanoparticles (5 nm, 19 nm, 44 nm); Figure 6.3b shows the corresponding negative ion AMs obtained using 532 nm laser radiation for desorption/ionization.

Of the three GNP sizes that were used, only sample particles containing 5 nm GNPs generated a detectable amount of WGG molecular ions (^{341}MNa+, ^{364}MNa$_2$+, ^{317}M-H-, ^{340}MNa-H and ^{420}MNaPO$_3$-). No detectable signal from the peptide was observed even after increasing the amount of WGG by more than 5 times in the experiments with the 19 nm and 44 nm GNPs. McLean et al. observed similar results that GNP matrix did not produce any detectable peptide ions in the negative ion mode using gold nanoparticles larger than 10 nm as a matrix for UV-MALDI (positive ions were detected) [*McLean et al.*, 2005]. Wen et al. also observed an increase in analyte ion signal for 30 nm versus 50 nm silicon based nanoparticles used as a UV-MALDI matrix [*Wen et al.*, 2007].

The mass of gold in a sample particle is estimated to be 2.5×10^{-15} g, 2.0×10^{-15} g and 2.0×10^{-15} g for the sample particles with 5, 19 and 44 nm GNPs respectively; this equates to a relatively similar mass of gold in all sample particles with different sizes of GNP. On the other hand, the total surface area of GNPs within a sample particle is

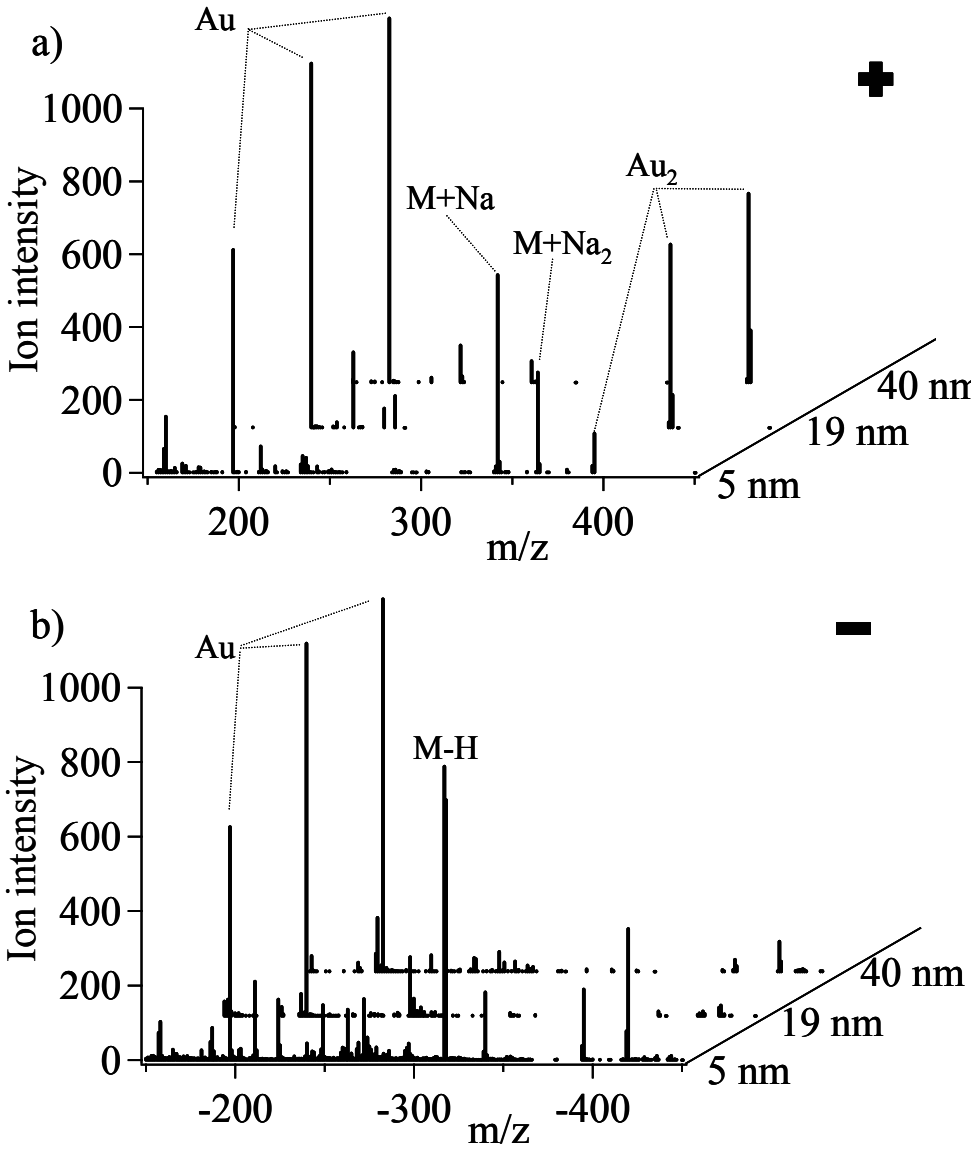

Figure 6.3 Average mass spectra that were generated from aerosol particles which contained different size gold nanoparticles are stacked and offset for comparison. Positive polarity is shown in a) and negative polarity in b). Laser radiation at 532 nm was used for desorption/ionization.

estimated to be 1.5 x 10^5 nm^2, 3.2 x 10^4 nm^2 and 1.4 x 10^4 nm^2 for 5, 19 and 44 nm GNP, respectively. This represents about an order of magnitude difference in the surface area between sample particles containing the 5 nm, 19 nm and 44 nm GNP. The mass of gold within the sample particle does not appear to be the controlling factor in the formation of analyte ion; surface area of gold is likely an important factor. Further experiments using a more refined set of GNPs with sizes between 2-19 nm and also gold nanoshells would be useful to further explore how mass and surface area of gold effect the ion signals.

6.4.4 Effect of LDI laser wavelength and power

Figure 6.4a shows the percentage of particles that generated a mass spectrum (hit percent) versus different LDI wavelengths (laser power ~ 1.2 mJ/pulse) with WGG peptide and 5 nm GNP. The hit percent is a metric for how effectively particles are desorbed and ionized at different wavelengths in single particle mass spectrometry. Because no experimental parameters are changed except for the wavelength of the LDI laser, the hit percent uniquely reflects the physiochemical property of the sample particles at a given wavelength. The hit percent is fairly constant (~3%) from 440 to 570 nm and then rapidly drops to almost zero at 600 nm. No mass spectra could be generated at 620 nm. The wavelength dependence of the hit percent is quite consistent with the wavelength dependence of optical absorption of GNP. Figure 6.4b shows the absorption spectrum of 5 nm GNP at the stock concentration. The peak of the SPR absorption centered at λ = 520 nm overlays the tailing edge of the atomic absorption of gold at shorter wavelengths and drops steeply at wavelengths longer than the peak SPR. The

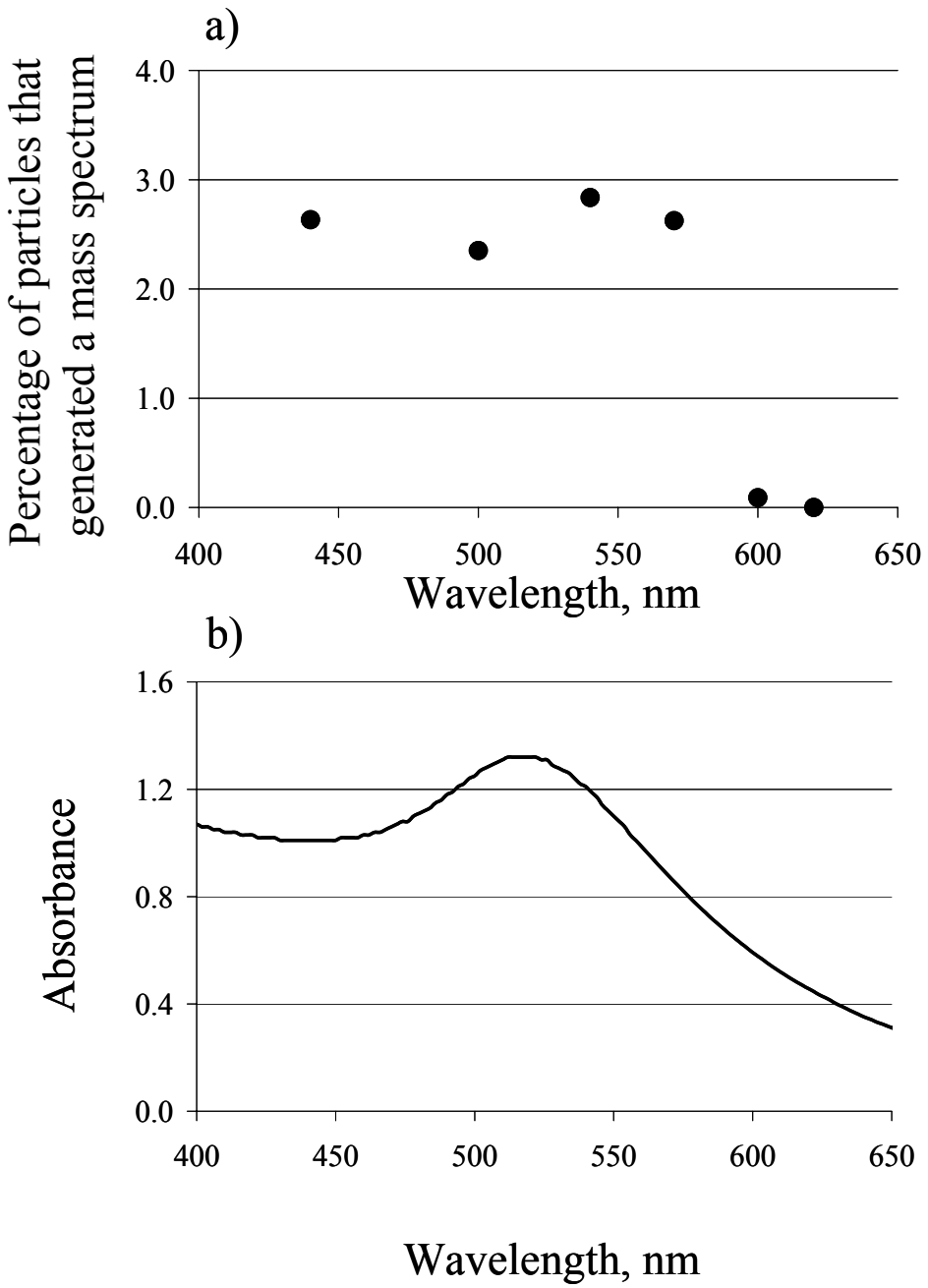

Figure 6.4 The percentage of particles that were detected with the tracking/sizing lasers and generated a mass spectrum is plotted versus the LDI wavelength in a). The absorbance of a solution of ~ 5 nm gold nanoparticles versus wavelength is shown in b).

similar wavelength dependences between the hit percent and the absorption spectrum of the GNPs clearly indicates that SPR plays a roll in VIS-LDI detection of the analyte ion.

Figure 6.5 a-b shows the laser wavelength and power dependence of the ion peak area for the sodiated WGG ion peak $[M+Na]^+$ and the peak area for the deprotonated WGG ion $[M-H]^-$ at different laser powers (0.4 mJ laser power bin widths). The vertical error bars represent twice the standard deviation in the measured areas.

Interestingly, $[M+Na]^+$ ion peak area (see Figure 6.5a) remains fairly constant with increasing laser powers at wavelengths of 500 and 540 nm, which are near the peak plasmon absorption of the GNP (520 nm, see Figure 6.4b). Such an anomaly on laser power dependence was only observed for $[M+Na]^+$ with 500 and 540 nm LDI laser wavelengths. On the contrary, as laser power increases, 440 nm LDI laser irradiation yielded more $[M+Na]^+$ ion and reached even larger intensity at the higher laser power conditions over the other wavelengths. However, at the lowest laser power conditions the 500 nm LDI laser irradiation yielded the largest peak area. The $[M-H]^-$ peak area increased with laser power for all LDI wavelength conditions although the $[M-H]^-$ peak area at 440 nm is consistently less than at 500 and 540 nm wavelengths (Figure 6.5b). Our goal is not to explain the desorption/ionization mechanisms that might be occurring at the different wavelengths, however, current results strongly suggest that a different mechanism in LDI with GNPs exists at or near the SPR versus the LDI mechanism at shorter wavelengths (e.g., $\lambda = 440$ nm).

In general, more fragment ions and increased total ions are expected using higher laser power conditions. Figure 6.5c-d are consistent with this and show the total positive

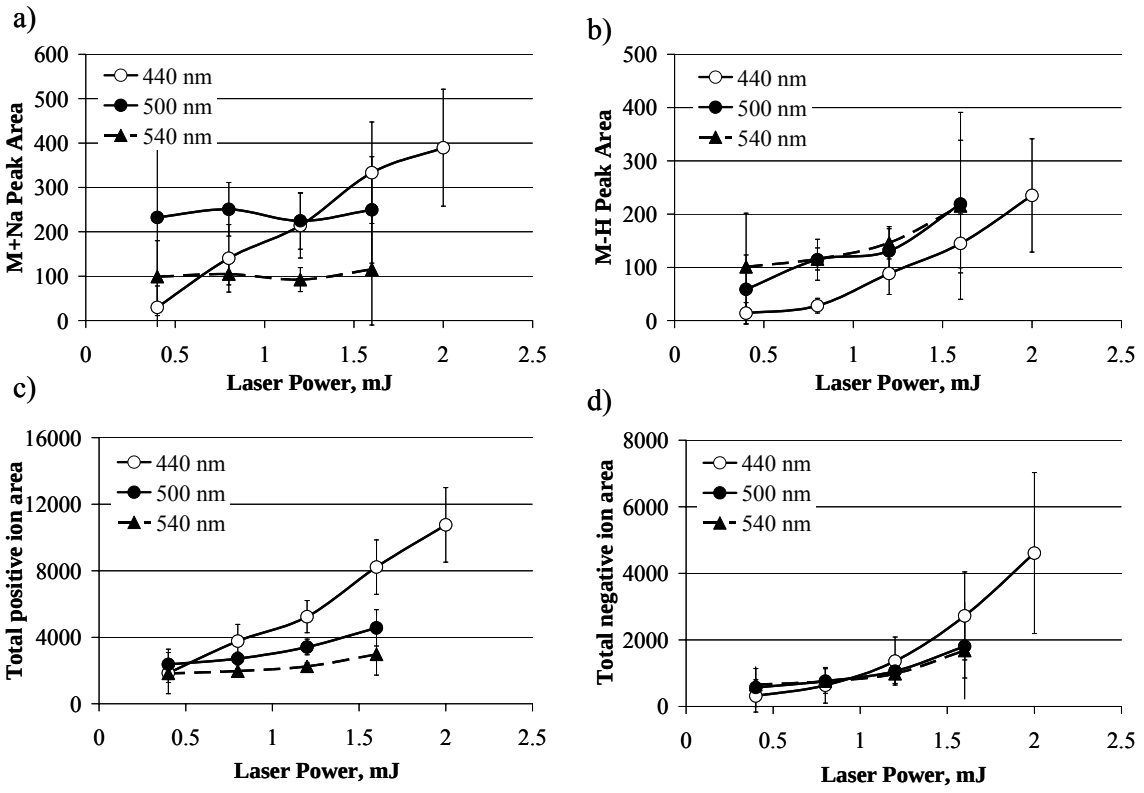

Figure 6.5 Peak area is plotted versus laser power for different desorption/ionization wavelengths for a) sodiated WGG ion (M+Na), b) deprotonated WGG ion (M-H), c) total sum of positive ion peak areas, and d) total sum of negative ion peak areas. The data was generated using the 5 nm gold nanoparticle matrix.

and negative ion area (sum for all m/z) steadily increases with increasing laser power. Figure 6.5c-d also shows the total ion peak area is generally highest at 440 nm and lower at 500 and 540 nm for a given laser power. This is presumably due to the higher energy per photon at shorter wavelengths, which may be causing both the creation of more overall ions and more fragmentation. Figure 6.6 shows a series of positive polarity AM for different LDI wavelengths (average laser power ~ 1.6 mJ/pulse). Although the major mass spectral features are similar among the different LDI wavelengths, there are less fragment ions as the LDI wavelength becomes longer. Figures 6.5 and 6.6 clearly demonstrate that lower laser powers and a laser wavelength resonant to SPR absorption, (λ ~ 520 nm) generate more intense quasi-molecular ion $[M+Na]^+$ and $[M-H]^-$ species with less fragmentation than excitation at an off-resonant condition (λ = 440 nm).

6.4.5 Analysis of sugars

The GNP matrix described thus far has been shown to assist the VIS-LDI of a small peptide prior to mass spectrometric analysis. The technique is also tested for the analysis of sugar. Figure 6.7 shows the positive and negative ion AM for samples containing the 5 nm GNP matrix with either D-ribose or L-arabinose (stereoisomeric sugars) using a Q-switched frequency doubled Nd:YAG laser (λ = 532 nm). Similar to the detection of the WGG peptide using VIS-MALDI, incorporating the GNP as a matrix was essential for detection; i.e. no mass spectrum could be obtained without the GNPs. The positive ion AM for each sugar has the same molecular/fragment ions with very similar intensities and both appear almost identical. However there are unique differences in the negative ion AM for each sugar. D-ribose has a significant peak at m/z

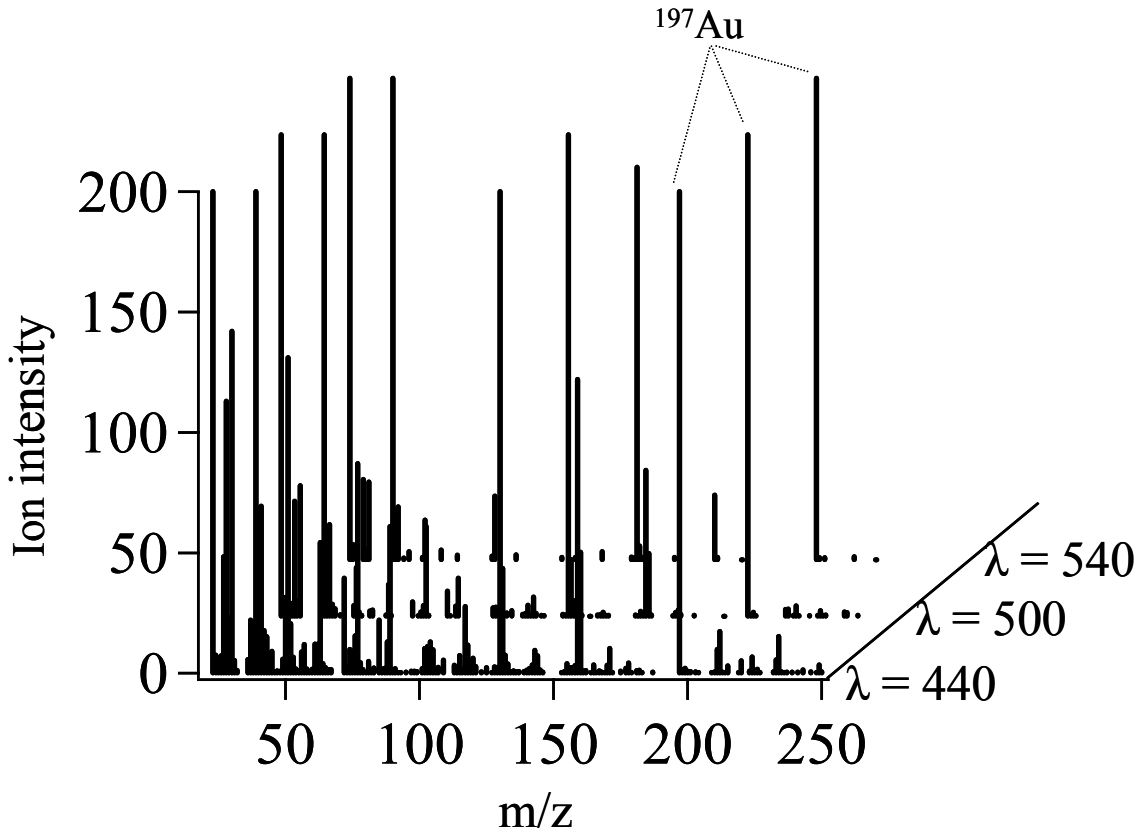

Figure 6.6 Stacked plots of the average mass spectrum generated from particles ionized at λ = 440, 500 and 540 nm.

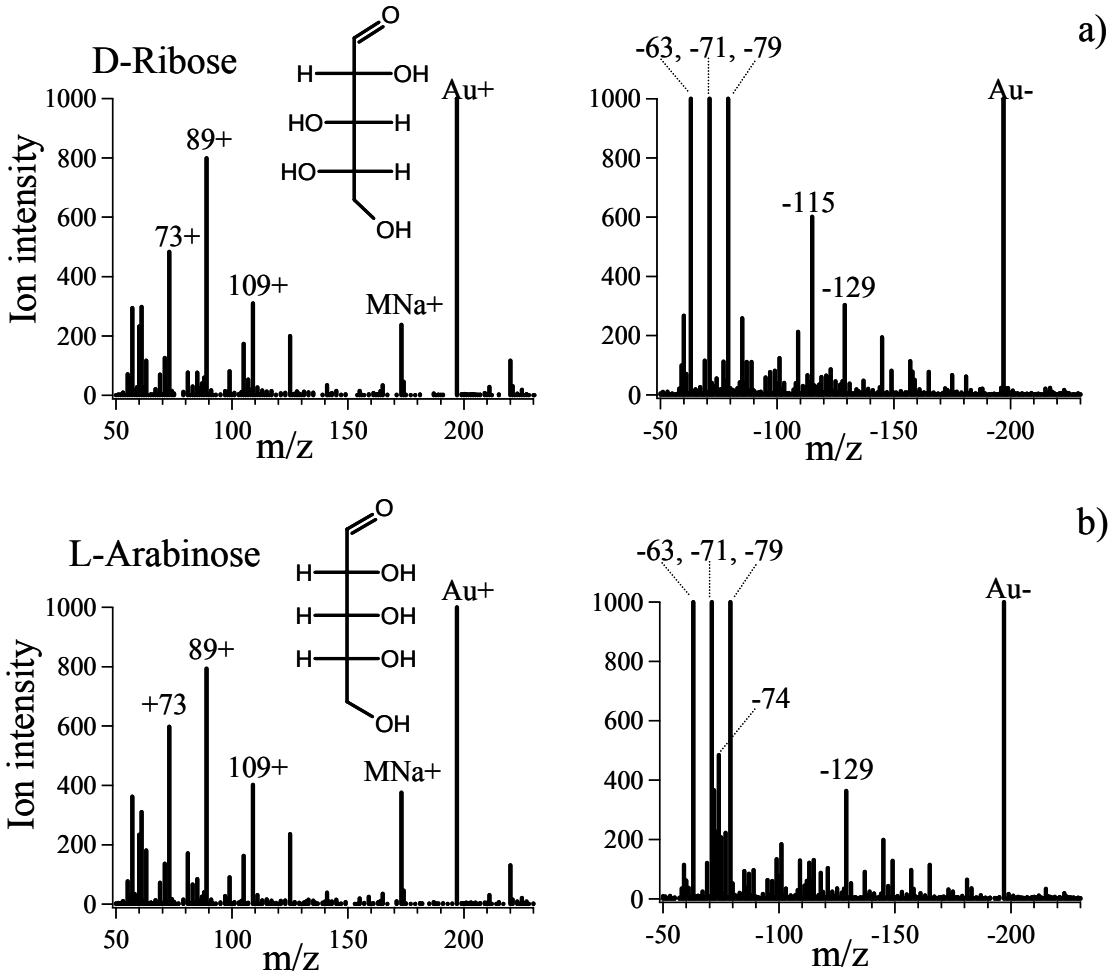

Figure 6.7 A positive and negative polarity average mass spectrum is shown that was generated from aerosol particles containing a 5 nm gold nanoparticle matrix and the sugar a) D-ribose or b) L-arabinose.

-115 while L-arabinose does not; L-arabinose has an ion peak at m/z -74 while D-ribose does not. These unique negative fragment ions could potentially be used to differentiate these two isomers. This result demonstrates that the VIS-MALDI technique with GNP matrix can also be applied to the analysis of other small molecules such as sugars.

6.4.6 VIS-MALDI using other metal particle matrices

Other noble metal nanoparticles could also possibly serve as a matrix for VIS-MALDI. Because silver nanoparticles also have a plasmon absorption in the visible wavelength region (maximum at $\lambda \sim 440$ nm), we tested a 14 nm silver nanoparticle (SNP) matrix with the WGG analyte. Figure 6.8 shows the positive and negative ion AM from particles containing SNPs and WGG peptide using laser radiation at a wavelength of 520 nm. The WGG peptide concentration was estimated to be similar to the experiments with GNPs and the average dried sample particle contained ~ 3000 SNPs. The positive ion spectrum contains only 4 significant peaks; three attributed to silver and silver cluster ions (Ag^+, Ag_2^+, Ag_3^+), and a peak at m/z 130+. There was no appreciable amount of WGG molecular ion present in the positive polarity mass spectra, however m/z 130+ could possibly be a fragment of the WGG analyte because this peak was not observed in SNP control experiments. It may be possible that smaller SNP may improve its performance as a VIS-MALDI matrix as observed for GNPs, however, further experiments are necessary.

The negative ion mass spectra showed a relatively intense peak attributed to the deprotonated WGG ion (^{317}M-H). There are also fragment ions at m/z 26-, 42-, 74-, 87-, 145-, 159-, 160- and 161-, which were not present in silver nanoparticle control

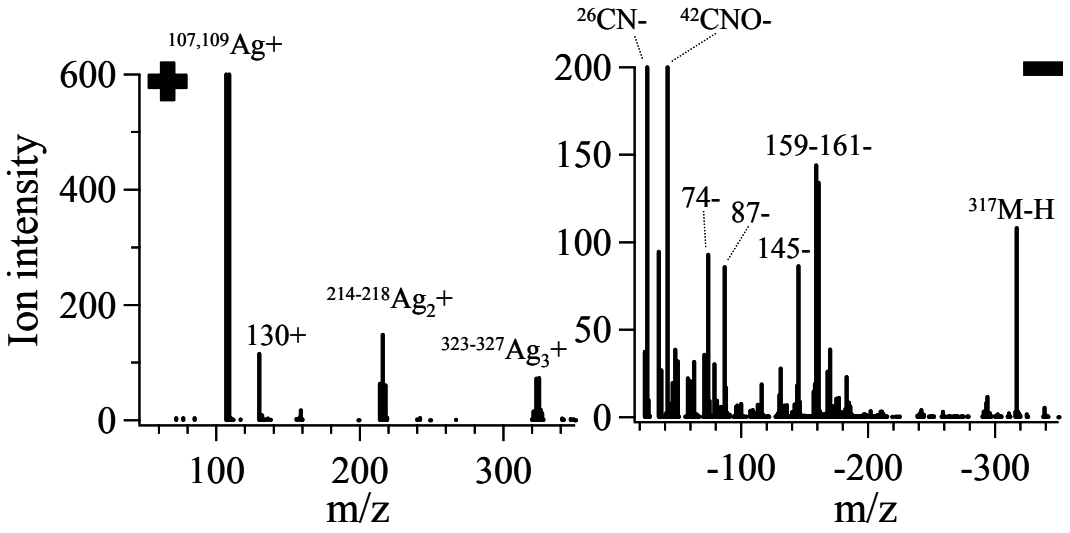

Figure 6.8 Positive and negative polarity average mass spectrum from aerosol particles containing 14 nm silver nanoparticles and the peptide WGG. Aerosol particles were desorbed and ionized using 540 nm laser radiation.

experiments and are therefore attributed to fragments of the WGG analyte. The amount of fragmentation using the SNP matrix appears to be more severe than with the 5 nm GNP matrix experiments. Desorption/ionization using an LDI wavelength near the peak plasmon absorption of the SNPs (λ = 440 nm) generated positive polarity mass spectra with similar features (peaks and intensity) to λ = 520 nm, however significantly less overall negative ion intensity was observed (data not shown). Further experiments using silver nanoparticles are necessary to understand this result. Although the 14 nm SNP matrix does appear to facilitate the VIS-LDI process of this peptide, given the above results the 5 nm GNPs appear to facilitate this process better.

An attempt was also made to use titanium oxide particles as a matrix for the VIS-MALDI technique. Titanium oxide particles have no SPR and little absorption in the visible wavelength range. As expected, no mass spectra were obtainable with a titanium oxide particle matrix at wavelengths ranging between 440-640 nm using laser powers similar to the experiments with gold and silver (< 3.0 mJ/pulse). This is further evidence that for noble metal nanostructures, the plasmon absorbance in the visible wavelength region is promoting the VIS-MALDI process.

6.5 Conclusion

This work demonstrates that the plasmon absorption of GNPs can be used to facilitate the VIS-LDI of a small peptide and sugar molecules from individual aerosol particles. Experiments using different sizes of GNPs at the same mass loading density suggests that the surface area of gold is an important factor that effects analyte ion intensity; increased surface area equated with obtaining an increased analyte ion signal.

Desorption/ionization near the maximum plasmon absorption of the GNP yields more intense negative polarity analyte ion signal than at shorter wavelengths. Furthermore, less analyte fragmentation was observed in mass spectra at wavelengths near the peak SPR versus shorter wavelengths. The technique has been shown to have potential for small molecule characterization. Silver nanoparticles, which also have a visible wavelength SPR, also facilitate the visible wavelength laser desorption/ionization process, however, under our experimental conditions GNPs were a superior VIS-MALDI matrix.

6.6 Acknowledgements

We would like to thank Professor Judy Kim and Diana Schlamadinger from the department of chemistry and biochemistry at the University of California San Diego for providing the tunable wavelength laser and assisting with its calibration and operating procedures.

Chapter 6, in full, is in preparation for submission to The Journal of Physical Chemistry-C for publication in 2007. Spencer, M.T., H. Furutani, S. J. Oldenburg, T. Darlington, K. A. Prather. The text is reprinted with permission from American Chemical Society.

6.7 References

Barnes, W.L., A. Dereux, and T.W. Ebbesen, Surface plasmon subwavelength optics, *Nature*, *424* (6950), 824-830, 2003.

Chen, L.C., T. Ueda, M. Sagisaka, H. Hori, and K. Hiraoka, Visible laser desorption/ionization mass spectrometry using gold nanorods, *Journal of Physical Chemistry C*, *111* (6), 2409-2415, 2007a.

Chen, L.C., J. Yonehama, T. Ueda, H. Hori, and K. Hiraoka, Visible-laser desorption/ionization on gold nanostructures, *J. Mass Spectrom.*, *42* (3), 346-353, 2007b.

Cohen, L.H., and A.I. Gusev, Small molecule analysis by MALDI mass spectrometry, *Anal. Bioanal. Chem.*, *373* (7), 571-586, 2002.

Cornett, D.S., M.A. Duncan, and I.J. Amster, Liquid-mixtures for matrix-assisted laser-desorption, *Anal. Chem.*, *65* (19), 2608-2613, 1993.

DeCarlo, P.F., J.G. Slowik, D.R. Worsnop, P. Davidovits, and J.L. Jimenez, Particle morphology and density characterization by combined mobility and aerodynamic diameter measurements. Part 1: Theory, *Aerosol Sci. Technol.*, *38* (12), 1185-1205, 2004.

Dreisewerd, K., The desorption process in MALDI, *Chemical Reviews*, *103* (2), 395-425, 2003.

Duff, D.G., A. Baiker, and P.P. Edwards, A new hydrosol of gold clusters .1. Formation and particle-size variation, *Langmuir*, *9* (9), 2301-2309, 1993.

Furutani, H., S.J. Oldenburg, L. Aluwihare, and K.A. Prather, Gold nanoparticle matrix for the enhancement of low molecular weight negative ions of saccharides by single particle laser desorption/ionization mass spectrometry, *Anal. Chem.*, *Submitted March, 2007*.

Furutani, H., S.J. Oldenburg, and K.A. Prather, Single particle matrix-assisted laser desorption / ionization mass spectrometry with a novel gold nanoparticle matrix, *Anal. Chem.*, *Submitted March 2007*.

Gard, E., J.E. Mayer, B.D. Morrical, T. Dienes, D.P. Fergenson, and K.A. Prather, Real-time analysis of individual atmospheric aerosol particles: Design and performance of a portable ATOFMS, *Anal. Chem.*, *69* (20), 4083-4091, 1997.

Holecek, J.C., K.A. Denkenberger, J.E. Mayer, R.C. Moffet, G. Poon, R.O. Sanchez, T. Rebotier, H. Furutani, Y. Su, S. Guazzotti, and K.A. Prather, Development of an

aircraft aerosol time-of-flight mass spectrometer, *Anal. Chem.*, *manuscript In preparation*, 2007.

Kamat, P.V., Photophysical, photochemical and photocatalytic aspects of metal nanoparticles, *J. Phys. Chem. B*, *106* (32), 7729-7744, 2002.

Karas, M., and F. Hillenkamp, Laser desorption ionization of proteins with molecular masses exceeding 10000 Daltons, *Anal. Chem.*, *60* (20), 2299-2301, 1988.

Kelly, K.L., E. Coronado, L.L. Zhao, and G.C. Schatz, The optical properties of metal nanoparticles: The influence of size, shape, and dielectric environment, *J. Phys. Chem. B*, *107* (3), 668-677, 2003.

Kim, J., K. Paek, and W. Kang, Visible surface-assisted laser desorption/ionization mass spectrometry of small macromolecules deposited on the graphite plate, *Bull. Korean Chem. Soc.*, *23* (2), 315-319, 2002.

Kinumi, T., T. Saisu, M. Takayama, and H. Niwa, Matrix-assisted laser desorption/ionization time-of-flight mass spectrometry using an inorganic particle matrix for small molecule analysis, *J. Mass Spectrom.*, *35* (3), 417-422, 2000.

Kirk, J.S., and P.W. Bohn, Surface adsorption and transfer of organomercaptans to colloidal gold and direct identification by matrix assisted laser desorption/ionization mass spectrometry, *J. Am. Chem. Soc.*, *126* (18), 5920-5926, 2004.

Kreibig, U., and L. Genzel, Optical-absorption of small metallic particles, *Surf. Sci.*, *156* (JUN), 678-700, 1985.

Link, S., and M.A. El-Sayed, Shape and size dependence of radiative, non-radiative and photothermal properties of gold nanocrystals, *Int. Rev. Phys. Chem.*, *19* (3), 409-453, 2000.

Liu, P., P.J. Ziemann, D.B. Kittelson, and P.H. McMurry, Generating particle beams of controlled dimensions and divergence 1: Theory of particle motion in aerodynamic lenses and nozzle expansions, *Aerosol Science & Technology*, *22* (3), 293-313, 1995a.

Liu, P., P.J. Ziemann, D.B. Kittelson, and P.H. McMurry, Generating particle beams of controlled dimensions and divergence 2: Experimental evaluation of particle motion in aerodynamic lenses and nozzle expansions, *Aerosol Science & Technology*, *22* (3), 314-324, 1995b.

McLean, J.A., K.A. Stumpo, and D.H. Russell, Size-selected (2-10 nm) gold nanoparticles for matrix assisted laser desorption ionization of peptides, *J. Am. Chem. Soc.*, *127* (15), 5304-5305, 2005.

Oldenburg, S.J., R.D. Averitt, S.L. Westcott, and N.J. Halas, Nanoengineering of optical resonances, *Chem. Phys. Lett.*, *288* (2-4), 243-247, 1998.

Otto, A., I. Mrozek, H. Grabhorn, and W. Akemann, Surface-enhanced Raman-scattering, *Journal of Physics-Condensed Matter*, *4* (5), 1143-1212, 1992.

Overberg, A., M. Karas, U. Bahr, R. Kaufmann, and F. Hillenkamp, Matrix-assisted infrared-laser (2.94-mu-m) desorption ionization mass-spectrometry of large biomolecules, *Rapid Commun. Mass Spectrom.*, *4* (8), 293-296, 1990.

Overberg, A., M. Karas, and F. Hillenkamp, Matrix-assisted laser desorption of large biomolecules with a TEA-CO2-laser, *Rapid Commun. Mass Spectrom.*, *5* (3), 128-131, 1991.

Prather, K.A., T. Nordmeyer, and K. Salt, Real-time characterization of individual aerosol particles using time-of-flight mass spectrometry, *Anal. Chem.*, *66* (9), 1403-7, 1994.

Schurenberg, M., K. Dreisewerd, and F. Hillenkamp, Laser desorption/ionization mass spectrometry of peptides and proteins with particle suspension matrixes, *Anal. Chem.*, *71* (1), 221-229, 1999.

Smith, C.J., S.Y. Chang, and E.S. Yeung, Characterization of neutral red as a visible-wavelength MALDI matrix, *J. Mass Spectrom.*, *30* (12), 1765-1767, 1995.

Su, Y., M.F. Sipin, H. Furutani, and K.A. Prather, Development and characterization of an aerosol time-of-flight mass spectrometer with increased detection efficiency, *Anal. Chem.*, *76* (3), 712-719, 2004.

Sun, Y.G., and Y.N. Xia, Gold and silver nanoparticles: A class of chromophores with colors tunable in the range from 400 to 750 nm, *Analyst*, *128* (6), 686-691, 2003.

Sunner, J., E. Dratz, and Y.C. Chen, Graphite surface assisted laser desorption/ionization time-of-flight mass-spectrometry of peptides and proteins from liquid solutions, *Anal. Chem.*, *67* (23), 4335-4342, 1995.

Tanaka, K., H. Waki, Y. Ido, S. Akita, Y. Yoshida, and T. Yohida, Protein and polymer analyses up to m/z 100,000 by laser ionization time-of-flight mass spectrometry, *Rapid Commun. Mass Spectrom.*, *2* (8), 151-3, 1988.

Tang, K., S.L. Allman, R.B. Jones, and C.H. Chen, Comparison of rhodamine dyes as matrices for matrix-assisted laser desorption ionization mass-spectrometry, *Org. Mass Spectrom.*, *27* (12), 1389-1392, 1992.

Ugarov, M.V., T. Egan, D.V. Khabashesku, J.A. Schultz, H.Q. Peng, V.N. Khabashesku, H. Furutani, K.S. Prather, H.W.J. Wang, S.N. Jackson, and A.S. Woods, MALDI matrices for biomolecular analysis based on functionalized carbon nanomaterials, *Anal. Chem.*, *76* (22), 6734-6742, 2004.

Wei, J., J.M. Buriak, and G. Siuzdak, Desorption-ionization mass spectrometry on porous silicon, *Nature*, *399* (6733), 243-246, 1999.

Wen, X.J., S. Dagan, and V.H. Wysocki, Small-molecule analysis with silicon-nanoparticle-assisted laser desorption/ionization mass spectrometry, *Anal. Chem.*, *79* (2), 434-444, 2007.

7 Conclusion and Future Directions

7.1 Conclusion

Knowing the sources, chemical composition, chemical transformations and morphology of aerosol particles is necessary to understand the environmental impact of particles. The majority of this dissertation has been devoted to using aerosol generation and particle size measurement techniques in direct combination with ATOFMS to give the atmospheric science and ATOFMS research communities' new ways to differentiate between particle sources, obtain quantitative chemical information, and measure particle density/morphology. Additionally, field measurements have shed new light on the chemical properties, morphologies, long range transport and chemical transformation of ambient particles.

Chapter 2 discussed results from the analysis of aerosolized new oil, used oil, unleaded fuel and diesel fuel samples using ATOFMS. A comparison of the petrochemical particle mass spectral signatures was then compared to the mass spectra from heavy duty diesel vehicle (HDDV) and light duty vehicle (LDV) particle emissions. The goal of this analysis was to obtain a better understanding of the unburned particle components that are emitted from cars and trucks to help differentiate between these sources during ambient sampling. Laboratory generated unleaded fuel and diesel fuel particle mass spectra did not match the majority of particle mass spectra from LDV or HDDV particles suggesting that there is not a significant fraction of unburned fuel on the exhaust particles. However, there were similar metal ions observed between the unleaded

fuel samples and LDV emissions suggesting LDV exhaust metals could be from metals in the fuel. Used HDDV oil mass spectra were characterized by an intense $^{40}Ca^{+}$ ion peak and less intense organic carbon (OC) and elemental carbon (EC) peaks. The HDDV oil mass spectra closely matched the mass spectra for the most dominant particle type (> 0.5 μm) emitted from diesel trucks. This suggests that a significant fraction of the unburned component of diesel exhaust particles is from lubricating oil. The used HDDV oil mass spectra are a unique indicator for HDDV exhaust particles.

Elemental carbon (EC) and organic carbon (OC) are two chemical species that have been observed as the dominant mass fraction in ambient particulate matter, and occur as both internal and external mixtures. The goal of the work presented in Chapter 3 was to generate a calibration curve that would allow us to obtain quantitative chemical information about the fraction of OC and EC in ambient particles. Historically this has been difficult for reasons highlighted in Chapter 3. The calibration curve was accomplished by generating mono-dispersed EC particles, coating them with a known thickness of OC and measuring their mass spectra using ATOFMS. The amount of EC and OC on particles was then related to the intensity of the corresponding marker ions in the mass spectra to generate a calibration curve relating ion intensity to the OC mass fraction. The calibration curve was then applied to ambient aerosols collected in Riverside, California. The trend and the mass fraction of OC measured with the ATOFMS was comparable to that measured using a standard semi-continuous thermal/optical method. These results show that obtaining quantitative information on the mass fraction of OC and EC in particles is possible using ATOFMS.

A modification of the experimental technique outlined Chapter 3 allowed us to measure the effective density of individual particles using a differential mobility analyzer (DMA) in conjunction with ATOFMS. The effective density is a function of both the material density and shape of the particle; effective density is equal to the material density for spherical particles. Chapter 4 discussed results using this technique to measure the effective density and chemical composition of particles from Riverside, California. During the summer in Riverside, the majority of chemically different particle types on a given day had the same effective density and generally appeared to have a spherical morphology. Although distinct particle types were observed, it is hypothesized that the majority of the mass on the particles is from condensation of secondary organic and inorganic species onto the primary core of the particle. Individual particle types would still be identifiable due to the various primary cores of the particles, but they would exhibit similar densities due to the presence of the same dominant coating of secondary species on each particle. Conversely, in the fall when Santa Ana winds brought relatively clean and dry air to the area, chemically different particle types also had different effective densities. During the Santa Ana event, when the potential for secondary processing was dramatically reduced due to the clean air conditions, the primary particles retained their distinct source chemical signatures and densities.

Chapter 5 discussed the results from ambient field measurements made on a remote island in the Republic of Maldives, located in the north Indian Ocean. The goal of this field campaign was to characterize the chemical composition of aerosol particles during the monsoonal transition period. During the monsoonal transition period the fraction and total number of particle types could be correlated to the direction of the incoming air

mass. Throughout the study biomass/biofuel accounted for approximately 75% of the EC soot particle numbers when the air mass originated from India. These EC and biomass particles were observed to be mixed with appreciable amounts of sulfate indicating that they had undergone a large degree of processing during transport. Because sulfate could significantly enhance the absorption of light by soot particles, this observed mixing state offers a possible explanation for the increase in solar heating measured during INDOEX atmospheric brown cloud episodes. The results described in Chapter 5 suggest that biomass and EC particles transported over the Indian Ocean should be represented as internally mixed with sulfate in regional climate models.

While ATOFMS is primarily used for atmospheric measurements, it can also be utilized for other analytical applications. In particular, ATOFMS can also be used to analyze compounds that are ionized using matrix assisted laser desorption/ionization (MALDI). Traditional MALDI techniques have had only limited success as a method for analyzing small molecules, due to the large number of interfering fragment ions from the organic acid matrices in the low mass region ($m/z < 400$). Chapter 6 presented results from experiments using noble metal nanoparticles as a matrix for facilitating visible wavelength (VW) desorption/ionization of small molecules from individual particles during ATOFMS analysis. Matrix assisted laser desorption/ionization mass spectrometry using visible wavelength laser radiation has had limited success due to the small number of matrix compounds capable of absorbing visible light. Chapter 6 showed that plasmon absorption of gold and silver nanoparticles within the visible wavelength region facilitates their use as matrices for visible wavelength LDI. Furthermore, because the

gold nanoparticles yield relatively few fragment ions, they are well suited as a matrix for the analysis of small molecules.

7.2 Future Directions

As is often typical of scientific research, most of the work discussed in this dissertation has been an incremental step that allows us to move forward to try and answer a new line of scientific questions. Analysis of oil and fuel aerosols in combination with car and truck particle emissions has given us the markers to identify freshly emitted particles from these sources. The next important question to answer is how these source markers change as particles age. Secondary organic and inorganic processing can significantly change the composition of primary particles. Can we still differentiate between diesel truck particles and light duty vehicle particles after a significant amount of atmospheric processing? If so, what are the identifying markers and are they the same markers under various ambient conditions? These questions must be addressed for accurate source apportionment of aged and transported anthropogenic particles.

Understanding the extent of atmospheric processing that particles undergo during aging and transport will require an accurate quantitative method for measuring specific chemical species. Aerosol time-of-flight mass spectrometry has the potential to yield quantitative chemical information from ambient data; however there is a lot of work that needs to be done. A logical next step entails more thorough lab analyses that explore the ATOFMS ion response to different core sizes of EC particles coated with various types and amounts of organic carbon. These studies would provide a much more robust

calibration curve and shed light on understanding how marker ions respond to changes in EC/OC mass fractions. Furthermore, ambient particles are much more complex than simply OC and EC and generally also contain inorganic ions such as sulfate, nitrate and ammonium. Establishing a calibration for the effects of these inorganic species on EC, OC and inorganic ion peak areas is also necessary to understand how changes in the particle matrix affect the measured ion intensities. Accomplishing these two projects would likely open up the potential for quantitative analysis of these specific chemical species from ambient ATOFMS data.

Another approach for extracting quantitative information from single particles is through the combination of size, chemical composition and effective density measurements by inline DMA-ATOFMS analysis. If the particles are spherical the effective density is equal to the material density which can then be used to determine the mass of the particle. This technique can be used to monitor changes in aerosol particle density, morphology and chemical composition simultaneously, which makes it a potentially powerful tool to relate changes in particle mass and shape to changes in chemical composition. Further, drying the aerosol before analysis using the DMA-ATOFMS technique could yield information about the amount of water contained on different particle types. The next step for this technique is to exploit it in various ambient environments and begin to relate changes in aerosol physical/chemical properties to changes in meteorology.

During APMEX the majority of EC and biomass particle types contained a significant amount of sulfate, suggesting these particles had undergone secondary processing during transport. An interesting result, however, is the virtual absence of

aged OC and nitrate, which are typically observed in areas influenced by urban air pollution. ATOFMS measurements in parts of India and south Asia where the transported air pollution originated would be useful to understand the chemistry of aerosols in the region. These measurements would give us information regarding the different particle types and the degree of processing that has occurred to particles prior to transport across the Indian Ocean. It is possible that aged OC and nitrate containing particles are present in the original pollution plume but are selectively scavenged during transport over the north Indian Ocean. A better understanding of the secondary processing that occurs during transport would also be gained. The APMEX data should also be compared to the spectral signature for aerosol forcing that was measured during the field campaign. Changes in the number concentration of specific particle types could potentially be correlated with changes in the aerosol spectral forcing signature. This could give us better information on which particle types are key to understanding aerosol radiative forcing.

There are many directions in which to take the gold nanoparticle VW-MALDI project. First, a more detailed analysis of the effect of different gold nanoparticle shapes and sizes on analyte ion intensity would be useful to better understand the relationship between surface area of gold and ion signal. Chapter 6 discussed the possibility of different ionization mechanisms using LDI at wavelengths near the peak plasmon resonance of gold nanoparticles versus shorter wavelengths. A more refined analysis using more closely spaced and shorter LDI wavelengths would be useful to understand these differences in the ion formation mechanisms at LDI. Analysis of a broader range of small molecules using the VW-MALDI technique would also be useful to fully explore

the potential benefits and limitations of this method for different small molecule types. Separating low abundance analytes from a complex solution could be useful for applications such as disease diagnostics. Modification of the gold nanoparticle surface can be used to selectively bind specific molecules in a complex mixture. These surface modified gold nanoparticles can be separated from the complex mixture and then VW-MALDI analysis could possibly be done directly to detect if they have bound to a specific analyte.

7.3 Final Thought

The work presented in this dissertation sincerely reflects the satisfaction I have had developing new analytical chemistry methods and making environmental field measurements. I hope that the research presented here invigorates my passion for this type of work within others, so that they will enjoy contributing their ideas to analytical and environmental chemistry as much as I have.